

**Applications of Laser Spectroscopy
to
Analytical Chemistry,
Environmental Monitoring
and Medicine**

Thomas Johansson

**Doctoral Thesis
Division of Atomic Physics
Lund Institute of Technology**

Lund 2002

Printed at KFS AB, Lund, Sweden
September 2002

Lund Reports on Atomic Physics, LRAP 286
ISSN 0281-2762
LUTD2(TFAF-1049)1-64(2002)
ISBN 91-628-5369-4

Till alla jag älskar . . .

Abstract

Sammanfattning

List of papers

1. Introduction	1
2. Interaction between light and matter	3
2.1. The nature of light	3
2.2. Basic aspects	3
2.3. Practical spectroscopy	6
2.3.1. Absorption Spectroscopy – the Beer Lambert Law	6
2.3.2. Fluorescence spectroscopy	7
2.3.3. Scattering	7
2.3.4. Light propagation in scattering and absorbing media	8
3. Fluorescence spectroscopy techniques	12
3.1. Background	12
3.2. Basic set-up of fluorescence equipment	12
3.2.1. Light sources	12
3.2.2. Light collectors	13
3.2.3. Light selectors	14
3.2.4. Detectors	14
3.3. Spectroscopy combinations	15
3.3.1. Point detection	15
3.3.2. Line detection	17
3.3.3. Area detection	21
3.4. Multivariate analysis techniques	25
3.4.1. Background	25
3.4.2. Principal component analysis	25
4. Applications adapted to analytical chemistry	27
4.1. Overview and historical background	27
4.2. Separation methods (chromatography)	27
4.2.1. Pressure driven chromatography	27
4.2.2. Electrophoresis	28
4.2.3. Electro-osmotic flow	28

4.3. Capillary electrophoresis	29
4.3.1. Injection techniques in capillary electrophoresis	31
4.3.2. Detection techniques in capillary electrophoresis	31
4.4. Analysis of levitated drops	33
4.4.1. Acoustic levitation	34
4.4.2. Monitoring of a levitated drop	34
5. Environmental monitoring by fluorescence LIDAR techniques	36
5.1. Background	36
5.2. Laser-induced fluorescence of monuments	37
5.2.1. Introduction	37
5.2.2. Evaluation of spectral signatures	37
5.3. Laser-induced fluorescence of seawater	38
5.3.1. Spectral signatures along a route	38
5.3.2. Depth resolved measurements	39
5.3.3. Fluorescence of <i>Posidonia Oceanica</i>	39
6. Medical applications	40
6.1. Introduction	40
6.2. Tumour selective substances	40
6.3. Fluorescence diagnostics	41
6.3.1. Introduction	41
6.3.2. Point measurements	41
6.3.3. Fluorescence imaging	42
6.4. Photodynamic therapy	43
6.4.1. Mechanisms of photodynamic therapy	43
6.4.2. Light sources	44
6.4.3. Treatment of superficial skin lesions	44
6.5. Interstitial photodynamic therapy	44
6.5.1. Introduction	44
6.5.2. IPDT system	45

Acknowledgements

Contributions by the author to different papers

Reference List

Abstract

In this thesis spectroscopic techniques have been used in the fields of analytical chemistry, environmental and medical applications. In analytical chemistry, laser induced fluorescence was used to image the separation of substances during capillary electrophoresis. Here, an optical fibre imaging technique facilitated a higher sensitivity compared with a lens imaging technique. The motion of the substances was also monitored. In a similar experiment, laser induced fluorescence was used to image substances that do not exhibit fluorescence. Levitated drops have also been used as a wall-free cuvette during the study of fat-cell behaviour and protein precipitation, where laser induced fluorescence detection was used in the first part and light scattering detection in the second part.

For environmental monitoring a lidar (light detection and ranging) system was used. Here, measurements have been performed at different monumental buildings to detect both biodeteriogen invasion and protective treatment. The system was also moved onto a ship for experiments in the Mediterranean Sea. Laser induced fluorescence was here used for monitoring of chlorophyll contents in the seawater together with distributed organic matter (DOM). With the use of depth resolved measurements, the water absorption was studied.

In medical applications, laser induced fluorescence techniques have been used for spectral imaging of human normal and tumour tissue. For the treatment of the tumours, photodynamic therapy was employed. Three to six optical fibres, connected to a diode laser, were used and inserted in the tumour tissue. A sensitising agent was utilised to demarcate tumour tissue by fluorescence, and also to induce cell death.

Sammanfattning

Det ljus som vi vanligen ser, har spritts av objekten i vår omgivning. Ett annat ljusfenomen är fluorescens, som kan användas inom olika områden för analys av prover. Olika substanser ger skilda fluorescensprofiler. Om dessa inte helt överlappar varandra kan substanserna särskiljas. Områden, där ljusdiagnostik har använts inom ramen för detta arbete, är kemisk analys, miljömätteknik och cancerdiagnostik. Likaså har ljus använts för cancerbehandling.

Inom analytisk kemi används många olika detektionsmetoder. Här har i huvudsak laserinducerad fluorescens använts inom separationstekniken kapillär elektrofores. I denna teknik används mycket tunna rör (kapillärer) för separation av substanser med hjälp av ett elektrisk fält. För detektion i dessa kapillärer behövs en känslig metod och fluorescens kan då användas. För effektiv ljusinsamling användes optiska fibrer vilket gav en högre känslighet med en faktor 10. En annan analysmetod inom analytisk kemi är att med ljus belysa svävande droppar innehållande substansen av intresse. Även här utnyttjas fluorescensmekniken för detektion. Ett exempel på ett sådant experiment är att undersöka fettceller med avseende på deras fettsyreproduktion. Vid en tredje typ av undersökning studerades vilka betingelser som behövs för att kristallisering av protein skall ske. Detta undersöktes med hjälp av ljusspridningsteknik.

Fluorescens användes också för undersökning av algbeväxning på historiska byggnader som Lunds domkyrka och Parmas katedral. För att kunna mäta på alla svåråtkomliga ställen användes en metod för mätning på långt avstånd. Här skickas en laserpuls iväg och fluorescensen samlas in med hjälp av ett teleskop. Med denna metod kan alger liksom andra substanser på byggnadsfasader detekteras. Samma system användes för att mäta alghalten och organiska föroreningar i Medelhavet utanför Italiens västkust. Här riktades laserstrålen rakt ner i havet från ett undersökningsfartyg, och fluorescensen från olika djup samlades in.

Inom medicinen användes en fluorescensmetod för att diagnosticera cancer. Detta skedde också med hjälp av laserbelysning. För att åstadkomma detta används en hjälpsubstans för att erhålla en specifik fluorescenssignal från cancertumörer. Samma substans användes också vid behandling av cancer. Då utnyttjades rött ljus, vilket här kom från en 2 Watts diodlaser. Detta ljus överför sin energi till substansen, vilken i sin tur exciterar syret i vävnaden. Då fås en syreform som är starkt reaktiv vilket leder till celledöd.

List of papers

1. S. Santesson, E. Cedergren, T. Johansson, T. Laurell, J. Nilsson and S. Nilsson, Screening of protein nucleation conditions using levitated drops, Manuscript.
2. S. Santesson, M. Andersson, E. Degerman, T. Johansson, J. Nilsson and S. Nilsson, Airborne cell analysis, *Analytical Chemistry* **72**, 3412 (2000).
3. T. Johansson, M. Petersson, J. Johansson and S. Nilsson, Real-time imaging through optical fiber array-assisted laser-induced fluorescence of capillary electrophoretic enantiomer separations, *Analytical Chemistry* **71**, 4190 (1999).
4. J. Johansson, T. Johansson and S. Nilsson, Fluorescence imaging of light absorption for axial-beam geometry in capillary electrophoresis, *Electrophoresis* **19**, 2233 (1998).
5. G. Cecchi, M. Bazzani, C. Cucci, D. Lognoli, I. Mochi, L. Pantani, V. Raimondi, R. Carlà, B. Breschi, D. Novelli, T. Johansson, P. Weibring, H. Edner and S. Svanberg, Probing the marine environment with fluorescence lidars - Evaluation of three fluorosensors in a field campaign, Manuscript.
6. P. Weibring, T. Johansson, H. Edner, S. Svanberg, B. Sundnér, V. Raimondi, G. Cecchi and L. Pantani, Fluorescence lidar imaging of historical monuments, *Applied Optics* **40**, 6111 (2001).
7. D. Lognoli, G. Cecchi, I. Mochi, L. Pantani, V. Raimondi, R. Chiari, T. Johansson, P. Weibring, H. Edner and S. Svanberg, Fluorescence lidar imaging of the Parma cathedral and baptistry, Submitted to *Applied Physics B*, July (2002).
8. T. Johansson, G. Valentini, S. Andersson-Engels, G. Canti, A. Pifferi, P. Taroni, R. Cubeddu, K. Svanberg and S. Svanberg, Spectroscopic characterisation of non-melanoma skin lesions using multi-colour and lifetime fluorescence imaging, Manuscript.
9. M. Stenberg, M. Soto Thompson, T. Johansson, S. Pålsson, C. af Klinteberg, S. Andersson-Engels, U. Stenram, S. Svanberg and K. Svanberg, Interstitial photodynamic therapy. Diagnostic measurements and treatment in rat malignant experimental tumours, *SPIE* **4161**, (2000) Eds. I. J. Bigio, G.J. Pupples, K. Svanberg and R.W. Steiner.
10. T. Johansson, M. Soto Thompson, M. Stenberg, C. af Klinteberg, S. Andersson-Engels, S. Svanberg and K. Svanberg, Feasibility study of a system for combined light dosimetry and interstitial photodynamic treatment of massive tumors, *Applied Optics* **41**, 1462 (2002).

11. M. Soto-Thompson, T. Johansson, N. Bendsoe, A. Derjabo, J. Kapostins, S. Pålsson, U. Stenram, S. Andersson-Engels, J. Spigulis, S. Svanberg and K. Svanberg, Photodynamic therapy of basal cell carcinoma with multi-fibre contact light delivery, Manuscript.

Additional work is presented in

A. H. Nilsson, M. Wiklund, T. Johansson, H.M. Hertz and S. Nilsson, Microparticles for selective protein determination in capillary electrophoresis, *Electrophoresis* **22**, 2384 (2001)

B. L. Schweitz, M. Petersson, T. Johansson and S. Nilsson, Alternative methods providing enhanced sensitivity and selectivity in capillary electroseparation experiments, *Journal of Chromatography* **892**, 203 (2000)

C. V. Raimondi, P. Weibring, G. Cecchi, H. Edner, T. Johansson, L. Pantani, B. Sundnér, and S. Svanberg, Fluorescence imaging of historical buildings by Lidar remote sensing, *SPIE* **3496**, 15 (1998)

D. P. Weibring, G. Cecchi, H. Edner, T. Johansson, L. Pantani, V. Raimondi, B. Sundnér, and S. Svanberg, Non destructive control of historical buildings by fluorescence Lidar, Proc. 6th Int. Conf. on Non-Destructive Testing and Microanalysis for the Diagnostics and Conservation of the Cultural and Environmental Heritage, Rome May 17-20, 1999, p. 431

E. L. Pantani, G. Ballerini, G. Cecchi, E. Edner, D. Lognoli, T. Johansson, V. Raimondi, S. Svanberg, P. Tiano, L. Tomaselli and P. Weibring, Experiments on stony monument monitoring by laser-induced fluorescence, *J. Cult. Heritage* **1**, 345 (2000)

F. P. Weibring, D. Lognoli, R. Chiari, G. Cecchi, H. Edner, T. Johansson, L. Pantani, S. Svanberg, D. Tirelli and M. Trambusti, Lidar remote sensing of the Parma Cathedral and Baptistery, *SPIE* **4402**-16 (2001).

1. Introduction

Mankind has used both fire and light from time immemorial. First of all fire was discovered, thereafter new and different light sources were developed such as the torch and today the electric light. In the year of 1958 A.L. Schawlow and Ch.H. Townes published a paper about essential requirements for laser action. A few years later, the Nobel Prize in Physics 1964 was awarded to N.G. Basov, A.M. Prokhorov and Townes for their development of the maser and laser principles. However, light had been used in technical applications long before the laser was invented, e.g. in spectroscopy, but with the laser a new star was born. The laser is a powerful tool and today it is used in various areas. It would be possible to fill several pages with a listing of applications where the laser technology is used.

One of the applications where lasers can be used is to get a fundamental understanding of how and why atoms and molecules act as they do. Here, the laser light is used to induce an action in the system and its response is studied. Atoms and molecules have unique energy level structures and interact with light of unique wavelengths in spectroscopic processes. Dilute gases or even single atoms can be studied. In order to try to explain this nano-cosmos, theoretical models are constructed. When the number of molecules increases these nano-cosmos types of models do not work, because the systems become too complicated. In these cases the approach is to study the mean behaviour of all molecules, i.e. to model the material. For the study of samples, connected to the title of this thesis, very often the mean behaviour is studied during experiments. Here, macro models are used. One can mention how light is absorbed, for example within tissue. It would be very hard and time consuming to use models of how the cell organelles and the complex molecules interact with light. Instead, models of how light interacts with a volume with some mean characteristic are used in, for example, photodynamic cancer treatment. By this method the behaviour of a single cell can be studied, although the actual organelle mechanisms are hardly seen.

When investigations of a system are performed, techniques employing light can be favourable since non-destructive measurements can be done. Nonintrusive, noncontact and remote recordings of the object properties can be made. Finally, *in situ* and *in vivo* measurements can be made with light detection techniques.

The advantages described above have been used throughout the experiments reported in this thesis, which deals with applied laser spectroscopy. Laser radiation cannot only be used for sensitive chemical analysis of samples in spectroscopic processes of different kinds. It can also be used to induce molecular reactions, both in chemistry and in the life sciences. Such aspects relate to photosynthesis in plants and algae, but also to the photochemical destruction of cancer tumours; processes which have also been studied in the present work.

Although the fields of applications studied in this thesis - analytical chemistry, environmental monitoring and medicine - may seem diverse, we will find that the principles lying behind are very similar and encourage cross-disciplinary work of the kind presented. Laser-induced fluorescence was shown as useful for probing separation processes in the chemistry laboratory, as for studying the vertical water column in the Mediterranean Sea in ship-borne measurements, to map out areas of biodeteriogen invasion on medieval cathedral facades and to localise human cancer. Clearly, the geometrical scales are vastly diverse. Similarly, photon propagation and light scattering are governed by the same principles, whether they were studied in microdroplets with minute contents of protein precipitate, in maritime laser bathymetry, or in a malignant tumour requiring the correct dose of photodynamically active, cell killing light.

2. Interaction between light and matter

2.1. The nature of light

Normally we interpret light as something we can see, or rather detect with our eyes. In a more physical view it is a kind of electromagnetic radiation. This radiation can be described as a wave, but light can also be interpreted as moving energy quanta. Depending on the experiment, one or the other of the two descriptions is more adequate. We talk about the duality of light. The radiation is characterised by its wavelength λ or its frequency ν , fulfilling the relation $\nu\lambda=c$ (c velocity of light). According to the quantum theory, the energy of a quantum (photon) is $E=h\nu$, where h is Planck's constant.

Visible light has wavelengths ranging from 400-700 nm. In the study of light interaction with matter, frequently referred to as spectroscopy, we also have to deal with electromagnetic radiation outside this range. The region from 100-400 nm, referred to as ultra-violet light (UV), is also commonly used in spectroscopy, as is the 700 nm-100 μm range, called infrared light (IR); see Figure 1.

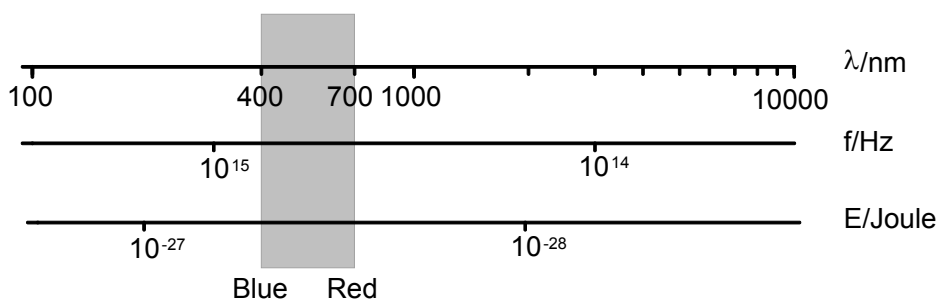


Figure 1 Electromagnetic radiation expressed in different units

2.2. Basic aspects

Atoms and molecules can only be internally arranged in certain allowed configurations, each with a well-defined intrinsic energy. These configurations are thus often represented with an energy-level diagram. Atoms and molecules have characteristic energy levels, which are governed by the laws of quantum mechanics. In principle, the Schrödinger equation yields the possible energy levels, but only simple systems can be calculated exactly. However, many approximate methods, employing lots of computer power, such as the density-functional theory (Nobel Prize to W. Kohn and J.A. Pople 1998) can handle quite complex systems. Normally, most of the atoms or molecules are in the lowest energy state. An impinging photon can transfer its energy to the atom and promote it to a higher

state. However, the energy of the photon to be absorbed must match the energy level separation (energy conservation).

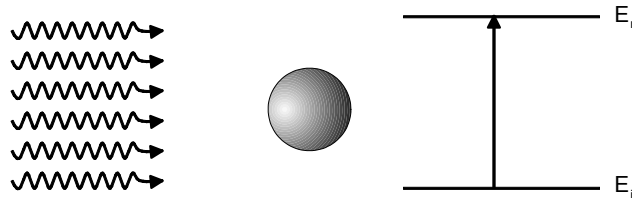


Figure 2 Interaction between radiation and an atom

When a photon, with energy $E=E_n-E_i=h\nu$ (Figure 2), interacts with an atom and the energy is transferred to the atom, we refer to this process as resonance absorption. If there is a slight mismatch between the energy of the photon and the energy-level separation, there still exists a probability for absorption corresponding to the natural radiation width ($\Delta\nu_n$) of the upper level. This width reflects the Heisenberg uncertainty of a level with lifetime τ according to $\Delta\nu_n=1/(2\pi\tau)$. Another situation pertains when the atom already is excited and the radiation interacts with the system. In this case an energy quantum may be released from the atom, which is called stimulated emission. The probability for this process is the same as for absorption. The photon emitted has the same direction and phase as the incoming photon and this coherence increases the radiation throughput through the medium. An atom can also emit radiation without any disturbances from the surroundings. The theory of this spontaneous emission will not be treated here due to the complexity of quantum electrodynamics that must be used.

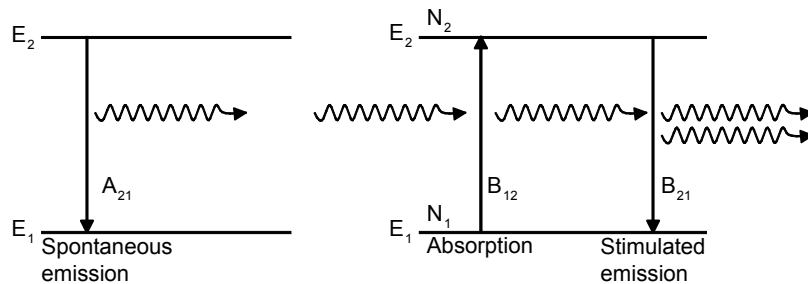


Figure 3 Different radiative processes

The Einstein coefficients B_{12} , B_{21} and A_{21} are used to describe the rate of the absorption and emission of photons; see Figure 3. The change in the population of a two-level system can be written as

$$\frac{dN_1}{dt} = -\frac{dN_2}{dt} = -B_{12}\rho(\nu)N_1 + B_{21}\rho(\nu)N_2 + A_{21}N_2$$

This means that the change in N_1 equals the change in N_2 and Boltzmann's law defines the distribution of the population at thermal equilibrium

$$\frac{N_1}{N_2} = \exp\left(\frac{h\nu}{kT}\right)$$

From these relations, and the Planck radiation law, we can infer, that $B_{12}=B_{21}$ and an expression for A_{21} can be derived as

$$A_{21} = B_{21} \frac{16\pi^2 \hbar \nu^3}{c^3}$$

By defining $A_i = \sum(A_{ik})$ the decay rate from an energy level is expressed as $N = N_0 \exp(-t/\tau)$ where $\tau = 1/A_i$. A calculation of the mean time before an atom decays from a higher state to a lower one, results in $t_{\text{mean}} = \tau$ with the variance τ . The mean lifetime is also used to express the natural radiation width, $\Delta\nu_N = 1/2\pi\tau$, which points out the smallest frequency range an emission has due to the lifetime of the energy level. After resonance absorption the atom decays back to the ground level while resonance radiation is emitted. There are possibilities for the decay back to terminate at levels above the ground level. If so, the light emitted is called fluorescence radiation.

When the difference of the energy levels does not correspond to the photon energy of the incoming radiation, no absorption, but weak scattering effect may still occurs. The different scattering processes are named after Rayleigh, Raman and Mie. Rayleigh and Raman scattering occurs when the wavelength of the radiation is large compared to the size of the scatterers. In Rayleigh scattering, the emitted wavelength is the same as the incident one (elastic scattering), while in Raman scattering, a shift towards longer (Stokes shifted) or shorter (Anti-Stokes shifted) wavelengths occurs. In a quantum mechanical description of the scattering effect, virtual energy levels are introduced according to Figure 4. The scattering intensity I increases with decreasing wavelength ($I \propto 1/\lambda^4$). The inelastic Stokes and anti-Stokes components have an intensity of approximate 1/1000 of the Rayleigh scattering.

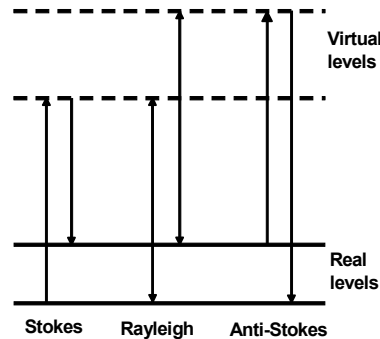


Figure 4 Rayleigh and Raman processes

Mie scattering is, like the Rayleigh scattering, an elastic radiation process originating from scattering towards particles considerably larger than the wavelength of the incoming light.

2.3. Practical spectroscopy

2.3.1. Absorption Spectroscopy – the Beer Lambert Law

If a beam of light is sent into a sample, which can be a gas, a liquid or a solid, photons with the right energy will be absorbed. In principle, the rate of the photon absorption could be treated by quantum mechanics, i.e. the solution of the Schrödinger equation. This is, however, a very complex task. Instead a more practical and phenomenological approach can be taken. By using the Beer-Lambert law, the absorption can be related to the concentration of the species.

If light with intensity P_0 is directed onto a cuvette the intensity decreases exponentially through the sample. The intensity P at the position x is obtained from the relation $P=P_0e^{-\mu_a x}$; see Figure 5, where μ_a is the absorption coefficient. μ_a describes the probability per unit distance for an absorption event to occur. More exactly, the probability for absorption in the infinitesimal distance dx is $\mu_a dx$. The inverse of the absorption coefficient ($1/\mu_a$) is in the absence of scattering the mean free path for a photon. This method can thus be used to measure the absorption coefficient of a sample. The method is commonly used in spectrophotometers. One restriction of this method is that the sample must be homogenous and non-scattering, which often is the case in many chemical applications. In scattering media, such as biological tissue, the Beer-Lambert law cannot be directly applied. Instead other methods to describe the light propagation in the sample are used, such as transport theory.

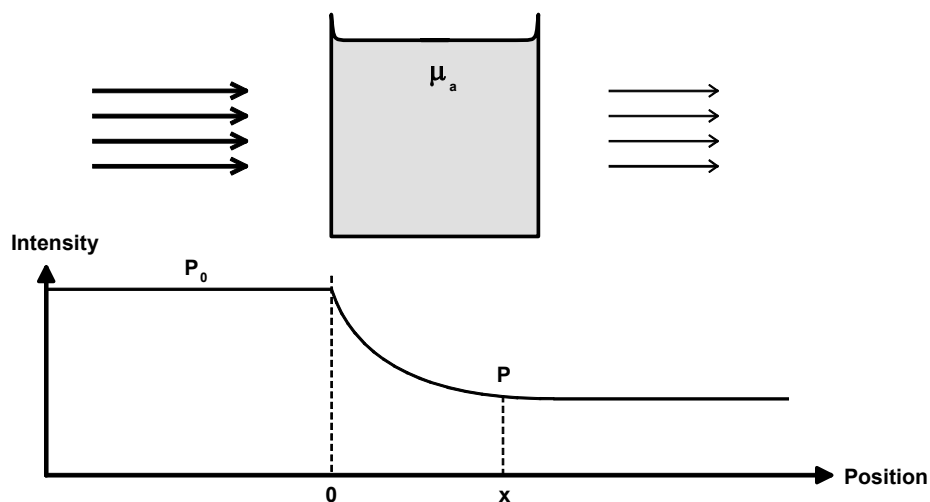


Figure 5 Light absorption in a cuvette with an absorbing medium

2.3.2. Fluorescence spectroscopy

The phenomenon when light is absorbed and then re-emitted at another wavelength is called fluorescence; see Figure 6. Fluorescence is very often used in practical spectroscopy because of its high sensitivity. Since a wavelength shift occurs, the detection can be made without any disturbance of the excitation light. This is an important feature in contrast to absorption measurements, where scattered light can cause problems, which are due to an increase of the background signal.

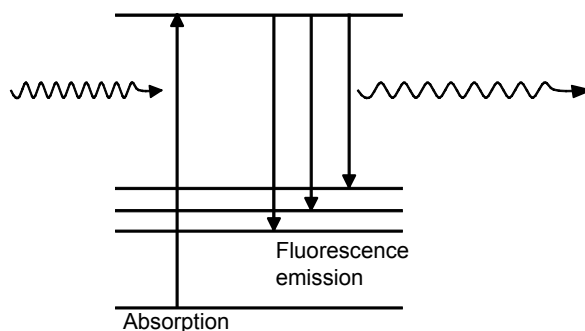


Figure 6 The basics of fluorescence

2.3.3. Scattering

If light is not absorbed it may be scattered in the sample by inhomogeneities with differences in refractive index. In fact, absorption and scattering most frequently occur concurrently. In the same way as μ_a describes absorption, scattering is characterised by a

scattering coefficient, μ_s . It describes how many times per unit length a photon will change direction on average. The probability distribution function (phase function) of the new direction is often described by a single parameter, the anisotropy factor (g). It is defined as the average *cosine* of the deflection angle. If the photons are most likely scattered in the forward direction, then g has values close to one, and if the scattering is isotropic then g is close to zero. Very often, the scattering medium behaves like a collection of small particles, and the scattering can therefore be described as Mie scattering, which in its pure form deals with spherical particles. The angular probability distribution can often be described with a Henyey-Greenstein function (Figure 7), and has been shown to adapt fairly well to skin [1].

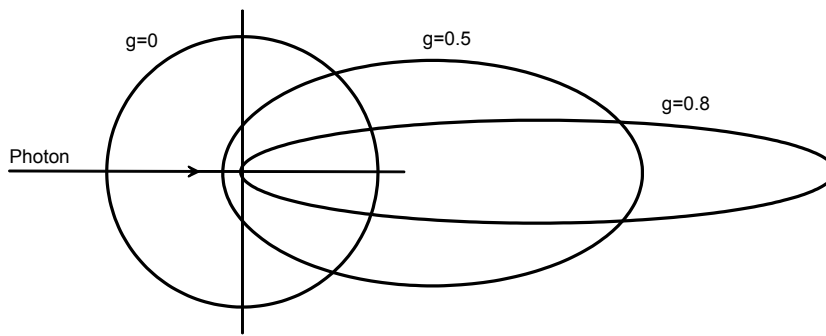


Figure 7 The Henyey-Greenstein function for different g -values

To characterise how far the photons must travel before light can be regarded as isotropic, the inverse of the reduced scattering coefficient (μ_s') is used. It is defined as $\mu_s' = (1-g)\mu_s$. Another important property in light propagation through scattering media is the total attenuation coefficient defined by $\mu_t = \mu_a + \mu_s$. The inverse of μ_t , ($1/\mu_t$), is called the mean free path and explains how far a photon will travel on average before either absorption or scattering will occur. A further useful concept is the linear transport coefficient μ_{tr} , defined as $\mu_{tr} = \mu_a + (1-g)\mu_s = \mu_a + \mu_s'$. The inverse of μ_{tr} , ($1/\mu_{tr}$), defines the distance after which the scattered light is fully isotropic.

2.3.4. Light propagation in scattering and absorbing media

In the description of light propagation in many natural materials, such as biological tissue, the duality of light can be utilised in treating the light, sometime seen as waves and sometimes as particles. When light is reflected off the tissue, it can be treated as a wave, where the reflection depends on the angle of incidence, polarisation and the index of refraction. Inside the tissue, the light can be considered as particles when the photons are absorbed or scattered.

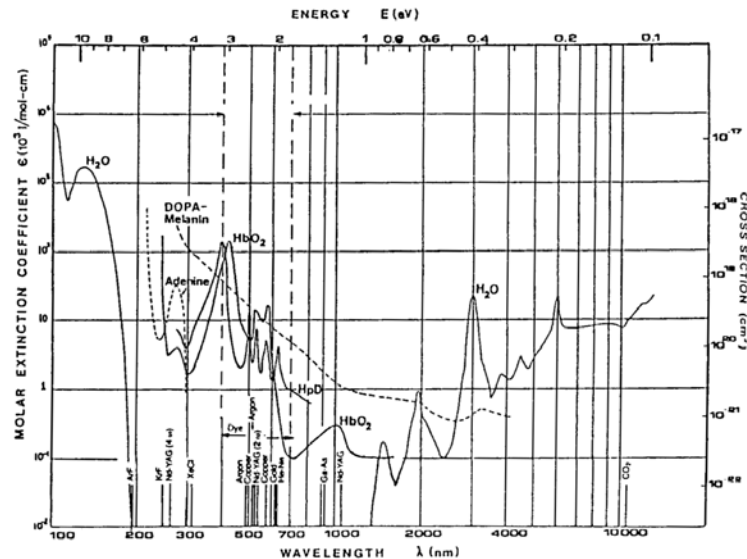


Figure 8 Absorption coefficients of different species in human tissue [2]

The behaviour of light, in e.g. human tissue, depends strongly on the absorption of the major constituents such as haemoglobin, protein and water; see Figure 8. In the short wavelength region up till about 600 nm we see that most light is absorbed while absorption is low in the near IR region. Then scattering instead becomes the dominating factor, which means that light can travel a long way before it is absorbed, but it will be scattered many times. When the light is absorbed, the energy will mostly be transferred into heat in the absorbing volume. All these circumstances around the absorption and scattering effects point out that it is very important to correctly model the behaviour of the light inside the tissue. Modelling the light transport is important when light is used for treatment such as in photodynamic therapy (PDT) of tumours, or in optical mammography [3,4]. Transport aspects are also important in fluorescence diagnostics due to two aspects. The first is how the excitation light is transmitted inside the tissue, and the second one is how the fluorescence light is propagating on its way towards the detector.

Transport theory treats the light energy (or intensity) flow inside tissue and it is based on a statistical approximation of the photon transport. Studying the energy flow in a small volume element of the tissue is of the basis of transport theory; see Figure 9. Transport theory does not consider light waves or phase behaviour, which means that no diffraction or interference effects are involved. The only important aspect is how the light is absorbed and scattered, or in energy terms, how the energy in volume elements is increased or decreased due to absorption and/or scattering under the simultaneous influence of a light source, which, for example, can be the tip of a cancer treating optical fibre (Papers 9, 10 and 11) [5,6]. The three tissue property constants discussed above; the absorption coefficient (μ_a),

the scattering coefficient (μ_s) and the anisotropy factor (g), are used to describe how the light flows inside the tissue. Normally, transport theory does not include fluorescence or other processes where the light wavelength is altered. However, special extended methods can solve this problem [7,8].

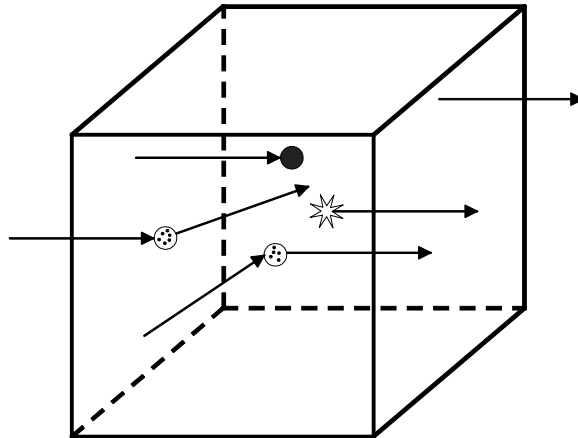


Figure 9 Photon events in transport theory

When the transport equation is to be solved, different techniques can be used. One way is to re-arrange the transport equation into a diffusion equation. As the name implies, further assumptions are made such as that the light is being diffuse (almost isotropic). This means, that the diffusion equation is not valid close to a light source, where a memory from the injection of light is still kept. However, the diffusion equation frequently yields good results far away from the light sources for situations when the absorption is much smaller than the scattering. This is because the light becomes isotropic after a sufficient number of scattering events. We understand, that due to this, μ_s must be much larger than μ_a , since otherwise the photons are absorbed before they get a chance to behave like diffuse light. The diffusion equation is difficult to solve for a complex geometry, and analytical solutions only exist for simple cases. To solve the diffusion equation for complex geometries, numerical methods are used.

The *finite element method* (FEM) is a numerical method with which mathematical problems can be solved. It is widely used in applications in the fields of, e.g., chemistry, acoustics and electromagnetic-wave propagation, where partial differential equations are to be solved. It is therefore suitable to solve the diffusion equation with this method [9]. The volume, for which the light fluence is wanted, is divided into smaller elements and the connections between the nearby elements are defined according to the partial differential equation. In-between these connections a linear behaviour is assumed. This results in a

linear system, which can be solved mathematically. Books in this subject can be found [10,11].

Another approach to obtain values for the light fluence rate is to use the probabilistic Monte Carlo model. No analytical solution of the transport equation is then provided, since we deal with a statistical method. The name “Monte Carlo” refers to “throwing the dice”, referring to that the scattering and absorption somewhere in the volume is governed by prescribed statistical laws – or by chance. The basic idea is presented in Figure 10 [12,13]. First, a photon is sent towards the object and here it will be reflected away or transmitted

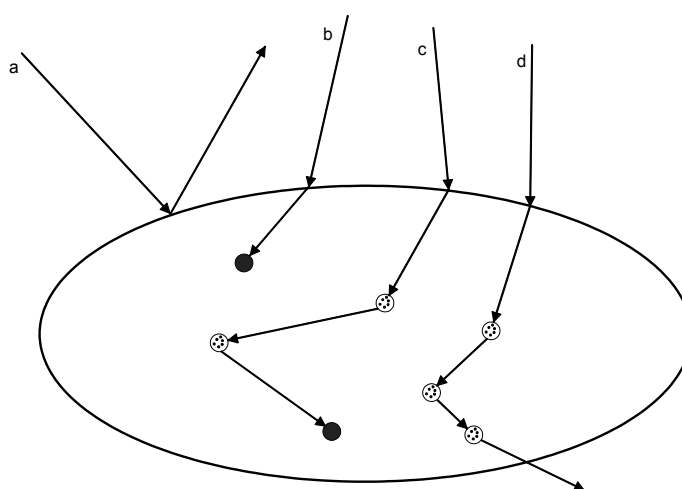


Figure 10 Schematic events in a Monte Carlo simulation

into the tissue, which depends on the difference in refractive index of the two media. If the photon is reflected off the tissue, then another photon path is simulated. If not, the photon will travel a certain distance in the medium before an event will take place. The distance is derived from its probability distribution function, which is a function of μ_t . If the event is an absorption, then the position in the medium is noted. If the photon is to be scattered, a scattering angle is calculated with the help of the Henyey-Greenstein probability function, and a new distance to the next event is calculated. This scattering is continued until the photon is absorbed, and this event is added to the absorption map of the medium, or the photon leaves the sample through its boundaries. Then a new photon path is followed. In reality, the flow of photons is millions per second. Here, the signal-to-noise ratio of the calculated distributions depends on how many photons are simulated. The number of simulated photons needed depends on how large the volume is, and for a volume of some cm^3 , approximately several millions of photons have to be followed, requiring substantial computer time.

3. Fluorescence spectroscopy techniques

3.1. Background

Optical measurement techniques are widely used for determination and quantification of various substances. Fluorescence spectroscopy is frequently employed for this purpose. It is both selective and sensitive, and the measurements are mostly noninvasive.

The origin of fluorescence was briefly explained earlier in Section 2.3.2. The so-called Jablonski diagram for a substance with a given energy level set-up explains the appearance of the fluorescence spectrum. However, very sharp peaks are obtained only for dilute gases. In liquids and solids at room temperatures, the peaks are broadened due to perturbations between the molecules. This results in spectra with wide peaks, and for complex molecules, as within tissue, the spectra obtained are mostly broad intensity distributions; see Figure 11.

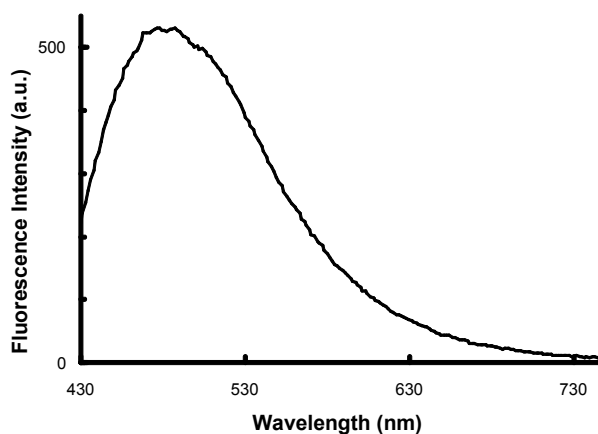


Figure 11 Fluorescence spectrum from human tissue

3.2. Basic set-up of fluorescence equipment

3.2.1. Light sources

A simple and schematic set-up for fluorescence measurements is shown in Figure 12. The components used can be of various types and degrees of complexity. Sensitivity and selectivity in the measurements depend both on the equipment used and of the substances in the sample. For excitation, a continuum source, a line light source or a laser is used. They are mostly used in different types of experiments, exploiting their different characteristics.

The continuum source in conjunction with a dispersive element is excellent to use because of the possibility to choose any excitation wavelength in the region where the source emits radiation. The limited power per wavelength interval makes this solution less favourable for sensitive measurements. Also, the suppression of the excitation light in the wavelength region where the emission is detected must be sufficient. This may sometimes pose a problem in practice. A line light source has sharp and intense emission lines, defined by the enclosed atoms. A laser is a light source, which has a high intensity per wavelength interval. Many lasers have a fixed wavelength but the technical development has made it possible to construct lasers/laser equipment, with continuously variable wavelength, e.g. dye lasers or optical parametric oscillators.

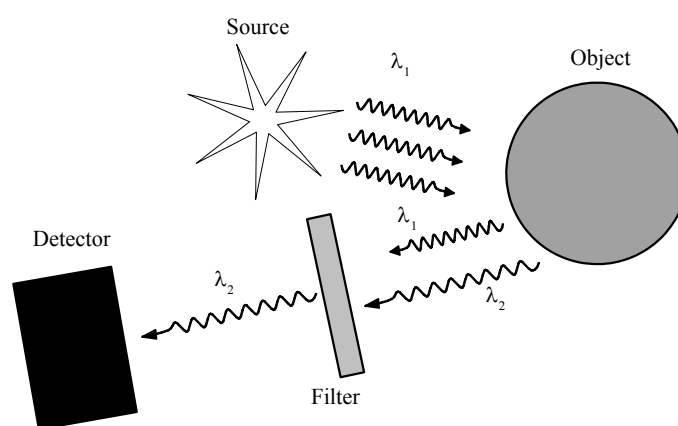


Figure 12 A simple set-up for fluorescence measurements

3.2.2. Light collectors

When a substance emits fluorescence, it is emitted isotropically in all directions. Without the use of a highly efficient collecting device, the detected signal is often very low and fluorescence imaging is difficult. For point-monitoring purposes, an optical fibre can be used, both to guide the excitation light and for collecting the fluorescence light. With the distal fibre tip in contact with the sample, the collection efficiency will be high. This makes it also possible to collect the fluorescence from places that are difficult to access, e.g. in measurements inside a blood vessel. An optical fibre is also frequently used when the equipment must be at a certain distance from the subject under investigation. If an image is desired, the most common method is to use one or several lenses to reproduce the fluorescent area onto an imaging detector, such as a CCD (see below). The disadvantage of lenses is the limited transmission in the short-UV and far-IR region. In cases when these wavelengths are of interest, it is preferable to use a focusing mirror for imaging purposes, which is also automatically achromatically compensated.

3.2.3. Light selectors

Before the light from the sample hits the detector, the undesirable light must be rejected; e.g. elastically scattered light in fluorescence detection measurements. Two different techniques can be used here. One technique is to place a filter with the appropriate wavelength transmittance in front of the detector. This is an excellent technique when only one wavelength region is of interest. A similar technique is to reflect the interesting light with dichroic mirrors. Here, one or more wavelength regions can be reflected onto the detector and different fluorescence emission wavelengths can in this way be detected by different detector elements; see Paper 8. Another technique is to use a dispersive component in front of the detector. With such a unit, not only the excitation light is rejected, but also the emitted light is divided into a continuous spectrum, where the range of interest is directed towards the detector. A prism or a grating can be used for this purpose. Together with a line or area detector, the entire spectrum can be acquired simultaneously as described below.

3.2.4. Detectors

Many different detectors exist, e.g. photo-multiplier tubes (PMT), diode-array detectors or two-dimensional charged-coupled devices (CCD). The principle is to convert the incoming photons to a current. Some detectors have a built-in amplification, as the avalanche diode and the photo-multiplier tube. The PMT is a very sensitive device and is one of the most used light detectors. When the incoming photon hits the cathode, the deposited photon energy may release an electron from the cathode. The material used in the cathode must match the energy of the photon, however, the materials used have a broad absorption spectrum. If the energy of the photon is less than the binding energy of the electron in the material, no electrons will be released. Even if the photon energy is sufficient to release an electron, the probability is below one. This probability is denoted the quantum efficiency and for most materials employed only up to 30% of the photons give rise to an electron. For wavelengths longer than 900 nm, the quantum efficiency is so low that hardly any photons can release electrons. When the electrons leave the cathode, they are moving through a chain of dynodes and the few electrons are multiplied in a chain reaction up to 10^6 times before they reach the anode. A PMT thus provides a relatively strong detector current even for low detected light levels. A potential problem is the dark current of the PMT. This is the current without any incoming photons. By cooling the PMT, the dark current is reduced. Disregarding the dark current, the output from the PMT is proportional to the light intensity. For low light applications, the PMT can be used for single-photon measurements. In this case, the level of the current is not measured, instead the current spikes, corresponding to individual photons, are counted.

A *line* detector is used if single-point detection is insufficient. In diode-array detectors (DADs), the current originates from an electron-hole pair recombination by the photon energy. The DAD is a common detector device in so called *spectrophotometers*, which are frequently used for absorption measurements in chemistry laboratories. Here, photons from

the light source pass through the sample cuvette and fall on the detector. Most often low-concentration samples are used, and frequently a high light intensity is obtained on the detector. The DAD is well adapted for this purpose because it can store a large number of electrons before saturation occurs. For low light level detection, charged-coupled devices (CCDs) are often used. Here, the current originates in the same manner as in a DAD, but the read-out procedure is different and the active area and volume of the diodes are smaller. The sensitivity of a CCD is not that high as in a PMT, but the noise is low and they are small and quite inexpensive. If an *area* detector is required, the CCD technique is favourable due to its size and suitable characteristics. Each imaging element, named pixel, can be as small as a few square microns, and today there are CCDs with up to several millions of pixels. To increase the sensitivity of a CCD an imaging micro-channel plate (MCP) is used. This works as many micro PMTs but the construction of a single micro-channel is much less complicated than for a PMT. At the end of the MCP tubes there are no anodes, instead the electrons hit a phosphorous screen. This screen emits more photons than the incoming light flux onto the MCP, and the CCD picks up the screen image.

3.3. Spectroscopy combinations

The available large variety of light sources, collectors, analysers and detectors makes it possible to construct many types of analysis instruments. Not all possibilities will be explained here, only a brief description of different combinations that have been used in the present work, and related techniques will be given. The material is divided up according to the detection scheme, where integrated intensity only may be recorded, one-dimensional linear imaging or two-dimensional area imaging is performed. For a more comprehensive exposition, books can be found on this subject (See, e.g., [14]).

3.3.1. Point detection

Point detection is the most ordinary technique regarding fluorescence studies. Light is sent onto the sample and a single detector measures the emitted light. Various excitation sources, as mentioned before, can be used. In older spectrometers, a prism or a grating was used to disperse the light, and a slit selected the appropriate wavelength, which was then detected. The dispersing element must be turned with this set-up, to sequentially acquire the full spectrum. This takes a quite long time and the intensity of the excitation light must be constant during the scan. Also, most of the light is not used because it is at any moment scraped off by the slit and is not detected. A similar technique is to have a filter wheel in front of the detector. In modern instruments most frequently an imaging (CCD) detector is placed in the focal plane of a spectrometer, and the whole spectrum is simultaneously recorded, and a good photon "economy" is achieved. A less sensitive technique is to use a DAD detector instead (See, e.g., [15]). The technique is also not very sensitive for fluctuations in the intensity of the excitation source, since all wavelengths are detected in parallel. A technique described in Ref. [16], uses 10 different dye lasers for the excitation light and a filter wheel in front of the spectrometer to reject elastically scattered excitation light.

For measurement of tissue fluorescence (Papers 8,9 and 11) an optical fibre-based point-monitoring fluorescence system was used (Figure 13) [17] [TJ1]. The system is based on a small, low-power nitrogen laser that emits 100 μJ pulses with a repetition rate of 15 Hz. The laser radiation, with wavelength 337 nm, is optionally used to pump a dye laser emitting 405 nm light with the pulse energy of 10 μJ . This light is focused into a 600 μm optical fibre and the distal end is put in gentle contact with the sample of interest. Part of the fluorescence light is guided back in the same optical fibre and directed toward the detector by the use of a dichroic mirror. A lens is used to focus the fluorescence onto the

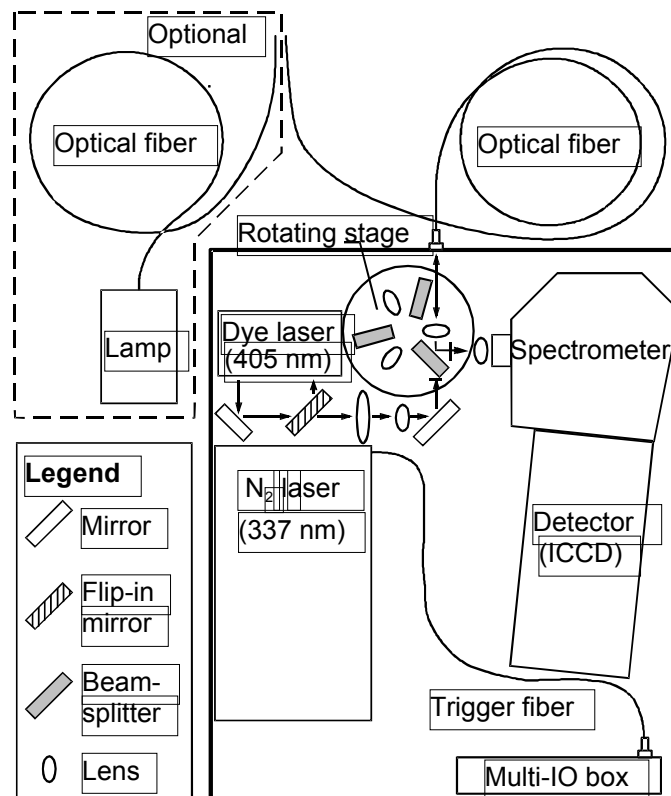


Figure 13 Schematic set-up of a point monitoring fluoro sensor

slit of a spectrometer, which is connected to an image intensified CCD camera. The ambient light is rejected by the use of a short gate width on the MCP preceding the detector. To increase the signal-to-noise ratio in the spectra recorded, 20 pulses were integrated. The spectrometer used has a fixed grating and the spectra obtained range from about 400 to 800 nm with a typical resolution of 5 nm. Spectroscopic systems which are capable of electronically capture the whole spectrum in parallel are frequently referred as Optical Multichannel Analysers (OMAs).

3.3.2. Line detection

Sometimes the spectroscopic properties along a line across a sample are of interest. It is then possible to spread the excitation light along the line and detect the emission with a line detector or an imaging detector. To detect a certain wavelength, a filter is placed in front of the detector or, if a full spectrum is desired from each point along the line, a dispersing element is used in conjunction with an imaging detector (imaging spectrometer). A second line detection approach is developed from the point detecting technique described above, and is advantageous if the ambient light is intense or a low-power light source is used. Then all the excitation light is directed onto a single spot to allow suppression of the background light. After this, the spot is moved along the line and all spectra are detected sequentially, and the line image can be constructed from the data. Here, a long scanning time is needed and the intensity of the light source should be stable. The technique is only applicable for stationary objects.

Laser-induced fluorescence can also be detected from a distance. Then the *Light detection and ranging* (LIDAR) technique is used; see Figure 14. Here, a short light pulse is sent toward the sample and the induced radiation is detected using a time gate. This is the so-called fluorescence lidar. In atmospheric lidar measurements, back scattering is collected range-resolved along the transmitted beam, mapping the particle distribution, or the pollutant gas concentration in the differential absorption lidar (DIAL) variety of the technique [18-20]. In the present work, different line detection techniques have been used in some applications. These have been used to monitor the fluorescence and absorption in seawater, and in small-bore columns (capillaries).

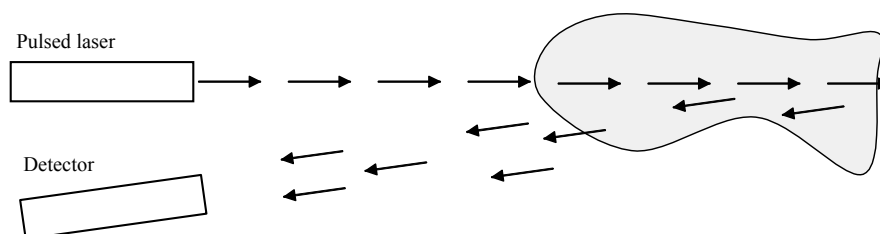


Figure 14 The principle of the lidar technique

In separation techniques used in analytical chemistry, detection is mostly made at the end of the separation system. A technique to measure the fluorescence along a capillary was introduced by Nilsson et al. in 1995 [21]. The excitation light was focused to a line along the capillary by the use of a cylindrical lens (Figure 15 [TJ2]). The fluorescence light was collected with a lens, which imaged the capillary onto the detector. A filter in front of the detector selected the fluorescence light and rejected the elastically scattered excitation light. For another type of capillary imaging technique, see [22].

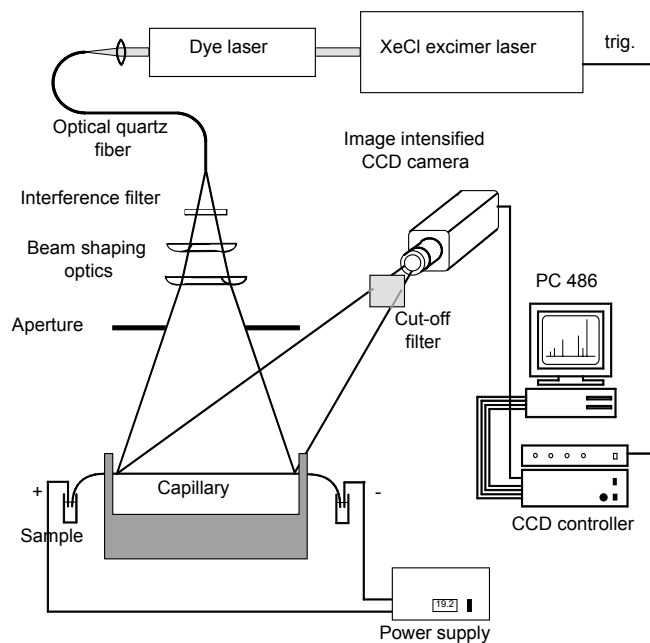


Figure 15 Set-up used for fluorescence imaging of a capillary [21]

In Paper 3, a new technique has been introduced to increase the detection efficiency. Optical fibres were aligned to collect the fluorescence from a capillary; see Figure 16. An optical fibre located close to the capillary efficiently collects the emitted light from a

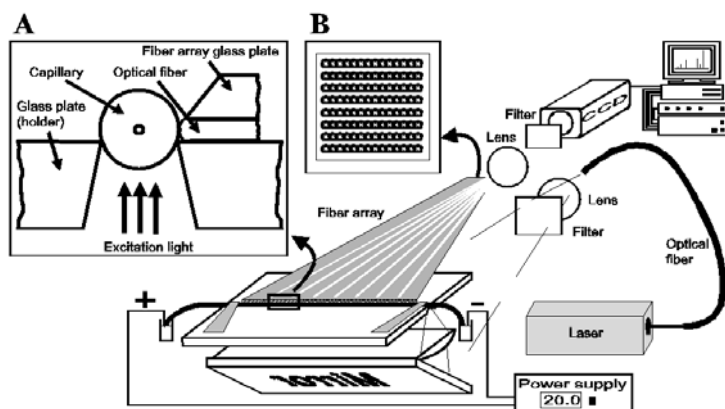


Figure 16 The use of a fibre array for fluorescence imaging of a capillary

certain volume in the capillary. With this set-up, a high light collection efficiency is obtained. To achieve the same efficiency with a lens system, the lenses must be large,

heavy and often expensive. Parabolic mirrors can also be used, but the system will still be large and unwieldy. To have the fluorescence from the length of the capillary a few hundreds of optical fibres must be aligned accurately along the capillary. A special optical fibre array was therefore designed and special arrangements have to be considered for the construction of the array. The input assembly, which is placed along the capillary, was constructed with the fibres side by side, while they in the other end were arranged in a special matrix configuration to match the detector; see Figure 16. Instead of glueing all the fibre ends to one wide fibre matrix, smaller quantities of fibres were glued together. These small arrays were glued on top of each other (laminated). The advantage with this arrangement is that small lenses can be used to image this fibre matrix onto the CCD camera. The order of the fibres from the collecting end to the output end has to be organised to be able to reconstruct the correct linear order.

The higher light collection efficiency of the fibre array is due to the large solid angle that the fibre ends have, as seen from the capillary compared with a lens at a certain distance from the capillary. To facilitate the emitted light from the inside of the capillary to be collected by the fibre array, a special arrangement was made. An optical fibre with the diameter of 100 μm and the numerical aperture (NA) of 0.22 collects light from a cone with acceptance angle of 13 degrees. When such a fibre is placed close to a capillary with an outer diameter of 275 μm , the maximum angle at which the emitted light hits the fibre end is higher than 13 degrees and will therefore not be transmitted by the fibre. To solve the problem, the collecting end of the fibre array is polished to a cylindrical shape as shown in the inset in Figure 4, Paper 3. Now, the light rays, which have the highest angle against the fibre end, are refracted at the surface to a higher degree than without the cylindrical shape. Inside the fibre, the light ray is now within the acceptance angle. With this arrangement the ratio of the light collection efficiency between the fibre array and a lens system (diameter 35 mm, focal length 50 mm) is as shown in Figure 4 of Paper 3. The ratio depends on the distance between the fibre array and the capillary. A shorter distance between the fibre array and the capillary increases the solid angle that the fibre end exhibits. When such a fibre is close to a capillary, with an inner diameter of 50 μm and an outer diameter of 375 μm , the theoretical improvement is approximately 30 times, neglecting the losses due to refraction at the air-glass interface. To achieve this improvement the fibre array must be highly aligned against the capillary. This was one of the major experimental problems when the array was employed during experiments. In practice the increase in sensitivity was approximately 10 times.

In Paper 4 another line imaging technique for capillaries was used to image substances, which do not emit fluorescence. These substances are detected only by absorption techniques or with indirect methods [23]. A disadvantage with absorption measurement is the low sensitivity. Here, a combination of direct absorption and fluorescence is used.

The set-up in such an experiment is shown in Figure 17. A description of the separation technique can be found in Section 4.3. The excitation light is directed onto the end of the

capillary, which is filled with a fluorophore dissolved in an electrolyte. The light propagates through the length of the capillary and to detect the fluorescence along the capillary, a CCD with an objective lens is mounted perpendicularly to the capillary. To reject the elastically scattered light, a filter is placed in front of the objective. Due to the higher refractive index of the capillary compared with the solvent, no total reflection is obtained of the excitation light. The light therefore escapes through the capillary wall and the intensity of the excitation light decreases along the capillary, resulting in a lower fluorescence signal along the capillary away from the source. The intensity along the capillary decreases also due to the absorption of the fluorophore in the solution. These two circumstances result in an exponential fall-off. At locations of substances, the fluorescence signal decreases with a higher rate due to a higher absorption. This intensity decrease is used to image the location of the absorption.

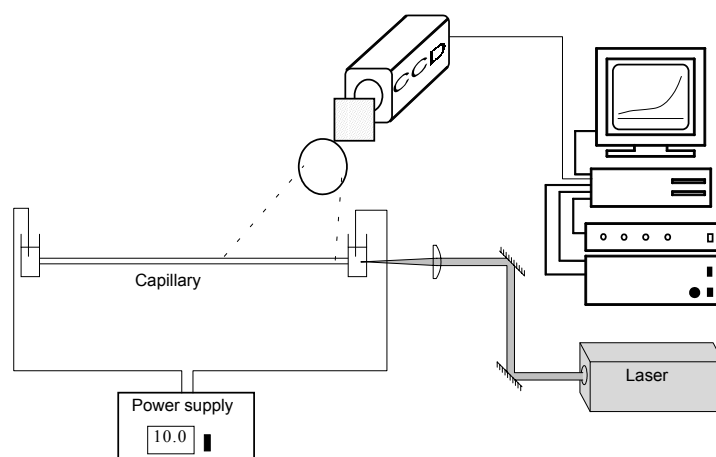


Figure 17 Set-up for axial excitation

A LIDAR/DIAL system [24], was used to measure the fluorescence from Mediterranean Sea water (Paper 5). The studies were performed from the Italian research vessel "Urania". The detection was made using a fully spectrally resolving technique, illustrated in Figure 18. In the focus of the telescope, a fibre bundle, consisting of seven fibres arranged in a circular shape, collects the fluorescence. In front of the fibre bundle, a filter is placed to reject the elastically scattered excitation light. The distal end of the fibre bundle is rearranged to a linear array to connect the fibre bundle to the spectrometer. This imitates the input slit of the spectrometer. Normally, the slit width is approximate 100 μm resulting in a spectral resolution of 2.5 nm for the spectrometer used. With these 400- μm wide fibres, the resolution is limited to 10 nm. The spectrometer used is an imaging unit with an image-intensified time-gated CCD detector. By binning the pixels along the slit direction, the fluorescence from all the seven fibres is added.

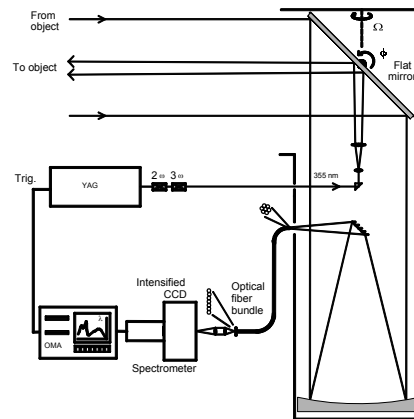


Figure 18 Fluorescence lidar system

With the time-gated CCD detector, only the fluorescence from one distance interval can be measured at a time. A delay generator between the laser and the gated CCD was used to change the delay time, corresponding to the distance between the sample volume and the CCD. The delay generator was controlled by a computer, which resulted in rapid adjustments of the delay between measurements. A program controlling the system altered the probed depth from the water surface to a preset depth in a cyclic manner. In this way, fluorescence from different depths, and different positions of the vessel were collected. The width of the time-gate of the CCD was preset to 40 ns, which corresponds to a vertical resolution of about 4 m in the water column.

3.3.3. Area detection

For studies of two-dimensional objects, the simplest approach is to distribute the light over the area and collect the emitted light with an objective or a focusing mirror, which forms an image on a two-dimensional detector. With a filter in front of the detector, the intensity at a selected wavelength region can be measured. To achieve spectroscopic data in the picture, different techniques can be used. One technique is to acquire the images sequentially with different filters, but this approach suffers from the same disadvantages as mentioned before for point and line detection. A better technique is to use a Cassegrainian telescope in front of the detector. This telescope collects the light and focuses four identical images onto the detector at different areas. By using different filters in the four light paths, four images are simultaneously collected. The light efficiency is low due to the fact that the light is directed into four different light paths. To increase the efficiency, an arrangement of a number of dichroic mirrors can be used. The first dichroic mirror reflects one part of the spectrum onto the detector while the remaining light is transmitted. After this, the following dichroic

mirrors are reflecting other wavelength regions onto other parts of the detector. This technique utilises much more of the light.

If a wide wavelength region with high-resolution spectral images is necessary, other techniques are used. Here, some type of scanning technique must be used. One variety is the so-called push broom scanning. It is similar to the line detection technique described above. The excitation light is spread along a line and the emitted light is wavelength resolved with a spectrometer and detected by the use of an imaging detector. By scanning the area sequentially, it can be fully spectrally imaged. If stronger specific signals are needed, e.g. because of strong ambient light, a point scanning technique can be used. Instead of spreading the light onto an entire line, the light is focused as a spot onto the target and detected with a point detector.

In Paper 2 the change in pH is measured in an area, or rather a volume, with an imaging technique. In chemistry, the knowledge of the pH of the solution is sometimes important. The pH controls in what state, protonated or deprotonated, the compounds in the solution are. The most common way to measure the pH is to place a pH electrode in the solution. If a small volume is to be measured, this technique cannot be used. Instead, light detection techniques are preferable. To utilise a pH dependent light detection, a fluorophore is used for which the absorption coefficient depends on the pH in the solution. The fluorophore has two major absorption peaks, which depend on the pH in the solution. For one of the absorption coefficients it is decreasing with a decrease in pH and the opposite is true for the second absorption coefficient. At the same time, the fluorescence emission wavelength is the same. The pH of the solute can therefore be determined by measuring the fluorescence intensity at the two different excitation wavelengths.

For the purpose of measuring pH, a system was constructed to monitor the fluorescence at the two different absorption wavelengths. Two similar arrangements have been used for these experiments and the first set-up used is shown in Figure 19. The excitation source is the same, a mercury lamp. In the first set-up, the light is focused into an optical fibre with the use of a parabolic mirror. When the light has passed through the fibre, a low-pass filter is used to reject the infra-red light. After this, an arrangement with two interference filters is placed in a holder side by side. The holder is attached to an electromagnet to make it possible to change the filter in the excitation light beam. To excite the pH-dependent fluorophore at the two absorption peaks, the two wavelengths 405 and 435 nm in the mercury emission spectrum are used, and the interference filters are adapted to these wavelengths. After the filter arrangement, a lens is used to focus the light onto the sample. A cooled CCD camera, with a camera objective and a filter in front to reject the scattered excitation light, is used to detect the emitted fluorescence.

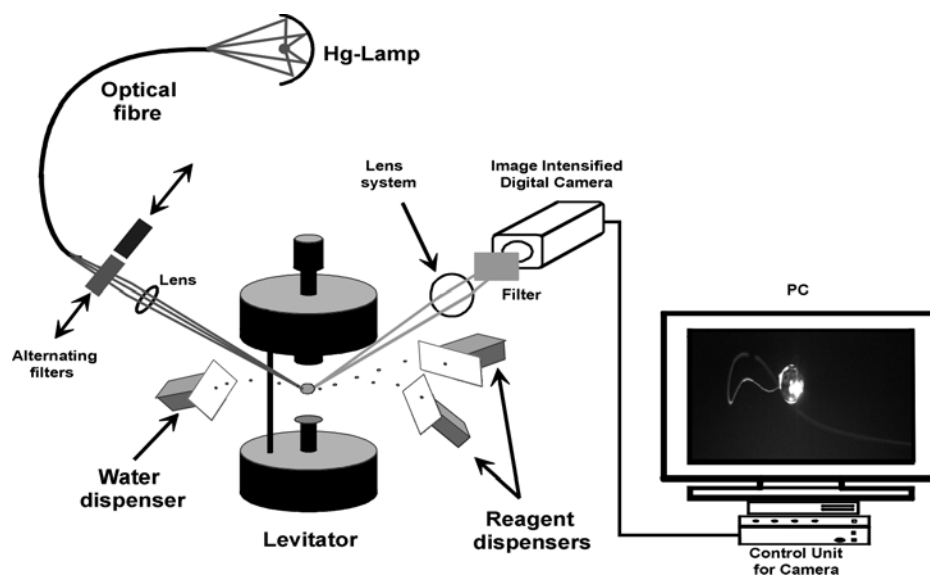


Figure 19 Instrumental set-up for fluorescence imaging of a levitated drop

The other set-up does not focus the light into a fibre. Instead, the light is directly focused onto the sample by the use of a high numerical aperture Fresnel lens and a positive glass lens. The low-pass filter and the interference filters are placed in the first focus and after this, the second lens is used to focus the light onto the sample. This arrangement has a higher throughput of light onto the sample compared with the first set-up, because only a small amount of light from the mercury lamp is focused into the fibre in the first set-up.

The pH of the sample is evaluated by the intensity ratio of the two fluorescence images as described in Paper 2. To calibrate the pH scale, different solutions with varying pH were measured. In Paper 2 the task was not to classify the absolute pH of the sample, but rather to indicate pH changes in the solution.

As discussed above, a fluorescence LIDAR system was used for seawater column measurements. Another utilisation of a LIDAR system is measurements of the fluorescence from surfaces of historical buildings as described in Papers 6 and 7. The set-up is similar to the one used for the water experiments; the only difference is that the mirror, which was used to reflect the excitation light downwards, is removed and the laser beam is directed onto the walls as shown in Figure 1 in Paper 6. The mobile lidar system was parked at a distance of about 60-80 meters from the building to be studied. Because of the large distance and also the fact that the measurements were made in full daylight, the point scanning approach was chosen.

A short gate width was used in these measurements to suppress scattered sun light in the recorded signals. A short gate width can also cause problems. The distance between the sampled area and the detector varied during a scan over a large area and to ensure that the

fluorescence at different positions was captured with a high efficiency, the gate width must be sufficiently large.

Tissue fluorescence can be measured with a fibre probe, but with such a technique only small areas can be examined. To acquire fluorescence images, the multispectral imaging technique using dichroic mirrors was applied in Paper 8. The excitation source in this set-up is a frequency-doubled Alexandrite laser emitting laser radiation at 390 nm, 20 Hz with about 4 mJ of pulse energy. The light is focused into a 600- μm optical fibre where the distal end is located approximately 15 cm above the area, thus exposing approximate 30 cm^2 . Both reflected ambient white light and the fluorescence light are guided through an optical lens system or an endoscope to the detection unit. After the optical system, a filter is used to reject the excitation light. When the remaining light has passed through this filter, a beam splitter is used to direct the light into different light paths to reach a normal colour CCD camera, and a gated image-intensified CCD (Figure 20). In front of the image-intensified CCD camera, two dichroic mirrors and a broad band mirror is placed to separate the different colour information in the fluorescent light into separate images. The first dichroic mirror reflects light with a wavelength between 420-480 nm onto one part on the CCD. The rest of the light is transmitted to the second dichroic mirror, where light with a wavelength between 580-750 nm is reflected onto another part of the CCD. The remaining light, which is between 480 and 580 nm, is reflected by the mirror onto a third part of the CCD. This set-up has the advantage of higher light efficiency compared with the first system designed for this purpose, that used a Cassegrainian telescope in combination with different absorbing filters [25,26]. For orientation purposes, the colour CCD camera was used to simultaneously acquire normal white light images during the examination.

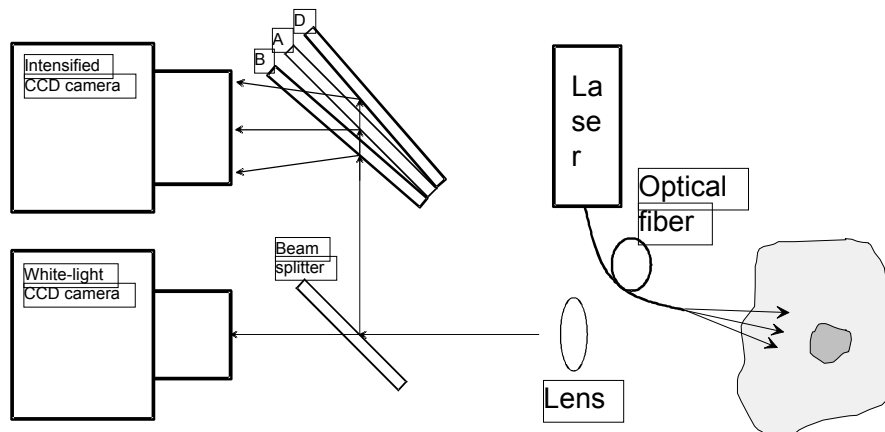


Figure 20 Set-up of system for multispectral imaging

Following acquisition of both the white light and fluorescent images, a computer is used to process the information and indicate interesting areas of interest. The three fluorescent images are combined and presented as a single artificial image using a contrast function, developed to demarcate malignant tumour. The contrast image can also be overlaid on the white-light image for orientation.

3.4. Multivariate analysis techniques

3.4.1. Background

Today, when the instruments for analysis of samples are complex, the collected data often contain a lot of information. The screening of new medical drugs is one example where a large amount of data is produced. In spectroscopy, the information may be a complex composite spectrum from the sample. Fluorescence spectroscopy imaging produces an even larger amount of data. The classical way to analyse the results is based on knowledge of which substances are present in the sample. Often the intensity at a certain wavelength of the spectrum is the parameter that describes the amount of the substance. Frequently, this method is sufficient and many spectrophotometers primarily use this technique. Sometimes an intensity ratio can be advantageously utilised to characterise the sample. Variations, due to the excitation intensity and the geometry, are minimised with this technique. Here, the need of a substantial knowledge of the constituents is important. Otherwise irrelevant ratios might be calculated. The ratio technique might also produce irrelevant results if spectra from different species are overlapping and another disadvantage occurs when low-level signals with substantial amount of noise are encountered, resulting in noise amplification.

To evaluate information and eliminate the problems described above, other more powerful techniques can be used. Also, if only little or no knowledge of the sample characteristics is available, a new method for analysing and classifying the material is needed. Valuable techniques that can be used in such cases are the *multivariate methods*. They constitute a very complex and diverse field of methods for the evaluation of recorded data. A few approaches, such as the least square method (LSM), principal component analysis (PCA), multiple linear regression (MLR), principal component regression (PCR) and partial least square regression (PLS-R) can be mentioned [27]. With these methods many problems, such as those mentioned before, are minimised. A large effort has gone into this area of research and we will not go into any details here. In this thesis, principal component analysis, as described below, has been used in Papers 3,6 and 7 for evaluation of the data acquired.

3.4.2. Principal component analysis

Principal component analysis (PCA) is a method that does not need any prior knowledge about the data set. It is a method that explains the variation in the data in a comprehensive way. There exist a lot of computer programs for calculations and presentation purposes.

Here follows a short description of the PCA method. Figure 21 (left) shows a schematic plot of the intensity at two different wavelengths. A new central axis, as in the right part of the figure, is calculated where the $\Sigma(d_i)^2$ is minimised or in other words, the variance along the axis is maximised. One can see that most information is now along the single x_1 -axis without the need of a second dimension to describe an essential part of the information. The projection of a point onto the x_1 -axis is named the *score* and further, the plot is called a *score plot*. Also, the new axis, x_1 , is related to the old ones and in the co-ordinate transformation the coefficients describing the x_1 -direction, in the old co-ordinate system, form the *loading vector*. In spectral PCA, the value of the loading vector describes the correlation between the new axis and the old wavelengths. By drawing a diagram of these coefficients, conclusions of valuable wavelengths can be made. More detailed descriptions can be found in [28].

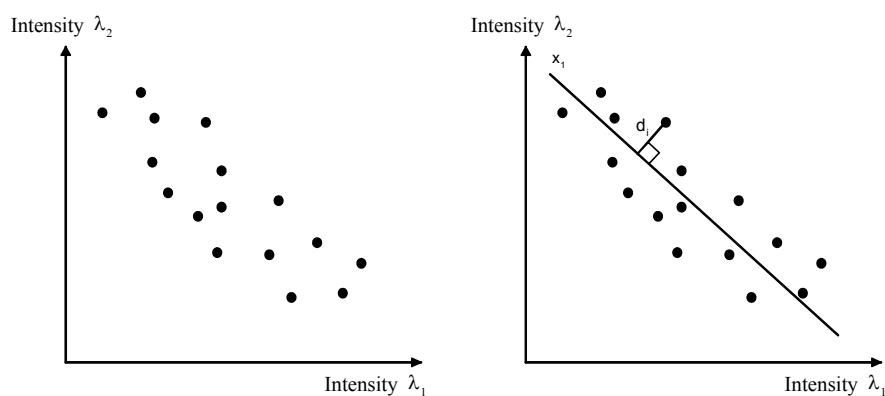


Figure 21 Schematic description of principal component analysis.

This is the result if only two wavelengths are used, but all wavelengths in the spectra can be used to construct a new multi-dimensional co-ordinate system with a corresponding score plot. These plots are quite hard to visualise but there still exist an axis, like x_1 , for which the spread is maximised, named PC1. The remaining dimensions (PC2-PCN) contain less and less variances. This means that some of the first components contain a large amount of the total variance of the data set and the corresponding loading vectors explain in which wavelength regions valuable information can be found. With the use of this knowledge, the spectral signatures can be examined in these wavelengths regions and hopefully they can be related to the fluorescence of substances in the sample.

4. Applications adapted to analytical chemistry

4.1. Overview and historical background

There are several reasons why chemical analysis is performed on an object or other specimen. Two important motivations are identification and quantification of the sample. To have the answer, preparations and separations might be used. Before high-technology equipment existed, the methods for analysis were limited. By the use of the human senses and, for example, trying to dissolve the sample in water, conclusions were made. Clearly, the ability of such simple methods were very limited. Successively, the methods developed and became better and different. Today, highly automated systems are used.

Although many spectroscopic techniques, such as emission spectroscopy, have a direct multi-species capacity, the sample frequently has to be separated into its different species before analysis. One of the most common techniques used is chromatography. Although the name originates from a first type of separation techniques, it presently is used for a large class of different separation methods.

4.2. Separation methods (chromatography)

The Russian botanist Mikhail Tswett was one of the first to use the chromatography technique in the beginning of the 20th century. He used glass columns filled with calcium carbonate and separated different pigments from plants with the gravity working as the pumping force. The pigments appeared in different coloured bands along the column; therefore the name chromatography (Greek; *chroma* meaning colour, and *graphein* to write). This can be described as an imaging detection technique with the eyes used as the imaging detectors. Today, using various detection techniques, the substances can both be detected and quantified with much higher accuracy.

4.2.1. Pressure driven chromatography

A chromatographic separation is a complex course of events, and only the basics will be covered here. For more detailed explanations, standard books on this subject can be found [29]. The basic aspect is to use a stationary and a mobile phase. The stationary phase is a liquid or a solid, and it is bonded to the column wall or to a packing material. A gas, liquid or a super-critical liquid is used as the mobile phase and common techniques are gas chromatography (GC), high-pressure liquid chromatography (HPLC) and super-critical chromatography (SCC). The sample will be injected into the mobile phase as a small band or zone in the beginning of the column. The separation depends on the difference in the partition ratio, K , of the samples (analytes). For an analyte, the partition ratio is defined as the ratio of the analyte present in the stationary phase and the mobile phase, respectively. The analyte that has the highest partition ratio will stay a longer time in the stationary phase compared with the other, meaning it will move slowly compared with an analyte with a low partition ratio. Factors affecting the separation efficiency include diffusion of the analytes

and a mass-transfer effect. These effects are explained by an equation named after van Demter.

4.2.2. Electrophoresis

Another much used separation technique is electrophoresis. This mechanism was brought into practice by the Swedish chemist Arne Tiselius in 1937, and the method is based on separation in an electrical field (Greek; *phores* meaning carrying). Tiselius separated different proteins in tubes filled with electrolyte solution, using a voltage supply connected to both ends of the separation tube.

The mechanism active in electrophoresis is based on the different velocity of the analytes in an electric field. Due to the charge of the analyte and the electrical field, an electrical force is pulling the analyte towards the oppositely charged terminal. Dissimilar ions have different relative velocities and the property, which describes this, is called the electrophoretic mobility (μ_e). This quantity for an ion depends on the charge, size and shape. Small and highly charged analytes most often have a high mobility. During the movement in the electrolyte, a frictional force retards the analyte. When these two forces are in balance, a steady state is reached and the analyte is moving with a constant velocity through the separation tube.

A current is generated in the tube due to the voltage, and the intensity of the current depends on the cross-section of the tube and the composition of the electrolyte. The current, which is generated, increases the temperature of the solution and the temperature rise results in a higher thermal diffusion and convection, which will deteriorate the separation. To minimise this problem a modified technique named gel electrophoresis was introduced and is still used. A gel that does not convey any current, but minimises the convection, is introduced into the tube instead of the free solution. This gel can also be used on a plate or made into a larger block on which the voltage supply can be connected. The technique is improved even more if a small-bore capillary is used. Because of the lower heat generated, a free solution can be used in such thin capillaries. In the first experiments, the capillaries were a few millimetres in diameter but with better manufacturing techniques the capillaries today have an inner diameter of some 100 μm down to only a few μm . These small capillaries enable the use of even higher voltages, which make the separation even better due to the low influence of the diffusion. The technique is called capillary electrophoresis and is described in Section 4.3.

4.2.3. Electro-osmotic flow

A surface of silica will be negatively charged when in contact with a wetting solution at $\text{pH} > 2$. The negatively charged surface originates from the deprotonation of the silanol groups (SiOH) to the anionic form (SiO^-), which depends of the pH of the solution. Cations are attracted to these groups and are relatively strongly attached to the negatively charged wall.

Outside of this layer a diffuse layer is formed. This diffuse layer consists of both cations and anions but with an excess of cations, and a double-layer is formed. When the electrolyte is connected to a voltage supply, the diffuse layer of cations will move toward the cathode. This is named electro-osmotic flow (EOF) with corresponding mobility (μ_{EOF}). In capillary electrophoresis where thin capillaries are used, this effect is highly influencing the analyte migration. Due to the small diameter, the diffuse layer of cations will pull the solution inside the capillary. This EOF will not affect the separation. The only effect is that all the analytes are moving with the bulk flow toward the cathode.

The EOF is highly dependent of the amount of cations attracted to the capillary surface, which in turn depends on the surface charge, and thus the pH of the electrolyte. Another effect, which also changes the double-layer and in consequence the EOF, is the ionic strength of the buffer. The behaviour of the layers versus the ionic strength is described with double-layer theory. An increase of the ionic strength compresses the double-layer and the magnitude of the EOF is decreased. With this technique a flow profile is generated that is extremely flat compared with a pressure driven separation system.

4.3. Capillary electrophoresis

The set-up of a capillary electrophoretic (CE) system is shown in Figure 22 [30,31]. A capillary with a length of generally 10-60 cm and an inner diameter of 5-150 microns is used. To achieve an electrophoretic separation system, the capillary is filled with an electrolyte, and both ends of the capillary are inserted into vials filled with the same electrolyte. Different techniques are used for injecting the sample and these will be discussed later on, but they all have in common that a thin band of the sample is introduced into one end of the capillary. After this, a high voltage supply is connected to the two vials to start the electrophoretic separation. The EOF starts to pump the electrolyte from one vial to the other and the different analytes in the sample start to move relative each other. To observe the analytes inside the column and to quantify the separation, different detection techniques are used, and the result can be shown in a diagram.

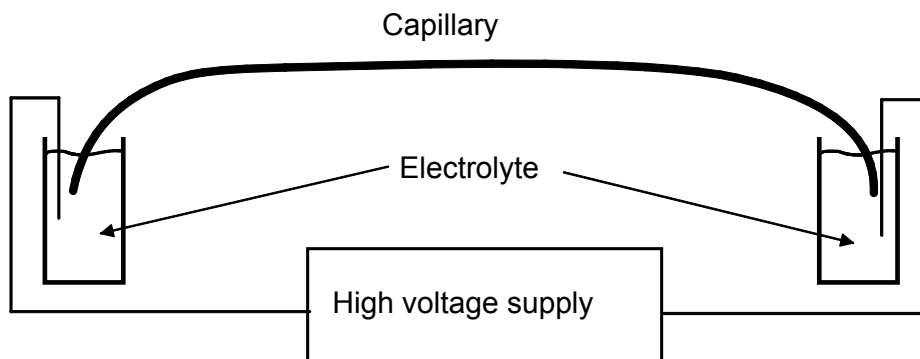


Figure 22 Schematic set-up for capillary electrophoresis separation

CE is favourable for separation of charged species compared with chromatographic techniques. This is due to the differences between the techniques, e.g. the separation mechanism, EOF and the use of a thin capillary. Band broadening is one effect that can destroy the separation and therefore must be controlled in all separation systems. With the use of a thin capillary, the effect of Joule heating is minimised. The capillary with the electrolyte inside acts as a wire unit and the power (P) generated is given by the equation

$$P = \frac{U^2 a}{\rho l}$$

where U is the voltage over the capillary, a is the cross-section area, ρ is the resistivity of the electrolyte and l is the length of the capillary. This generated heat is devastating due to the temperature difference between the electrolyte and the environment surrounding the capillary. The temperature gradient produced inside the capillary will affect the density of the buffer, resulting in convection, which introduces band broadening. There will also be a viscosity gradient across the capillary due to the temperature gradient. The same kind of ions at different radii will therefore be exposed to different frictional forces and the consequence is different relative electrical mobility at different radii, and the result is band broadening. Band broadening arises also due to a higher thermal diffusion at higher temperature. A thin capillary should therefore be used to minimise these effects. A cooling fan, which removes the heat generated, can also be used but it is more effective to put the capillary in a liquid cooling system.

The separation mechanism in capillary electrophoresis is different compared to techniques in chromatography and can be used to separate charged species only. However, it is remarkably efficient for the separation of such compounds. While other techniques rely on different partition ratios between the solid and the mobile phase, capillary electrophoresis uses the difference in electrical mobility. Both mechanisms are well suited for separation

purposes. The disadvantage with chromatography systems is that a pump force must be used to perform the separation. The resulting pump flow, which has a laminar or parabolic flow profile, introduces band broadening. A capillary electrophoretic system does not need a bulk flow for separation purposes because the separation is caused by the difference in electrical mobility. This results in a 10-100 times higher separation efficiency for a CE system compared with a pressure driven system.

An increase of the electrical field makes the analytes migrate faster. Also the speed of the EOF increases with increasing electrical field. This does not affect the separation because the migration and the EOF increase linearly. The time for the separation will therefore be shorter and subsequently the band broadening is minimised.

4.3.1. Injection techniques in capillary electrophoresis

There are two major techniques used for injecting the sample into the capillary, i.e. hydrodynamic injection and electrokinetic injection. In hydrodynamic injection the inlet end of the capillary is inserted into a vial with the sample. Different techniques are used to make the sample flow into the capillary. One way is to pressurise the sample vial, another is to lower the pressure of the outlet vial, and the third technique is to raise the sample vial a few centimetres relative the outlet vial. The volume loaded depends on the difference in pressure between the inlet end and the outlet end of the capillary, the dimension of the capillary, the viscosity of the buffer and the time of the injection. Normally, an injected zone has the width of a few millimetres. Hydrodynamic injection is a simple technique and the elevation technique was used in Papers 3 and 4. One disadvantage with the hydrodynamic method is the laminar flow of the sample entering the capillary as mentioned before.

Connecting a high voltage supply between the sample vial and the outlet vial performs an electrokinetic injection. The speed with which the analyte migrates into the capillary depends on the μ_e of the ion and the μ_{EOF} . Thus, analytes with a low mobility or a mobility opposite the EOF will be discriminated.

4.3.2. Detection techniques in capillary electrophoresis

The most common detection technique is light absorption in the ultra-violet (UV) and visual (Vis) range, named UV-Vis absorption. One of the major advantages with absorption measurements is that most substances absorb light somewhere in the UV-Vis wavelength region. Most often the absorption is transformed to absorbance (A), which is defined as $A = \log(P_0/P)$. In CE, the absorbance measurements are made directly through the column, so called on-column detection. On-column detection has the advantage of causing no additional band broadening due to the loss of connection to external detection devices. On the other hand, the thin capillaries used result in short optical path lengths. Absorbance measurements become better if long optical path lengths are used, because the sensitivity depends linearly on the path length.

Another detection technique, which is more sensitive than the light absorbance, is to detect fluorescence from the analytes. The excitation wavelength is selected to suit the species in the sample. A filter with a given transmission wavelength, or a dispersing element, as mentioned before, is used in front of the detector. This technique is far more sensitive than the absorption method, but not many substances exhibit intrinsic fluorescence. A technique to circumvent this is to tag the analytes with a fluorophore. If UV light of very short wavelength is used for excitation, more species exhibit fluorescence but the background fluorescence will also increase.

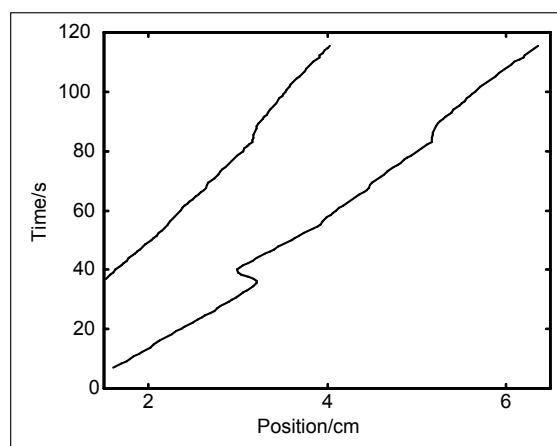


Figure 23 Unexpected behaviour recorded in capillary electrophoresis

In Papers 3 and 4, the fluorescence was measured along the capillary during the entire separation. With this technique, the mobility of the analytes is monitored, and non-linear movements can be detected, which are hardly discovered with an end-point detector. Figure 23 shows an unexpected behaviour of a separation, where one peak suddenly changes its direction. A complete explanation of this has not yet been found.

Band broadening is also monitored with the imaging technique and the band broadening due to diffusion is calculated and compared with literature data. This results in a good internal agreement.

In Paper 4, a novel technique was used to image absorption of substances along the capillary; see Section 3.3.2. Actually, light absorption is measured with the use of fluorescence techniques. The advantage with this method is the increase in sensitivity compared with the general light absorption technique used in CE. Here, it is further used to image the absorption along the entire capillary. Figure 3 in Paper 4 shows the fluorescence intensity when an absorbing molecule moves inside a capillary, and Figure 5 in the same paper shows one processed image to disclose the actual peak. The simple set-up resulted in fluctuations of the excitation light inside the capillary, which generated ghost peaks. These

fluctuations are most likely due to vibrations of the capillary, and refractive index fluctuations of the electrolyte at the capillary ends. This can be eliminated with a modified technique, but the basic method was demonstrated in this paper. To further increase the sensitivity, one can integrate the intensity along the location of a peak. A normal peak width is about a few millimetres, which can be compared with the absorption path length of 50-200 μm used in general capillary methods.

In [32] the problem was the same, to detect a non-fluorescent sample. Here, the sample was modified to facilitate fluorescence detection. First, two different monoclonal antibodies are covalently bound to fluorescent latex particles. Second, the latex particles are mixed with the sample producing a latex-antibody-protein-antibody-latex complex. This solution can now be separated in a CE system where the complex is separated from the single latex particles. The separation was monitored with a fluorescence imaging system described in Ref. [33]. Limitations with this technique are that only proteins, for which monoclonal antibodies are available, can be detected. On the other hand, the proteins are enriched with this technique.

When the capillary has been used for many separations, species from the sample adsorb to the inner surface of the capillary resulting in an increased background signal. These species can easily be removed by flushing the capillary with a cleaning agent but background fluorescence remains even though such precautions are made. Also, the high voltage used during CE separation attracts dust towards the capillary, which also contributes to the background signal. For this purpose, background subtraction of the signal intensity detected must be made. An unconventional technique to remove the background was used in Paper 3 where the PCA technique was applied. The entire set of fluorescence intensity data was used to calculate PCs, where the first component describes the largest variation in the data set and the moving peaks are mainly interpreted as noise. By subtracting this first component from the data set, the baseline is removed. Figure 3 in Paper 3 shows the fluorescence intensity at a certain time during the signal processing. With this technique small time dependent changes in the background are removed.

4.4. Analysis of levitated drops

Levitation in the area of chemistry is a technique where the sample volume is floating in the air, i.e. in wall-free test tube, with an air interface instead of a boundary to other materials. In this way, no walls are interacting with the species in the sample. Also, adsorption of the substances onto the sample container is avoided. For detection purposes, this is an advantage because of a lower background signal since there are no walls for the species to adsorb to. Another advantage is the low consumption of sample and reagent although also other micro techniques exist. When such small volumes are used, the surface-to-volume ratio increases and forces at the surface will influence the sample. This wall-free technique is therefore favourable compared to other micro-container techniques because the low adsorption to the air-solution interface as mentioned before.

There exist different approaches to levitate objects. The most common ones are optical levitation, electrostatic levitation, aerodynamic levitation, diamagnetic levitation and acoustic levitation. In Papers 1 and 2, acoustic levitation was used for the investigation of cell behaviour and screening of protein precipitation for use in protein crystallisation.

4.4.1. Acoustic levitation

The technique to force an object in an acoustic field is known since the 19:th century. Today, acoustic levitators are used to trap objects thus holding them freely in the air. A levitator can be constructed in different ways. In one type, a sound wave is sent from an actuator and is reflected back at a reflector. If the distance between the actuator and the reflector equals an even number of wavelengths, a standing wave arises. In this acoustic field, objects with higher acoustic impedance are forced to the antinodes of the standing wave. This type of levitator is used in Papers 1 and 2.

Rayleigh first made investigations of acoustic radiation forces on objects. Later on, the theory was extended to include levitated liquid drops. A description will not be given here. The technique has been used earlier in analytical chemistry [34].

4.4.2. Monitoring of a levitated drop

The entire system used in the experiments, described in Papers 1 and 2, was shown in Figure 19. The central part is the levitator and for sample delivery a droplet dispenser is used. This dispenser delivers 30-100 pl droplets at a rate of 0 to 9000 droplets per second. Also reagent solutions are added to the drop with this technique. Because of the wall free sample holding, the volume decreases due to evaporation and a dispenser is delivering droplets of the same kind as the solution in the drop. The addition of droplets to the drop is used in experiments where the concentration of the substances should be constant; see Figure 3 in Paper 2. The detection system was described earlier in Section 3.3.3.

Different techniques have been used for the determination of some properties of the levitated drop. To determine the pH of the drop, laser-induced fluorescence (LIF) was used. Here, the change in pH is monitored by the use of 8-hydroxypyrene-1,3,6-trisulfonic acid (HPTS), which is a pH-dependent fluorophore. HPTS has two major absorption wavelengths, 405 and 450 nm, and independently of the excitation wavelength it fluoresces at 511 nm. Excitation light with the wavelength 435 nm is absorbed in a lower amount compared with light of 450 nm. The cross-section for absorption at the different wavelengths depends on the deprotonation of the HPTS molecule. By acquiring images of the emitted fluorescence from the drop at the two excitation wavelengths and calculating the intensity ratio, a relative pH is determined. By adding water to the drop, evaporation effects were prevented. Otherwise, the fluorescence ratio is changing during evaporation as seen in Figure 3 in Paper 2. To calibrate the system, different pH solutions were used. Figure 3 in Paper 2 also shows the decrease in fluorescence intensity ratio when acetic acid is added to the drop.

In Paper 2, the task was not to determine the absolute pH of the drop. The aim was rather to detect the increase and decrease of the pH due to adipocyte (fat cell) lipolysis (fat mobilisation), where every free fatty acid (FFA) can release a proton. FFA:s are produced when adipocytes are stimulated with isoprenaline, which is a synthetic beta-adrenergic agonist. By adding insulin, the reaction is inhibited. Figure 24 shows the change in pH in an experiment and when insulin is added, the reaction is inhibited.

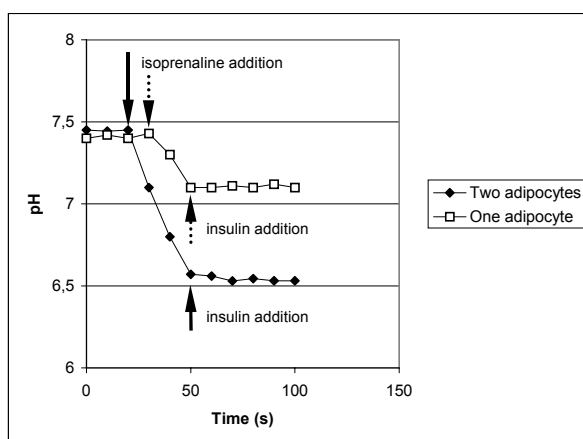


Figure 24 Changes in pH during an experiment with fat cells

In another experiment, protein crystallisation was studied (Paper 1) [35]. When molecules, e.g. salts or proteins, in a solution are slowly brought into supersaturation, small aggregates of the molecules are formed. This is the beginning of a precipitate or a crystal. The theoretical and practical knowledge of the process is not yet fully described for the formation of macromolecules. Here, the formation of protein nuclei was detected by imaging of scattered white light. The experimental set-up is similar to the one for fluorescence measurements. A technique named right angle light scattering (RALS) was used for these experiments. Here, a light beam is directed towards the levitated drop and the camera (at 90 degrees angle), without any filter, collects the images of the scattered light. By monitoring the mean intensity of the scattered light from an area in the image, excluding specular reflections from the light source, a change in intensity is detected when the concentration of the aggregates increases as shown in Figure 25. However, calibration of the concentration of aggregates was not made because the aim was to indicate the onset of precipitation. This was recorded when the scattered light intensity was above the limit of detection, indicating the formation of aggregates.

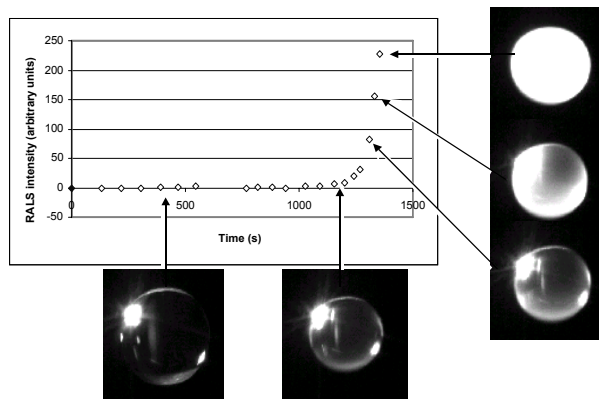


Figure 25 Image series of a levitated drop during a precipitation experiment of a protein

5. Environmental monitoring by fluorescence LIDAR techniques

5.1. Background

The environment we are living in is exposed to various pollutants and the research in environmental monitoring is extensive, both in terms of measurements of pollutant concentrations and on their effects on the environment. In Papers 6 and 7, different historical buildings are monitored with a remote sensing technique and the same technique is used to monitor the water in parts of the Mediterranean Sea; see Paper 5.

Environmental monitoring is often performed by collecting samples for subsequent analysis in a laboratory, and the methods described in the previous chapter can be used for the separation and quantification of such samples. Even though these methods are used extensively, the drawbacks with such methods can be that the substance properties are changing on the way to the laboratory. One method to analyse the samples is to use remote laser-induced fluorescence for direct environmental monitoring *in situ*. LIDAR is mostly used for detection of absorbing air pollutants, such as different gases (See, e.g. [19,20]), but with a slight modification it can be employed to measure fluorescence at long distances. Here, the technique is denoted fluorescence LIDAR and the system used was described in Section 3.3.2.

5.2. Laser-induced fluorescence of monuments

5.2.1. Introduction

For monitoring of historical building fluorescence LIDAR has various advantages compared to traditional sampling techniques. In this technique the full fluorescence emission spectrum is recorded for each location examined. Point measurements of different stones from both the Lund Cathedral and Italian monuments, have been recorded earlier. Scanning the beam in the x-y directions produced fluorescence maps. The possibility to do *in situ* and non-destructive monitoring is a major advantage. For practical reasons, the feasibility of monitoring at long distances is attractive. This includes the monitoring of objects and areas that are difficult to access. The LIF technique itself is favourable since sometimes substances that cannot be discovered by the naked eye can be detected. In addition, the resulting spectra are suitable to distinguish different object properties. Fluorescence maps are also attractive because the status of every spot of an investigated object, e.g. a historical monument, can be controlled.

5.2.2. Evaluation of spectral signatures

The fluorescence emission spectra collected were in the range from 395 nm to 715 nm. This range was selected since the spectral signature of certain protective treatments, exhibit a strong fluorescence around 400 nm, and the fluorescence from chlorophyll in cyanobacteria and green algae falls in the reddish region. To increase the signal-to-noise ratio, the fluorescence light from 6-12 laser pulses were accumulated. An ambient background file was also acquired before every set of measurement and subtracted from the spectra recorded. Examples of different spectra from various monument stone types are shown in Figure 3 in Paper 6.

Two different techniques have been used for spectroscopic imaging. The first one is the so-called ratio imaging, which is a straightforward method. A ratio map is constructed where the fluorescence intensity from two wavelengths regions is used. Here, the characteristic fluorescence from the species must be known. Otherwise, the image constructed will not show any relevant information. On the other hand, if appropriate regions are used, the image shows substantial information on the scene. Fluorescence intensity variations due to the geometry of the object investigated, are also compensated for in ratio imaging, and also fluctuations of the excitation light. Figure 3 in Paper 6 shows a picture of the northern portal of the Lund Cathedral with the corresponding fluorescence spectra at selected points. In Figure 7 in the same paper, a ratio map is shown, using the $I(600\text{ nm})/I(448\text{ nm})$ value.

The second method involves principal component analysis, where wavelength regions with a high information content are indicated. Because of the mathematical approach, where so-called PC vectors are formed, the results involve spectral information from all the areas and wavelength regions. This means that a PC vector does not contain information from a pure substance, which can be a complication. A slightly modified method was used for the

construction of Figure 8 in Paper 6. Here, the chlorophyll signal is separated from the full spectrum. PCA is then made on this data set and the resulting image is as mentioned above. The two loading vectors are here indicating that the residual information at the wavelengths where chlorophyll emits fluorescence is important. Instead, if the entire data set is used, the resulting components are a mixture of the spectral signatures. By selecting different areas in the score plot, and displaying them in different colours, an image with areas with the same spectral signature is constructed as seen in Figure 10 in Paper 6. In Paper 7, a similar technique was used for evaluation of the spectra recorded.

5.3. Laser-induced fluorescence of seawater

The same equipment, as employed when the historical monuments were monitored, was used for the investigation of Mediterranean waters in ship-borne experiments. Measurements from both the surface layer and at different depths were made. Also, the spectral signature of the pollution indicator *Posidonia Oceanica*, collected from the sea bottom, was studied.

5.3.1. Spectral signatures along a route

In a certain area of the sea, two different streams of seawater are crossing each other forming a front. At the same time as the ship moved from the north heading south through the front, fluorescence spectra were acquired. The fluorescence was acquired from the top water layer and the chlorophyll intensity was normalised to the water Raman signal. An example of such a recording is shown in Figure 12 in Paper 5.

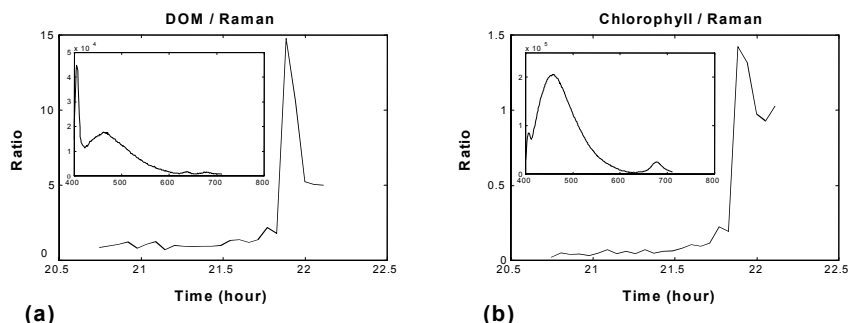


Figure 26 DOM/Raman and chlorophyll/Raman ratios along a route heading for Civitavecchia. The inserts show two different kinds of spectra.

Another route was also monitored, which was when the ship headed towards the coastline and into the harbour of Civitavecchia. In Figure 26, the Distributed Organic Matter (DOM) signal and the chlorophyll signal are monitored. A minor increase is seen, as the ship approaches the coastline and a strong increase in both signals is clearly observed when the ship enters the harbour.

5.3.2. Depth resolved measurements

At another location in the Mediterranean Sea, fluorescence spectra were acquired at different depths. This was performed with a computer controlled delay generator connected to the detector as discussed above. The first spectrum was acquired from the surface and approximate four meters down into the water. The delay was then changed, corresponding to four meters of water column. This was continued down to 20 meters depth and after this the sequence started at the surface again. With this technique, every depth was measured every third minute. Figure 17 in Paper 5 shows an example of the fluorescence spectra at the depths measured. The expectation was to detect the sea bottom, but sufficiently shallow waters could not be entered for safety reasons.

The excitation light is strongly absorbed in water and the fluorescence emitted below the surface is also absorbed on its way to the surface. Due to the wavelength dependent absorption coefficient for water, the profile of the fluorescence spectrum will change. This results in non-comparable spectra from different depths if no correction is made. On the other hand, the ratio between two spectra recorded from different depths can show the wavelength dependent absorption coefficient of the certain water type as illustrated in Figure 27.

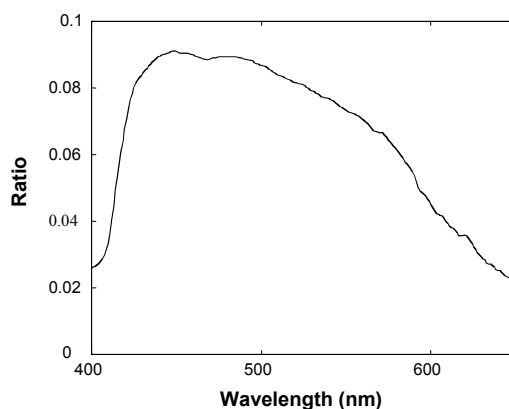


Figure 27 Ratio between two water spectra acquired from different depths

5.3.3. Fluorescence of *Posidonia Oceanica*

The seaweed *Posidonia Oceanica* can be used for monitoring of, e.g. toxic metal accumulation over longer time periods. To accomplish the measurements, *Posidonia* samples were retrieved from the sea bottom at different times and fluorescence spectra were recorded at different positions on the plants (Figure 21 in Paper 5). Also samples of *Posidonia* were put into bottles for further laboratory analysis.

6. Medical applications

6.1. Introduction

It has been shown in the last two chapters that lasers and light spectroscopy can be used in various applications. In this last chapter, the use of lasers and laser spectroscopy in the field of human health care is shown. It would be impossible to cover the large field of laser use in medicine, and below we focus on aspects explored in the present work. The advantages of laser spectroscopy in the medical field are similar to those in the areas previously described; it facilitates *in-situ*, non-destructive and real-time measurements.

Laser technology has been used in medical applications during the last decades. One application is to induce necrosis by locally increasing the tissue temperature. If the temperature is increased up to approximately 44 °C, enzymatic reactions are altered. At 60 °C the proteins start to denature and at 100 °C boiling of the liquid inside the cells is damaging the cell membranes. At last, carbonisation occurs for temperatures higher than 200 °C. Another application is to use the laser in surgery for bloodless cutting, which is due to the carbonisation of the incision. A third application is to thermally coagulate blood in the retina of diabetic patients and in the skin of portwine stains.

In this thesis, medical laser techniques have been used for fluorescence measurements, mainly to classify skin and deeper lying tissue as healthy or cancerous. Cancerous tissue has also been treated by the use of photodynamic therapy [36], which combines laser radiation and a photosensitising agent.

6.2. Tumour selective substances

To increase the fluorescence demarcation between healthy and cancerous tissue, a chemical agent is often used. A drug is administered to the patient orally, through an intravenous injection or topically. After a time period of a few hours, the agent is to a higher degree accumulated in the cancerous tissue compared with the normal tissue and the agent, or a product to the agent, contributes to the fluorescence. Many of the tumour selective substances can also be used for photodynamic treatment. For such purposes, the dose of the substance is higher.

Research in this field was long focusing on hematoporphyrin derivate (HPD). This agent is selectively retained in cancerous cells. A disadvantage with HPD is the long time before the agent is eliminated from the body - several weeks. During this time the patient is very sensitive to light and must keep out from direct sunlight. Today, a commonly used substance is delta-amino levulinic acid (ALA), which is a precursor to haem in the haem cycle. ALA is a naturally constituent in the body and is therefore non-toxic in low dose. When ALA is administered to the patient, protoporphyrin IX (PpIX), one of the intermediate products in the haem cycle, is produced at a high rate. An elevated

concentration is obtained in a period of a few hours [37-39]. This PpIX is selectively accumulated in premalignant or malignant tissues and is the actual tumour marker. An advantage with the ALA compared with the HPD approach is the higher clearance rate, resulting in the patient being sensitive to light for a few hours only. Two major absorption peaks are used for medical purposes. The first one is located at 405 nm and the second one is at 635 nm. Excitation light with 405-nm wavelength is often used for fluorescence purposes due to the high absorption of the PpIX, which results in a strong fluorescence at 635 and 705 nm (Figure 28). For treatment purposes, light with the wavelength of 635 nm is used for irradiation of tumours, since tissue absorption is lower at this wavelength, resulting in a better penetration of the treatment light.

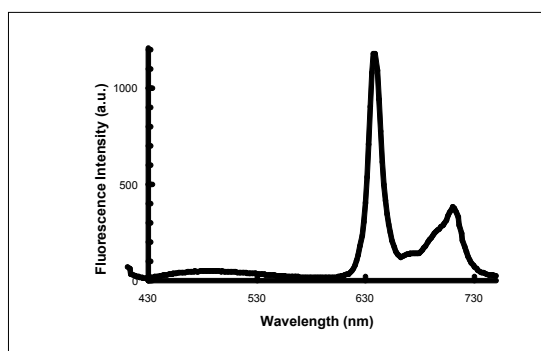


Figure 28 Fluorescence spectrum from tumour tissue after it was exposed to ALA

6.3. Fluorescence diagnostics

6.3.1. Introduction

For tissue diagnostics[4,15,17,40], ALA has been used as a sensitising agent. The two systems described earlier in Sects 3.3.1 and 3.3.3 were used to measure the fluorescence.

6.3.2. Point measurements

In connection with treatments of tumours in rats and humans, the point measuring equipment was used. Here, the fluorescence intensity across the tumour was measured at different times during the treatment process. If the fluorescence from the same spot in the middle of the tumour is measured at different times before the treatment, the build up of PpIX can be followed. Fluorescence profiles across the tumour 6 hours after ALA cream application are shown in Figure 5 of Paper 11, and the fluorescence peaks at 635 and 705 nm clearly indicate the build up of PpIX in the tumour compared with the healthy tissue. Another observation is also made. At the same time as the red fluorescence increases in the tumour, the fluorescence in the blue region is decreasing. In healthy tissue the situation is

the opposite, a high blue fluorescence and nearly no fluorescence at all in the red region. The natural fluorescence in tissue is called autofluorescence. This fluorescence originates from different endogenous substances in the tissue.

6.3.3. Fluorescence imaging

In Paper 8, the imaging technique, described in Section 3.3.3 was used. Here, the fluorescence in the three different images is used to construct a dimensionless contrast image. This is easiest explained by looking at the fluorescence spectra from healthy tissue and tumour tissue (Figure 5 in Paper 11). By dividing the fluorescence intensity in the red region with the intensity in the blue region, a ratio is calculated that is high for tumour tissue and low for healthy tissue. An advantage by using a dimensionless ratio is that spatial intensity variations of the excitation light are not influencing the ratio level. The only difference is that the noise is higher in those areas where the intensity of the excitation light is low.

Our equipment is acquiring three images in different wavelength regions and the contrast function most often used is

$$F = \frac{A - k_1 D}{B + k_2}$$

Here, A is the fluorescence intensity image integrated in the region 580-750 nm, which is mainly the PpIX fluorescence. The image marked D is in the wavelength region from 480 nm to 580 nm. This image is multiplied with the constant k_1 and subtracted from the intensity A to reduce the influence of the tissue autofluorescence superimposed on the PpIX fluorescence in region A. This means that the constant k_1 is chosen so that $k_1 D$ equals the intensity of A in healthy tissue. This results in that the numerator is close to zero for healthy tissue, which has only faint fluorescence in the red region, and a positive value is obtained in areas with a high PpIX concentration. The denominator B from the blue region (420 to 480 nm), which originates from endogenous fluorophores (autofluorescence), is used to obtain a dimensionless unit and to increase the ratio in tumours tissue. By adding a positive constant (k_2), the influence from noise in low intensity regions in B is reduced.

One problem appeared at one step in the development of the system. The blue dichroic mirror, which is supposed to reflect blue light only, has a faint reflection in the reddish region. This results in that the bluish image B, the intensity of which should decrease in the tumour areas, has an incorrect behaviour. The image D was therefore used as denominator in the evaluation of data collected with the system during the period before this problem was corrected, and the contrast function used was

$$F = \frac{A - k_1 D}{D + k_2}$$

Figure 5 in Paper 8 shows the resulting fluorescence ratio image superimposed on the white light image.

6.4. Photodynamic therapy

6.4.1. Mechanisms of photodynamic therapy

Photodynamic therapy is one of the methods for treating tumours [41]. Here the substance ALA is also used for treatment purposes [42,43]. In this case, a higher concentration of the ALA substance is given, compared with the diagnostic modality. To induce cell death (necrosis) in the tumour, red light of about 635 nm wavelength is used. The treatment mechanism is based on a light-induced chemical reaction requiring three components. The first one is a sensitising agent, in this case ALA converted in the haem cycle to PpIX. The second one is energy to start the chemical reaction, here light at 635 nm, and the last one is oxygen. When PpIX absorbs the light, the molecules are excited to another molecular configuration requiring more internal energy. This excess energy is then used to transfer oxygen molecules to their excited singlet state through two steps; see Figure 29. Singlet oxygen is very aggressive to human tissue and oxidises different substances, which results in cell death. The advantage with this photodynamic therapy compared with other tumour treating techniques, is that cell death is not induced in healthy tissue, which among other things is due to the lower amount of PpIX in the such tissue.

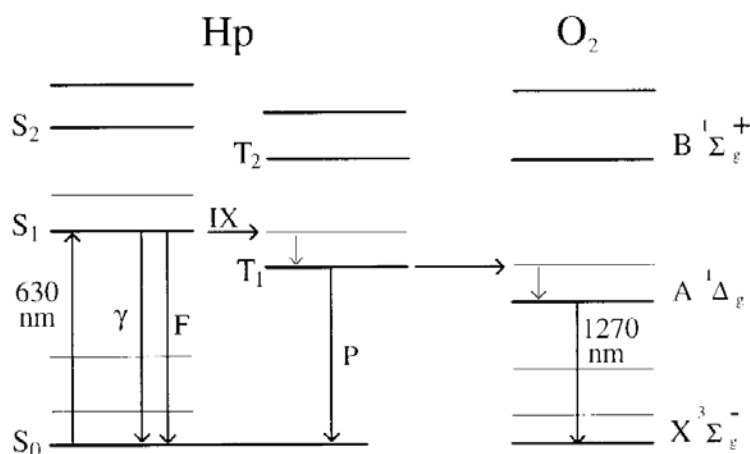


Figure 29 Energy level diagram showing the energy transfer from haematoporphyrin to oxygen during PDT

6.4.2. Light sources

For light excitation in photodynamic therapy, different excitation sources can be used. A property that must be fulfilled though, is a high fluence rate in the wavelength region where PpIX absorbs light. Because of the need of a large penetration depth, light with the wavelength 405 nm cannot be used. Instead, light of 635-nm wavelength is most often utilised. Today, various sources exist, e.g. filtered continuous lamps and lasers. Of these sources, the laser is the better one due to the high brightness in the wavelength region where PpIX absorbs light. In our equipment, a fibre coupled diode laser is used. Actually, it consists of many diodes that are focused into the same optical fibre resulting in a power of up to two Watts of light at 635 nm.

In light administration to the tumour, two different techniques can be used. The first one is to fix the distal end of the optical fibre at a certain distance from the tumour, and illuminate its surface with the expanded light beam. This technique is a modality used for treatment of most skin lesions. For treatment of some lesions inside the body or thick skin lesions, a second technique may be used. Here, the light is administrated through many fibres that are inserted into the lesion (interstitial PDT (IPDT)), or brought in direct contact with the lesion; see Papers 9-11.

6.4.3. Treatment of superficial skin lesions

Many treatment scenarios can be used. Here, the main steps in common for most of them are presented. Before a treatment can start, the size (area) of the lesions is measured. This area is used to calculate the laser power needed to have a fluence rate of approximate 100 mW/cm². The total light dose given to the lesions is typically 60 J/cm², which results in a treatment time of about 10 minutes. An increase in the temperature of the lesions may result if a higher fluence rate is used. A temperature higher than 43 °C for a prolonged time may also induce tissue responses and even necrosis and this is avoided to have a better control over the treatment.

ALA is a powder, and for the treatment of skin lesions [44], the ALA is mixed into Essex cream. Three to six hours before treatment this mixture is topically applied onto the lesion and approximately 1 cm outside its border. Before the ALA is applied fluorescence measurements are performed and spectra are also acquired a few times before the treatment to inspect the build-up of PpIX in the lesion. At the treatment, the distal end from the laser is fixed at a distance chosen so that the lesion and the area 1 cm outside the border is irradiated.

6.5. Interstitial photodynamic therapy

6.5.1. Introduction

Only thin superficial tumours can be treated with the technique just described, due to the low penetration depth of the light, approximately a few millimetres. To treat thicker

tumours or tumours inside the body, another PDT technique must be used; interstitial photodynamic therapy [45].

IPDT uses the same methodology as PDT, i.e. ALA may be used as the sensitising agent and light with 635-nm wavelength can be used to initiate the reaction. ALA cream is not effective for tumours thicker than 3 mm, as mentioned before, due to the long time for the ALA substance to diffuse into the entire mass of the tumour. Instead, ALA can be dissolved and injected with a syringe into the blood stream or locally into the tumour. ALA powder may alternatively be dissolved in orange juice, which the patient drinks a few hours before the treatment.

6.5.2. IPDT system

The major difference between PDT and IPDT is how the light is administered into the tumour. For optimised administration of the light into a volume, multiple optical fibres are favourable [46,47].

Figure 30 shows the set-up of the system used in Papers 9,10 and 11. The light source is the same fibre coupled laser used for the superficial PDT treatments. Instead of pointing with the fibre onto the tumour, it is connected to a beam-splitting unit. Here, an optical arrangement divides the light into six optical fibres, which are inserted into the tumour. To cause a treatment as uniform as possible for the volume and to minimise the treatment time, the fibre tips must be arranged at specific positions. These positions depend on the shape of the tumour and a computer program is used to determine these positions. The program solves the diffusion equation with the finite element method (FEM) for the six fibres separately, and an iteration of the fibre positions is made until the smoothest light fluence inside the tumour is obtained. In these calculations, the shape of the lesion must be known (or assumed), and the optical properties for both the lesion and the surrounding tissue are assumed as well. When the iteration is made, not only the positions of the fibres are varied, but also the light power emitted from each individual fibre.

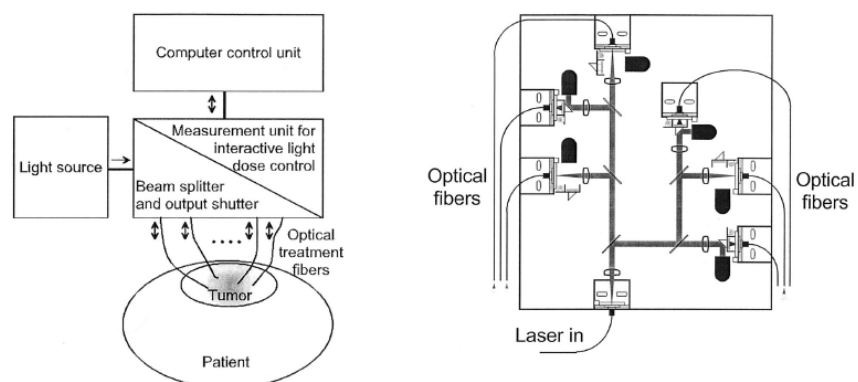


Figure 30 Set-up of the IPDT system. To the left, a schematic drawing of the entire system is shown and to the right, the configuration of the beam-splitting unit is displayed

At each light path inside the beam-splitting box, light sensitive diodes are mounted on rotating axes. These can individually be positioned in the light path with the sensitive side towards the fibre end. When a diode is rotated into the light path, the output light is blocked. The light transmitted from the tissue into the box is then detected by the diode in this mode. Each fibre can thus be used either as a light emitter or as a detector. By having one fibre at a time transmitting laser light into the tumour and the other diodes measuring the light, the light fluence is determined at each individual fibre tip. Figure 7 in Paper 10 shows the fluence at each fibre tip during a treatment. These measurements are also used to discover if the light emitted from the fibres behaves incorrectly. This is the consequence, for example, if blood is coagulated on the fibre tip resulting in a high absorption of the light in that point and the treatment time is prolonged. The system was used in tumour treatments of experimental animals as well as patients as described in Papers 9,10 and 11.

Acknowledgements

I would like to thank my supervisor Sune Svanberg very heartily for his strong support and never ending happiness; I cannot find a person with a bigger heart. I am also very grateful to my other two supervisors Stefan Andersson-Engels and Staffan Nilsson for all their time they have spent with me, and Katarina Svanberg for an important medical perspective of the work.

It would be impossible to thank all the people who have helped me. The members of the Medical Group and the entire Atomic Physics Division, as well as the people at the Technical Analytical Chemistry division are all deserving my gratitude.

I am also conveying many thanks to my collaborators in Italy.

All my Friends, you all know how good friends you are!

My dear Family, thank you for your love and support through the years!

My beloved Louise, I LOVE YOU. Do you want to marry me sometime?

THANK YOU ALL!

Summary of papers

- Paper 1. A system for studying protein precipitation in a levitated drop was constructed. With this method, proper conditions for protein crystallisation can be found faster than with conventional methods.
- Paper 2. The behaviour of fat cells was studied in experiments on levitated drops. Free fatty acids from the fat cells decreased the pH in the drop, which was detected with fluorescence techniques.
- Paper 3. A novel system for efficient light collection in imaging detection on a capillary electrophoretic system was developed and tested in separations of enantiomer amino acids. To increase the light collection, optical fibres were used.
- Paper 4. A further novel system for the detection of separating analytes in a capillary was developed utilising a combination of optical absorption and fluorescence. Absorbing molecules were detected in the fluorescence decrease in a background fluorophore.
- Paper 5. A fluorescence lidar system for maritime water column measurements was integrated based on the Lund mobile lidar system. Field experiment on board the Italian research vessel *Urania* were performed in collaboration with Italian partners regarding distributed organic matter (DOM) and chlorophyll, as well as the seaweed *Posidonia Oceanica*.
- Paper 6. Fluorescence imaging of the Lund cathedral was performed in pioneering experiments of this kind. A scanning fluorescence lidar system was used and different types of stones as well as the presence of biodeteriogens were detected using multi-variate analysis on the recorded spectra.
- Paper 7. A similar project as in Paper 6 was performed, but now at the Cathedral and Baptistery in the Italian town of Parma, exhibiting other types of building materials. In particular, the presence of stone conserving treatments as well as algal growth was studied.
- Paper 8. Laser-induced fluorescence was used in point-monitoring and imaging diagnostic measurements on patients with basal cell carcinoma. The tumours were sensitised by application of a cream containing δ -amino levulinic acid (ALA). In particular, two different imaging systems operating in the frequency- and time domains, respectively, were intercompared.

- Papers 9,10 A system for interstitial and interactive photodynamic therapy of malignant tumours was used in treatments of tumours induced in laboratory rats. The feasibility of the concept was demonstrated. Fluorescence measurements of the illumination bleaching of protoporphyrin IX, induced from ALA application, were performed as part of the dosimetry.
- Paper 11. Patient treatments using photodynamic therapy were performed in a collaboration with Latvian oncologists and physicists. Multi-fibre contact light delivery was applied for the first time as a new modality for efficient eradication of thick tumours. Valuable experience for future interstitial treatments of deep-lying tumours was obtained.

Contributions by the author to different papers

- Paper 1.** Responsible for the detection set-up. Development of evaluation software. Contributions to manuscript.
- Paper 2.** Responsible for the detection system, and contributor to the manuscript preparation.
- Paper 3.** Main responsible for the paper. Constructor of the experimental set-up. Main part of manuscript writing.
- Paper 4.** Contributions to the experimental work. Development of the evaluation algorithm.
- Paper 5.** Main responsible for the Swedish part of the project. Preparations for field campaign, field test measurements, data evaluation, figure preparation.
- Paper 6.** Substantial part of preparations and field experiment. Main responsible for data analysis and figure preparations.
- Paper 7.** Substantial part of preparations and field experiment. Contributions to evaluation.
- Paper 8.** Substantial part of data collection, evaluation and figure preparations regarding the Swedish fluorosensor work.
- Paper 9.** Substantial part of equipment preparation and animal investigations. Contributions to evaluation and manuscript.
- Paper 10.** Main responsible for the paper. Substantial part in equipment preparation and animal investigations. Contributions to data evaluation and manuscript.
- Paper 11.** Substantial part in preparation of equipment and in the clinical work.

Reference List

1. S.L. Jacques, C.A. Alter and S.A. Prahl, Angular dependence of HeNe laser light scattering by human dermis, *Lasers in the Life Sciences* **1**, 309-333 (1987)
2. J.-L. Boulnois, Photophysical processes in recent medical laser developments: a review, *Lasers in Medical Science* **1**, 47-66 (1986)
3. W.M. Star, Light dosimetry *in vivo* , *Physics in Medicine and Biology* **42**, 763-787 (1997)
4. G.J. Müller et al., Medical optical tomography: Functional imaging and monitoring, SPIE Institute Series no. 11 (SPIE, 1993)
5. Z. Amin, W.R. Lees and S.G. Bown, Interstitial laser photocoagulation for the treatment of prostatic cancer, *British Journal of Radiology* **66**, 1044-1047 (1993)
6. S. Andrejevic-Blant, A. Woodtli, G. Wagnieres, C. Fontolliet, H. van den Bergh and P. Monnier, Interstitial photodynamic therapy with tetra(m-hydroxyphenyl)chlorin: tumor versus striated muscle damage, *International Journal of Radiation Oncology Biology Physics* **42**, 403-412 (1998)
7. M. Keijzer, R.R. Richards-Kortum, S.L. Jacques and M.S. Feld, Fluorescence spectroscopy of turbid media: Autofluorescence of the human aorta, *Applied Optics* **28**, 4286-4292 (1989)
8. J. Wu, M.S. Feld and R.P. Rava, Analytical model for extracting intrinsic fluorescence in turbid media, *Applied Optics* **32**, 3585-3595 (1993)
9. S.R. Arridge, M. Schweiger, M. Hiraoka and D.T. Delpy, A finite element approach for modeling photon transport in tissue, *Medical Physics* **20**, 299-309 (1993)
10. N. S. Ottosen and Petersson, H., Introduction to the Finite Element Method (Prentice Hall International (UK), 1992)
11. S. S. Rao, The Finite Element Method in Engineering (Pergamon Press, 1989)
12. L. Wang, S.L. Jacques and L. Zheng, MCML - Monte Carlo modeling of light transport in multi-layered tissues, *Computer Methods and Programs in Medicine* **47**, 131-146 (1995)

13. A. J. Welch and M. J. C. van Gemert, Optical-Thermal Response of Laser-Irradiated Tissue (Plenum Press, New York, NY, 1995)
14. S. Svanberg, Atomic and Molecular Spectroscopy – Basic Aspects and Practical Applications (Springer Verlag, 2001)
15. U. Gustafsson, S. Pålsson and S. Svanberg, Compact fibre-optic fluorosensor using a continuous wave violet diode laser and an integrated spectrometer, *Review of Scientific Instruments* **71**, 3004-3006 (2000)
16. R.A. Zângaro, L. Silveira, Jr., R. Manoharan and G. Zonios, Rapid multiexcitation fluorescence spectroscopy system for in vivo tissue diagnosis, *Applied Optics* **35**, 5211-5219 (1996)
17. C. af Klinteberg, M. Andreasson, O. Sandström, S. Andersson-Engels and S. Svanberg, Compact medical fluorosensor for minimally invasive tissue characterisation, to appear
18. R. M. Measures, Laser Remote Sensing: Fundamentals and Applications (John Wiley & Sons, 1984)
19. E. Durieux, L. Fiorani, B. Calpini, M. Flamm, L. Jaquet and H. van den Bergh, Tropospheric ozone measurements over the Great Athens area during the MEDCAPHOT-TRACE campaign with a new shot-per-shot dial instrument: Experimental system and results, *Atmospheric Environment* **32**, 2141-2150 (1998)
20. P. Weibring, J. Swartling, H. Edner, S. Svanberg, T. Caltabiano, D. Condarelli, G. Cecchi and L. Pantani, Optical monitoring of volcanic sulphur dioxide emissions - Comparison between four different remote-sensing spectroscopic techniques, *Optics and Lasers in Engineering* **37**, 267-284 (2002)
21. S. Nilsson, J. Johansson, M. Mecklenburg, S. Birnbaum, S. Svanberg, K.G. Wahlund, K. Mosbach, A. Miyabayashi and P.O. Larsson, Real-time fluorescence imaging of capillary electrophoresis, *Journal of Capillary Electrophoresis* **2**, 46-52 (1995)
22. J.V. Sweedler, J.B. Shear, H.A. Fishman, R.N. Zare and R.H. Scheller, Fluorescence detection in capillary zone electrophoresis using a charge-coupled device with time-delayed integration, *Analytical Chemistry* **63**, 496-502 (1991)
23. E.S. Yeung and W.G. Kuhr, Indirect detection methods for capillary separation, *Analytical Chemistry* **63**, 275-282 (1991)

-
24. P. Weibring, H. Edner and S. Svanberg, Versatile mobile lidar system for environmental monitoring, to appear
 25. S. Andersson-Engels, J. Johansson and S. Svanberg, Medical diagnostic system based on simultaneous multispectral fluorescence imaging, *Applied Optics* **33**, 8022-8029 (1994)
 26. K. Svanberg, I. Wang, S. Colleen, I. Idvall, C. Ingvar, R. Rydell, D. Jocham, H. Diddens, S. Bown, G. Gregory, S. Montán, S. Andersson-Engels and S. Svanberg, Clinical multi-colour fluorescence imaging of malignant tumours - initial experience, *Acta Radiologica* **39**, 2-9 (1998)
 27. H. Martens and T. Naes, *Multivariate Calibration* (Wiley & Sons Ltd, 1991)
 28. K. Esbensen, S. Schönkopf, T. Midtgaard, and D. Guyot, *Multivariate Analysis in Practice* (CAMO ASA, 1998)
 29. D.A. Skoog, D.M. West, and F.J. Holler, *Fundamentals of Analytical Chemistry* (Saunders College Publishing, 1988)
 30. L. Schweitz, M. Petersson, T. Johansson and S. Nilsson, Alternative methods providing enhanced sensitivity and selectivity in capillary electroseparation experiments, *Journal of Chromatography* **892**, 203-217 (2000)
 31. D. Heiger, *High performance capillary electrophoresis* (Agilent Technologies, 2000)
 32. H. Nilsson, M. Wiklund, T. Johansson, H.M. Hertz and S. Nilsson, Microparticles for selective protein determination in capillary electrophoresis, *Electrophoresis* **22**, 2384-2390 (2001)
 33. J. Johansson, D.T. Witte, M. Larsson and S. Nilsson, Real-time fluorescence imaging of isotachophoretic preconcentration for capillary electrophoresis, *Analytical Chemistry* **68**, 2766-2770 (1996)
 34. E. Welter and B. Neidhart, Acoustically levitated droplets - a new tool for micro and trace analysis, *Fresenius Journal of Analytical Chemistry* **357**, 345-350 (1997)
 35. R. Giegé, J. Drenth, A. Ducruix, A. McPherson and W. Saenger, Crystallogensis of Biological Macromolecules. Biological, Microgravity and Other Physico-Chemical Aspects, *Progress in Crystal Growth and Characterisation* **30**, 237-281 (1995)
 36. F. Stewart, P. Baas and W. Star, What does photodynamic therapy have to offer radiation oncologists (or their cancer patients)?, *Radiothermal Oncology* **48**, 233-248 (1998)

37. J. Johansson, R. Berg, K. Svanberg and S. Svanberg, Laser-induced fluorescence studies of normal and malignant tumour tissue of rat following intravenous injection of δ -amino levulinic acid, *Lasers in Surgery and Medicine* **20**, 272-279 (1997)
38. N. van der Veen, H.L.L.M. van Leengoed and W.M. Star, *In vivo* fluorescence kinetics and photodynamic therapy using 5-aminolaevulinic acid-induced porphyrin: increased damage after multiple irradiations, *British Journal of Cancer* **70**, 867-872 (1994)
39. Q. Peng, T. Warloe, K. Berg, J. Moan, M. Kongshaug, K.-E. Giercksky and J.M. Nesland, 5-aminolevulinic acid-based photodynamic therapy: Clinical research and future challenges, *Cancer* **79**, 2282-2308 (1997)
40. G. Wagnieres, C. Depeursinge, P. Monnier, M. Savary, P. Cornaz, A. Chatelain and H. van den Bergh, Photodetection of early cancer by laser-induced fluorescence of a tumour-selective dye: apparatus design and realization, SPIE Proceeding (1990)
41. H.I. Pass, Photodynamic therapy in oncology: mechanisms and clinical use, *Journal of the National Cancer Institute* **85**, 443-456 (1993)
42. J.C. Kennedy, R.H. Pottier and D.C. Pross, Photodynamic therapy with endogenous protoporphyrin IX: Basic principles and present clinical experience, *Journal of Photochemistry and Photobiology B, Biology* **6**, 143-148 (1990)
43. K. Svanberg, T. Andersson, D. Killander, I. Wang, U. Stenram, S. Andersson-Engels, R. Berg, J. Johansson and S. Svanberg, Photodynamic therapy of non-melanoma malignant tumours of the skin using topical δ -amino levulinic acid sensitization and laser irradiation, *British Journal of Dermatology* **130**, 743-751 (1994)
44. C. Fritsch, G. Goerz and T. Ruzicka, Photodynamic therapy in dermatology, *Archives of Dermatology* **134**, 207-214 (1998)
45. T.J. Dougherty, R.E. Thoma, D.G. Boyle and K.R. Weishaupt, Interstitial photoradiation therapy for primary solid tumors in pet cats and dogs, *Cancer Research* **41**, 401-404 (1981)
46. S.F. Purkiss, R. Dean, J.T. Allardice, M. Grahn and N.S. Williams, An interstitial light delivery system for photodynamic therapy within the liver, *Lasers in Medical Science* **8**, 253-257 (1993)
47. C.P. Lowdell, D.V. Ash, I. Driver and S.B. Brown, Interstitial photodynamic therapy. Clinical experience with diffusing fibres in the treatment of cutaneous and subcutaneous tumours, *British Journal of Cancer* **67**, 1398-1403 (1993)

Screening of Protein Nucleation Conditions Using Levitated Drops

Sabina Santesson,¹ Eila Cedergren,² Thomas Johansson,³
Thomas Laurell,⁴ Johan Nilsson,⁴ and Staffan Nilsson^{1*}

¹Technical Analytical Chemistry,

²Biochemistry,

³Atomic Physics,

⁴Electrical Measurements,

Lund University, P. O. B. 124, SE-221 00 Lund, Sweden.

ABSTRACT

The growth of suitable protein crystals is an essential step in the structure determination of a protein by X-ray diffraction, but at present crystals are mostly grown using trial-and-error procedures. Protocols that rapidly screen for the crystal nucleation step are lacking. Presented here is an approach to minimise the consumption of protein material while searching for the nucleation conditions. Acoustically levitated protein-containing drops (0.25–1.5 μL volume) are injected with crystallising agents using piezoelectric flow through dispensers (pL volume range), and volume calculations give the concentrations of all components in the drop at any time. The precipitation in the drop is monitored using right angle light scattering (RALS). A *precipitation diagram* is constructed that gives the protein/precipitant concentration boundaries between the minimum and the maximum detectable protein precipitation. Supersaturation is the prerequisite for crystal nucleation. Guided by the concentration values obtained from the precipitation diagram when approaching the supersaturation region, separate crystallisation drops are mixed and left to equilibrate. Several proteins have been tested using precipitation screening in levitated drops. The results confirm the time and material saving qualities of this method. A range of conditions can be screened using small amounts of protein to roughly determine solubility characteristics before crystallisation trials are initiated. D-serine dehydratase is described, which was found to be highly soluble in water and easily crystallises above 15 mg protein/mL between pH 6–8 in various salts and PEG 4000. Earlier attempts to crystallise the enzyme had failed presumably because the protein concentration had been chosen too low.

INTRODUCTION

Future perspectives in the field of structural biology, after the sequencing of the complete genomes of 30 species to date, will be joint efforts by international consortia to determine the three dimensional (3D) structures of all the proteins eventually identified. This involves research institutions as well as pharmaceutical industry. Protein crystallographers aim at determining high resolution structures in massive numbers at highly efficient synchrotron beam sources, for instance at Stanford (see <http://www.jcsg.org/scripts/prod/home.html>). This implies that methods need to be developed that meets the demand for quick prediction of the physico-chemical conditions required for the formation of single crystals of individual proteins or macromolecular complexes used in X-ray experiments. Crystallisation screening kits for proteins as well as nucleic acids are commercially available (*e.g.* from Hampton Research, Laguna Niguel, CA, USA, see www.hamptonresearch.com). Robots exist, which minimises human intervention in the practical work of setting up large-scale crystallisation trials.

Why then the need for new approaches? We lack protocols, which rapidly screen for the crystal nucleation step, a prerequisite for the growth of crystals in the first place. The theoretical and practical frames of crystallogenesis are well established for small molecules but not yet for macromolecules. Protein crystallisation is a complex phenomenon, involving the protein-solvent system, the interface between the crystal and the liquid, the transport of molecules in the liquid phase, and the kinetics of nucleation and growth. The process of nucleation and growth of crystals are usually discussed in terms of the classical theory of nucleation and crystal growth (1). Many of the aspects of protein nucleation and crystal growth are not thoroughly understood at present, thus preventing a rational approach to prediction of the nucleation conditions (2). However, it seems clear that while some proteins may, and do, nucleate according to the mechanism described in the classical nucleation theory, others do not (3). It has been suggested that one possible process by which nucleation occurs in such cases could be a two-step nucleation mechanism involving formation of a metastable liquid-liquid immiscible system where the protein nuclei are formed inside small metastable droplets of high protein concentration (4).

Protein crystals are usually grown by a somewhat organised trial-and-error procedure, for which the outcome is difficult to predict. If the wrong parameters are chosen, new trials must be made, thus wasting a large quantity of protein material. Generally, it is not known why a certain set of parameters of temperature, solvent composition, and supersaturation is the optimal one for crystal growth. This uncertainty is at least partly due to the

fact that a basic understanding of the crystal growing process of proteins from aqueous solutions is lacking (5).

Phase diagrams. In general, a phase diagram in crystallisation is the quantitative description of the parameters required for a solid phase to form and be in equilibrium with the liquid phase. It gives information at which conditions amorphous precipitation appears, when nucleation (formation of 3D crystalline cores) of the solute occurs and in which regions of the phase diagram nuclei grow to large crystals or never can form. In a phase diagram, the dependence of, among other things, pH, temperature, and type of crystallising agent on the solubility of the solute is described.

In protein crystallisation, the experimental determination of a phase diagram for a given protein under given physical conditions would be highly useful and provide a rational approach to choosing the proper conditions for crystal growth (6, 7). In macromolecular crystallography, however, this is seldom the practice. First, phase diagrams must be established from experimental determinations of the protein crystal solubility under systematically varied crystallisation conditions, thus requiring crystals already obtained. Second, large amounts of precious material are needed when constructing phase diagrams. Furthermore, in a proteomics project, the main goal is to rapidly solve many 3D structures to understand function. Very often, proteins whose crystallising conditions are not found are just excluded while the scientists move on to solve the structures of the proteins that do crystallise (8).

Analytical approach. Presented here is an approach to minimise the consumption of material while searching for that zone in the phase diagram where a protein could form nuclei. Supersaturation is the driving force for nucleation and has a major influence on the nucleation induction time (4, 8, 9). By assuming that precipitation of the protein out of the solution is a sign of supersaturated conditions, we initially search for these conditions. The protein solution is rapidly forced through the undersaturated towards the metastable, supersaturated state, thus allowing *only* amorphous precipitation to occur. No crystalline nuclei are given the time to form. This is done to *quickly* gain information about the precipitation limit of the protein under given conditions, to obtain rough boundaries between low and high supersaturation states during an experiment. Then nucleation tests need to be performed in separate crystallisation experiments.

Our analytical approach is based on equipment for ultrasonic (acoustic) levitation to create microenvironments where the only contacting surface is the surrounding gaseous medium, commonly air. Different techniques for sample levitation have previously been developed,

including optical trapping, electrostatic levitation, aerodynamic levitation, and acoustic levitation (10), some of which have been used in crystal growth experiments trying to mimic microgravity (11) or have been suggested useful in attempts to provide a statistical understanding of nucleation (12). In our system, specially designed flow-through dispensers realise delivery of crystallising agents in the picolitre (pL) scale to an acoustically levitated protein-containing drop. Microscope imaging is used to achieve continuous control of the drop volume and right angle light scattering (RALS) to monitor the onset of precipitation in the drop.

Using this approach, a wide range of protein and crystallising agent concentrations is covered using minimum amounts of material. This is achieved by injecting crystallisation agents into small drops (0.25-1.50 μ L) that are freely suspended in air in an acoustic levitator. The possibility to vary the drop volume (and thus the concentrations of the drop constituents) allows for a whole range of concentrations to be screened using a single levitated drop. A restricted number of crystallising agents is screened over the pH range 5.5-8.5. They represent three classes of precipitants: polyethylene glycols (PEG), salts and the viscous alcohol 2-methyl 2,4-pentanediol (MPD). Knowledge of the protein characteristics will determine the pH range or needed additives. If possible, the protein should preferably be dissolved in water.

EXPERIMENTAL SECTION

Proteins used: Two alcohol dehydrogenases (EC 1.1.1.1) were used, yeast alcohol dehydrogenase (YADH) purchased from Fluka BioChemika (lot 37066/1) and horse liver alcohol dehydrogenase (LADH) from Dr. Hans Werner Adolph, Saarbrücken University, Saarland, Germany. *E.coli* 2'-deoxyuridine 5'-triphosphate nucleotidohydrolases (dUTPase) (EC 3.6.1.23), in 10 mM 3-(N-morpholino)propane sulphonic acid (MOPS) pH 7.0, was a gift from Dr. Rebecca Persson, Lund University, Lund, Sweden. D-serine-dehydratase (D-SD) (EC 4.2.1.14) (13) was a gift from Prof. Dr. Klaus Schnackerz, Würzburg University, Würzburg, Germany.

Precipitation solutions. Commercial kits (Crystal screen 1 (HR2-110) and Crystal Screen cryo (HR2-122)) from Hampton Research (Laguna Niguel, CA, USA) used routinely in standard vapour diffusion experiments (14) for crystallisation trials of macromolecules were tested for use with the flow-through droplet dispensers. These kits contain the most commonly used crystallising agents and are based on using a sparse matrix sampling technology for quick testing of a wide range of pH, ionic additives, and various crystallising agents (15).

For D-SD, the approach was to follow the "Stura footprinting solubility strategy" (16) modified for our purposes according to Table 1.

The PEG solutions were prepared in 0.1 M imidazole malate buffer, mixed from 2M solution of imidazole and 2M solution of malic acid to give the desired pH over the interval 5.5-8.5 and diluted to 0.1M. Ammonium sulphate solutions were prepared in 0.1M imidazole malate buffer over the pH range and adjusted when needed. Phosphate solutions were made from 4M NaH_2PO_4 and 4M K_2HPO_4 to pH 7.0. The pH was adjusted to 6.5 using phosphoric acid and to pH 8 using NaOH. The citrate solution was prepared in 0.01M sodium borate buffer. 2M malonate pH 7.2 was also used, since it has previously been shown that malonate has a high success rate as crystallising agent (17). 0.1% NaN_3 was added to all solutions.

For the other proteins, knowledge of the properties of the protein or previously used crystallisation conditions determined the actual choice of crystallising agents according to Table 2.

Polyethylene glycol (PEG 400 and PEG 4000) was from Hampton Research; imidazole from Fluka; malate from Sigma; NaH_2PO_4 , K_2HPO_4 , $(\text{NH}_4)_2\text{SO}_4$, sodium citrate, MgCl_2 , and NaN_3 from Merck; Tris(hydroxymethyl)-aminomethane (Tris) and Hepes-Na-salt (N-(2-Hydroxyethyl)piperazine-N'-2-ethane sulfonic acid-Na-salt) from Serva Feinbiochemica. All chemicals were of the highest purity available.

Instrumental set-up. The instrumental set-up is shown in Fig. 1. A drop of protein solution is trapped in a node of a standing wave in an ultrasonic levitator (18, 19) APOS BA 10 (Dantec Dynamics GmbH, Erlangen, Germany). The acoustic levitator operates with a frequency of 100 kHz and generates the standing wave with equally spaced nodes and antinodes between an ultrasonic radiator and a solid reflector.

Flow-through droplet dispensers, developed in-house using silicon micromachining methods (20), are used for the additions of crystallisation agents and water. The dispenser droplets are ejected from a flow-through channel formed by joining two microstructured silicon plates, 13 mm long, 6 mm wide and 250 μm thick each. The flow-through channel measures 8 mm \times 1 mm \times 50 μm and has a volume of 400 nL. In the centre of the channel, a protruding pyramid shaped nozzle is formed. A multilayer piezoelectric element is connected to a push-bar in the channel wall opposing the nozzle. By applying a short voltage pulse across the piezoelectric element it elongates and pushes into the channel generating a pressure pulse in the liquid. The increased pressure accelerates the liquid in the nozzle and a droplet is ejected (Fig. 2). This process can be repeated at a rate up to several kHz. The volume of the ejected droplets, typically in the range of 50–100 pL, is dependent on the size of the nozzle, the shape of the voltage pulse and liquid parameters like surface tension, viscosity and density. The dispenser and examples of applications are more extensively described elsewhere (18-22). The dispensers used for the

levitation experiments had nozzles of 40×40 μm size and were mounted on XYZ-micropositioning stages to facilitate alignment. During the levitation experiments, the dispenser for crystallising agent addition was set to continuously eject 65 pL droplets at a rate of 50 Hz. The additions were stopped when the drop volume in the levitator was too large for levitation, or when an increase in the RALS signal indicated precipitation in the drop.

For surveillance of the drop volume and the monitoring of precipitation using RALS, a SMZ800 stereoscopic zoom microscope from Nikon Corporation, Yokyo, Japan, a KL200 cold light source equipped with a halogen light bulb (8V/20W) from Schott Glaswerke, Wiesbaden, Germany, a progressive scan CV-M10RS CCD camera from JAI Corporation, Yokohama, Japan, and a framegrabber from National Instruments Corporation, Austin, TX, USA were used. The light source and the microscope were oriented at right angles.

Volume and precipitation monitoring. A computer program was created in the LabVIEW™ (National Instruments Corporation, Austin, TX, USA) and Matlab™ (The MathWorks Inc., Natick, MA, USA) environment for drop volume calculation. The basic idea behind the volume calculation is to record a picture of the drop and to determine the drop diameter. The drop volume can then be estimated by assuming rotational symmetry of the drop around the z-axis (Fig. 3).

The digitised picture is transferred to a software routine written in Matlab™. Here the image processing toolbox is used which allows custom made algorithms. First, the noise in the picture is reduced by using a 2-dimensional digital filter (Wiener filter) (23) with the size of 5×5 pixels. Second, edge detection is made using Matlab's built-in function. Due to the transparency of the drop some parts of the edge around the drop are missing. Therefore, the edges around the drop must be connected which is achieved by using a closure algorithm that connects adjacent edges. By using an algorithm called "convex image" a new picture is created in which all the edges are enclosed into a convex picture, resulting in a black background and a uniform white drop. By dividing the picture of the drop into lines of pixels with a right and a left half it is possible to calculate the volumes of each rotational symmetric half. The radii at different z-positions are denoted $r_{l,z}$ (left) and $r_{r,z}$ (right), giving the volume for this disc segment as

$$V_z = \pi \cdot \frac{(r_{l,z}^2 + r_{r,z}^2)}{2} \cdot \Delta z$$

where V_z is the volume and Δz is the height of one pixel. The total volume of the drop is then summarised over all the discs.

High supersaturation in the protein drop generates precipitates that scatter light. LabVIEW™ provides the user with a function that calculates the mean intensity of a selected area in the picture. By using this function the increase in intensity of the right angle scattered light is monitored. The intensity is dependent on many factors, including the particle concentration, size, size distribution, and shape. However, in a precipitation screening experiment, it is only of interest to determine the *onset of precipitation*, i.e. the smallest detectable increase of scattering intensity from the baseline. This is expected to be dominated by the change in particle size and concentration whereas the influence of the other factors is of less importance. Therefore, the scattered intensity is a qualitative measure of the mass of precipitate. The area selected for the measurement must be smaller than the smallest drop size during the whole experiment and be chosen so as to avoid regions with specular reflections from the light source. In the levitated drop, precipitates assemble in the bottom of the drop due to sedimentation, so the area selected for measurement must be located in the lower half of the drop picture to obtain a change in signal at the lowest possible amount of precipitate. The CCD camera gives a readout signal in arbitrary units that is proportional to the scattered intensity plus the bias-potential.

Precipitation screening procedure. A drop of approximately 1 μL volume is levitated in the acoustic levitator. The drop can be positioned in the levitator either by using a Hamilton syringe of appropriate volume or injected using a flow-through dispenser. The flow-through dispensers are further used for addition of crystallising agents, water or buffer to the levitated drop. The drop is continuously monitored through a microscope by a CCD camera connected to a computer. Microscope imaging is used to achieve constant control of the drop volume, such that the concentrations of protein and crystallising agent in the levitated drop can be calculated at any time. The relationship between protein and crystallising agent concentrations is displayed in precipitation diagrams (Fig. 6). These diagrams are needed during the levitation experiments to determine which concentration intervals for the different components are of interest in further experiments.

Nucleation tests. The major use for the precipitation diagrams is to guide in the choice of proper conditions for nucleation tests. The nucleation tests were performed using batch crystallisation under paraffin oil in microtiter plates. The drops were mixed according to data extracted from the precipitation diagrams, assuming medium to high supersaturation in the mixture. The same protein solutions and the same crystallising agents were used as in the precipitation screening experiments. Generally, a wide range of protein and precipitant concentrations was explored using 3-

5 drops of 2-4 μL volume. At conditions where microcrystals could be observed the nucleation tendency of the macromolecule was confirmed. All experiments were performed at room temperature.

Optimisation experiments. After the precipitation screening and nucleation tests, optimisation trials are needed to find the conditions for single crystal growth. Which kind of crystallisation technique that is used in this stage is largely dependent on choice and preferences.

RESULTS AND DISCUSSION

The analytical approach described here allowed us to develop a three-step screening strategy. The initial nucleation screen in stage one allows determination of the maximum concentration at which a particular protein can be solubilised before any crystallisation experiments are performed. In stage two, various crystallising agents are screened to find the boundaries within which a supersaturated protein solution becomes unstable (manifested in precipitation) (24) and finally is totally precipitated. An image series of a levitated protein-containing drop during a screening experiment is shown in Fig. 4. A graphical representation of the RALS signal during an experiment is shown in Fig. 5. The limit of detection is 2.8 arbitrary units at CI = 95% ($t = 1.86$). Any signal identical to or larger than this value is assumed to represent precipitation in the drop. The limit of detection is 2.8 arbitrary units at CI = 95% ($t = 1.86$). Any signal identical to or larger than this value is assumed to represent precipitation in the drop. The limit of detection was calculated as the minimum detectable quantity Δx_{\min} based on three experiments by

$$\Delta x_{\min} = \bar{x}_1 - \bar{x}_b > t_s (N_1 + N_2) / N_1 N_2$$

where the subscript b denotes blank determinations, t is the statistical t -value, s is the standard deviation, N_1 is the number of experimental series and N_2 the number of replicate measurements within each series. Blank determinations are here defined as measurements of the baseline level when no precipitation occurs.

The concentrations of protein and crystallising agent in the drop are calculated at the point when the RALS signal increases from the baseline level, and once again when the RALS signal reaches its maximum value. This information is then displayed in precipitation diagrams (Fig. 6), thus giving a rough estimate of the supersaturation region. Finally, in stage three, separate crystallisation drops are mixed guided by the data obtained and the ability of the macromolecule to form microcrystals is observed. After conditions for nucleation has been established an optimisation step for the formation of large, single crystals must be performed (not treated in this work).

This method is especially useful if standard crystallisation trials have failed to give the conditions for crystal growth, as exemplified below with results from D-SD. Moreover, amorphous precipitation or nucleation of the protein is not always the outcome of a crystallisation trial. Phenomena occurring under “unsuitable” conditions are *e.g.* gelling of the protein, two-phase system formation or precipitation of the crystallising agent. This is also rapidly established using our screening method, meaning that unsuitable precipitants can be excluded early on without wasting more than a minute amount of protein (usually 10-50 µg) on these crystallising agents.

LADH. To evaluate the reliability of the levitation technique for precipitation screening, LADH was tested, a protein known to crystallise readily under various conditions. LADH has been crystallised by dialysis at low ionic strength in alcohol containing solutions since the 1960's (25). Salt precipitation has rarely yielded crystals useful for X-ray analysis, but when the “Stura footprinting solubility strategy” (16) was tried at room temperature, rod shaped crystals formed of the apo-enzyme (without co-factor or inhibitor added) when precipitated with ammonium sulphate, phosphate or citrate over a wide pH range. The protein solutions contained 25-40 mg enzyme/mL in the mixture as the starting point for crystallisation using the vapour diffusion (14) method.

1.5 M ammonium sulphate was injected into levitated 1 µL protein-containing drops to different degrees of precipitation. As can be seen in Fig. 4, a qualitative judgement of the light intensity and thus the degree of precipitation in the drop is easy to make. Heavy precipitation, similar to that shown in Fig. 4f, was also partially dissolved by injection of buffer or water into drops, indicating a reversible process. In this series of experiments, drops at different stages of precipitation or with precipitates dissolved to different degrees were taken from the levitator and placed under oil (26) to equilibrate. This was done to investigate the ability of the protein to nucleate. Microcrystals of LADH were observed in drops brought to a moderate or a high precipitation (similar to Fig. 4c and d), confirming that the precipitation screening was successful in establishing conditions where nucleation occurs.

***E.coli* dUTPase.** *E.coli* dUTPase had resisted crystallisation at neutral pH using a large number of crystallising agents offered in commercially available kits (Hampton Research). Our survey at pH 7 (Table 2) in the search for the protein concentration range needed for crystallisation using levitated drops showed that at least 30 mg protein/mL was needed to get crystals. This is in contrast to the concentration range found for the crystals used for X-ray analyses, which is 1.5-2 mg/mL, between pH 4.5 to 5.5 in low PEG concentrations (27, 28), explaining why the conditions for

crystallisation at neutral pH were not previously found since the search had been performed using too low protein concentration.

D-SD. Conditions for the crystallisation of a ternary inhibitor complex between pyridoxal-5'-phosphate (PDP) and the enzyme D-serine dehydratase (D-SD) purified from *E. coli* has been published (13). Attempts have been made to crystallise the binary complex of D-SD and PDP using Hampton screen kits and a protein concentration of 10 mg/mL, but poor crystal quality and a total lack of reproducibility in crystal formation has hampered any structure determination. D-SD-PDP was used as a pilot project to evaluate the usefulness of our new approach to first investigate the solubility properties of the enzyme in levitated drops before any crystallisation experiments were performed. An ammonium sulphate precipitate of the enzyme-PDP-complex was dissolved in water to a final concentration of 60 mg protein/mL and used throughout the experiment as the stock solution. The crystallisation agents used are listed in Table 1.

The precipitation diagram for D-SD-PDP with ammonium sulphate at pH 7 is shown in Fig. 6a. Based on these data, three protein concentrations (15, 20 and 25 mg protein/mL) and a range of ammonium sulphate concentrations were selected for nucleation tests. The nucleation tests were performed in batch mode (2-4 μ L drops, 3-5 drops) and mixed under paraffin oil so that the protein solution reached the final concentrations of components that were picked from the diagram. The crystallisation solutions were left to equilibrate at room temperature and observed after some days. The nucleation tests showed that D-SD-PDP easily forms crystals. In the imidazole malate buffer system crystals appeared from pH 6 to 8. The largest crystals grew at pH 7 in mixtures containing 15 mg/mL protein and between 0.8-1.1 M ammonium sulphate. The crystals were all growing as thin "flakes" in clusters (Fig 7). These could be used as macro seeds. An optimisation procedure could include variation of the temperature, finding the correct buffer system and regulating the nucleation rate. The nucleation rate can be decreased by addition of a thin layer of oil (29) (Hampton Research) on top of the reservoir solution or crystallisation in a gel (30).

Another good condition for crystal formation observed for D-SD-PDP was using PEG4000. The precipitation graph is shown in Fig. 6b. At 30 mg protein/mL in 20% PEG4000 at pH 7 in imidazole malate one single, thin crystal grew. Unfortunately, this crystal dissolved at about 25°C. In this particular experiment, 85 μ g protein was used for the levitation experiments. Nucleation tests required an additional amount of 415 μ g, resulting in *a total amount of 500 μ g D-SD to find conditions for*

single crystal growth. This demonstrates excellently the material saving properties of this method.

When malonate or phosphate were used as crystallising agents mainly microcrystals formed. At the highest protein concentration (30 mg/mL) using phosphate as precipitant, a tendency for single crystal formation was observed. Thus, nucleation occurs at all concentrations of protein and salt over the range tested. Citrate was excluded from the nucleation tests due to anomalous behaviour in the levitation experiments.

Nucleation tests using PEG400 in the presence of 0.2 M ammonium sulphate gave no crystals. Drops were not mixed using PEG400 alone, but the levitation experiments (Fig. 6c) show that D-SD-PDP is highly soluble in imidazol malate buffer. Up to 25% PEG can be mixed with 50 mg/mL protein and 75% PEG with 25 mg protein/mL. This provides an explanation why the Hampton screen kit did not generate crystals when using PEG solutions and 10 mg/mL protein. The protein and precipitant concentration ranges were simply chosen wrongly.

Influence of the ultrasonic field. The possible influence of the ultrasound on precipitation can be disregarded since separate nucleation tests have confirmed the conditions established with our method. Drops levitated in an acoustic levitator are also subject to induced ultrasonic streaming, thus making them less suitable for crystal growth experiments. It has been suggested that the induced ultrasonic streaming dissolves formed nuclei (31), but the use of an electrostatic (11) or electrostatic-acoustic hybrid levitator (32), shown useful in crystal growth experiments, would be equally useful in the screening method and thus give the added possibility of growing crystals after the conditions have been established. However, our objective has not been to grow crystals in a levitated drop, but to screen for conditions where crystallisation might occur.

Flow-through dispensers for addition of crystallising agents. The maximum viscosity of the liquid to be ejected by the current dispenser is limited to 65 mPas. Higher viscosity will impair the droplet formation. Liquids with higher viscosities may be used if the dispenser is heated. However, the materials in the dispenser limit the heating to below 100°C. Fig. 2 shows the ejection of low viscosity liquid (water, left) and high viscosity liquid (water with 50 % glycerol, right). It is important to match the shape of the voltage pulse applied to the dispenser to the properties of the liquid used. Otherwise formation of small and unwanted satellite droplets may result from the thin filament connecting the liquid in the nozzle and the droplet, seen in the right image (Fig. 2). Solutions with high salt concentration also negatively affect the dispenser due to crystallisation of salt in the nozzle. This may be circumvented by the recently introduced compound dispenser (33) that uses a second layer of a

salt-free liquid to cover the primary liquid upon ejection. To date, we have been forced to work exclusively with solutions of low viscosity and low concentration and then rely on the evaporation of the levitated drop to obtain higher concentrations. This works well but is a little time-consuming since increasing the concentration of crystallising agent is dependent on evaporation time.

Volume determination and precipitation monitoring. The volume estimation is affected by image blurring. Such blurring can result from movement of the drop in the node. Correct focusing of the microscope on the edges of the drop is also important, especially since the focus needs to be adjusted when the drop volume increases or decreases. The focus must be at the edges of the drop to ensure a sharp image. To a large extent, these two effects can be minimised if care is taken during the experiments not to disturb the drop and to make sure that the focus is changed when needed. However, an effect that can not be overcome is the discretisation of the drop, i.e., that the estimated radii can be half a pixel too large or too small. Supposing a disc with the radius of 100 pixels where the estimated radius is half a pixel too large will result in a disc volume overestimated by approximately 1%. Generally, some of the radii's will be too large while others will be too small so the resulting error will be smaller than this. Another error of the volume determination is if the drop is not rotational symmetric, which is assumed. One way to overcome this problem could be to take pictures of the drop at different angles at the same time. This is not investigated in this paper.

Visual examination of the image of the drop to determine when precipitation occurs is an entirely subjective operation, which constitutes a problem if exact concentrations are desired. The RALS detection by the microscope and CCD camera eliminates this problem. The detection method described here would benefit in sensitivity by the use of a laser instead of the cold light source. The present method, however, is cheap, easy to use, and seems to give adequate enough information. However, what can not be obtained using this method is the identification of which molecules are being precipitated. It is not always the macromolecule that precipitates, but salt crystals can also form. One possibility to achieve this identification could be to utilise Raman spectroscopy, which has been previously used for detecting nucleation in hanging protein drops (34) and also in combination with acoustic levitators in the crystallisation of small molecules (35).

CONCLUSIONS

We have shown that the precipitation diagrams established using our method and the acoustic levitator are directly useful tools in the search for

crystallising conditions. By utilising the evaporation of the drop as well as the possibility of varying the amount of additions, the composition of the levitated drop is easily varied with regard to protein, additives and crystallising agent concentration, allowing for a whole concentration range to be screened using a single protein-containing levitated drop. The use of the dispensers is crucial to enable additions in these small volumes. Conditions where nucleation can not occur are also rapidly detected using the levitation method, thus unsuitable precipitants can be excluded early on without wasting more than a minute amount of protein on these crystallising agents. The method is time, labour and material saving.

ACKNOWLEDGEMENTS

Financial support from European Commission BIOMED2, BMH 4CT97-2711 (DG12-SSMI). Prof. Dr. Klaus Schnackerz, Würzburg University, Würzburg, Germany is thankfully acknowledged for the gift of the enzyme D-serine dehydratase and Dr. Inna Kuranova, Moscow Crystallographic Institute, Moscow, Russia, for assistance with the nucleation tests.

REFERENCES

- (1) Chernov, A. A. *Modern Crystallography III: Growth of Crystals* Springer Verlag, Berlin, 1984.
- (2) Haas, C.; Drenth, J. *J. Phys. Chem. B* **2000**, *104*, 368-377.
- (3) Yau, S.-T.; Vekilov, P. G. *Nature* **2000**, *406*, 494-497.
- (4) Haas, C.; Drenth, J. *J. Cryst. Growth* **1999**, *196*, 338-394.
- (5) Haas, C.; Drenth, J. *J. Phys. Chem. B* **1998**, *102*, 4226-4232.
- (6) Ataka, M. *Phase Transitions* **1993**, *45*, 205-219.
- (7) Saridakis, E. E. G.; Stewart, P. D. S.; Lloyd, L. F.; Blow, D. M. *Acta Cryst.* **1994**, *D50*, 293-297.
- (8) Giegé, R.; Drenth, J.; Ducruix, A.; McPherson, A.; Saenger, W. *Prog. Crystal Growth and Charact.* **1995**, *0030*, 237-281.
- (9) Rosenberger, F.; Meehan, E. J. *J. Cryst. Growth* **1988**, *90*, 74-78.
- (10) Lierke, E. G. *Forsch. Ingenieurwes.* **1995**, *61*, 201-16.
- (11) Rhim, W.; Chung, S. *J. Cryst. Growth* **1991**, *110*, 293-301.
- (12) Izmailov, A. F.; Myerson, A. S.; Arnold, S. *J. Cryst. Growth* **1999**, *196*, 234-242.
- (13) Obmolova, G.; Teplyakov, A.; Harutyunyan, E.; Wahler, G.; Schnackerz, K. D. *J. Mol. Biol.* **1990**, *214*, 641-642.
- (14) Davies, D. R.; Segal, D. M. In *Methods in Enzymology*; Jacoby, W. B., Ed.; Academic Press: New York and London, 1971; Vol. XXII, pp 266-269.

- (15) Jancarik, J.; Kim, S. H. *J. Appl. Cryst.* **1991**, *24*, 409-411.
- (16) Stura, E. A.; Nemerow, G. R.; Wilson, I. A. *J. Cryst. Growth* **1992**, *122*, 273-285.
- (17) McPherson, A. *Protein Science* **2001**, *10*, 418-422.
- (18) Petersson, M.; Nilsson, J.; Wallman, L.; Laurell, T.; Johansson, J.; Nilsson, S. *J. Chromatogr. B* **1998**, *714*, 39-46.
- (19) Santesson, S.; Andersson, M.; Degerman, E.; Johansson, T.; Nilsson, J.; Nilsson, S. *Anal. Chem.* **2000**, *72*, 3412-3418.
- (20) Laurell, T.; Wallman, L.; Nilsson, J. *J. Micromech. Microeng.* **1999**, *9*, 369-376.
- (21) Onnerfjord, P.; Nilsson, J.; Wallman, L.; Laurell, T.; MarkoVarga, G. *Anal. Chem.* **1998**, *70*, 4755-4760.
- (22) Gaspar, S.; Mosbach, M.; Wallman, L.; Laurell, T.; Csöregi, E.; Schuhmann, W. *Anal. Chem.* **2001**, *73*, 4254-4261.
- (23) Gonzalez, R. C.; Woods, R. E. *Digital Image Processing*, Addison-Wesley Publishing Company Inc., 1993.
- (24) Zeppezauer, M. In *Methods in Enzymology*, Jacoby, W. B., Ed.; Academic Press: New York and London, 1971; Vol. XXII, pp 253-266.
- (25) Zeppezauer, E.; Söderberg, B.-O.; Brändén, C.-I.; Åkeson, Å.; Theorell, H. *Acta Chem. Scand.* **1967**, *21*, 1099-1101.
- (26) Chayen, N. E. *Structure* **1997**, *5*, 1269-1274.
- (27) Dauter, Z.; Wilson, K. S.; Larsson, G.; Nyman, P. O.; Cedergren-Zeppezauer, E. S. *Acta Crystallogr.* **1998**, *D54*, 735-749.
- (28) Gonzalez, A.; Larsson, G.; Persson, R.; Cedergren-Zeppezauer, E. S. *Acta Crystallogr.* **2001**, *D57*, 767-774.
- (29) Chayen, N. E. *J. Appl. Cryst.* **1997**, *30*, 198-202.
- (30) Garcia Ruiz, J. M.; Moreno, A. *Acta Crystallogr.* **1994**, *D50*, 484-490.
- (31) Ishikawa, Y.; Komada, S. *FUJITSU Sci. Tech. J.* **1993**, *29*, 330-338.
- (32) Chung, S. K.; Trinh, E. H. *J. Cryst. Growth* **1998**, *194*, 384-397.
- (33) Nilsson, J.; Bergkvist, J.; Ekström, S.; Wallman, L.; Laurell, T. *Compound Microdispensing*. Micro Total Analysis Systems, Monterey, CA, USA 2001; Kluwer academic publishers; 75-77.
- (34) Schwartz, A. M.; Berglund, K. A. *J. Cryst. Growth* **1999**, *203*, 599-603.
- (35) Davies, A. N.; Jacob, P.; Stockhaus, A.; Kuckuk, R.; Hill, W.; Hergenroder, R.; Zybin, A.; Klockow, D. *Appl. Spectrosc.* **2000**, *54*, 1831-1836.

FIGURE CAPTIONS

- Figure 1.** Instrumental set-up for precipitation screening of nucleation conditions of proteins. A levitated drop (a), trapped in a node of a standing wave between the ultrasonic transducer (b) and the reflector (c) of an acoustic levitator. A piezoelectric flow-through dispenser is used for additions, featuring a picolitre droplet outlet (d_i), a flow-through channel inlet (d_{ii}) and outlet (d_{iii}). The dispenser is operated by a dispenser control unit (e) comprising voltage, pulse and function generators. For levitated drop surveillance, a microscope (f) equipped with a CCD camera (g) is used, combined with a cold light source at 90° (h) for drop illumination and a PC (i) for drop volume calculation and precipitation monitoring.
- Figure 2.** Dispenser performance using water (left) and 50% glycerol (right).
- Figure 3.** A schematic pixel-picture of a drop showing how the volume is calculated from the different radii.
- Figure 4.** Image series of levitated D-serine-dehydratase drop during a screening experiment: a, initial protein drop; b, “limit”, first signs of precipitation; c-e, precipitation; and f, total precipitate. The differences in drop shape and size are due to variations of the drop volume during additions and/or evaporation. The images were obtained using 6.3X magnification.
- Figure 5.** Right angle light scattering measurement of a drop containing YADH-NADH upon MPD addition. The RALS signal starts to increase at 1153 s which corresponds to concentrations in the drop of 25 mg/mL protein and 19 % (w/v) MPD. The average of the signals before 1000 s, representing the background and mainly caused by the CCD bias-potential, has been subtracted. The repeatability of the determined concentrations of protein and precipitant in the drop was ± 0.3 mg/mL protein and ± 0.2 % (w/v) MPD (n = 3).
- Figure 6.** Precipitation graphs of D-SD-PDP with a). ammonium sulphate pH 7.0, b). PEG 4000 pH 7.0, c). PEG400 pH 7.0.
- Figure 7.** Images of D-SD-PDP crystals obtained using batch crystallisation under oil. The conditions were 15 mg protein/mL and 0.9 M ammonium sulphate.

Figure 1.

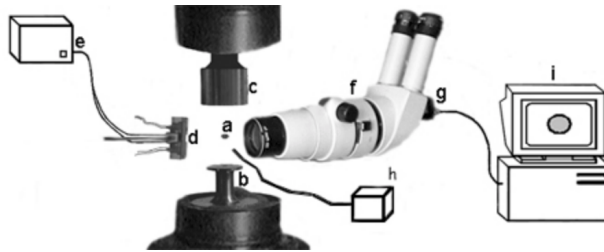


Figure 2.

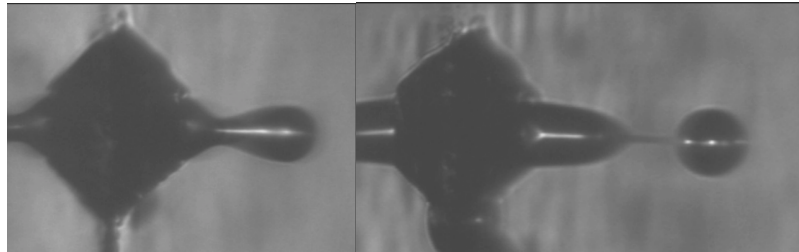


Figure 3.

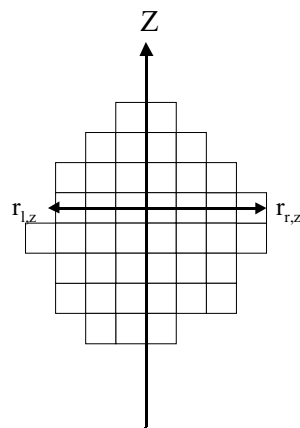


Figure 4.

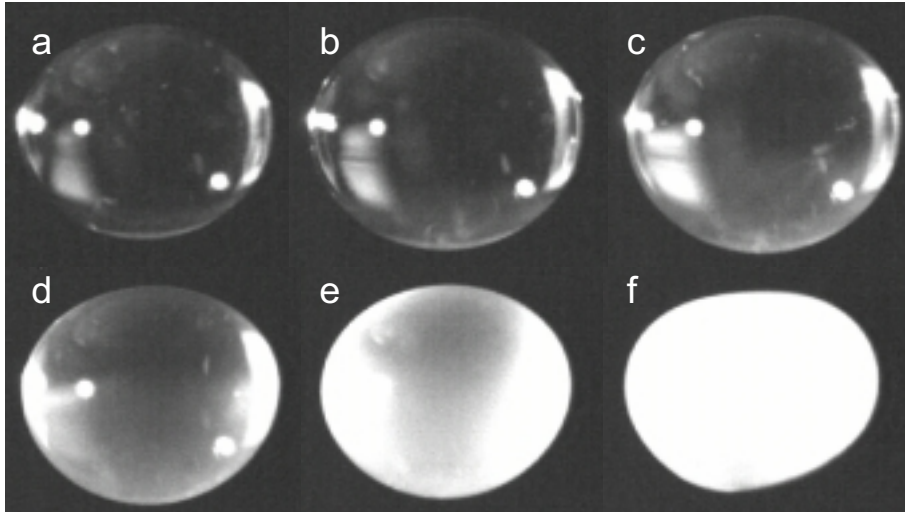


Figure 5.

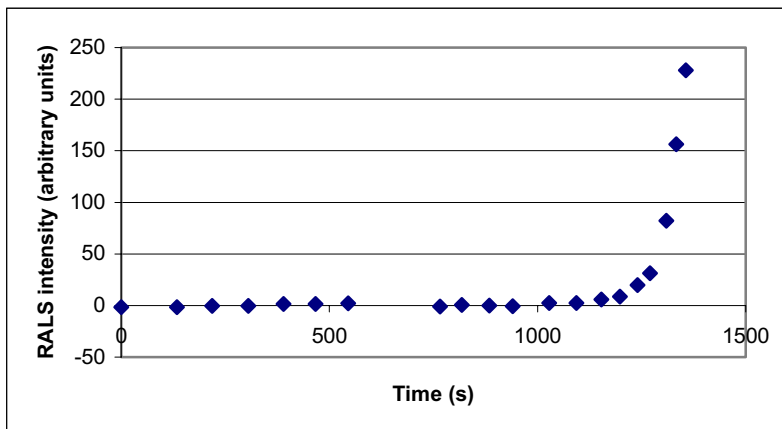


Figure 6.

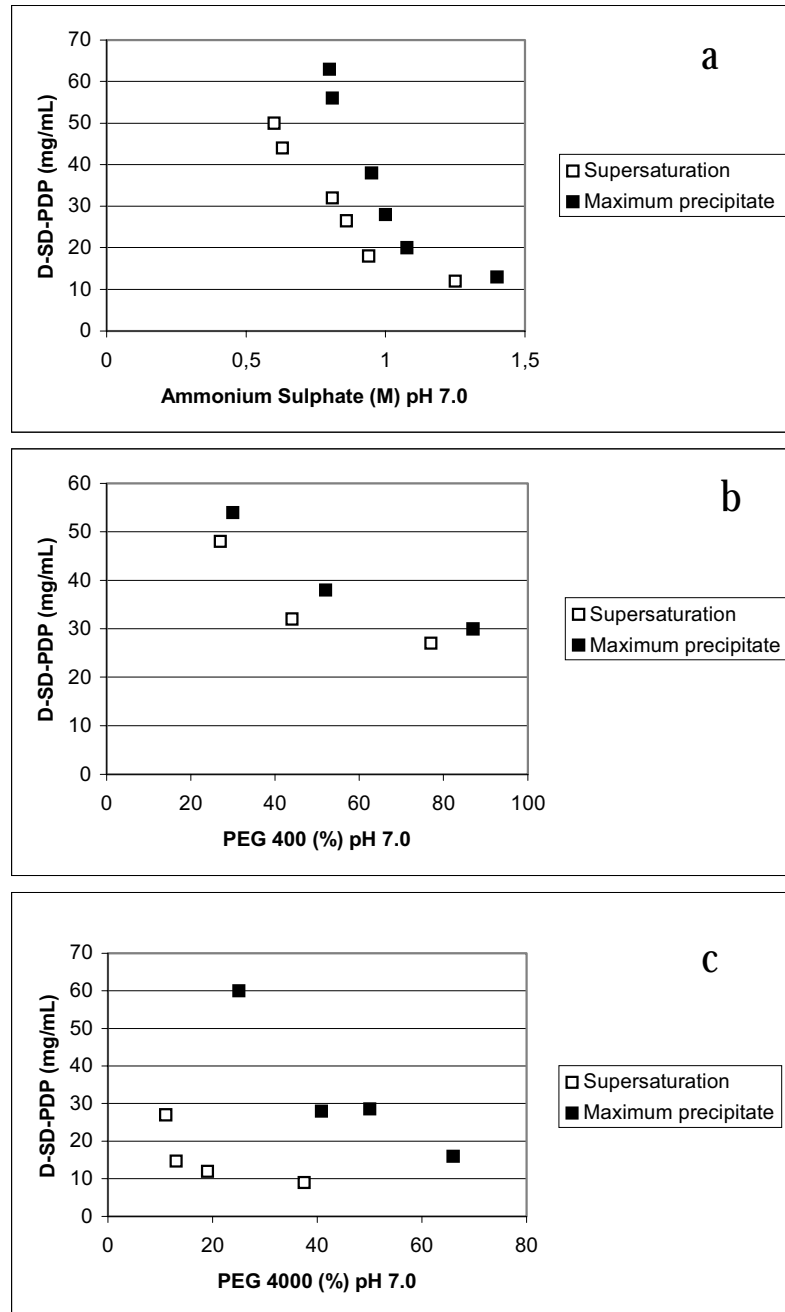


Figure 7.

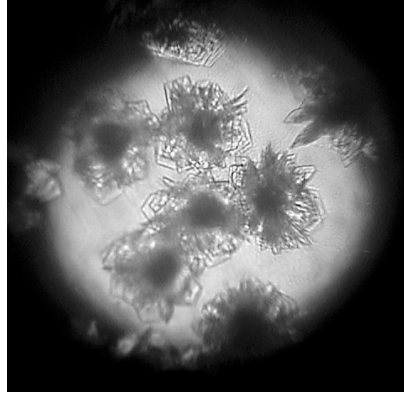


Table 1.

Protein	CRYSTALLISING AGENTS
D-SD (60 mg/mL in H ₂ O)	42% PEG 400 in imidazole/malate buffer pH 5.5
	25% PEG 4000 in imidazole/malate buffer pH 7.0
	1.5M Ammonium Sulphate pH 5.5, 7.0, and 8.5
	2M Phosphate pH 6.5, 7.0, and 8.0
	1.5M Citrate pH 8.5
	2M Malonate pH 7.0

Table 2.

Protein	CRYSTALLISING AGENTS
<i>E. coli</i> dUTPase (50 mg/mL in 10 mM MOPS pH 7)	22.5% (w/v) MPD in 0.1M HEPES pH 7.5, 30% (w/v) glycerol in 15 mM MgCl ₂
LADH (50 mg/mL in 0.1 M Tris/HCl pH 8.4)	1.5M ammonium sulphate in 50mM Tris/HCl buffer over the pH range 7.5- 9.5
YADH (40 mg/mL in 50 mM Tris/HCl pH 8.0 10 μM ZnCl ₂)	20% (w/v) MPD in 0.1M Im/Mal buffer

Airborne Cell Analysis

Sabina Santesson,[†] Martin Andersson,[†] Eva Degerman,[‡] Thomas Johansson,[§] Johan Nilsson,^{||} and Staffan Nilsson^{*†}

Department of Technical Analytical Chemistry, Department of Cell and Molecular Biology, Section for Molecular Signalling, Department of Atomic Physics, and Department of Electrical Measurements, Lund University, P. O. Box 124, SE-221 00 Lund, Sweden

A miniaturized analysis system for the study of living cells and biochemical reactions in microdroplets was developed. The technique utilizes an in-house-developed piezoelectric flow-through droplet dispenser for precise reagent supply and an ultrasonic levitator for contactless sample handling. A few-cell study was performed with living primary adipocytes. Droplets (500 nL) containing 3–15 individual cells were acoustically levitated. The addition of β -adrenergic agonists into the levitated droplet using the droplet dispenser stimulated adipocyte lipolysis, leading to free fatty acid release and a consequent pH decrease of the surrounding buffer. The addition of insulin antagonized lipolysis and hence also the decrease in pH. The changes in pH, i.e., the cell response in the droplet, were followed using a pH-dependent fluorophore continuously monitored by fluorescence imaging detection. An image analysis computer program was employed to calculate the droplet intensities. To counteract droplet evaporation, found to affect the fluorescence intensities, a separate dispenser was used to continually add water, thus keeping the droplet volume constant.

Small-scale analysis of chemical events and intracellular dynamic processes in single cells are expanding areas of interest in the pharmaceutical, biological, and medical sciences. Improved knowledge of the chemical composition and dynamics of single cells should lead to a better and broader understanding of how individual cells function in their natural cellular environment. Future advances in these areas require the development of analytical techniques capable of monitoring such minute cellular changes induced by ligands, drugs, activators, or inhibitors.¹ During the cell life span, great variations in chemistry, structure, and physiology are observed due to aging, transformation, and cell cycle turnover. Variations due to aging were, for example, shown for the enzyme content of human erythrocytes.² Analysis of single cells, involving both cell signaling and cell content, therefore offers more detailed information than analysis of whole-cell populations, in which case, the obtained information only concerns the reactions of the cell average. Single-cell insights might also benefit clinical diagnosis and treatment.² Recent

advances in analytical instrumentation and methodology now promise biochemical analyses of cellular content, communication, and differentiation.^{3–15} Many techniques for studying dynamic events at the single-cell level have been developed, including fluorescence imaging techniques,^{16–18} capillary electrophoresis,^{9–14} flow cytometry,⁷ open tubular liquid chromatography,¹⁹ and microcolumn liquid chromatography.¹⁵

One severe problem with analysis in this microscale (volumes below 1 μ L and concentrations in the pico- or nanomolar range) is unspecific adsorption on the walls of the equipment used to handle and analyze the sample.²⁰ This could cause diminishing or complete elimination of interesting substances. The material of the equipment could also interact with the sample so that reactions are disturbed or prevented. Another problem is optical interference caused by surrounding walls. The low concentration of analytes also sets special demands on the analysis protocol.

A unique system for the analysis of intra- and extracellular events on a level of a single cell or a few cells using novel analytical tools are now being developed by us. The aim was to develop a method for secondary high-throughput screening (HTS) of new drug candidates by holding living cells in a buffer droplet levitated

- (3) Yeung, E. S. *Anal. Chem.* **1999**, *71*, A522–A529.
- (4) Krylov, S. N.; Zhang, Z. R.; Chan, N. W. C.; Arriaga, E.; Palcic, M. M.; Dovichi, N. J. *Cytometry* **1999**, *37*, 14–20.
- (5) Ewing, A. G.; Strein, T. G.; Lau, Y. Y. *Acc. Chem. Res.* **1992**, *25*, 440–447.
- (6) Cooper, B. R.; Jankowski, J. A.; Leszczyszyn, D. J.; Wightman, R. M.; Jorgenson, J. W. *Anal. Chem.* **1992**, *64*, 691–694.
- (7) Gagro, A.; Rabatic, S.; Ivancic, I.; Bendelja, K.; Jelacic, J.; Sabioncello, A.; Misulic, J.; Buneta, D.; Dekaris, D. *Period. Biol.* **1999**, *101*, 17–26.
- (8) Jankowski, J. A.; Schroeder, T. J.; Ciolkowski, E. L.; Wightman, R. M. *J. Biol. Chem.* **1993**, *268*, 14694–14700.
- (9) Jankowski, J. A.; Tracht, S.; Sweedler, J. V. *TrAC, Trends Anal. Chem.* **1995**, *14*, 170–176.
- (10) Olefirowicz, T. M.; Ewing, A. G. *Chimia* **1991**, *45*, 106–108.
- (11) Moroz, L. L.; Gillette, R.; Sweedler, J. V. *J. Exp. Biol.* **1999**, *202*, 333–341.
- (12) Yeung, E. S. *J. Chromatogr., A* **1999**, *830*, 243–262.
- (13) Malek, A.; Khaledi, M. G. *Anal. Biochem.* **1999**, *270*, 50–58.
- (14) Orwar, O.; Fishman, H. A.; Ziv, N. E.; Scheller, R. H.; Zare, R. N. *Anal. Chem.* **1995**, *67*, 4261–4268.
- (15) Cooper, B. R.; Wightman, R. M.; Jorgenson, J. W. *J. Chromatogr., B* **1994**, *653*, 25–34.
- (16) Barnes, M. D.; Ng, K. C.; McNamara, K. P.; Kung, C. Y.; Ramsey, J. M.; Hill, S. C. *Cytometry* **1999**, *36*, 169–175.
- (17) Johansson, T.; Petersson, M.; Johansson, J.; Nilsson, S. *Anal. Chem.* **1999**, *71*, 4190–4197.
- (18) Nilsson, S.; Johansson, J.; Mecklenburg, M.; Birnbaum, S.; Svanberg, S.; Wahlund, K. G.; Mosbach, K.; Miyabayashi, A.; Larsson, P. O. *J. Capillary Electrophor.* **1995**, *2*, 46–52.
- (19) Oates, M. D.; Cooper, B. R.; Jorgenson, J. W. *Anal. Chem.* **1990**, *62*, 1573–1577.
- (20) Welter, E.; Neidhart, B. *Fresenius J. Anal. Chem.* **1997**, *357*, 345–350.

* Corresponding author: (phone) +46 46 2228177; (fax) +46 46 2224525; (e-mail) Staffan.Nilsson@teknik.lth.se.

(1) Chen, G.; Ewing, A. G. *Crit. Rev. Neurobiol.* **1997**, *11*, 59–90.
(2) Yeung, E. S. *Acc. Chem. Res.* **1994**, *27*, 409–414.

in an ultrasonic field. By presenting different substances to the cells in the droplet, it can be established whether these substances can cause the cells to react in desired ways by binding to the cell receptors and hereby initializing cell responses. In the pharmaceutical industry, HTS is used to screen 10^5 – 10^6 drug candidates per day, possibly yielding 500–1000 positive substances that need to be studied further. For these candidates, a secondary screening procedure is needed to evaluate their effects on living cells and cell systems, a procedure that could be facilitated using the method presented here. To date, miniaturization efforts of HTS assays have been most successfully applied to bacterial and soluble protein-based assays, but it was recently shown that a mammalian cell-based assay might be successfully performed in 3 μ L using a 1536-well plate format.²¹

Adipocytes and the process of lipolysis have been used as a model system. In humans, there are $\sim 2.7 \times 10^{10}$ adipocytes per individual. The average diameter of one cell varies between 30 and 100 μ m dependent upon fat content. Each adipocyte contains about 0.04–0.6 μ g of lipid and 0.3–0.7 μ g of protein. The adipocyte contains the usual subcellular organelles but also a large lipid droplet, composed mainly of triacylglycerols, that pushes the other cell constituents into a small rim of cytoplasm at or around its edge. The primary function of the adipocyte is to efficiently store energy in the form of triacylglycerols. These stores can be mobilized in the form of fatty acids by activation of hormone-sensitive lipase (HSL),²² resulting in the release of free fatty acids (FFA) into the circulation. These FFA are then used as energy substrates in, e.g., skeletal muscle.²³

The proposed mechanism for stimulation and inhibition of lipolysis in adipocytes²⁴ is schematically shown in Figure 1. Stimulation of adipocytes with β -adrenergic agonists results in activation of adenylate cyclase (AC), production of cAMP, and activation of cAMP-dependent protein kinase (PKA). PKA phosphorylates HSL, leading in turn to activation of enzyme activity, increased lipolysis, and release of FFA from the cell (one proton is also released per FFA). The ability of insulin to antagonize lipolysis can to a large extent be explained by its ability to lower cAMP, which is mainly the result of activation of phosphodiesterase (PDE) 3B. The signaling pathway from the insulin receptor to PDE3B is as yet only partially understood, but phosphatidylinositol 3-kinase (PI3K) is likely to be involved, and protein kinase B (PKB) could be the kinase that mediates the PI3K-dependent activation of PDE3B.²³

In these experiments, a synthetic β -adrenergic agonist (isoprenaline) was added to a levitated, adipocyte-containing droplet to stimulate lipolysis, leading to FFA release from the cells and a consequent pH decrease of the surrounding buffer droplet. To antagonize lipolysis and the decrease in pH, insulin was added. The changes in pH were followed using an extracellular pH-dependent fluorophore, 8-hydroxypyrene-1,3,6-trisulfonic acid (HPTS), a low-toxicity, highly water-soluble, membrane-imper-

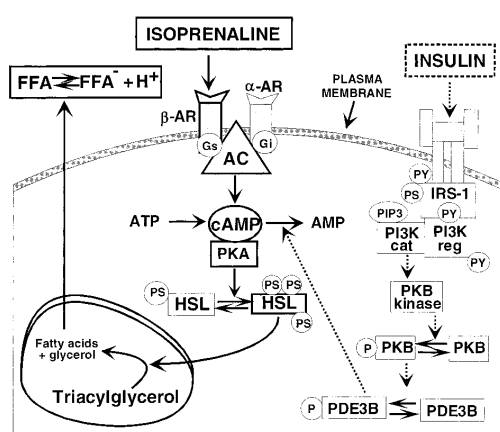


Figure 1. Proposed mechanism for the stimulation and inhibition of lipolysis in adipocytes. *Stimulation of lipolysis.* Stimulation of the β -adrenergic receptor with β -adrenergic agonists (e.g., isoprenaline) results in activation of adenylate cyclase (AC), production of cAMP, and activation of cAMP-dependent protein kinase (PKA). PKA phosphorylates hormone-sensitive lipase (HSL), leading to activation of the enzyme and increased lipolysis giving extracellular release of FFA. *Inhibition of lipolysis.* The signaling pathway from the insulin receptor to phosphodiesterase (PDE) 3B is likely to involve phosphatidylinositol 3-kinase (PI3K) with protein kinase B (PKB) mediating the PI3K-dependent activation of PDE3B. The ability of insulin to antagonize lipolysis can to a large extent be explained by its ability to lower cAMP, mainly the result of activation of PDE3B. (Other abbreviations: AR, adrenergic receptor; Gs, stimulatory GTP-binding protein; Gi, inhibitory GTP-binding protein; PY, phosphotyrosine; PS, phosphoserine; PT, phosphothreonine; IRS-1, insulin receptor substrate 1; PIP3, phosphatidylinositol 3-phosphate).

meant pH indicator with a pK_a of ~ 7.3 in aqueous buffers. This is in the middle of the physiological pH range, which makes HPTS an ideal fluorophore for physiological pH measurements.^{25–27} By irradiating the fluorophore in the buffer with light of specific wavelengths, the fluorescence from the droplet can be continually monitored with a charge-coupled device (CCD) camera.

A classic way to measure the lipolysis is to use pH-stat titration,²⁸ where the pH decrease is measured using a pH glass electrode, and a titration using NaOH is performed. The cell suspension (usually 10 mL with $\sim 100\,000$ cells/mL) is kept in incubation vials (i.d. 25 mm), and magnetic stirrers are needed for extensive mixing of the cell suspension to prevent flotation of cells (adipocytes have density lower than water). Due to the ultrasonically induced streaming within the levitated droplet, no mixing is required when the airborne approach is used.

EXPERIMENTAL SECTION

Adipocytes and Buffers. Isolated adipocytes from male Sprague–Dawley rats, prepared by collagenase digestion,^{29–30}

(21) Maffia, A. M.; Kariv, I.; Oldenburg, K. R. *J. Biomol. Screening* **1999**, *4*, 137–142.

(22) Nilsson, S. Purification and Characterisation of an Amphiphilic Enzyme, Hormone-Sensitive Lipase, by High Performance Liquid Chromatography. Doctoral dissertation, Lund University, 1988, p 35 (ISBN 91-7900-589-6).

(23) Galton, D. J. *The Human Adipose Cell: A Model for Errors in Metabolic Regulation*; Butterworth: London 1971; Chapter 1.

(24) Degerman, E.; Befrage, P.; Manganiello, V. *J. Biol. Chem.* **1997**, *272*, 6823–6826.

(25) Wolfbeis, O. S.; Fűrlinger, E.; Kroneis, H.; Marsoner, H. *Fresenius Z. Anal. Chem.* **1983**, *314*, 119–124.

(26) Wolfbeis, O. S. *Fresenius Z. Anal. Chem.* **1985**, *320*, 271–273.

(27) Zhujun, Z.; Seitz, W. R. *Anal. Chim. Acta* **1984**, *160*, 47–55.

(28) Nilsson, N. Ö.; Befrage, P. *J. Lipid Res.* **1979**, *20*, 557–560.

(29) Rodbell, M. *J. Biol. Chem.* **1964**, *239*, 375–380.

(30) Honnor, R. C.; Dhillon, G. S.; Londos, C. *J. Biol. Chem.* **1985**, *260*, 15122–15129.

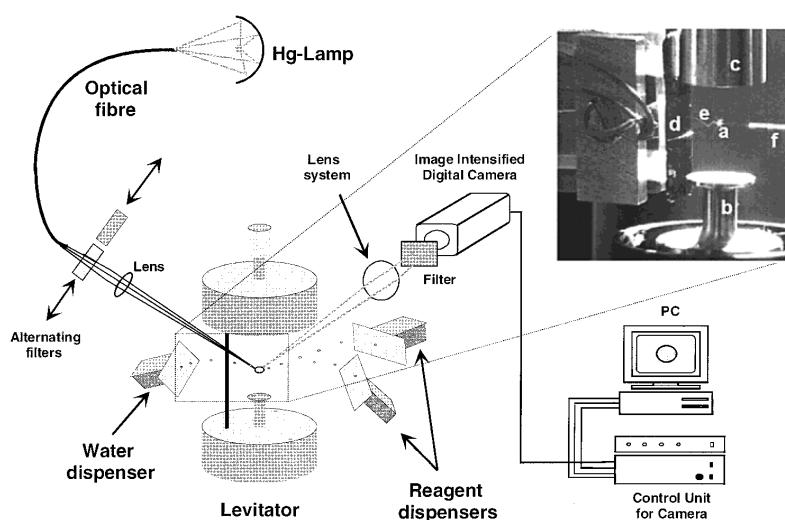


Figure 2. Instrumental setup for airborne cell experiments using fluorescence imaging detection consisting of a Hg lamp, an optical fiber, two alternating interference filters (405 and 435 nm), a cylindrical lens, an acoustic levitator, a lens system, and another interference filter (510 nm). A CCD camera is used to collect images of the levitated droplets, which are then analyzed by a specially designed, in-house-developed computer program for image analysis of the levitated droplets. Three continuous flow-through droplet dispensers are used for additions to the levitated droplet, one for the addition of water and two for the addition of reagents (isoprenaline and insulin). Inset: A levitated droplet (a) in a nodal point of the ultrasonic standing wave created by multiple reflections between the ultrasound transducer (b) and the reflector (c). The flow-through droplet dispenser (d) is used for additions to the levitated droplet. The flight trajectory of the dispenser droplets (e) is affected by the pressure field in the levitator. A capillary (f) with 375- μm o.d. is used for the levitated cell-containing droplet positioning in order to ease detachment of the droplet.

were kept suspended in a Krebs–Ringer–HEPES buffer pH 7.40 (118.6 mM NaCl, 4.74 mM KCl, 2.54 mM CaCl_2 , 1.19 mM KH_2PO_4 , 1.19 mM MgSO_4 , 25 mM HEPES) containing 1% (w/v) bovine serum albumin (BSA), 2 mM glucose, and 200 nM adenosine (storage buffer). Every 2 h, the storage buffer was removed and the cells were washed with new storage buffer. Immediately prior to the levitation experiments, the storage buffer was exchanged for a pH 7.40 buffer with low buffering capacity (titration buffer; 131 mM NaCl, 4.74 mM KCl, 2.54 mM CaCl_2 , 1.19 mM KH_2PO_4 , 1.19 mM MgSO_4) containing 1% (w/v) BSA, 2 mM glucose, and 200 nM adenosine. The cell number of the levitated droplet was determined by counting the cells using a microscope after each levitation experiment.

Cell Survival Test. An insulin sensitivity test was performed on the cells to test the biological response and the ability of the cells to survive the ultrasonic field. Adipocytes (1–2% cell suspension) were preincubated at 37 °C with [^3H]glucose for 30 min. The ability of insulin to stimulate lipogenesis was tested by adding insulin in the range of 0.01–1 nM to the cells. After 10 min, a toluene-based extraction buffer was added to stop the reactions. The amount of radioactivity found in the organic phase represents the amount of glucose converted to lipids.^{31–32}

Reagents. Isoprenaline was obtained from Sigma (St. Louis, MO) and human insulin from Novo Nordisk (Gentofte, Denmark). The pH-dependent fluorophore used was the trisodium salt of 8-hydroxypyrene-1,3,6-trisulfonic acid (HPTS) from Molecular

Probes (Eugene, OR), previously reported to be an ideal fluorophore for extracellular measurements in the near-neutral pH range, and exhibiting a pH-dependent absorption shift and an emission maximum at 511 nm, allowing ratiometric measurements using an excitation ratio of 435/405 nm.^{25–27} For testing the pH dependence of the fluorophore in the levitated droplet, 10 μM acetic acid was prepared from glacial acetic acid (100%) from Merck (Darmstadt, Germany). The water was prepared using a Milli-Q system from Millipore (Bedford, MA).

Deployment of Droplets and Additives. To introduce the cell-containing droplet in the ultrasonic field, a 0.8 \times 40 mm syringe was used. For ease of handling, the droplet of sample was removed from the tip of the syringe by a fused-silica capillary. The droplet was not drawn in by the capillary, only allowed to hang from the tip, after which it was deposited in the ultrasonic field. The droplet volume was \sim 500 nL. To compensate for the water/solvent evaporation and to add reagents to the droplet, in-house-developed flow-through droplet dispensers were used.

Instrumental Setup. The instrumental setup is shown in Figure 2. A buffer droplet containing the desired number of cells and the pH-sensitive fluorophore is levitated in an ultrasonic levitator APOS BA 10 (DANTEC/invent Measurement Technology GmbH, Erlangen, Germany). The acoustic levitator is a device that generates a standing wave with equally spaced nodes and antinodes by multiple reflections between an ultrasonic radiator and a solid reflector.^{20,33–34} The levitator operates with a frequency of 100 kHz.

Flow-through droplet dispensers, developed in-house using silicon micromachining methods, are used for the additions of

(31) Moody, A. J.; Stan, M. A.; Stan, M.; Gliemann, J. *Horm. Metab. Res.* **1974**, *6*, 12–16.

(32) Garland, P. B.; Randle, P. J. *Nature* **1962**, *196*, 987–988.

water and reagents, in this case, isoprenaline and insulin. Water is added to counterbalance droplet evaporation. The dispenser droplets are ejected from a flow-through channel formed by joining two microstructured silicon plates, 13 mm long, 6 mm wide and 250 μm thick each. The flow-through channel measures 8 mm \times 2 mm \times 50 μm and has a volume of 1 μL . In the center of the channel, a protruding pyramid-shaped nozzle is formed. A multilayer piezoelectric element is connected to the channel wall opposing the nozzle. By applying a short voltage pulse across the piezoelectric element it elongates and pushes into the channel generating a pressure pulse in the liquid. The increased pressure accelerates the liquid in the nozzle and a droplet is ejected. This process can be repeated at a rate up to several kilohertz. The volume of the ejected droplets is dependent on the size of the nozzle, the shape of the voltage pulse, and liquid parameters such as surface tension, viscosity, and density. The dispenser and examples of applications are more extensively described elsewhere.^{34–35} The dispensers used for the levitation experiments had nozzles of 40 \times 40 μm size and were mounted on XYZ-micropositioning stages throughout the experiments in order to facilitate alignment. During the levitation experiments, the dispenser for water addition was set to eject 65-pL droplets at a rate of 10 Hz. The reagent additions were tuned to give the correct concentration in the levitated droplet (100 nM isoprenaline and 1 nM insulin).

For excitation of the droplet fluorophore, a mercury lamp from OPSIS AB (Furulund, Sweden), and an optical quartz fiber (diameter 600 μm) was used in combination with lenses and two alternating interference filters (405 and 435 nm). An interference filter (510 nm) and a lens system (focal distance 75 mm) were placed at a 90° angle. A CCD camera with 1100 \times 330 pixels, thermoelectrically cooled to -40 °C with Peltier elements (Princeton Instruments, TEA/CCD-1100-PB, Trenton, NJ) was used to collect images of the droplets. Eight images are used for the calculation of one data point in the resulting diagram. Four of the images are exposed with 405-nm excitation light and the other four with 435-nm excitation light. The four images from each filter are added together for further image analysis using the computer program described. It takes ~4 s to expose these eight images and to transfer the data to the computer. In these experiments, the system was set to obtain these eight images during a cycle of 10 s.

The integrated intensity of a droplet was calculated as the total sum of intensities for all pixels in the image. The procedure of background correction was performed in the Matlab environment (The MathWorks Inc., Natick, MA), and the possibility of excluding abnormal images during, for example, experimental start-up or changes in experimental setup was implemented.

Result Evaluation. Each image of a droplet consisted of 109 \times 91 = 11 011 pixels with registered intensities. The droplets in these images typically had a diameter of ~35 pixels. The intensity at pixel (i, j) will be denoted z_{ij} . The integrated sum over all intensities in an image was calculated as

$$\sum_i \sum_j z_{ij} \quad (1)$$

without any background correction.

To adjust the images for backgrounds, a more complex procedure was used because the position of the droplets had to be determined. For each series of images considered, the sum of intensities of all selected images was calculated for each individual pixel. The resulting image was used for edge detection using the Sobel approximation³⁶ of the derivative, which returns the edges at the points where the gradient of the image is at maximum. The edge determined from the total sum image was then acting as a basis for masking the position of the droplets for all the individual images for the series of images studied. The selected area was expanded using dilatation 5 times³⁶ to ensure that the remaining part of the image contained no fragments of the actual droplets in any of the individual images and that the border of the selected area was smooth. The area outside the droplets was then defining the background and a polynomial describing the background surface was fitted to each individual image, omitting the pixels in the selected droplet area. The intensity of the background pixels for each image was fitted as a function of the x and y -coordinates (obtained from i and j , scaled to range from 0 to 1),

$$\hat{z}_{ij} = b_0 + b_1x_i + b_2y_j + b_3x_iy_j + b_4x_i^2 + b_5y_j^2 \quad (2)$$

The b -coefficients of eq 2 were determined using the method of least squares, i.e., minimizing $\sum_i \sum_j (z_{ij} - \hat{z}_{ij})^2$. Each individual image was then background corrected by subtracting the surface defined by the b -coefficients

$$\tilde{z}_{ij} = z_{ij} - \hat{z}_{ij} \quad (3)$$

The integrated sum of intensities for background-corrected images was then calculated by

$$\sum_i \sum_j \tilde{z}_{ij} \quad (4)$$

and the ratio of the sum of the intensities at two different excitation wavelengths (I_{435}/I_{405}) could be determined. A schematic representation of the result evaluation procedure is shown in Table 1.

RESULTS AND DISCUSSION

The ultrasonic levitator is easy to use. Droplet positioning is best achieved by removing a droplet of sample of appropriate volume (~500 nL) from the tip of a syringe by a fused-silica capillary that is then deposited in the ultrasonic field (Figure 2, inset). The detachment of the droplet from the capillary is more easily achieved than using the needle of the syringe. Accurate free hand positioning of the droplet requires some practice. After positioning, the levitated droplet may perform oscillations, but it can be readily stabilized by adjusting the distance between the transducer and the reflector and by setting the ultrasonic power

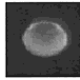
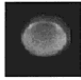
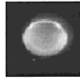
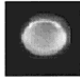
(33) Lierke, E. G. *Acustica* **1996**, *82*, 220–237.

(34) Petersson, M.; Nilsson, J.; Wallman, L.; Laurell, T.; Johansson, J.; Nilsson, S. *J. Chromatogr., B* **1998**, *714*, 39–46.

(35) Önerfjord, P.; Nilsson, J.; Wallman, L.; Laurell, T.; MarkoVarga, G. *Anal. Chem.* **1998**, *70*, 4755–4760.

(36) *Image Processing Toolbox User's Guide*; The MathWorks Inc.: Natick, MA, 1997.

Table 1. Result Evaluation Procedure for the Airborne Cell Experiments (Schematic Representation)^a

Excitation wavelength	Emission wavelength	CCD images of levitated droplet	Images corrected for background	Integrated sum of intensities
435 nm	510 nm			I_{435}
405 nm	510 nm			I_{405}

^a The droplet fluorophore (10 nM HPTS, droplet volume 500 nL) is excited at two alternating excitation wavelengths (405 and 435 nm), and the emission data are obtained at 510 nm. The integrated sum of intensities (represented here by I_{435} and I_{405}) for background-corrected images is calculated, and the ratio of the sum of intensities at the two excitation wavelengths (I_{435}/I_{405}) is determined

properly. With optimal settings the droplet is spherical. Small droplets, especially the dispenser droplets, are susceptible to draught and care must be taken to avoid violent movements.

Advantages of the levitation method are the small amounts of essentially everything needed for the experiments, such as fluorophore, cells, and reagents. The absence of contacting surfaces is also a major advantage since this prevents adsorption of low-concentration compounds to the walls of the equipment. Experiments are also very fast using adipocytes, between 60 and 120 s, during which time both the activation and inhibition of lipolysis are studied. The time needed between experiments is limited to ~60 s, excluding the postexperiment microscope counting of adipocytes in the droplet. The total time needed for experiments will depend mainly on the type of cells, drug candidates, and reactions studied.

Droplet Evaporation. The fluorescence intensities and the fluorescence intensity ratios were affected by the continuous evaporation of the droplet (Figure 3a). To avoid the effect of evaporation, one dispenser was continually operated at a frequency of 10 Hz during experiments, meaning an addition of water at the rate of ~1.4 nL/s at ambient temperature (22 °C) and relative humidity (75%). The actual water supply rate is dependent on the levitated droplet size and the temperature together with the environmental humidity and airflow. The process of evaporation/supply is, however, self-stabilizing to some extent. If the supply rate is slightly higher or lower than the evaporation rate at the current droplet size, the droplet will grow or diminish until the supply/evaporation rates are identical. It is important that a steady state is established before the experiment is commenced. Figure 3a shows how the fluorescence intensity ratio was stabilized when the droplet dispenser was used and operating at a frequency of 10 Hz.

Compared to using a saturated (100% relative humidity) environment, the use of the dispenser is advantageous since it is operationally much easier. Additionally, there is no risk of condensation on the optical surfaces deteriorating the detection. It is also imperative that additions of reagents can be made easily, which would pose a problem of design if a process chamber were to be used. The volume of added reagent can also be kept at a minimum, which is important since volume changes in the

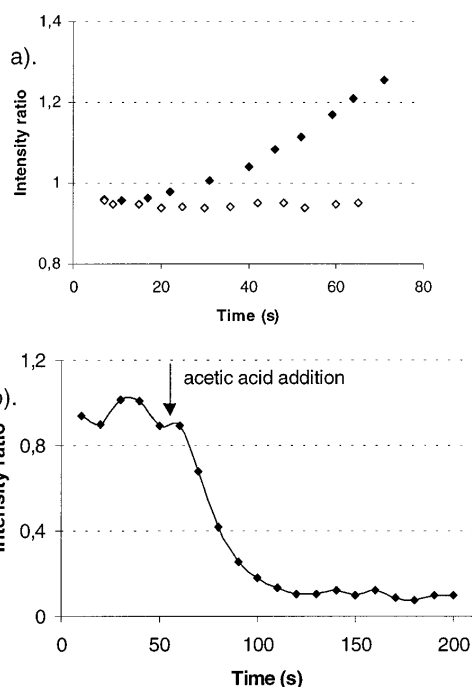


Figure 3. (a) Effect of evaporation of the levitated droplet on the fluorescence intensities and the fluorescence intensity ratios (◆). This effect can be avoided and the droplet volume controlled by continuous water addition using the flow-through dispenser operating at 10 Hz (◇). (b) The fluorophore pH dependence in a levitated droplet. The arrow indicates the start of continuous addition of 10 μ M CH_3COOH by the droplet dispenser operating at 10 Hz.

levitated droplets affect the intensity ratios. In these experiments, the additions of reagents have been achieved using ~500 pL of reagent injected into the levitated droplet, representing ~1/1000 of the original droplet volume. This is not enough to cause deviation of the intensity values with volume changes mentioned above.

Fluorophore pH Dependence. The pH dependence of HPTS in levitated droplets was tested using acetic acid. Figure 3b shows the intensity ratios obtained when 10 μ M acetic acid was added continuously (dispenser operating at 10 Hz) to a levitated droplet containing 10 nM HPTS in titration buffer. The slope of the line is determined by the magnitude of the pH change in the titration buffer, and pH can thus be easily related to the intensity ratios. During this experiment, only one dispenser was used; therefore, no stabilization of the intensity values (evaporation control) could be performed before the addition of acid. As seen in Figure 3b, this results in an unstable line before the acid addition. Upon adding the acid, the dispenser was set to operate at 10 Hz, thus compensating for evaporation as well as affecting the pH.

Result Evaluation. Before the result evaluation can take place, the droplet images have to be corrected due to different aberrations. Aberrations introduced by the system are mainly of three different kinds. First, the levitated droplet may slightly move from its original position during experiments. Second, the optics used is optimized to resolve objects of 100 μ m, the levitated droplet

being larger. These two aberrations cause a slight blurring of the images. The third aberration is caused by the readout of the CCD chip and can be compared to having a high, constant baseline. The background subtraction procedure used for this work is analogous to ordinary baseline subtraction using a second-degree polynomial to describe the baseline in, for example, chromatography, but here a surface was considered rather than a line. The edge finding and dilatation procedure used was chosen as one of many useful ways to mask the drops and to correct for the background. Other ways that may be used to mask the droplet involve other edge-finding procedures or setting threshold values.

Cell Survival Test. The insulin sensitivity test performed on cells exposed to the ultrasonic field for 15–20 min showed that exposed cells responded as well as nonexposed cells (control group) to insulin with regard to lipogenesis, i.e., the ability of the cells to convert glucose into lipids (data not shown). In this test, [^3H]glucose is supplied to the cells, and the amount of ^3H incorporated into the lipids of the cells is measured. Levitation experiments performed show that the lipolytic function of the cells is also maintained after exposure to the ultrasonic field (this paper).

Lipolysis in the Droplet. The fluorescence intensity ratios (I_{435}/I_{405} measured at emission wavelength 510 nm) of 500-nL levitated droplets, each containing 12 adipocytes in titration buffer with 10 nM HPTS are shown in Figure 4a (representative experiments). Adipocyte lipolysis in one of the droplets was initiated by the addition of isoprenaline to a final concentration of 100 nM, leading to a decrease in pH in the levitated droplet. In the other droplet, lipolysis was also initiated by the addition of 100 nM isoprenaline, leading to a decrease in pH, but lipolysis was antagonized after 30 s by the addition of insulin to a final concentration of 1 nM. A continuous droplet dispenser was operating at a frequency of 10 Hz during both experiments to avoid the effects of evaporation. Lipolysis of three individual adipocytes after the addition of 100 nM isoprenaline to the levitated droplet is represented in Figure 4b. The intensity ratios can be related to pH by a titration procedure, where acid is added to the droplet to establish the relation intensity ratio/pH (Figure 3b).

The Future. The development of HTS and new drug engineering techniques can provide a lot of potentially interesting drug candidates in short order. Use of the levitation technique as a secondary screening procedure can offer a means of systematic evaluation of the effect of a new drug on living cells in a short time and using small amounts of material. By exposing living cells to a drug, capable of binding to its receptors, the intracellular response of the cell can be obtained within minutes. The technique could also be used for early revealing of side effects by studying cell–cell communication in a levitated droplet (work in progress at S.N.'s laboratory). Due to the minimal number of cells needed, the method could decrease the number of animal trials in the screening procedure for new drugs. It could also find use as a means of analyzing living cells obtained from biopsies or bone marrow, e.g., in cancer diagnostics, by analyzing individual living cells and comparing their reactions with those of control cells. The use of primary adipocytes and not cultured or transformed cells in these experiments was justified by the wish to mimic reality as closely as possible, and future plans also concern primary cells.

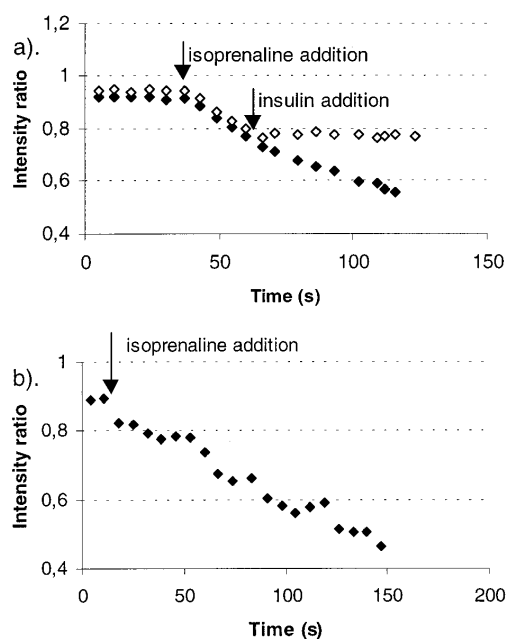


Figure 4. (a) Lipolysis of 12 individual adipocytes in a levitated droplet initiated by the addition of 100 nM isoprenaline and detected using fluorescence imaging technique. In one of the experiments (◆), lipolysis was allowed to continue throughout the experiment. In the other (◇), lipolysis was terminated by the addition of 1 nM insulin. The number of cells, the amount of FFA released, and the consequent magnitude of the pH change in the buffer determine the slope of the line. (b) Lipolysis of three individual adipocytes in a levitated droplet initiated by the addition of 100 nM isoprenaline and detected using fluorescence imaging.

Future development of the system will focus on building a pH-stat titration system for use with levitated droplets, to keep the pH steady at a value acceptable to the cells. To avoid the postexperiment microscope counting, a system for the automatic injection of cells into the levitated droplets needs to be developed, e.g., by means of a flow-through droplet dispenser. If the dispenser can be used for cell and droplet positioning in the ultrasonic field, this would also mean the possibility of using volumes smaller than 500-nL droplets. When the droplet is manually introduced into the levitator, air bubbles are more frequently formed within the droplet if the volume is small (below 500 nL). These air bubbles can cause total disintegration of the levitated droplet and will also disturb detection by scattering of the fluorescent light, which affects the intensity of the images. Four images are added together to decrease the noise from this artifact. When the dispensers are used to build up the volume in the levitator, no bubbles are formed. The use of smaller volumes would also positively affect the time response of the system, since the pH changes observed due to lipolysis will give a higher readout signal in a smaller volume.

Temperature control would also be desirable in order to keep the cells comfortable, e.g., by using a process chamber around the levitator where the temperature is externally controlled.

ACKNOWLEDGMENT

The authors thank the Swedish Research Council for Engineering Sciences, the Swedish Research Council for Natural Sciences, the Crafoord Foundation, The Royal Physiographic Society in Lund, the C. F. Lundström Foundation, the Carl Trygger Foundation for Scientific Research, and the R.W. Johnson Pharmaceutical Research Institute for their financial support. The authors are also indebted to Robert Zivin for valuable discussions. This work was in part presented at the 12th International Symposium on High Performance Capillary Electrophoresis

(HPCE'99), Palm Springs, CA, January 23–28, 1999, at the 13th European Conference on Solid-State Transducers (Eurosensors XIII), The Hague, The Netherlands, September 12–15, 1999, and at the 3rd European Conference on Micro & Nanoscale Technologies for the Biosciences (NanoTech'99), Montreux, Switzerland, November 30–December 1, 1999.

Received for review February 4, 2000. Accepted April 29, 2000.

AC000140R

Real-Time Imaging through Optical Fiber Array-Assisted Laser-Induced Fluorescence of Capillary Electrophoretic Enantiomer Separations

Thomas Johansson,^{†,‡} Maria Petersson,[†] Jonas Johansson,^{‡,§} and Staffan Nilsson^{*,†}

Technical Analytical Chemistry, Center for Chemistry and Chemical Engineering, Lund University, P.O. Box 124, SE-221 00 Lund, Sweden, and Division of Atomic Physics, Lund Institute of Technology, P.O. Box 118, SE-221 00 Lund, Sweden

An advanced detection system based on laser-induced fluorescence imaging for capillary electrophoresis (CE) is presented. An optical fiber array was constructed for collection and transportation of the emitted fluorescent light to the charge-coupled device (CCD) camera. The fiber array makes the setup compact compared with a setup where the capillary is imaged through a camera objective. The imaging detector captures the sample zones in motion during the migration through the capillary. This allows unique studies on dynamic events otherwise unrevealed. During the study, unexplained nonlinear migration behavior was revealed. Enantiomer separations of dansylated amino acids using cyclodextrins, imaged between 1.5 and 12 cm of a 28-cm-long 50- μm i.d. capillary, were used for evaluation of the system. Comparing the optical fiber array with a camera lens system, the signal-to-noise ratio (S/N) was 10 times higher. This is due to a combination of both higher signal and lower noise levels. To improve the S/N ratio further, a computer program for signal processing was designed. Using dichlorofluorescein, a concentration limit of detection (CLOD) of 350 pM was achieved and improved 10 times to 35 pM with computer postprocessing using 79 images. This is equal to 400 zeptomole for a 3-mm-long sample zone in a 50- μm i.d. capillary.

Capillary electrophoresis (CE) is a valuable analytical tool owing to its high separation efficiency, flexibility, and ease of introducing new modes of operation. CE still presents a challenge to detector technology because of the constraints of nanoliter analyte volumes and micrometer detection path lengths. Laser-induced fluorescence (LIF) is one of the most sensitive optical detection schemes available for CE today. The best on-column concentration limits of detection (CLOD) are in the 100 fM range.¹ The excitation light is usually focused near the end of the capillary, and a photon detector measures the emitted fluorescence. The operator must therefore wait until the analytes have moved to the

detection window before any conclusions about the separation can be made. This makes method development time-consuming and often results in excessive separation times. In addition, investigation of the course of events during the separation is not possible. The recently introduced methodologies of real-time detection and monitoring, using Schlieren shadowgraph² and absorbance imaging of capillaries,^{3,4} fluorescence imaging of capillaries,^{5,6} HPLC glass columns,⁷ and TLC plates,⁸ offer the opportunity to study the separation as it develops. Imaging can also be performed across rather than along the capillaries, which allows simultaneous detection of 100 or more capillaries laying side by side.⁹

LIF imaging of a capillary through a camera lens system onto a charge-coupled device (CCD) camera, giving consecutive images of the capillary, was previously developed in our laboratories.^{5,10–12} To detect samples of lower concentrations than was possible with this system, the system has to be improved. A decrease in CLOD can be achieved by increasing the collection efficiency through using a larger diameter objective or placing an optical fiber array¹³ perpendicular to the capillary. The first approach is inconvenient with respect to both size and cost. Using the second approach, the fiber array is used for the collection and transport of the fluorescence from the analytes to the CCD camera (Figure 1). The collection efficiency will increase and a system of this type can be made significantly smaller than one using a camera objective. The size, weight, and cost of the fiber array system will not increase significantly when increasing the section of the capillary imaged. The system can easily be built into a box. The

- (2) Wu, J.; Pawliszyn, J. *Anal. Chem.* **1992**, *64*, 2934–2941.
- (3) Palm, A.; Lindh, C.; Hjerten, S.; Pawliszyn, J. *Electrophoresis* **1996**, *17*, 766–770.
- (4) Culbertson, C. T.; Jorgenson, J. W. *Anal. Chem.* **1998**, *70*, 2629–2638.
- (5) Nilsson, S.; Johansson, J.; Mecklenburg, M.; Birnbaum, S.; Svanberg, S.; Wahlund, K.-G.; Mosbach, K.; Miyabayashi, A.; Larsson, P.-O. *J. Capillary Electrophor.* **1995**, *2*, 46–52.
- (6) Razez, S.; Tamura, A.; Khademizadeh, M.; Masujima, T. *Chem. Lett.* **1996**, 93–94.
- (7) Tamura, A.; Tamura, K.; Wada, K.; Masujima, T. *Chem. Pharm. Bull.* **1994**, *42*, 704–706.
- (8) Liang, Y.; Baker, M. E.; Yeager, B. T.; Denton, M. B. *Anal. Chem.* **1996**, *68*, 3885–3891.
- (9) Ueno, K.; Yeung, E. S. *Anal. Chem.* **1994**, *66*, 1424–1431.
- (10) Johansson, J.; Johansson, T.; Nilsson, S. *Biomedical Optoelectronics in Clinical Chemistry and Biotechnology*, *SPIE* **1995**, 2629, 2–9.
- (11) Johansson, J.; Witte, D. T.; Larsson, M.; Nilsson, S. *Anal. Chem.* **1996**, *68*, 2766–2770.
- (12) Behnke, B.; Johansson, J.; Zhang, S.; Bayer, E.; Nilsson, S. *J. Chromatogr., A* **1998**, *818*, 257–259.

* Corresponding author. Fax: +46 46 2224525. E-mail: Staffan.Nilsson@TEKNK.LTH.SE.

[†] Lund University.

[‡] Lund Institute of Technology.

[§] Current address, Astra Hässle AB, SE-431 83 Mölndal, Sweden.

(1) Timperman, A. T.; Khatib, K.; Sweedler, J. V. *Anal. Chem.* **1995**, *67*, 139–144.

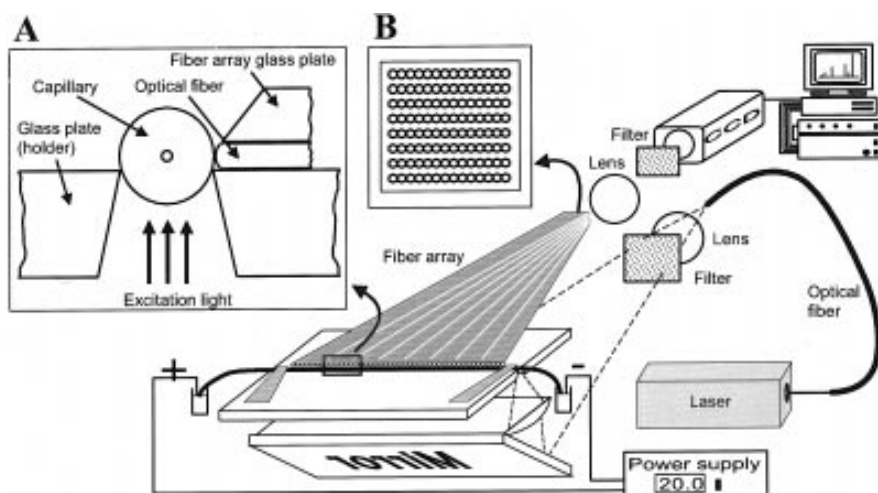


Figure 1. Survey of setup for fluorescence imaging of capillary electrophoresis using the fiber array. Inset A: Fiber array collecting end, close-up of capillary and fiber array alignment. Inset B: Fiber array output end. The interface to the camera consists of eight rows of optical fibers.

use of single-point fiber-optic illumination and detection has been demonstrated for an array consisting of eight parallel capillaries.¹⁴

Information about the separation and the analytes' electrophoretic behavior along the capillary is extracted by using the large amount of data which is generated by an imaging system. A custom-made computer program was developed to process and display the data. Analyte position, velocity, band broadening, diffusion coefficient, and separation efficiencies are parameters that are extracted as a function of the position in the capillary from the electropherograms. Such information might reveal sample adsorption or irregularities in the capillary.

To evaluate the performance of the fiber array an enantiomer separation was imaged. The enantiomer separation of dansyl-DL-amino acids (DNS-AAs) has been dealt with in reports concerning various chiral selectors and electrophoretic techniques. An early approach was the use of a chiral complex formation¹⁵ later followed by the use of chiral micelles.^{16,17} Natural and modified cyclodextrins were either included in gels,¹⁸ added to the separation electrolyte,^{17,19} mixed with chiral micelles,²⁰ or used in nonaqueous media.²¹ Furthermore, proteins²² and macrocyclic antibiotics²³

were used as chiral selectors for the enantiomer separation of DNS-AAs. In the present work, native β -cyclodextrins are incorporated in the electrolyte for the enantiomer separation of three DNS-AAs.

The use of a CCD video camera⁶ to detect the achiral separation of DNS-AAs in a capillary during an electrophoretic run has been reported. The moving zone was observed after being illuminated by an UV lamp and monitored in a 10-cm region (20–30 cm) of a 59-cm-long capillary. However, the detectability was poor (sample concentration 10^{-2} M) due to the UV excitation, and the peaks were distorted due to overloading. In addition, only a small part of a long capillary was imaged.

In this work, we describe a technique to fabricate and use a 10-cm-wide fiber array. The performance of the fiber array was evaluated using DNS-AAs. Enantiomer separations were studied because the narrow peaks were partly or totally resolved which put high demands on the resolution of the detector system. The CLOD of this system was determined and compared with that of the camera lens system by identical experiments using dichlorofluorescein. The effects of signal postprocessing with the custom-made computer program are clearly shown.

EXPERIMENTAL SECTION

Chemicals. Unless stated otherwise, chemicals were of pro *analysis* grade. The water was prepared using a Milli-Q system (Millipore, Bedford, MA). Methanol (gradient-grade), sodium hydroxide (5 M), sodium dihydrogen phosphate monohydrate, anhydrous disodium hydrogen phosphate, and crystalline disodium tetraborate were obtained from Merck (Darmstadt, Germany). Boric acid was from Riedel-de Haën (Seelze, Germany). β -cyclodextrin (food-grade) was from AVEBE (Stadex, Malmö, Sweden). Dansyl-DL-aspartic acid (99%), dansyl-DL-glutamic acid (99%), and dansyl-DL-valine (99%) were from Sigma Chemical Co. (St Louis, MO). 2',7'-Dichlorofluorescein (approximately 90% (TLC)) was from Lambda Physik (Santa Clara, CA).

(13) Mesáros, J. M.; Luo, G.; Roeraade, J.; Ewing, A. G. *Anal. Chem.* **1993**, *65*, 3313–3319.

(14) Quesada, M. A.; Zhang, S. *Electrophoresis* **1996**, *17*, 1841–1851.

(15) Gassmann, E.; Kuo, J. E.; Zare, R. N. *Science (Washington, D.C.)* **1985**, *230*, 813–814.

(16) Cohen, A. S.; Paulus, A.; Karger, B. L. *Chromatographia* **1987**, *24*, 15–24.

(17) Terabe, S. *Trends Anal. Chem.* **1989**, *8*, 129–134.

(18) Guttman, A.; Paulus, A.; Cohen, A. S.; Grinberg, N.; Karger, B. L. *J. Chromatogr.* **1988**, *448*, 41–53.

(19) Tanaka, M.; Asano, S.; Yoshinaga, M.; Kawaguchi, Y.; Tetsumi, T.; Shono, T. *Fresenius J. Anal. Chem.* **1991**, *339*, 63–64.

(20) Okafo, G. N.; Bintz, C.; Clarke, S. E.; Camilleri, P. *J. Chem. Soc., Chem. Commun.* **1992**, 1189–1192.

(21) Valko, I. E.; Siren, H.; Riekkola, M.-L. *J. Chromatogr., A* **1996**, *737*, 263–272.

(22) Sun, P.; Wu, N.; Barker, G.; Hartwick, R. A. *J. Chromatogr.* **1993**, *648*, 475–480.

(23) Armstrong, D. W.; Gasper, M. P.; Rundlett, K. L. *J. Chromatogr., A* **1995**, *689*, 285–304.

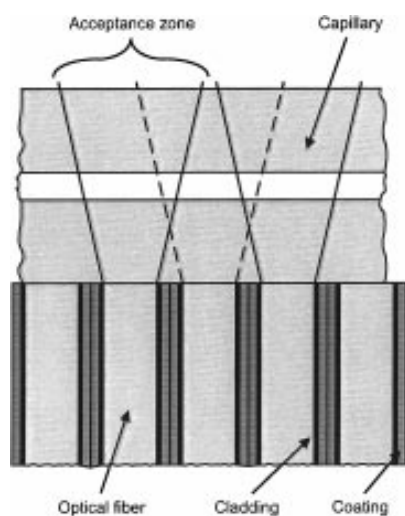


Figure 2. Cross section of the fiber array and the capillary showing the acceptance zone along the length of the capillary. If the acceptance zone is too wide the resolution decreases because of the overlapping areas and if too narrow a part of the emitted light will not be collected.

Electrolyte Preparation. The phosphate buffer used in the electrolyte solution was prepared by mixing stock solutions of 20 mM NaH_2PO_4 and 20 mM Na_2HPO_4 to pH 6.5. Methanol (1 mL) and the 20 mM phosphate buffer pH 6.5 (10 mL) were then mixed. β -Cyclodextrin was dissolved in this mixture to a final concentration of 12 mM and used as an electrolyte. The borate buffer was prepared by mixing stock solutions of 50 mM H_3BO_3 and 12.5 mM $\text{Na}_2\text{B}_4\text{O}_7$ to pH 9.0.

Sample Preparation. Stock solutions of the dansylated-DL-amino acids were prepared in methanol and stored at -20°C . The stock solutions were diluted in water daily before being used. The solutions of dichlorofluorescein were prepared in the borate buffer.

Capillary Electrophoresis Procedure. A power supply (0–30 kV, Zeta elektronik, Höör, Sweden) was used to generate the potential across the capillary. The separation capillary was of polyimide-coated fused silica, 28.0 cm \times 50- μm i.d. \times 375- μm o.d. (Polymicro Technologies, Phoenix, AZ). A 10.5-cm-long detection window, beginning 1.5 cm after the inlet end, was created by glowing off the protective coating using a match. The burnt area was first washed with ethanol, then with water, and finally wiped with a soft paper tissue. The detection window was examined under a microscope for unwanted remaining parts of the protective coating. The capillary was secured in a holder (Figure 1). At the beginning of each working day the capillary was rinsed, first with 0.1 M NaOH, then with water, and finally with electrolyte. Furthermore, prior to each injection the capillary was rinsed with electrolyte. The sample was introduced on the anode side of the capillary by gravity through lowering the cathode end of the capillary 10 cm for 10 s. A constant voltage of 10 or 20 kV was applied, generating a current of 10–30 μA . The temperature was ambient (20°C).

Fiber Array Construction. An approximately 300-m-long optical fiber (Polymicro Technologies, Phoenix, AZ) (100- μm core,

110- μm inclusive cladding, 125- μm inclusive coating) was used to construct a 10-cm-long fiber array (Figure 1). This optical fiber was wound 800 laps around a plastic plate (11-cm-long, 15-cm-high, 15-mm-wide). A floatglass plate (10.5-cm-long, 25-mm-high, 8-mm-wide), where one of the long sides was beveled to an angle of 20 degrees, was attached onto the wound fiber, using epoxy glue (Araldit, Ciba, Switzerland). Adhesive tape (Scotch magic tape, 3M Svenska AB, Sollentuna, Sweden) was attached to the wound fiber 1 cm from the floatglass to secure it, and then the fiber was cut between the floatglass plate and the tape. To prepare the fibers for the polishing procedure, a second piece of beveled floatglass plate was glued to the first floatglass plate with the fibers sandwiched in between. The sandwiched fiber ends were covered with a hard adhesive (Norland Optical Adhesive no. 68, Norland Products, Inc., New Brunswick, NJ) and polished to mimic a cylindrical lens. This end of the fiber array is referred to as the collecting end (inset A, Figure 1). The other fiber ends, which were secured by tape, were divided into eight groups, approximately 100 fibers in each. These fibers were glued with epoxy glue onto 1-mm-thick plastic plates, keeping their relative order. The plastic plates were glued on top of each other (inset B, Figure 1). Finally, the fiber ends were covered with hard adhesive and polished flat, thus forming the fiber array output end.

Detection System. The detection system (Figure 1) consisted of a laser unit, either the fiber array or a camera objective (Nikkor 50-mm f1.8, Nikon, Tokyo, Japan), and a CCD camera with the Winspec 1.3 software (Princeton Instruments, TEA/CCD-1100-PB, Trenton, NJ). A krypton-ion laser (Coherent Laser Innova 300, Coherent, Santa Clara, CA) at 405 nm and an argon-ion laser (Spectra-Physics 171, Spectra-Physics, Mountain View, CA) at 488 nm were used in the DNS-AA and dichlorofluorescein experiments, respectively. The laser beam (50–800 mW) was coupled into a 50-m-long optical quartz fiber with a diameter of 1 mm. The opposite end of the fiber was fixed approximately 40 cm from the capillary. An interference filter (Schott, Mainz, Germany) was placed after the optical fiber. Cylindrical optics (Melles Griot, CA) focused the excitation light to a line profile along the capillary.

The fluorescent light from the analytes in the capillary was collected at a position perpendicular to the excitation light, either with the camera objective or the fiber array. The excitation light, the capillary, and the fiber array were aligned in a custom-made holder. To maximize the collection of the fluorescent light, the distance between the collecting end and the capillary was minimized (Figures 2 and 4). Alignment of the excitation light down the length of the capillary was achieved by filling the capillary with sample and then measuring the response along the capillary. Fine adjustments of the capillary and the optics were made until a sharp image with high intensity was acquired. A cutoff filter (GG430 or OG515, Schott, Mainz, Germany) was placed in front of the camera to prevent scattered light from the laser from reaching the 330×1100 pixel CCD camera. Spherical lenses ($f_{\text{obj}} = 42$ mm) projected an image of the fiber array output end onto the CCD camera without magnification. The CCD camera was thermoelectrically cooled to -40°C and controlled by a computer using the Winspec software. To collect all the photoelectrons and maximize the readout rate of images, a binning of the CCD pixels was applied. The center pixel row of one imaged

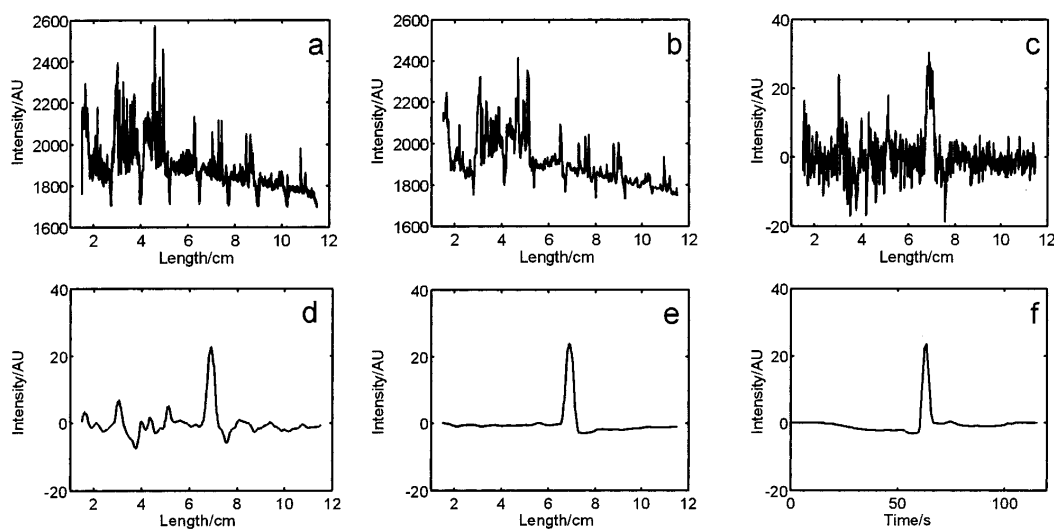


Figure 3. Electropherograms of 2 nM dichlorofluorescein dissolved in the electrolyte 50 mM sodium borate at pH 9.0 using $\lambda_{\text{ex}} = 488$ nm. A 50- μm i.d., 375- μm o.d., 28-cm total length capillary imaged between 1.5 and 11.5 cm was used. Hydrodynamic flow injection at the anode was done for 10 s at 10 cm, and the separation potential was 10 kV, generating a current of 13 μA . (a) Raw data (550 pixels/cm). The high intensity is from the background fluorescence. (b) Compressed data (75 pixels/cm). (c) After subtraction of the first component from a PCA from compressed data. (d) Data after low-pass filtering with a Blackman window. (e) To maximize the S/N ratio in the center of the detection window, 79 frames were summarized in a moving process. (f) The intensity at the pixel at 6.8 cm versus time, mimicking an end-point detection.

fiber array row (inset B, Figure 1) and the nearby 14-pixel rows were binned together to make a single line image of the fiber array row. Eight such lines were needed to make an image of the output end. With this configuration, a maximum of five exposures per second is achieved. The exposure time was set to 200 ms, and the readout rate used in the experiments was 0.5–2 Hz.

The CLOD was defined by the signal-to-noise ratio equal to two ($S/N = 2$) where the noise was taken as the standard deviation of the baseline noise.

DATA PROCESSING AND ANALYSIS

The Winspec software was used for data acquisition and CCD camera control. Another program (OTTO) was developed in-house using Visual Basic 4.0 and Matlab 5.1, to postprocess the detector signal. OTTO corrected the data for various distortions. Other purposes of the program were to display the experiments in different visualization modes and to extract electrophoretic data.

Processing of the data was done in this order: (A) Compression without loss of spatial resolution. (B) Correction of the intensity profile along the capillary. (C) Baseline correction. (D) Low-pass filtering in the spatial dimension. (E) Summarization of the moving peaks, like a moving average, in the time dimension.

(A) The spatial resolution of the optical fiber array was 125 μm while the CCD pixel size was only 25 μm . This means that the data file was five times larger than necessary due to the one-to-one imaging.²⁴ Therefore, it was possible to compress the data file without losing resolution or introducing peak distortion, thus making the processing faster. Five to seven pixels were binned for every optical fiber depending on different resolutions in the image field (Figure 3 a,b). The center pixel of every optical fiber

was located, and its intensity was summarized with the intensities of the adjacent pixels. To find the center pixel, the data were convolved with a function similar to a signal from one optical fiber to distinguish peaks from white noise.²⁵ A polynomial function was then fitted to the data points in a least-squares sense. The first and second derivatives of the polynomial function were used to define the positions of the optical fibers; thereafter, the intensities were summarized.

(B) Depending on the Gaussian power profile of the excitation light and the optical arrangement, the emitted light and the collection efficiency are not constant over the whole image field. Therefore the signal intensity was distorted over the imaged capillary length. The intensity was high in the middle and low at the edges. To correct for the intensity profile, the electropherograms were divided with a spatial correction file. The correction file was collected when the capillary was uniformly filled with fluorescein dissolved in buffer.

(C) One of the main purposes of the program was to increase the signal-to-noise ratio. To correct the baseline, the data was subtracted with the first principal component of a principal component analysis (PCA),²⁶ from the experimental data. The pixels and the images were used as variables and samples, respectively.²⁶ The baseline and the background fluorescence of the capillary were suppressed in this procedure (Figure 3c). This technique of processing the baseline could only be applied if the variance of the sample signal was small compared with the total variance. When this was not the case, the mean of the first 10–100 images, prior to the analyte entering the detection

(25) Lindgren, G.; Rootzén, H. *Stationära stokastiska processer*, 4th ed.; University of Lund: Lund, Sweden, 1992; Chapter 7.3.

(26) Martens, H.; Naes, T. *Multivariate calibration*, Wiley & Sons Ltd: New York, 1991.

(24) The image on the CCD chip has the same size as the object.

window, produced a background image. This background image was subtracted from all the images to make a straight and low baseline.

(D) After this, each image was processed with a digital low-pass filter²⁷ along the spatial dimension. This smoothed the data, and the results were different depending on the size and the shape of the filter (Figure 3d). The window method, with the Blackman function and different width of the window was used.

(E) If a higher S/N ratio was required, the peaks were summarized when they move over the 10-cm-wide detection window, like a moving average. This means that the intensities of the signal from a specific peak, taken from all images, were summarized, producing a higher signal-to-noise ratio (Figure 3e). Another reported work²⁸ has imaged 2 cm at the end of a 80-cm-long capillary. To increase the signal-to-noise ratio of the peaks, time-delayed integration on-chip was used which is the same idea as that presented here. The position of every peak in every image was calculated in two different ways. The first technique was used if the S/N ratio was 3 or more. The algorithm found the positions of the peaks in the images. The second technique was to test with different migration speeds in an iterative manner to find the speed that produced the highest signal-to-noise ratio. Here, the algorithm had to choose different constant velocities for each analyte, and this means that run parameters, such as current, must be constant. If not, peak height and the peak shape were distorted because of the nonlinear speed of the analytes. If the analyte has a true nonconstant velocity, the predetermined velocity must change during the time.

Another feature of the program is that the experimental data can be displayed in different speeds (images/second), forward, backward, with detail zooming, and in other modes of visualization. Up to eight different electropherograms can be presented simultaneously in overlay mode, which facilitates visual comparison. Different parallel experiments can be presented in the same diagram, making it possible to elucidate the experiments. It is also possible to construct a normal end point electropherogram (Figure 3f) in which the virtual detection point can be chosen. In this way we can compare an experiment from this system with that from a conventional end point detection system.

Using the program, migration time, analyte velocity, band broadening, and separation efficiencies are some properties of a separation that can be extracted from the electropherograms, and these parameters are viewed as a function of capillary length or time. It is thus possible to investigate if the separation parameters are constant or nonlinear.

RESULTS AND DISCUSSION

Design of the Fiber Array. The optical fiber array enables imaging of a considerable length of the separation capillary without increasing the distance between the capillary and the CCD camera. To image a larger part of the capillary with a camera objective, the distance between the capillary and the detection unit must increase. This gives a lower collection efficiency which is not the case with even more optical fibers along the capillary. The fiber array setup is compact because the output end is divided into short arrays which are laminated to a final size of 12.5×8

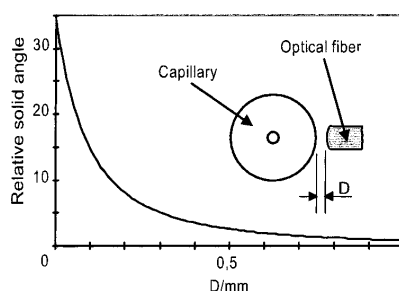


Figure 4. Relative solid angle versus distance from capillary. The relative solid angle is calculated by the solid angle for the fiber array setup divided by the solid angle for a camera objective setup.

mm (inset B, Figure 1). This small rectangular output end can be imaged on the CCD chip using small lenses with diameters of 5 cm. If a camera lens system to project the entire capillary is applied, the position of the camera has to be at a distance proportional to the capillary length which implies low collection efficiencies and a large size of the system. The use of small lenses also facilitates one-to-one imaging on the CCD chip to obtain good optical resolution.

The fiber array is also favorable because of its higher collection efficiency compared with that of a camera lens system. This higher collection efficiency is a consequence of the large solid angle that can be achieved when the fiber array is placed close to the separation capillary (Figure 4). In addition, the rounded shape of the collecting end will act as a lens and refract the light into the fibers, thus collecting a larger portion of the fluorescence from the inner of the capillary,²⁹ compared with a flat fiber end. A high acceptance cone of the fibers increases the solid angle of the fiber array but on the other hand also includes a larger portion of scattered laser light.

In the construction, the resolution in the axial dimension of the capillary as well as the acceptance zone of the fibers has to be chosen. The array used here has a resolution of approximately $125 \mu\text{m}$ and an acceptance zone as in Figure 2. This resolution is sufficient for most CE applications and is better than the $200 \mu\text{m}$ that is standard for most commercial CE instruments used with conventional UV-absorbance detection.

Experimental Setup. The laser power was typically set to 200 mW during the experiments, equal to 50 mW after the light has passed through the fiber from the laser and the filter, resulting in an intensity of approximately $0.4 \text{ mW}/\text{mm}^2$. In single-point LIF detectors, much higher intensities of as much as $10 \text{ W}/\text{mm}^2$ are used. High intensities, however, may cause bleaching of the sample. In imaging detection, the sample is exposed for a much longer period than in an end-point detector. Nevertheless, no bleaching effects were observed during imaging of the 10-cm-long detection window using the low intensity.

A $50\text{-}\mu\text{m}$ i.d. separation capillary was used in order not to compromise CE performance although this puts higher demands on correct alignment and focusing than does using capillaries of larger inner diameters. To maximize the solid angle the fiber array

(27) Proakis, J. G.; Manolakis, D. G. *Introduction to digital signal processing*; Macmillan Publishing Co.: New York, 1989; Chapter 8.

(28) Sweedler, J. V.; Shear, J. B.; Fishman, H. A.; Zare, R. N.; Scheller, R. H. *Anal. Chem.* **1991**, *63*, 496–502.

(29) Hecht, E. *Optics*, 2nd ed.; Addison-Wesley Publishing Company: Reading, MA, 1987.

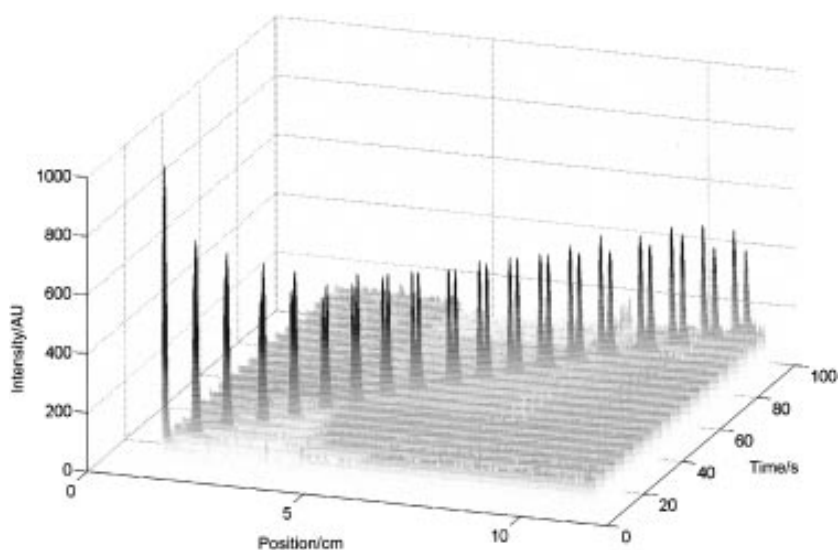


Figure 5. 3-D image of 10 μM DNS-Asp (dissolved in methanol and diluted in water) using $\lambda_{\text{ex}} = 405 \text{ nm}$. After 10 cm the two enantiomers are separated. The electrolyte contained 12 mM β -cyclodextrin in a mixture of 20 mM sodium phosphate at pH 6.5 and methanol (10 + 1). A 50- μm i.d., 375- μm o.d., 28-cm total length capillary imaged between 1.5 and 11.5 cm imaged without the fiber array was used. Injection at the anode was done for 10 s at 10 cm, and the separation potential was 10 kV, generating a current of 11 μA . See also "<http://www.teknik.lth.se/imaging>".

should be secured close and linear to the capillary (Figure 4). Any dislocation of the fiber array away from the capillary dramatically decreases the sensitivity. Close alignment lowers the collected background fluorescence from the capillary as well. Furthermore, if the excitation light is misaligned only 50 μm off the capillary center, most of the laser power is not used. A capillary holder was therefore constructed to facilitate alignment of the capillary with the fiber array. However, the alignment was not as robust as desired as a result of the handmade construction. In a totally integrated system with a fabricated holder such problems can easily be eliminated.

Proper focusing gives a sharper image which means sharper peaks but also that less pixel rows are used because of no blurring. Consequently, less information has to be transferred to the computer. This results in a higher image rate of the system and less noise per imaged length of the capillary. A cutoff filter was placed in front of the CCD camera as a small portion of excitation light reflected on and inside the capillary otherwise reaches the CCD camera.

The CCD camera exposure time should be kept short to prevent collection of photons from ambient light and long to collect as much fluorescence as possible. The experiments were therefore carried out in darkness to be able to increase the exposure time and subsequently lower the limit of detection. A long exposure time, on the other hand, gives a high signal but also image blurring as a result of motion of the peaks. As a result, the exposure time was set to 200 ms to have a high signal without blurring.

Real-Time Imaged Separation. The ability to real-time monitor the separation process *in situ* offers the analyst a tremendous advantage in the simultaneous optimization of the time and the resolution of a given separation. The entire enantiomer separation event of DNS-Asp is displayed in 3-D in Figure

5. See also "<http://www.teknik.lth.se/imaging>". The plate number achieved was 70 000 (measured at 11 cm), and the enantiomers were baseline-resolved as $R_s = 1.6$. Under the CE conditions used, cyclodextrins having no charge are transported toward the negative electrode by EOF, whereas the negatively charged DNS-AAs electrophoretically migrate toward the positive electrode. Analyte net transport is toward the negative electrode with the more strongly interacting enantiomer being the fastest one as the DNS-AAs are partitioned to the cyclodextrin cavity and are transported toward the negative electrode as well. The separation conditions using natural β -cyclodextrins added to a phosphate buffer containing a small amount of organic modifier are similar to conditions developed by Ward et al.³⁰ To achieve a faster enantiomer separation, completed after only 10 cm, the method was modified as follows: the capillary was shortened to be able to apply a high field, the separation buffer pH was lowered, and the β -cyclodextrin concentration was raised.

The enantiomer separations displayed in 2-D show straight lines, Figure 6. Excellent enantiomer separation was thus achieved for DNS-Asp, and partial enantiomer resolution was obtained for DNS-Glu and DNS-Val. The first split for DNS-Asp can be observed after about 3 cm. The migration velocity of DNS-Asp was 1.21 and 1.24 mm/s, respectively. Between every image the peaks had moved approximately 1.2 mm. From Figure 6 it can be calculated that it would take 18.9 cm to reach the same resolution of DNS-Val that was reached for DNS-Asp after 11 cm. A straight line indicates that the analyte migrated at a constant velocity throughout the imaged part of the capillary.

Performance of the Fiber Array. To judge the performance of the system, an experiment was performed in which the fiber

(30) Ward, T. J.; Nichols, M.; Sturdivant, L.; King, C. C. *Amino Acids* **1995**, *8*, 337–344.

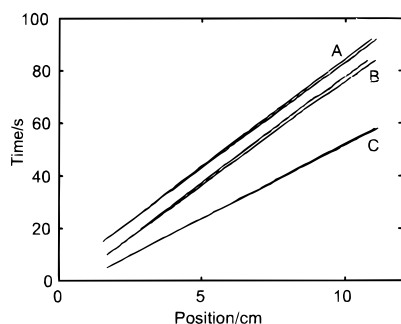


Figure 6. The peak position versus time for three different DNS-AA enantiomer separations superimposed into one image. (A) DNS-Glu, (B) DNS-Asp, and (C) DNS-Val. A time offset is added to A and B to separate them. The different migration speeds are from top to bottom, 1.21, 1.24, 1.23, 1.25, 1.76, and 1.78 mm/s.

array setup was compared with the previously reported setup based on a camera lens. An improvement of the intensity of the signal using the fiber array was approximately 5-fold from raw data. The final signal-to-noise ratio was approximately 10 times better for the array system. This is mainly because the fiber array does not collect background fluorescence from the capillary to the same extent as the camera lens system. The theoretical improvement, however, is suggested to be 33-times (Figure 4). The discrepancy between theoretical and experimental data is most likely due to complications of the alignment.

The concentration limit of detection (CLOD) was determined using dichlorofluorescein dissolved in electrolyte to eliminate stacking effects. The negatively charged dichlorofluorescein net transport was toward the negative electrode as a result of the high EOF at pH 9.0. A 2 nM dichlorofluorescein solution resulted in a S/N ratio of 11. This implies a CLOD (S/N = 2) of 350 pM. For a certain experiment the CLOD is decreased with signal processing to 70 pM. Using the camera lens system, a CLOD of 3.5 nM was obtained. The volume injected must be known to determine the quantity injected. The dichlorofluorescein volume injected was thus estimated by imaging of a continuous siphoning injection (Figure 7). The sample flowed into the 50- μm i.d. capillary at a rate of 0.3 mm/s corresponding to 0.6 nL/s. The volume injected during 10 s was thus 6 nL, leading to a plug length of 3 mm. This volume agrees with the volume injected using siphoning as calculated using the Poiseuille equation,³¹ a temperature of 25 °C, and the density and viscosity of water. These measurements and calculations agree with the real sample zone lengths of 3 mm for dichlorofluorescein imaged in the capillary (Figure 3e). A LOD of 400 zmol dichlorofluorescein was thus obtained using the fiber array.

Using the fiber array, it is possible to detect high-efficiency separations, and the spatial resolution provided by 125 μm fibers is in most cases more than required. Detection of the narrow nonresolved enantiomers of DNS-Val did not cause any problems. For comparison, a 125- μm -long sample zone corresponds to a volume of 250 pL in a 50- μm i.d. capillary. However, in applications such as ITP¹¹ or CEC,³² the focused sample volume may be smaller. The spatial resolution will only be limiting if two peaks are so close to each other that they are detected within the same optical fiber.

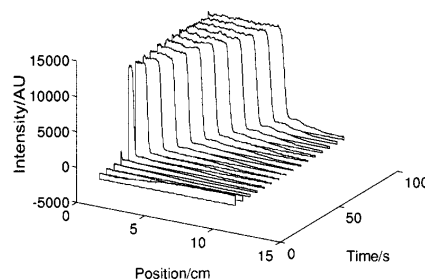


Figure 7. Imaging of the 50- μm i.d., 375- μm o.d., 28-cm total length capillary between 1.5 and 11.5 cm during a continuous injection of 250 nM dichlorofluorescein using a height difference of 10 cm. A buildup in front of the peak is also observed.

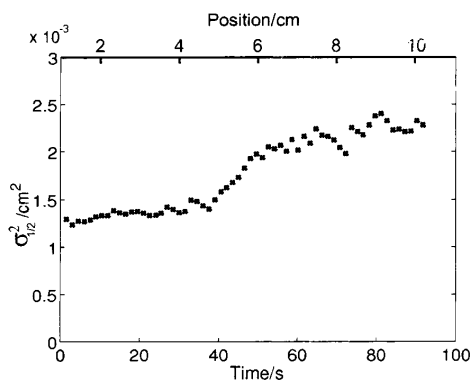


Figure 8. The total variance, σ_{tot}^2 , of DNS-Asp versus migration time. σ_{tot}^2 is calculated from $w_{1/2}^2/(8 \ln 2)$ where $w_{1/2}$ is the peak width at half-height extracted from the imaged data. The major contribution to the intercept value originates from the initial length of the sample band.

Real-Time Surveillance of Band Broadening during CE.

The band spread is directly monitored using imaging detection of the capillary. The total variance of a band can be divided into two categories: time-independent and time-dependent.³³ Ideally, the only time-dependent contribution to band broadening during the separation is longitudinal diffusion. The slope of the straight line obtained when the total variance is plotted versus time is then directly proportional to the diffusion coefficient. The intercept corresponds to the time-independent variance contribution.

The total variance (squared peak width at half-height divided by $8 \ln 2$) of the DNS-Asp peak without cyclodextrin during CE is shown in Figure 8. The variance increases linearly, as expected, but only for the first 40 s. For the next 10 s, the total variance increases at a much higher rate before it almost resumes its original slope. This can be due to some imperfection in the capillary causing additional band broadening from adsorption or nonhomogeneous EOF. Diffusion coefficients vary with temperature but excessive Joule heating were not expected due to the low currents. Local heating effects may not be neglected, though. The slope during the first 40 s in Figure 8 corresponds to a

(31) Landers, J. P. *Handbook of capillary electrophoresis*, 2nd ed.; CRC Press: Boca Raton, FL, 1997.

(32) Smith, N. W.; Evans, M. B. *Chromatographia* **1995**, *41*, 197–203.

(33) Jones, H. K.; Nguyen, N. T.; Smith, R. D. *J. Chromatogr.* **1990**, *504*, 1–19.

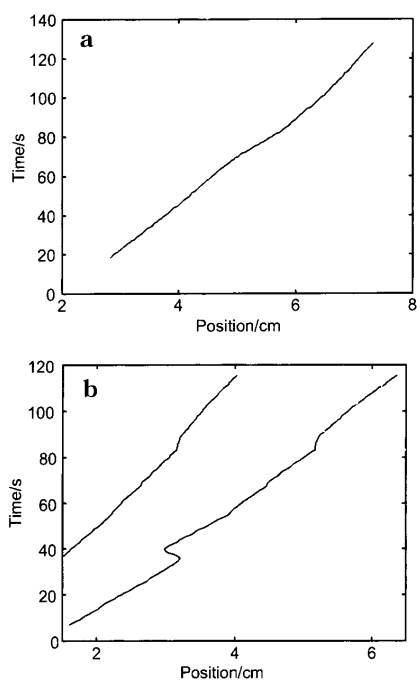


Figure 9. (A) An experiment where the current was unstable and therefore the peak has a nonlinear motion. (B) An unexpected phenomenon in which one peak changes migration direction and the other moves straightforward. See also "<http://www.teknik.lth.se/imaging>".

diffusion coefficient of $(2.4 \pm 0.5) \times 10^{-6}$ cm²/s for DNS-Asp. Slopes in the same order of magnitude were also observed for the other DNS-AAs as well as linear slopes. The diffusion coefficient for a DNS-AA is about $(5-9) \times 10^{-6}$ cm²/s.^{33,34} The major contribution to time-independent variance is here from the initial length (1 mm) of the injected band. Other studies^{35,36} have done more specific measurements about flow profiles in a small part of a capillary.

Unexpected Phenomena. In a few experiments unusual events were observed. For example, the imaging detector revealed a peak that slowed down (Figure 9A). In another run, an unidentified peak, possible contamination of the sample, appeared that suddenly changed migration direction (Figure 9B). See also "<http://www.teknik.lth.se/imaging>". The analyte of interest migrated in the expected direction throughout this event. In these runs the current was lower than that normally obtained. The strange behavior cannot be explained, but the experiment clearly discloses the unique features of imaging detection in separation methods such as CE, CEC and μ -LC.

Developments and Applications. The first 1.5 cm of the capillary at the injection end is not imaged in the present setup.

(34) Walbroehl, Y.; Jorgenson, J. W. *J. Microcolumn Sep.* **1989**, *1*, 41-45.

(35) Tsuda, T.; Ikeda, M.; Jones, G.; Dadoo, R.; Zare, R. N. *J. Chromatogr.* **1993**, *632*, 201-207.

(36) Taylor, J. A.; Yeung, E. S. *Anal. Chem.* **1993**, *65*, 2928-2932.

(37) Nilsson, J.; Wallman, L.; Laurell, T.; Johansson, J.; Nilsson, S. Submitted for publication.

(38) Preisler, J.; Yeung, E. S. *Anal. Chem.* **1996**, *68*, 2885-2889.

(39) Bayer, E.; Behnke, B.; Schewitz, J.; Johansson, J.; Nilsson, S. *HPLC '95*, Innsbruck, Austria, 1995.

Minor modifications make this possible,³⁷ enabling studies on sample introduction and the commonly practiced and highly useful technique of stacking. Any nonideal behavior can preferably be studied using imaging. The EOF may not be uniform throughout the whole capillary, for example, during stacking of large volumes. The EOF in a coated capillary, for example, has been studied using imaging.³⁸ Another example is the effect of gradients in LC/CEC.³⁹ Local differences of the capillary wall will also be revealed. The diffusion coefficient will be studied during the separation or when the sample is settled in the detection window.

CONCLUSIONS

The fiber array based LIF imaging system described here increases the sensitivity by a factor of 10 compared with that obtained with the camera lens based system. The shape of the collecting end of the fiber array increases the collection solid angle. By placing the fiber array close to the capillary more of the fluorescence light and less of the background fluorescence is collected compared with the camera lens system. Usage of the fiber array allows for small lenses in projecting the compact rectangular output-end onto a CCD. The setup will be small even if a length of 30 cm is imaged. The CLOD (S/N = 2) of dichlorofluorescein without postprocessing was 0.35 nM. By using signal processing algorithms on the large amount of data produced, the CLOD can be decreased further. The processing of one experiment increased the S/N by a factor of 10. An entire enantiomer separation can be monitored in real time using the imaging detector. Using the information, the separation events can be analyzed further with the custom-made program, and imaging detection also enables the band-broadening process to be studied during the separation. Imaging the entire length of the capillary and therefore showing all the separation events, is the strength of this method. The system can be developed further through making a wider, higher resolution fiber array and using new algorithms.

The combination of a fiber array to collect the fluorescence along the capillary, computer-aided digital signal processing for reduction of disturbances and evaluation of electrophoretic behavior, various methods of visualization for investigating the analytes' behavior, and the possibility of fitting the whole system in a box makes this system interesting for nonexpert users.

Additional information may be obtained from the author at the following web site: "<http://www.teknik.lth.se/imaging>".

ACKNOWLEDGMENT

M. Andersson is gratefully acknowledged for ideas concerning statistical computer algorithms. J. M. Mesáros and A. G. Ewing are gratefully acknowledged for valuable guidelines and discussions on how to construct a fiber array. The authors would like to thank Tekniska Forskningsrådet, Crafoordska Stiftelsen, Kungliga fysiografiska sällskapet i Lund, C. F. Lundströms Stiftelse, and Carl Tryggers Stiftelse för Vetenskaplig Forskning for their financial support. This work was in part presented at the 21st International Symposium on High-Performance Liquid Phase Separations and related techniques (HPLC '97), Birmingham, UK, 22-27 June 1997.

Received for review April 19, 1999. Accepted July 14, 1999.

AC990398L

Jonas Johansson¹
Thomas Johansson¹
Staffan Nilsson²

¹Division of Atomic Physics,
Lund Institute of Technology,
Lund, Sweden

²Department of Technical
Analytical Chemistry,
Chemical Center, Lund University,
Lund, Sweden

Fluorescence imaging of light absorption for axial-beam geometry in capillary electrophoresis

A new method for investigation of axial-beam absorption detection for improved detection limits in microcolumn separations is reported. The method is based on fluorescence imaging of light absorption along a separation capillary. The probing UV light is introduced at one end of the capillary and shows an exponential fall-off along the capillary. As the UV light propagates through the sample peaks, an additional loss in intensity will be observed. In order to view the absorption profile along the capillary, a background fluorophore is added to the buffer. A charge-coupled device (CCD) detector and imaging optics are placed beside the capillary to view the capillary in a direction perpendicular to the capillary. Signal integration is employed for consecutive exposures as well as for neighboring detector pixels in order to increase the signal-to-noise ratio. Measurements for stilbene 3 with sulforhodamine B as a background fluorophore are presented. The characteristics of the detection method and potential improvements are discussed.

1 Introduction

Capillary electrophoresis (CE) is a relatively new and fast growing separation technique [1, 2]. It has been used for many diverse applications and, more recently, has been coupled to other techniques such as mass spectrometry. The main advantages of CE are the speed of separation, the low amounts of sample used as well as buffer solution required for a separation, and its superior separation efficiency. It is also a versatile technique partly due to the fact that besides the separation based on molecular charge, it is also possible to include a stationary phase as in capillary chromatography, an entangled gel, micelles or printing of stationary structures with affinity to the analytes and many other options that can be used to extend the separation mechanisms. Two of the most useful detection techniques in microcolumn separation are UV absorption detection and fluorescence detection. Fluorescence detection provides a superior limit of detection (LOD), and the use of confocal microscopy detection is now more or less a standard arrangement for reaching single molecule LODs [3]. The main disadvantage is, however, that most molecules do not possess native fluorescence at a measurable level and, therefore, a tedious and uncertain derivatization step is most often necessary. UV detection, on the other hand, is a versatile technique that can be used in most cases due to the fact that most molecules possess useful absorptivity in the UV spectral range. The concentration LOD for UV detection is unfortunately in the range of 1 μM at the best, which should be compared with a 1 pM concentration LOD for a commercial fluorescence

detector for CE. Still, the ease of use makes the UV detector the straightforward choice and by far the most used detector. Some promising efforts have been made to improve the LOD. The most important properties of a detector are that it is applicable for most separations, it is easy to use and robust and, preferably, it is inexpensive. The main limiting factor in CE is the small column inner diameter, 100 μm or less, which limits the detection path length. This problem has been addressed in terms of post-column detection cells. With optical path lengths of up to 8 mm, LODs of about 100 nM have been obtained [4]. Another option is to direct the UV light into the microcolumn at one end and the detector at the other end [5]. This increased the optical path length to the width of the eluting peaks, which is between 0.2–1 mm for a good separation, thereby improving the LOD by a factor of 20–100 for a 50 μm capillary. Widely used alternatives have been indirect detection, absorbance or fluorescence. These detection methods meet the need for general use, but the LOD is still on the order of 10^{-5} and 10^{-7} M for indirect absorbance and fluorescence, respectively [6].

The crucial part in UV absorbance detection is the reduction of background noise. The main contribution to noise originates from fluctuations in the detection cell due to flow turbulence, temperature fluctuations and related factors as well as lamp intensity fluctuations. But even if it was possible to eliminate these factors there would still be the shot-noise limitation due to the limited dynamic range of the detector, which is proportional to the square root of the dynamic range. Thus, the best approach is to reduce the background fluctuations and at the same time increase the dynamic range. The double-beam detector [7] was reported to reduce the lamp noise and an LOD below 10^{-7} M was achieved. The usefulness of this approach is that the signal is normalized against a reference signal to lower the noise. Our approach is to utilize fluorescence imaging [8–12] as a way of normalizing the signal. The UV light is directed into one end of a capillary [5] but instead of detecting the light at the end of the detector, the light absorption is imaged perpendicularly to the capillary by adding a background fluorophore to the buffer solution and

Correspondence: Dr. Jonas Johansson, Astra Hässle AB, Product Analysis 1, SE-431 83 Mölndal, Sweden (Tel: +46-31-7761374; Fax: +46-31-7763768; E-mail: jonas.johansson@hassle.se.astra.com)

Dr. Staffan Nilsson, Department of Technical Analytical Chemistry, Chemical Center, Lund University, P.O. Box 124, S-221 00 Lund, Sweden (Tel: +46-46-2228177; Fax: +46-46-2224525; E-mail: staffan.nilsson@teknik.lth.se)

Abbreviations: LOD, limit of detection; PCA, principal component analysis

Keywords: Capillary electrophoresis / Fluorescence / UV detection

observing the fluorescence with a CCD camera. In this way the spatial absorption profile along 2.5 cm of the capillary was detected. Light source fluctuations, for instance, would affect the total intensity of the profile; however, the absorption profile would stay the same. Thus a self-normalizing detection setup is obtained. Furthermore, by using a CCD signal integration spatially across the CCD as well as along the time axis, a widely increased dynamic range was achieved. In this paper, the setup and the detection principle is explained and some early results are shown. A discussion about the problems that occurred and a future design, meeting the demand of ease-of-use, is included.

2 Material and methods

2.1 Chemicals

Unless stated, chemicals were of *pro analysi* grade. The water was prepared using a Milli-Q system (Millipore, Bedford, MA, USA). Sodium hydroxide (5 M), sodium dihydrogen phosphate monohydrate and disodium hydrogen phosphate anhydrous were obtained from Merck (Darmstadt, Germany). The phosphate buffer used in electrolyte solution was prepared by mixing stock solutions of 20 mM NaH_2PO_4 and 20 mM Na_2HPO_4 to pH 6.5. A background fluorophore was prepared by dissolving sulforhodamine B (Lambda Physics, Santa Clara, CA, USA) into methanol to a concentration of 0.01 M. The final electrolyte was prepared by diluting the background fluorophore to 2×10^{-5} M with buffer solution.

2.2 Sample preparation

Stock solutions of stilbene 3 (Lambda Physics) were prepared in methanol at a concentration of 0.02 M. The stock solution was diluted in 20 mM phosphate buffer, pH 6.5.

2.3 Capillary electrophoresis

The electrophoresis setup was a homemade system. A stabilized power supply (0–30 kV, Mark II Zeta Elektronik, Höör, Sweden) was used. Fused-silica capillaries of 100 μm inner diameter and 375 μm outer diameter were obtained from Polymicro Technology (Phoenix, AZ, USA). The capillary was mounted onto a holder and the outer protective polyimide coating was removed with fuming nitrous acid and wiped off with a soft tissue, thus creating a detection window of 25 mm. The total length of the capillaries was 30 cm. The inlet electrode vessels were 1.5 mL microfuge tubes. The outlet vessel was made in the lab by glueing a 12 mm microscope cover plate (acting as a window) onto a 10 mm, 5 mm deep plastic cup. The capillary was pierced through a hole in the cup and a 25 μm diameter platinum wire was pierced through a second hole to act as an electrode on the outlet side (insert of Fig. 1). Electrophoresis was typically run at 3–5 kV positive at injection. The injection was done hydrodynamically by lifting the inlet buffer vial approximately 5 cm for 15 s. This was monitored with the imaging system and was found to correspond to an ~ 3 mm sample plug.

2.4 Detection system

The experimental setup is shown in Fig. 1. The excitation source was a krypton-ion laser, Innova 301 (Coherent Lasers, Santa Clara, CA, USA) at 351 nm. Neutral-density filters (Schott, Mainz, Germany) were used to reduce the laser output power from typically 100 mW to 1–3 mW. The laser light was focused through the outlet vessel window onto the capillary end to a spot size less than 100 μm using a quartz lens ($F = 10$ cm, $D = 2.5$ cm). The fluorescence light from the background fluorophore was imaged onto an 1100×3300 pixel CCD detector using an $F = 10$ cm, $D = 5$ cm quartz lens. The CCD was cooled to -40°C and was connected to a PC to

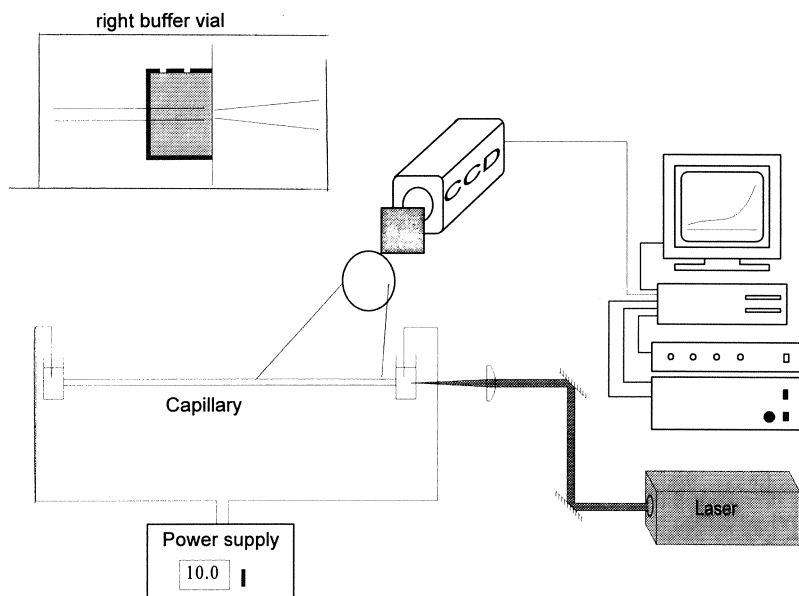


Figure 1. Experimental setup used for fluorescence imaging of light absorption. UV light enters the capillary through one of the buffer vials and into one end of the capillary. The absorption profile is imaged using a background fluorophore in the buffer solution and a CCD detector.

display and store the fluorescence profiles of the capillary. A GG530 (Schott) cut-off filter was placed in front of the camera to prevent the scattered light from being detected. Fifteen rows in the direction perpendicular to the capillary were binned together in order to collect all the photo electrons and to maximize the read-out rate of each frame. With this configuration the maximum rate was 2.5 images/s. The exposure time of the CCD was set to 100 ms.

2.5 Data processing

A software package for signal integration of moving peaks from a number of CCD frames has been reported earlier [13] and was utilized here with a minor modification. The data analyses include signal normalization, time derivation, signal integration and transformation to a time scale. This is explained under Section 3 with reference to Fig. 4. In addition, principle component analysis (PCA) modelling was investigated that was utilized to select any moving structures with a certain velocity in the capillary. The data shown here are not treated with the PCA model.

3 Results

The principle of the fluorescence imaging of light absorption in a microcolumn is shown in Fig. 2. Light is directed through the window of the outlet vial and into the separation capillary. The light is attenuated in an exponential fashion along its way in the capillary mainly due to refraction in the capillary walls and absorption by the background fluorophores. In these experiments the background fluorophore absorption was small. When a UV absorbing molecule propagates in the capillary, there will be additional light absorption and an anomalous absorption profile will result, as is indicated by the black curve in Fig. 2. The amount of residual light at any point in the capillary will, therefore, be the integral of light absorption, which in turn is proportional to the analyte concentration. Thus, the true concentration profile can be reconstructed by applying the first derivative of the signal. An example of an imaging experiment for a $10 \mu\text{M}$ solution of stilbene 3 is shown in Fig. 3. Fluorescence profiles along the 2.5 cm window is plotted as a function of time in a three-dimensional (3-D) display. The sample appears in the detection window after about 380 s. This is seen as a fall-off of the background fluorophore intensity due to the sample UV absorption. The sample was followed in the detection window for about 120 s.

The data post-processing is shown step by step in Fig. 4. The first step was to apply the time derivative of the signal. This is performed by subtracting one frame from another frame (raw data in Fig. 4a) with a small time delay between each other (Fig. 4b). If the time delay between the frames approaches zero, the result will be the true derivative but in this case a delay between 1 and up to 5 s is sufficient to provide a good time resolution. This will differ for different peak widths. The subtraction will give a good result if the mean intensities of the two frames is the same; for that reason all the

frames must be normalized to each other prior to the derivation step. In a second step, a number of frames were summarized together (Fig. 4c). Because the peaks are moving, this must be done using a moving sum technique. Every sample peak propagates at a given velocity in the capillary. To summarize the peaks from different frames, the program must calculate the positions for each sample peak (or velocity component) in the frames due to the different speed. When this is done, the intensity at different positions is summarized to a summed intensity and the calculations are made for every frame and position, resulting in a profile with higher signal-to-noise ratio. Still, the signals are displayed as a function of position rather than as a function of time as is conventionally done. The two representative forms are sim-

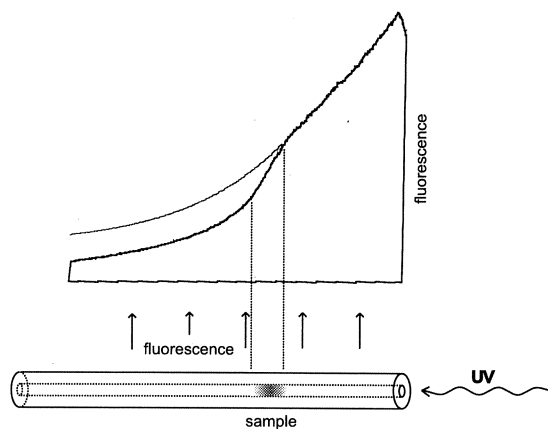


Figure 2. Detailed view of Fig. 1 showing the principle of the method. The graph shows a raw data absorption profile for 1×10^{-5} M stilbene 3 sample. An exponential line (grey line) is inserted in the figure to picture a profile without a sample.

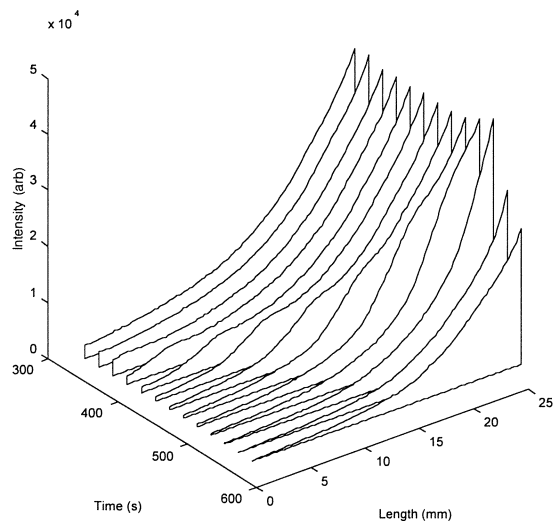


Figure 3. A 3-D plot of the intensity vs. position in capillary and elution time. The additional fall-off is clearly seen as it moves from left to right on the length scale and towards longer time. The sample was a 1×10^{-5} M stilbene 3 solution.

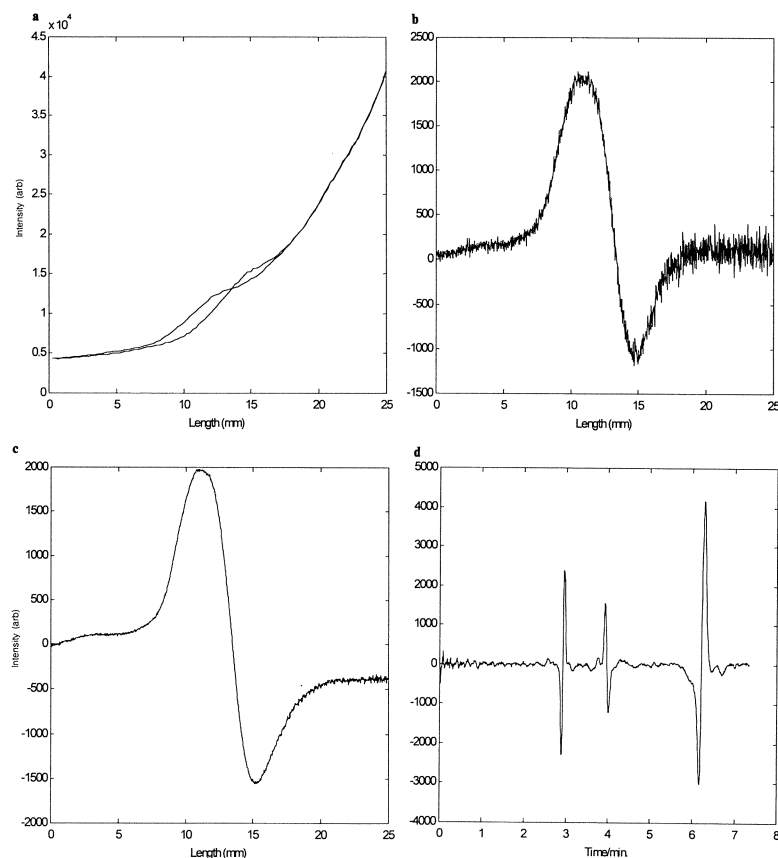


Figure 4. Principle of data post-processing. (a) Two selected raw data imaging profiles separated by five frames; (b) imaging profile after subtraction of one normalized profile with the other; (c) imaging profile after moving integration of 51 frames; (d) electropherogram after transformation to time axis. The sample was a 1×10^{-5} M stilbene 3 solution.

ilar but not identical; however, by simply transposing the position-time matrix the electropherogram can be displayed as a function of time instead. An example of this is shown in Fig. 4d. The two first peaks that appear are system peaks appearing for unknown reasons while the third peak is the sample.

From the subtracted profile one can see that the peak yields both a positive and a negative structure. This is due to the fact that the stilbene sample possesses strong fluorescence around 400 nm and a small fraction of this leaks through the cut-off filters and reaches the detector. The objective of using a fluorescent sample was that this made the experiments much easier since the UV/blue fluorescence could easily be seen by eye as the analytes propagated through the capillary. For instance, the actual length of the injection plug was easily confirmed. Note that the only effect of the fluorescence contribution was a small negative peak in the measured profiles and the positive peaks reported here are truly absorption characteristics. This can easily be understood from the raw data files in Fig. 4a, where the sample absorption yields a signal decrease that persists throughout the capillary to the left, whereas a fluorescence peak results only in a signal increase at that location and does not affect the detector pixels downstream.

Figure 5 shows stilbene 3 at a concentration of $1 \mu\text{M}$. The two first peaks that appear are system peaks that appear due to a problem with the sample injection, while the third peak is the sample. In this case the S/N was about 20, with the noise measured peak to peak across the detection window. As can be seen, useful S/N ratios can also be expected for sub- μM concentrations. For lower concentrations, however, problems arose with signal interferences of unknown origin that hampered detection/identification at lower concentrations. Some possible explanations for this phenomenon, which we believe has to do with the focusing of the light into the capillary, are given below.

4 Discussion

4.1 New imaging method

Here we report an investigation of axial-beam detection using a new imaging method with the aim of improved detection limits in microcolumn separation. This method is based on perpendicular imaging of the capillary using a background fluorophore. In some aspects it resembles fluorescence imaging detection and in other aspects indirect detection methods. Thus, the equipment used was

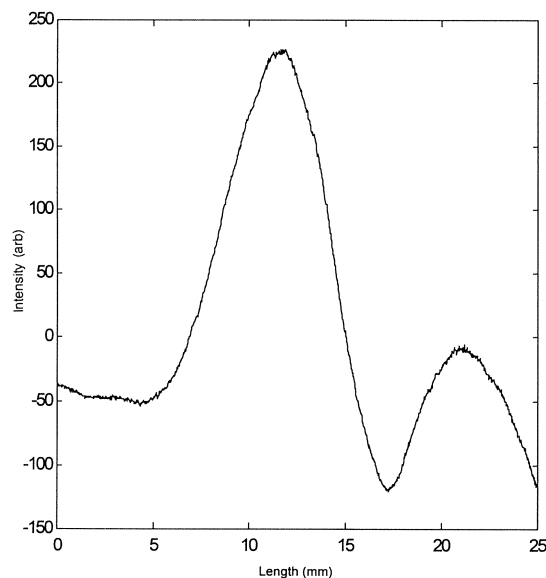


Figure 5. Imaging profile after signal derivation and moving integration of 91 frames. The sample was a 1×10^{-6} M stilbene 3 solution.

the same as that used in earlier experiments on fluorescence imaging during CE and other microseparation techniques. In terms of sample preparations there is a strong resemblance with indirect fluorescence. Note however, that there is an important difference in the detection principle. In indirect fluorescence detection the height of the detected signal is dependent on the sample molecule's ability to occupy a certain volume in the solution at the expense of background fluorophores, thereby yielding a lower detected fluorescence at that location. In fluorescence imaging of light absorption, however, the background fluorophore is merely utilized to spatially map the level of the UV light. Most likely both these effects can be present in fluorescence imaging of light absorption. Indirect absorption effects would be observed as a dip in the fluorescence profile while the axial absorption on which our technique relies manifests itself as an additional fall-off in the fluorescence profile, which proceeds throughout the capillary, as shown, *e.g.*, in Fig. 2. However, we did not observe a stronger interaction from indirect absorption effects.

There are several benefits of this method that could contribute to an increase in the detection limit compared with conventional UV detection. First of all, by illuminating from one end of the capillary, an improvement of about a factor of 10 can be expected for the 100 μ m diameter capillaries that were used in these experiments. For thinner capillaries the improvement factor would increase when the lengths of the sample peaks are comparable while the LOD for UV detection decreases with the capillary diameter. This principle has been reported earlier, however, with endpoint detection [5]. Secondly, combined with fluorescence imaging of

light absorption, a signal normalization is automatically achieved that strongly reduces the noise associated with lamp energy fluctuations, an instability in light coupling in the capillary, which was the limiting factor in [5]. Furthermore, by utilizing a CCD detector, signal integration in the length and time dimensions facilitates signal averaging to further improve dynamic range and LOD.

4.2 Interfering features

In practice, work remains to be done to take advantage of all the aspects that are stated in the above section. As was mentioned in Section 3, there are several interfering features in the electropherogram for sub- μ m concentrations. These appear as ghost peaks at random positions/elution times in the data set. First of all, the sample was checked for impurities and was investigated with commercial CE equipment without finding any by-products or impurities. Some problems are related to the injection of the sample. We did not have access to a proper pressurized injection module, and the injections were always broad, up to several mm in length. At some occasions there was an impression that the sample adhered to the inner wall of the capillary and the capillary had to be cleaned with 0.1 M NaOH. On the other hand, by studying the data matrices the conclusion was that most of the interferences derived from a time-dependent instability in the focusing of light into the capillary. The geometry of the light focusing is shown in the insert of Fig. 1. The light is focused through the first buffer vial wall and the buffer solution and into the capillary. As the separation proceeds the electric field will force buffer into the vial and this irregular flow will cause refractive index fluctuations at the capillary outlet. Furthermore, analytes or background fluorophores that move slower than the electroosmotic flow will accumulate at the capillary outlet. This may lead to a situation where the portion of light that propagates in the capillary wall instead of inside the capillary will vary with time and, thus, time-dependent structures may be detected that could be interpreted by the data post-processing as a moving peak. Probably, these fluctuations would have been less severe if a lamp, which has a larger focus, had been used. One future improvement that will be made is to use a flow-through vial to avoid concentration gradients from building up at the capillary outlet. A solution such as that in [5] could also be used with some modifications. It will further be interesting to use a D₂ lamp as excitation source and to investigate the extent of optical interference. With a lamp it would also be possible to go deeper into the UV region. The use of a thinner capillary would also yield a more stable plug flow.

As was stated in Section 1, the most important aspects of UV detection, making it the detection principle of choice, is its simplicity and versatility. Any new technique that is intended to replace or be a complement to UV detection has to meet these demands. Therefore, these aspects have to be discussed for our technique. The part that appears to be the most labor-intensive is the optical alignment of the fluorescence imaging and the coupling of the UV light into the capillary. In particular, the coupling of the UV light into the capillary needs special care in order to focus as much light as possible into the

lumen of the capillary. If this focusing is not done properly, a too large fraction of UV light may propagate in the capillary walls and may produce fluorescence along the capillary, causing an off-set to be added to the signal. Although this is not disastrous, it will impair the detection limit. We propose to solve the problems with optical alignment by using a prealigned setup. The separation capillary can be placed in a glass plate with a fitting channel etched on one side of the plate. By placing the capillary into the channel there would be no need to focus the imaging system, and only a small correction might be needed to ensure that the detection light is properly directed into the capillary. Remember that we have flexibility in choosing the background fluorophore, which in practice means choosing a fluorophore with a strong fluorescence in the red/NIR spectral region where the background fluorescence is low. A flow-through buffer vial can also be constructed in such a way that it can be positioned with precision in relation to the supporting plate and the capillary.

4.3 Sample bleaching

Another question that should be addressed is the bleaching of the sample. Since the sample is exposed to the UV light along the length of the capillary rather than just at the conventional 200 μm detection window, bleaching may constitute a problem both with respect to LOD and linearity. This problem (discussed in [5]) was solved by setting a limit to the UV light intensity depending on sample bleaching properties. However, in our case the UV light does not propagate along the full length of the capillary. Due to a refractive index mismatch and background fluorophore absorption the UV light intensity is already reduced to a very low level after a few cm. Consequently, an investigation of sample bleaching did not show any bleaching in our case. The use of a background fluorophore causes extra work but is routinely done in indirect detection methods. It could be mentioned here that we also experimented without a background fluorophore, using the scattered UV light for the imaging detection. However, the signal levels were much lower and very noisy, causing us to abandon this technique at an early stage.

4.4 Conclusions

In conclusion, axial-beam detection geometry was explored by means of a method termed fluorescence

imaging of light absorption. The aim of this investigation was to find a strategy for lowering the detection limit in microcolumn separations. In theory, the detection limit should be improved by (i) a longer sampling cross-section, (ii) signal integration by following the peaks within the 25 mm detection window, and (iii) adding signal from multiple CCD pixels together and thereby gaining in dynamic range. In practice, there were problems related to the outlet vial, where the UV light enters into the capillary, as well as problems related to the electrophoresis. For future use, a better design of the outlet vial, utilizing a flow-through geometry, has to be taken into consideration. With the improvements discussed here, the LOD could be lowered to the levels of low nM and the detector will be easy to use.

Financial support from Kungliga Fysiografiska Sällskapet i Lund, Crafoordska Stiftelsen, C. F. Lundströms Stiftelse, Carl Tryggers Stiftelse för Vetenskaplig Forskning, the Swedish Natural Science Research Council, and the Swedish Research Council for Engineering Sciences is gratefully acknowledged. Support by Software Martin Andersson is gratefully acknowledged.

Received February 27, 1998

5 References

- [1] Jorgenson, J. W., DeArman Lukacs, K., *Anal. Chem.* 1981, 53, 1298–1302.
- [2] Landers, J. P., *Handbook of Capillary Electrophoresis*, CRC Press, Boca Raton, FL 1997.
- [3] Nie, S., Chiu, D. T., Zare, R. N., *Anal. Chem.* 1995, 67, 2849–2857.
- [4] Chervet, J. P., Ursem, M., Salzmann, J. P., Vannoort, R. W., *J. High Resolut. Chromatogr.* 1989, 12, 278–281.
- [5] Xi, X., Yeung, E. S., *Anal. Chem.* 1990, 62, 1580–1585.
- [6] Yeung, E. S., Kuhr, W. G., *Anal. Chem.* 1991, 63, 275–282.
- [7] Tong, W., Yeung, E. S., *J. Chromatogr. A* 1995, 718, 177–185.
- [8] Nilsson, S., Johansson, J., *Selective Electro-separations in Capillaries with LIF/CCD Imaging Detection*, Kemistdagar i analytisk kemi, 1993, Lund, Sweden.
- [9] Johansson, J., Johansson, T., Nilsson, S., *Proc SPIE* 1995, 2629, 2–9.
- [10] Nilsson, S., Johansson, J., Mecklenburg, M., Birnbaum, S., Svanberg, S., Wahlund, K.-G., Mosbach, K., Miyabayashi, A., Larsson, P.-O., *J. Capill. Electrophor.* 1995, 2, 46–52.
- [11] Wu, J., Pawliszyn, J., *Am. Lab.* 1994, 26, 48–52.
- [12] Johansson, J., Witte, D. T., Larsson, M., Nilsson, S., *Anal. Chem.* 1996, 68, 2766–2770.
- [13] Johansson, T., Petersson, M., Johansson, J., Nilsson, S., *HPLC 97 Birmingham, UK* 1997, L-80, Abstract.

Probing the marine environment with fluorescence lidars

Evaluation of three fluorosensors in a field campaign

G. Cecchi¹, M. Bazzani¹, C. Cucci¹, D. Lognoli¹, I. Mochi¹,
L. Pantani¹, V. Raimondi¹, R. Carlà¹,
B. Breschi², D. Novelli², T. Johansson³, P. Weibring³, H. Edner³, and S. Svanberg³

¹ Italian National Research Council - Institute for Applied Physics "Nello Carrara" (CNR-IFAc), Via Panciatichi 64, I-50127 Firenze, Italy
E-mail: g.cecchi@ifac.cnr.it; phone: +39-055-4235263; fax: +39-055-410893.

² IDEA-ISE s.r.l., Via Roma 427, I-59100 Prato, Italy
E-mail: ideaise@ui.prato.it; phone: +39-0574-634680; fax: +39-0574-634680.

³ Department of Physics, Lund Institute of Technology, P.O. Box 118, S-221 00 Lund, Sweden
E-mail: Sune.Svanberg@fysik.lth.se; phone: +46-46-2227650; fax: +46-46--2224250.

Abstract

Three independent active fluorescence lidar systems were used and intercompared during an oceanographic campaign in the Tyrrhenian Sea. The route was selected to encounter different types of waters (mixing zone east of the Sardinia/Corsica Islands), coastal waters with anthropogenic pollution (Catania and Civitavecchia harbours) and colonisation of the Posidonia Oceanica (Egadi Archipelago). Two systems were mobile high-spectral resolution lidars while the third one was a time-resolving lidar prototype. The systems were used for the assessment of water columns by Laser Induced Fluorescence (LIF) measurements and were compared with passive data from a NOAA satellite. In addition, LIF measurements on the colonisation of the Posidonia Oceanica, which is an important bio-indicator, were carried out for samples collected at different depths in the water column.

1. Introduction

The global monitoring of the marine environment is a central issue for the environmental short- and medium scale policies at a world-wide level. The spatial and temporal scales required in the monitoring of oceans and seas on a global level call for the use of advanced sensors permanently operating from space as well as sensors at sea level that can provide complementary and sea-truth data.

Satellite multispectral sensors regularly provide a great amount of synoptic data regarding Sea Surface Temperature (SST), chlorophyll concentration and Suspended Sediment Concentration (SSC). This information, however, mainly refers to the first layers of the water column, depending on the wavelength band used in the sensor. Information from the thermal infrared bands, for instance, is relevant to only the first few microns of the sea water column.

Data from active sensors that can probe the water column in depth can yield additional information with respect to the passive ones. The merging between passive and active data can thus provide a better understanding of the marine environment as a whole. Moreover, active sensors are less sensitive to some disturbing factors like weather conditions and influence from the bottom in coastal waters, which can heavily affect data from satellite-based sensors.

The SALE-3 (Sea and Atmosphere Lidar Experiment) campaign was launched to intercompare three active fluorescence systems on board the Italian research vessel (R/V) *Urania*. Although part of the campaign was devoted to volcanic monitoring [1], most measurements carried out were directed to the investigation of several aspects concerning the monitoring of the marine environment. In particular, the experiment addressed the following issues:

a) *integration of active data with passive data from satellite*; this is a crucial issue for reliable and extensive monitoring of the marine environment. Lidar technique can actually provide data relative to the water column with good spatial and temporal resolution. These data, however, cannot have a satisfactory spatial coverage for an extensive monitoring. In this context the integration of active data from lidar sensors and passive data from satellite can produce effective results.

b) *water column assessment by Laser Induced Fluorescence (LIF)*; the LIF technique can help to investigate several aspects of different aquatic ecosystems. In particular, during the SALE-3 campaign experiments were carried out for depth-resolved data retrieval.

Finally, the in-field use of the fluorescence lidar systems constituted an actual basis both for sensor improvements and for the development of methods for the investigation of the marine environment.

Fig. 1 shows the route of the R/V *Urania* during the SALE-3 oceanographic campaign carried out from August 11 to August 30, 2000. The route was selected to cross different types of waters in the mixing zone between the Ligurian and Tyrrhenian Seas east of the Corsica/Sardinia interdivision. NOAA 12-AVHRR imagery were used to select the most appropriate ship route. Secondly, the Egadi archipelago west of Sicily provided the most important colonisation of the *Posidonia Oceanica*, which is known to be an important biological indicator/integrator for the marine environment. The areas east and north of Sicily were selected partly because of the geographical locations of some of the most prominent European volcanoes, but also in order to study different ecosystems, such as coastal waters in front of the Catania harbour.

2. Fluorosensor descriptions

Three independent fluorescence lidar systems were operated on board the ship during the measurement campaign. Two of the systems were mobile and previously much used in various field experiments while the third one was a newly developed experimental system. The former two systems were operated from the rear deck of the R/V *Urania*. The CNR-IFAc mobile system is shown in Fig. 2a. The optical module of the system (the telescope and the excitation sources) are housed in a section at the rear of the van. This section of the van is electro-magnetically shielded from the very lab, where the electronics is located. The optical module is connected to the electronics via an optical fibre bundle. The laser beam is directed via suitable optics on a first-surface aluminised

mirror, fixed at the railing of the ship, to fold the laser optical path into the water column. Fig. 2b shows the LTH mobile lidar system, with its roof-top transmission dome, sending the laser beam forward to a folding mirror and then vertically downwards into the water. The beam passed centrally through a 4-dm diameter sheet-metal tube installed for protection. The tube could be mounted at different height - one meter over the surface in open sea operation, and lower when the ship was at anchor. The folding mirror and the upper part of the protecting tube are more clearly seen in the photo insert. The third system was arranged to probe the sea just in front of the bow of the ship (Fig. 3). A first-surface aluminised mirror was used to fold the optical path to interrogate the marine environment.

2.1. Excimer-based mobile fluorosensor

An excimer-based mobile fluorescence lidar system, denoted FLIDAR-3, was operated by the CNR-IFAc team. A general description of this system is given in Refs [2,3]. The FLIDAR-3 has been used for the monitoring of the marine environment during several campaigns on board of R/Vs since 1991 [4].

Fig. 4 shows an overview of the optical and electronic arrangements of the system. It features two selectable excitation sources: an excimer laser (XeCl @ 308 nm; typical pulse energy at the output of the lidar system: 30 mJ; pulse duration: 10 ns) and an excimer-laser pumped dye laser (Coumarin 47, @480 nm; typical pulse energy: 3 mJ). The laser pulses are directed with a typical 2-Hz repetition rate into the water column via suitable deflecting optics. Backscattered signal is collected with a 25-cm diameter 1-m focal length Newtonian telescope. A fibre bundle conveys the signal from the telescope focal plane to the input slit of a 275-mm focal length spectrometer coupled to an intensified and gated 512-photodiode array detector. Control electronics, data acquisition and storing are controlled via a personal computer. The system is housed inside a small van (FIAT, Ducato Maxi) whose dimensions (w \times l \times h) are 2.1 \times 5.5 \times 2.5 m. The optical sensor (telescope and laser sources) is located in the rear section of the van that is electromagnetically shielded from the actual lab housing the electronics.

The FLIDAR-3 was continuously operated acquiring automatically a set of data every 20 minutes. The corresponding spatial resolution of the data along the track was about 3.5 km with a typical speed of the ship of 6 knots. GPS data are also recorded every second during the measurement.

Each data set (see Routine 1 in Table 1) consisted in three spectra: two spectra with excitation wavelength at 308 nm in the range from 300 to 600 nm and from 500 to 800 nm, respectively; the third one with excitation wavelength at 480 nm in the spectral range from 500 to 800 nm. Each spectrum, in fact, is the result of the acquisition of six spectra that are separately stored in the data set: three active spectra, obtained accumulating the signal over 15 laser shots, and three passive spectra, used for background evaluation, that are subtracted from the active ones. The acquisition and storing of a complete data set using the Routine 1 takes about 4 minutes.

High spectral resolution Raman data (see Routine 2 in Table 1) were acquired in 47 measurement stations distributed along the track. The routine acquires alternatively an active spectrum (Raman spectrum) and a passive spectrum (background) that is subtracted from the active one. Typically the final Raman data were obtained as a result of accumulation over 200 laser shots. The acquisition of Raman data took about 2 minutes.

Table 1 – Data acquisition routines for the FLIDAR-3 fluorosensor

<i>Label</i>	<i>Excitation wavelength</i>	<i>Longpass optical Filter</i>	<i>Spectral range</i>	<i>Grating</i>	<i>Spectral resolution n*</i>
Routine 1					
Spectrum A	308 nm	335 nm	300 – 600 nm	150 g/mm	2.4 nm
Spectrum B	308 nm	395 nm	500 – 800 nm	150 g/mm	2.4 nm
Spectrum C	480 nm	515 nm	500 – 800 nm	150 g/mm	2.4 nm
Routine 2					
Spectrum H	308 nm	320 nm	338 - 348 nm	2400 g/mm	0.16 nm

* spectral resolution data refer to a 100- μ m input slit width (as used in the field) and at 500 nm.

2.2. Nd:YAG-based mobile lidar system with CCD detection

The LTH mobile lidar system is normally adapted for atmospheric differential absorption lidar applications as described, e.g. in [5,6]. Occasionally it has been used in aquatic measurement campaigns, also in collaborative efforts similar to the present one [7,8]. Recently, the system has been fully refurbished with new laser and computer facilities as described in [9], and here only a brief description will be given. The general lay-out of the mobile system is shown in Fig. 5 and the optical and electronic arrangements for laser-induced fluorescence measurements are shown in Fig. 6.

The system is constructed based on a Volvo F610 truck, which is equipped with a laboratory compartment with a floor dimension of 6 x 2.3 m². The fluorescence lidar transmitter is a frequency-tripled Nd:YAG laser generating radiation at 355 nm in 8 ns long pulses at a repetition rate of 20 Hz. Typically the transmitted pulse energy was limited to 30 mJ in the marine probing experiments. The vertically looking Newtonian telescope has a 40-cm diameter. A 40 x 80 cm² folding mirror is placed over the telescope in a dome above the vehicle roof. The mirror normally directs the laser beam into the atmosphere, but in the present experiments via the folding mirror down into the water. The laser beam was expanded in a Galileian quartz lens telescope and transmitted coaxially with the telescope. The laser beam diameter was typically 4 cm in the present experiments.

The detection system for water fluorescence spectra is placed at the output of the telescope. The input end of a special fibre bundle, containing seven individual fibres densely packed in a circular surface, was placed in the focal plane. The bundle output was rearranged into a linear shape matching the input slit of the spectrometer. The spectrometer dispersed the fluorescence light and a spectral range of 350 nm was captured by the CCD detector with an effective spectral resolution of about 10 nm. The CCD was preceded with a gated and intensified microchannel plate, which was controlled by a digital delay generator. Using a system computer, the gate, typically set to 40 ns, would be successively delayed to accept signal from a selected range, e.g. from a selected depth interval. Frequently, the gate was left to let the system record the dominating LIF signal from the first few meters, e.g. when studying the spatial variation of the fluorescence in different areas of the Mediterranean Sea. Sometimes the delay generator was instead programmed to successively move the gate forward in 4 m intervals down to 20 m depth. Normally, 600 laser shots were integrated in each measurement before the gate was moved. The system could also be used to record the fluorescence spectra from plants

extracted from the sea, mostly *Posidonia Oceanica*. The plant samples were then placed on a surface of non-fluorescing material that was introduced into the laser beam above the upper end of the protecting tube shown in Fig. 2b.

2.3. Nd:YAG-based lidar system with PMT array detection

The time-resolving Nd:YAG laser system operating with a photomultiplier tube (PMT) array, named FLIDAR-N, was developed under contract of the Italian Ministry for the University and Scientific Research (MIUR). The system is described in [10] and here only a brief description will be given.

The FLIDAR-N has been specifically developed at CNR-IFAc to operate autonomously from ships of opportunity (such as ferries) for the monitoring of the marine environment. In the design criteria, particular attention has been paid to its reliability and ease of maintenance in view of this future employment. Fig. 7 gives a general description of the optical and electronic lay-out. The excitation source is a frequency-tripled commercial Nd:YAG laser (Continuum, Minilite II) emitting at 355 nm with a typical pulse energy of 8 mJ. The pulse repetition rate can be varied from 1 to 15 Hz. The collecting system consists of a 380-mm focal length modified Newtonian telescope having a diameter of 100 mm. The telescope output is connected via an optical fibre bundle to a spectrometer coupled to a 32-channel PMT array detector. The output channels are time-resolved by using a 500-MHz bandwidth 8-bit oscilloscope (Tektronics TDS-520). Control electronics drive the excitation source, data acquisition and storing. The whole system is controlled via a personal computer.

Fig. 3 shows a picture of the system as it was arranged in the front part of the ship. The system was installed on the upper deck of the ship and a mirror, installed at the bow of the ship, was used to deflect the laser beam into the water column. In this way the investigated area was not spoiled by the ship that could affect the measurements because of water mixing.

The FLIDAR-N operated autonomously from August 23-26, 2000 and particularly during August 25, 2000 when a set of data was acquired every 2 minutes. Each set of data consisted of a depth-resolved set of spectra, each spectrum having 32 channels uniformly distributed from 400 to 700 nm and being acquired every 2 ns along the water column.

3. Field measurements

Field measurements included a survey of the mixing zone east of Sardinia coast for the detection of water discontinuities based on the measurement of DOM content and its comparison with passive data from the NOAA AVHRR Band 4 that relates well to the Sea Surface Temperature (SST). Water column assessment by LIF measurements was performed in several areas with different sea water features. Experiments included measurements on *Posidonia Oceanica* samples. Depth-resolved data were also recorded. Both DOM and chlorophyll data were always normalised to the water Raman signal intensity in order to take into account the penetration depth of the laser beam into the water column [11].

3.1 Active-passive data integration

The ship route was selected to cross the mixing zone in front of the Bonifacio Strait where marine fronts could be encountered. In order to select the most appropriate route east of the Sardinia coast the NOAA 12-AVHRR imagery were used. In particular, the SST images were used to identify marine fronts since the latter have proven to be well related to sea surface temperature discontinuities [12].

Reception and processing of the NOAA 12-AVHRR imagery were carried out at the CNR-IFAc in Florence. As an AVHRR image was received at the CNR-IFAc station, it was geo-referenced and processed to produce an SST map of the Tyrrhenian Sea and then downloaded to the ship via a TCP/IP network connection.

The AVHRR sensors are installed on board the NOAA-12 and NOAA-14 satellites. Each satellite performs an acquisition every 12 hours, that is a potential 6-hour periodic monitoring of the investigated area. The coverage width is about 2700 km, with a 1.1 km spatial resolution at the sub-satellite point and with 10 bits radiometric resolution.

The AVHRR radiometer acquires images in five spectral bands [13]. Band 1 and Band 2 are in the visible/near infrared (0.58-0.68 μm and 0.725-1.1 μm , respectively) and are mainly affected by reflection processes. Band 1 relates to Suspended Sediment Concentration (SSC), while Band 2 is influenced by the chlorophyll concentration. Band 3 is in the middle infrared (3.55-3.93 μm) and is affected both by reflection and emission processes. Band 4 and Band 5 in the thermal infrared (10.5-11.5 μm and 11.5-12.5 μm , respectively) are affected by the emission process and related to SST.

Fig. 8 shows two grey-scale colour maps of the Band 4 of the AVHRR sensor pertaining to August 12 and 13, 2000 (map (a) and (b) in the figure, respectively). Lighter colours correspond to higher AVHRR band 4 intensities and consequently to higher temperatures. The route followed by the ship on August 13, 2000 is reported in the map (b) as a continuous line. Unfortunately, the AVHRR Band 4 image relative to the day when measurements were acquired (map (b) in the figure) features the presence of several clouds along the track followed by the ship. The effect of the presence of clouds is clear in the AVHRR data reported in Fig. 9.

Fig. 9 shows data along the route of the ship. The relevant route is shown as a continuous line in map (b) of Fig. 8. Data reported in Fig. 9 refer to: a) DOM-to-Raman ratio for 308-nm excitation obtained with the FLIDAR-3 operating from ship from 22:30 GMT of August 12, 2000 to 04:30 GMT of August 14, 2000, b) intensities of the NOAA AVHRR band 4 relative to August 13, 2000 (03:44 GMT), and c) intensities of the NOAA AVHRR band 4 relative to August 12, 2000 (04:42 GMT). Measurements were mainly acquired along two differently-oriented tracks: the former was east of Sardinia (in front of the Olbia port) near the mixing zone due to the Bonifacio Strait; the latter was the route towards the Ustica Island in the Southern Tyrrhenian Sea. The route followed by the ship in the former area was characterised by a low variability of SST that did not point out the presence of any marine front along the track. This feature was common to both the images relative to August 12 and 13, 2000. DOM-to-Raman ratios relative to the same track are not correlated to the SST data, but show a local variability. The spatial distribution in this area of the DOM values is shown in Fig. 10b together with the route followed by the ship (Fig. 10a). Lighter colours indicate higher DOM content. Their distribution points out a 'patch' of higher DOM values in a limited area. The reason why the DOM data vary in this area that shows very small SST variations needs further investigation and is not the object of this work. The SST map of August 13, 2000 is characterised by many clouds as pointed out by the high variability of the data along the route followed by the ship in the latter area (last part of curve (b) in Fig. 9). DOM-to-

Raman ratios acquired along the track were compared with the intensities of AVHRR Band 4 along the same route relative to the previous day, August 12, 2000 (curve (c) in Fig. 9). The data show some correlation with the DOM-to-Raman ratios confirming the usefulness of AVHRR imagery also for planning oceanographic campaigns for the detection of water discontinuities. A regression line of DOM-to-Raman ratios versus AVHRR Band 4 intensities relative to the route towards Ustica Island is shown in Fig. 11. In this plot data were normalised to their average.

The DOM-to-Raman data were also compared with the AVHRR Band 4 intensities obtained from the map relative to the August 13, 2000. A route slightly shifted with respect to that followed by the ship was selected on the map of the August 13, 2000 to avoid the effect of clouds. The 'shifted' route is marked with a dotted line in map (b) of Fig. 8.

Fig. 12 shows data for a) DOM-to Raman ratio for 308-nm excitation along the route shown in map (b) of Fig. 8 as a continuous line; b) NOAA AVHRR band 4 intensity, August 13, 2000, along the route followed by the ship and shown in map (b) of Fig. 8 as a continuous line; and c) NOAA AVHRR band 4 intensity, August 13, 2000, along the 'shifted' route and shown in map (b) of Fig. 8 as a dotted line. The comparison between curve (c) in Fig. 9 and curve (c) in Fig. 12 shows that the trend of SST data along the route towards Ustica Island was very similar. This area seemed to have more a constant trend with respect to the area in front of Olbia port where SST data changed significantly within 24 hours. A regression line of DOM-to-Raman ratios versus AVHRR Band 4 intensities relative to the 'shifted' route towards the Ustica Island is shown in Fig. 13. In this plot data were normalised to their average.

Typical LIF spectra as measured for 308-nm excitation are shown in Fig. 14: curve (a) refers to a spectrum taken in front of Olbia; curve (b) is a LIF spectrum obtained in the warmer waters along the route to the Ustica Island. Spectra were normalised to the water Raman signal intensity.

3.2 Water column measurements

Along track normalised data for DOM and Chlorophyll obtained with the FLIDAR-3 in the waters outside Catania harbour are shown in Fig. 15. The data were normalised to the intensity of the water Raman signal. Several transects were traced to and from the coast related to traverses of the volcanic plume from Mt Etna, simultaneously studied with the LTH system. This is pointed out in the figure which shows a dramatic increase of DOM and chlorophyll in areas close to the coastline. As an insert an individual spectrum is shown.

The dramatic change in water properties when the ship approached and entered the port of Civitavecchia is illustrated in Fig. 16, where data from the LTH fluorescence lidar system are shown. The DOM signal and the chlorophyll signal, in both cases normalized on the water Raman signal at 404 nm, are shown for the surface water in Fig. 16a and Fig. 16b, respectively. The very sharp increase in DOM as well as chlorophyll signals at 21:50 (GMT+2 hours) corresponds to the ship just passing the harbour piers and entering the basin. Both signals are again reduced shortly before the termination of the recording. This corresponds to the moments just before the ship at low speed was in the process of mooring to the quay. Inserts in the figures show examples of spectra on which the graphs are based. It was sometimes noticed that apart from the 690 nm chlorophyll peak in the fluorescence spectrum there was also a second peak at about 640 nm (see insert in Fig. 16a). This might be due to phycocyanine fluorescence emission as expected from

algae belonging to the *Cyanophyceae* group, but might also be due to some artificial aquatic tracer dye.

The LTH fluorosensor has the capability to also probe deeper layers of water using its time-gating capability. Such measurements were frequently performed. Examples of depth-gated spectra are shown in Fig. 17 for the depth intervals 0-4 m, 4-8 and 8-12 m. Clearly the signal intensity is quickly reduced. Gates below 12 m do not produce any signal. It is interesting to study changes in the spectral shape of water at different depths. In the interpretation of water spectra recorded for different depths it should be borne in mind that, even if the water properties are the same, there will be a change in the spectral shape recorded for deeper water, because of the self-filtering of the up-welling fluorescence light. It is well known, that oceanic water has its maximum transmission in the blue-green spectral region with increasing absorption towards both the UV and red spectral regions. Also, the wavelength of highest transmission moves strongly towards the red region with simultaneous strong transmission reduction for coastal/harbour waters [14]. Fig. 18 shows a demonstration of this fact. Here the influence of the water absorption is observable when averaged spectra from 4-8 m depth are divided by averaged spectra from 0-4 m. The recordings were made in the Favignana region west of Sicily. It should be noted that the surface layer of the sea could be influenced by mineral oils or other surface films which would change the spectral profile and also prevent the excitation beam from penetrating deep. An oil film would be manifested in the absence of a water Raman signal and the absence of a deeper layer fluorescence curve (the excited state lifetime of mineral oils is typically few ns). In the Favignana region we do not expect any influence of thin surface layers.

The FLIDAR-3 can also acquire high-spectrally resolved data by using a 2400 g/mm grating (see Routine 2 in Table 1). Such data of the water Raman signal were recorded in several measurement stations in the Southern Tyrrherian Sea to investigate water column temperature. The water Raman signal is due to the OH-stretch Raman mode of the water molecule and is sensitive to temperature variations [15]. Fig. 19 shows high spectral resolution water spectra, normalised to their area. Curve (a) refers to a Raman spectrum recorded near Ustica Island and curve (b) is a Raman spectrum taken in the open sea in front of Catania. During the measurement, water column temperature profiles were recorded with *in situ* standard measurements. The temperature averaged over a 7-m deep column was 28.2°C for the Ustica Island station and 26.9°C for the Catania station. As expected, when the temperature increases, the Raman signal at higher wavenumbers increases while that at lower wavenumbers decreases. The variation of the ratio, obtained by dividing the intensity integral between 3400-3700 cm^{-1} by that between 3100-3400 cm^{-1} for each of the two spectra, is about 1.8% and is comparable with the values found during lab experiments [16,17].

The SALE-3 campaign was also used for testing the prototype of the time-resolving fluorosensor, the FLIDAR-N. Fig. 20 shows an example of a data set taken off the coast in front of Catania with the FLIDAR-N for 355 nm excitation. The data feature both spectral and temporal resolution along the water column. The water Raman signal is superimposed on that of the DOM and can be depth-resolved down to about 7 m. A weaker fluorescence band at 680 nm, shown as an insert in the figure, indicates the presence of chlorophyll whose contribution is limited to the first water layer.

3.3 Posidonia measurements

Posidonia Oceanica Del. is a marine phanerogam plant, endemic to the Mediterranean Sea, that grows at depths not larger than around 40 m. It forms large meadows that

represent the most important ecosystem in the Mediterranean Sea. This plant is an important source of oxygen, a prevention factor for coastal erosion and a protection as well as a nursery area for many fish and invertebrate species. In addition, it has a primary role in the ecology of the Mediterranean basin, being one of the most important contributors to coastal primary production [18].

The prospect of a non-intrusive remote monitoring of these plants by LIF technique is therefore very attractive also because fluorescence could provide information about their physiological status. In this context some lidar experiments have been carried out in the laboratory on collected samples [19].

During the measurements in the Favignana area with rich *Posidonia Oceanica* sea floor colonisations it was eagerly attempted to capture its fluorescence *in situ* in time-gated recordings with the LTH system, corresponding to gating to the sea floor position. Such spectra would be a major motivation for a range-gated fluorosensor. The attempts were not successful due to the fact that the system depth range was limited, and, for safety reasons, the Captain could not sail the large ship to shallower waters than 13 m. From Fig. 17 it is clear that it is unlikely that a bottom fluorescence echo signal would be obtainable. From the signal-to-noise ratio in recordings such as in Fig. 17 it could be inferred that bottom spectra would be recordable for a depth lower than 10 m. Such measurements could easily be performed from a smaller ship or a towed barge, and would be an interesting aspect for a future measurement campaign. However, it should be borne in mind, that chlorophyll signals would be strongly attenuated by the increasing water absorption in the red spectral region (Fig. 18).

Fluorescence spectra for *Posidonia Oceanica* were instead recorded on plants extracted from the sea floor by divers. An arrangement of *Posidonia* leaves, all turned the same way and aligned with a common root position, is shown in Fig. 21 together with fluorescence spectra obtained with 355, 308 and 480 nm excitations. Spectra (a), (b) and (c) were recorded for different positions from the root with the 355 nm excitation by bringing the arrangement into the laser beam before it entered the water, as discussed above. Spectra (d), (e) and (f) were obtained on the same *Posidonia* samples for different positions from the root with the 308 and 480 nm excitations by placing the leaves over a panel of non-fluorescent material under the folding mirror (Fig. 2a) before the laser beam entered the water. It can be seen that the spectral signature changes considerably as a function of the position from the root both for the 308 and the 355 nm excitations, and a remote, seafloor *in situ* monitoring would see an effective mean spectrum, which might still contain valuable information on the status of the plants. In addition, the blue fluorescence band is usually higher, with respect to the red fluorescence band, for the 355 nm excitation than for the 308 nm one. This can be due to the fact that the NADPH, which significantly contributes to the blue fluorescence band, has a considerably higher molar absorptivity at 355 nm than at 308 nm [20].

Fig. 22 shows *Posidonia* fluorescence spectra recorded for 308 nm excitation on samples collected at around 15-m and 4-m depths (curve (a) and (b), respectively). The samples from 15-m depth were collected by using a grab sampler. These spectra were obtained averaging over 20 different leaf samples. For each sample spectra referring to the apical, distal and basal parts of the leaf were recorded. As it can be noticed from the figure, the samples from deeper waters (curve (a)) show a distinctive fluorescence peak at 575 nm, which is characteristic of an accessory pigment, the phycoerythrin, and a higher chlorophyll fluorescence band than that for the 4-m depth samples. The phycoerythrin is contained in the epiphytic algae that are mostly present on the apical part of the leaves. In general, samples from deeper waters showed a more extensive colonisation of epiphytic algae, as pointed out by the phycoerythrin fluorescence peak in curve (a). A higher

chlorophyll fluorescence intensity for the leaves from 15-m depth with respect to the blue-green fluorescence band can be due to the fact that plants living in deeper waters need a higher content of chlorophyll.

4. Conclusions

Three different fluorosensors were evaluated during the SALE-3 campaign allowing for a valuable integration/intercomparison of the results. The integration of lidar data from different fluorosensors was fruitful for the investigation of particular ecosystems, such as the *Posidonia Oceanica* meadows, where different excitation wavelength capability offered further advantages for the study of the sea floor vegetation. Actually, a key aspect of remote sensing experiments is the possibility of investigating sea bottom vegetation directly in the field rather than in the lab where it is extremely difficult to reproduce the proper environmental conditions. The results in the field, however, pointed out that an improvement of the signal-to-noise ratio is needed for an effective monitoring of sea floor vegetation, or that recording depths must not exceed 10 m. A main difficulty is that the optical absorption of water strongly attenuates vegetation fluorescence in the red spectral region.

The operation of the fluorosensors in autonomous mode was tested extensively showing good prospects for the use on ships of opportunity that would make lidar monitoring more effective and extensive, providing a massive data set of sea truth data. This would also be useful for satellite passive data integration.

Acknowledgements

This research was supported by the Italian National Research Council “Commissioni Navi” that provided the R/V *Urania* and by the Italian Ministry for the University and Scientific Research (MIUR) that supported the development of the fluorosensor FLIDAR-N under an ENEA-MIUR contract. The Swedish participation was supported by the Swedish Research Council and the K. and A. Wallenberg Foundation.

The authors wish to thank the commander of *Urania*, Capt. Emanuele Gentile and all the crew for their kind assistance and collaboration during the whole campaign.

References

1. P. Weibring, J. Swartling, H. Edner, S. Svanberg, T. Caltabiano, D. Condarelli, G. Cecchi, L. Pantani, "Optical monitoring of volcanic sulphur dioxide emissions - comparison between four different remote sensing techniques", *Optics and Lasers in Engineering* **37**, 267 (2002).
2. G. Cecchi, P. Mazzinghi, L. Pantani, R. Valentini, D. Tirelli, P. de Angelis, "Remote sensing of chlorophyll fluorescence on vegetation canopies: 1. Near and far field measurement techniques", *Rem. Sens. of Environ.* **47**, 18-28 (1994).
3. G. Cecchi, L. Pantani, B. Breschi, D. Tirelli, G. Valmori, "FLIDAR: a multipurpose fluorosensor-spectrometer", *EARSeL Advances in Remote Sensing* **1**, 72-78 (1992).
4. G. Cecchi, M. Bazzani, L. Pantani, V. Raimondi, "Lidar monitoring of Tyrrhenian and Northern Adriatic Seas", in *Laser in Remote Sensing*, C. Werner & W. Waidelich Eds., 101-104, Springer Verlag, Berlin (1993).
5. H. Edner, K. Fredriksson, A. Sunesson, S. Svanberg, L. Unéus, W. Wendt, "Mobile remote sensing system for atmospheric monitoring", *Appl. Opt.* **26**, 4330-4338 (1987).
6. P. Weibring, M. Andersson, H. Edner, S. Svanberg, "Remote monitoring of industrial emissions by combination of lidar and plume velocity measurements", *Appl. Phys. B* **66**, 383-388 (1998).
7. H. Edner, J. Johansson, S. Svanberg, E. Wallinder, G. Cecchi, L. Pantani, "Fluorescence lidar monitoring of Arno river", *EARSeL Advances in Remote Sensing* **1**, 42-45 (1992).
8. L. Alberotanza, P.L. Cova, S. Vianello, M. Bazzani, G. Cecchi, L. Pantani, V. Raimondi, P. Ragnarson, S. Svanberg, E. Wallinder, "Yellow substance and chlorophyll monitoring in the Venice Lagoon using remote laser-induced fluorescence", *EARSeL Advances in Remote Sensing* **3**, 102-111 (1995).
9. P. Weibring, H. Edner, S. Svanberg, Versatile mobile lidar system for environmental monitoring, Submitted to *Appl. Optics*.
10. G. Cecchi, I. Mochi, D. Lognoli, V. Raimondi, B. Breschi, D. Novelli, "Compact fluorescence lidar system with time resolution for the monitoring of marine environment", to appear.
11. M. Bristow, D. Nielsen, D. Bundy, R. Furtek, "Use of water Raman emission to correct airborne laser fluorosensor data for effects of water optical attenuation", *Appl. Opt.* **20**, 2889-2906 (1981).
12. M. Bazzani, R. Carlà, G. Cecchi, F. Meiners, L. Pantani, D. Tirelli, G. Valmori, "Remote sensing of coastal waters: the IROE activity in the PRISMA Project", in: *Earth Surface Remote Sensing II*, G. Cecchi and E. Zilioli Eds., *Proc. SPIE* **3496**, 166-174 (1998).
13. I.S. Robinson Ed., *Satellite Oceanography*, John Wiley and Sons, pp. 194-246 (1995).
14. N.J. Jerlov, *Optical Oceanography* (Elsevier, Amsterdam 1968).

15. G. E. Walrafen, M. R. Fisher, M. S. Hokmabadi, W. H. Yang, "Temperature dependence of the low- and high-frequency Raman scattering from liquid water", *J. Chem. Phys.* **85**, 6970-6982 (1986).
16. B. Breschi, G. Cecchi, L. Pantani, V. Raimondi, D. Tirelli, G. Valmori, P. Mazzinghi, M. Zoppi, "Measurement of water column temperature by Raman scattering", *EARSel Advances in Remote Sensing* **1**, 131-134 (1992).
17. G. Cecchi, V. Raimondi, "High spectral resolution lidar experiments for the monitoring of water column temperature", in *Remote Sensing of Vegetation and Sea*, G. Cecchi, G. D'Urso, E.T. Engman and P. Gudmandsen Eds., *Proc. SPIE* **2959**, 208-215 (1996).
18. D. Bay, "A field study of the growth dynamics and productivity of *Posidonia Oceanica* (L.) Delile in Calvi Bay, Corsica", *Aquat. Bot.* **20**, 43-64 (1984).
19. G. Cecchi, M. Kim, M. Bazzani, E. Maserti, J. McMurtrey, E. Chappelle, D. Tirelli, "Fluorescence responses of Mediterranean sea grass *Posidonia Oceanica*: summer 1997 ATOM-LIFT campaign", in *Advances in Laser Remote Sensing for Terrestrial and Hydrographic Applications*, R.M. Narayanan and J.E. Kalshoven Eds., *Proc. SPIE* **3382**, 126-132 (1998).
20. Z.G. Cerovic, G. Samson, F. Morales, N. Tremblay, I. Moya, "Ultraviolet-induced fluorescence for plant monitoring: present state and prospects". *Agronomie* **19**, 543-578 (1999).

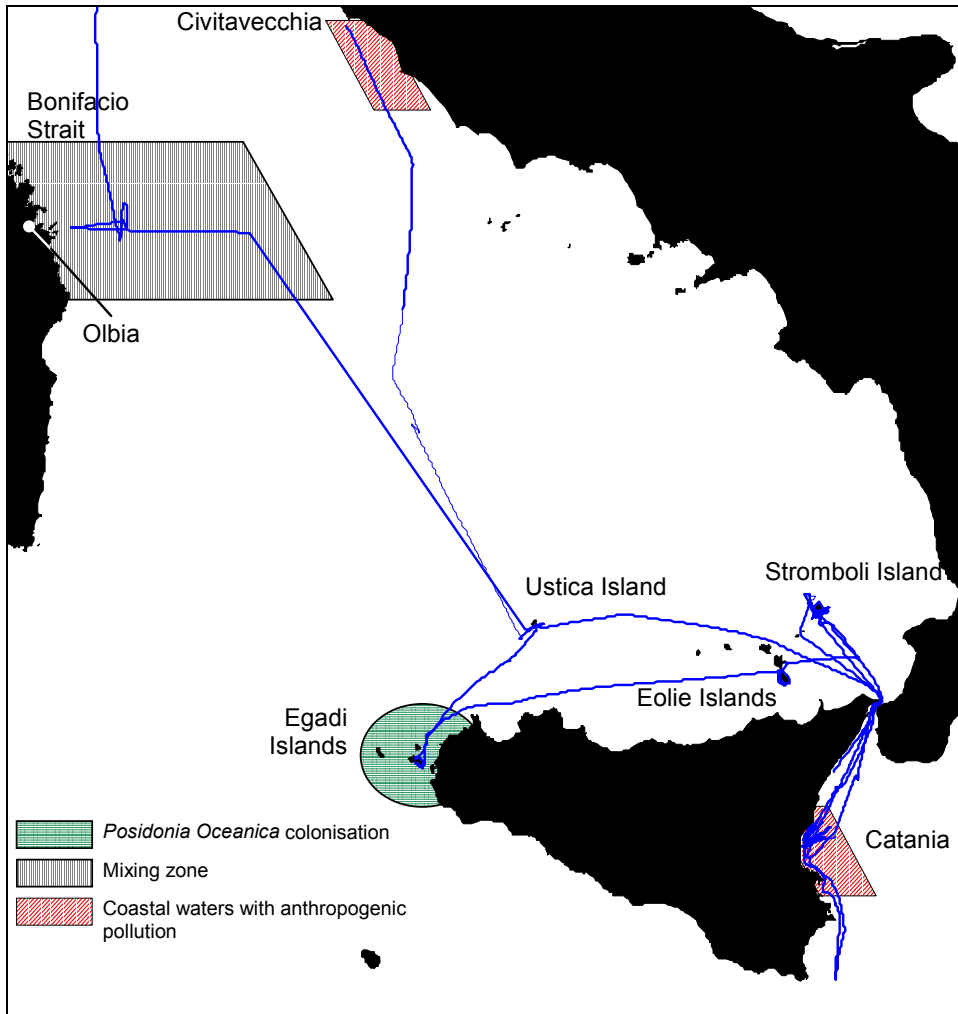
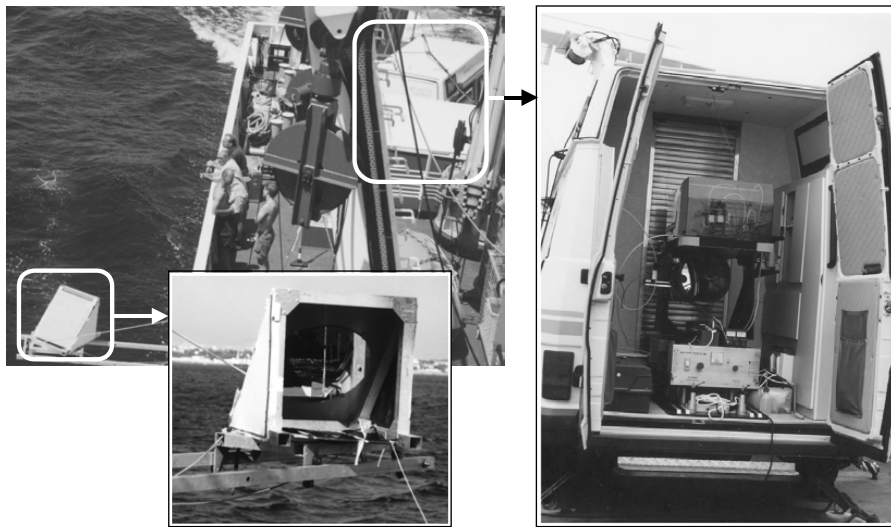
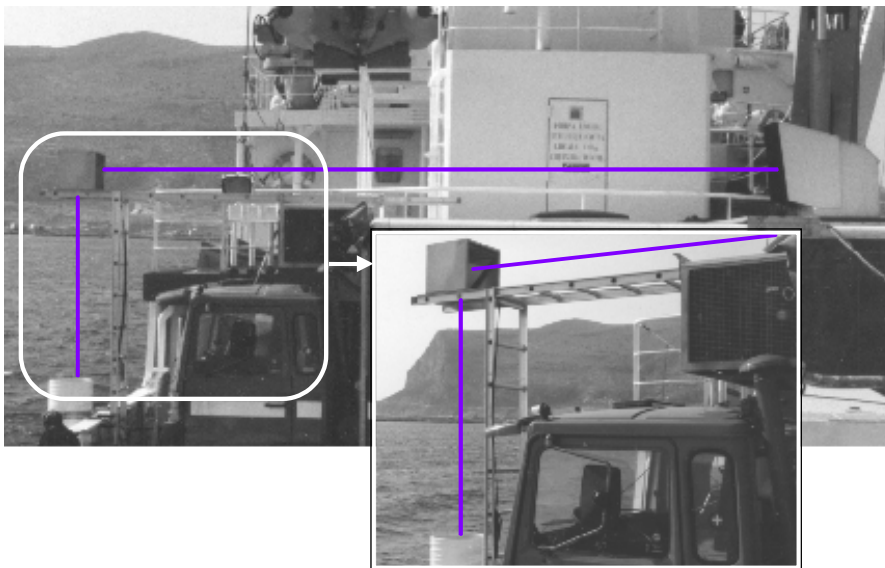


Fig. 1. Route of the R/V *Urania* during the SALE-3 oceanographic campaign in the Tyrrhenian Sea. Key areas are: (a) mixing zone east of Sardinia near the Bonifacio Strait; (b) Egadi Archipelago with colonisation of the *Posidonia Oceanica*; (c) Catania and Civitavecchia harbours.



(a)



(b)

Fig. 2. Photographs of the two mobile fluorescence lidar systems on the aft deck of the R/V *Urania*. Photo (a): CNR-IFAc mobile lidar system. The folding mirror, fixed at the railing of the ship, and a view of the van's rear section housing the optical sensor are shown in the inserts. Photo (b): LTH mobile lidar system. As an insert the folding mirror and the upper part of the protecting tube are shown.

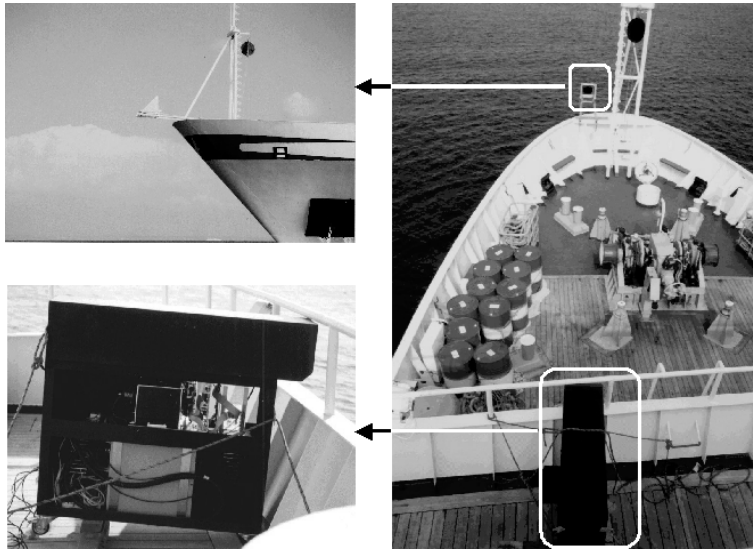


Fig. 3. Arrangement of the CNR-IFAc time-resolving fluorosensor in the front part of the oceanographic ship. A mirror fixed at the railing at bow of the ship was used to fold the laser beam into the water column.

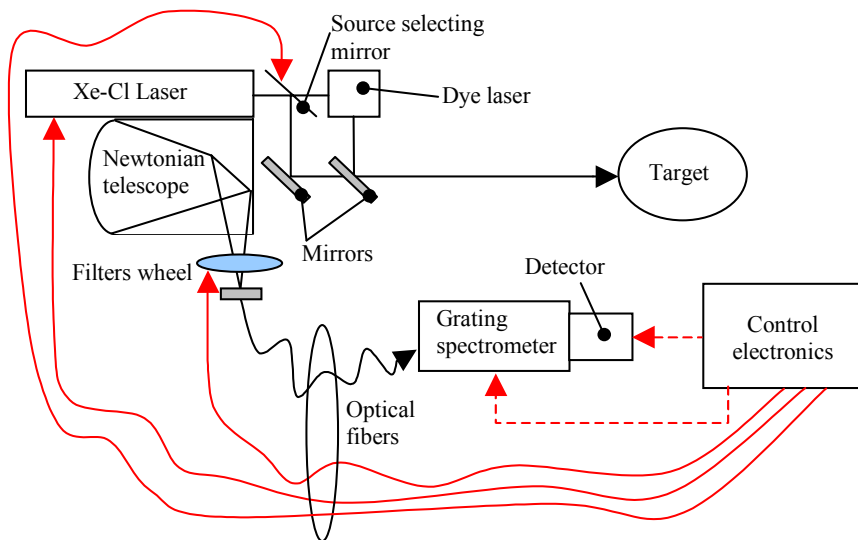


Fig. 4. Schematic optical and electronic arrangements for the CNR-IFAc mobile lidar system (FLIDAR-3).

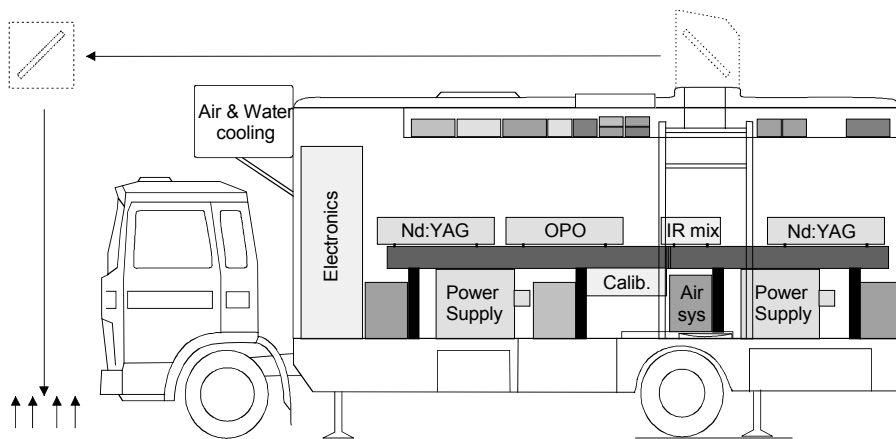


Fig. 5. Arrangement of the LTH mobile laser radar system adapted for marine monitoring.

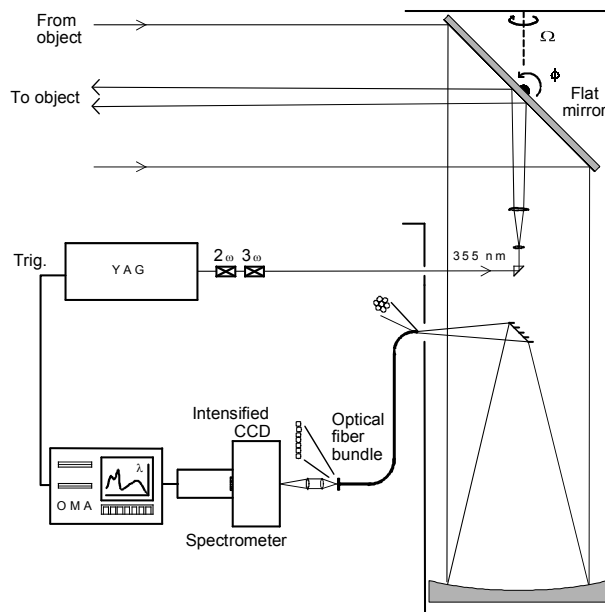


Fig. 6. Schematic optical and electronic arrangements for the LTH fluorosensor system.

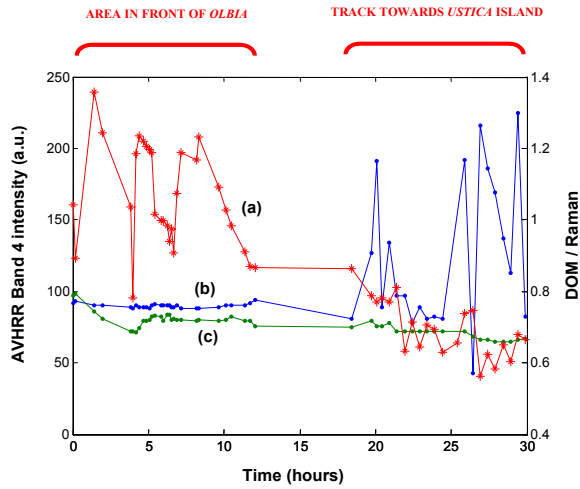


Fig. 9. Data along the route shown in Fig. 8 for: a) DOM-to-Raman ratio for 308-nm excitation obtained with the FLIDAR-3 related to August 13, 2000; b) NOAA AVHRR band 4 intensity, August 13, 2000; and c) NOAA AVHRR band 4 intensity, August 12, 2000.

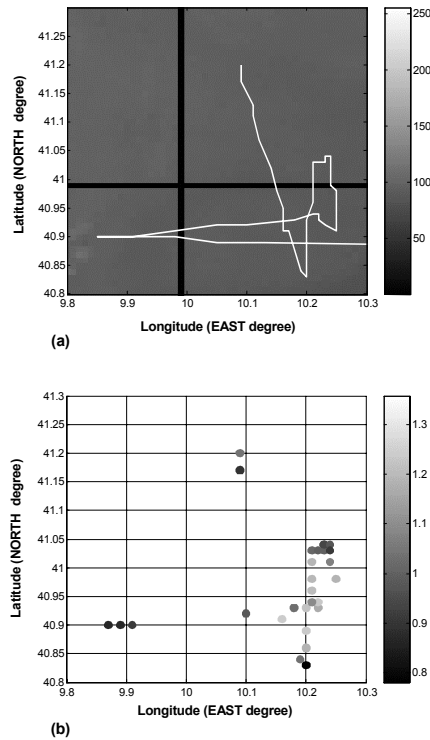


Fig. 10. (a) Route followed by the ship in the area east of Sardinia, in front of Olbia port; the route is superimposed to a zoom of the AVHRR Band-4 intensity image (August 13, 2000, 03:44 GMT); (b) spatial distribution of the DOM values in the area east of Sardinia, in front of Olbia port. DOM values are normalised to the water Raman intensity. Lighter colours stand for higher DOM values.

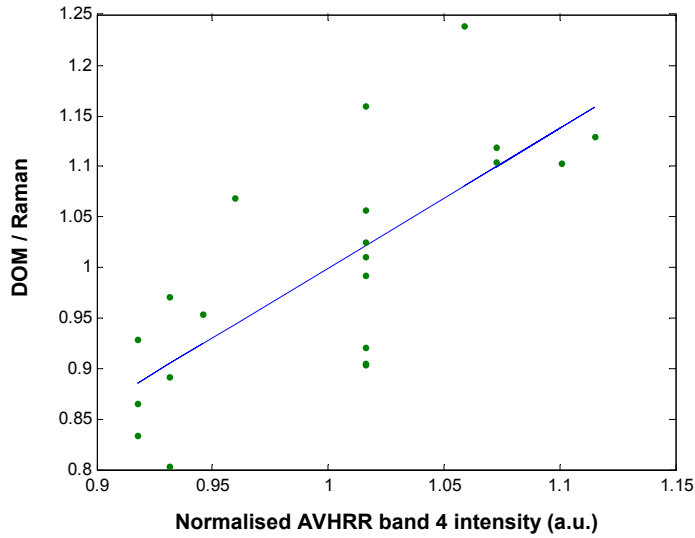


Fig. 11. Regression line for NOAA AVHRR band 4 intensities, relative to August 12, 2000, versus DOM-to-Raman ratios. Data were normalised to the average.

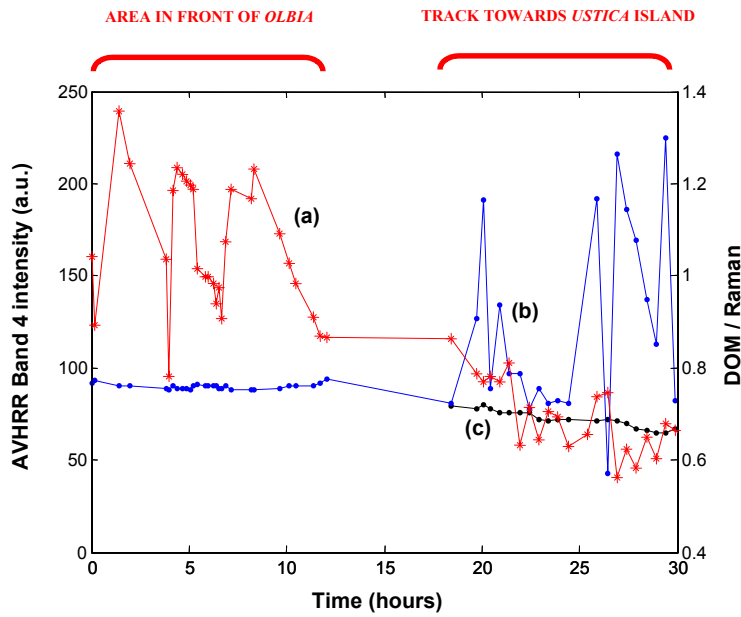


Fig. 12. Data for: a) DOM-to-Raman ratio for 308-nm excitation obtained with the FLIDAR-3 along the route shown in Fig. 8 on August 13, 2000; b) NOAA AVHRR band 4 intensity, August 13, 2000, along the route shown in Fig. 8; and c) NOAA AVHRR band 4 intensity, August 13, 2000, along a track shifted with respect to the ship route as shown in Fig. 8 (dotted line).

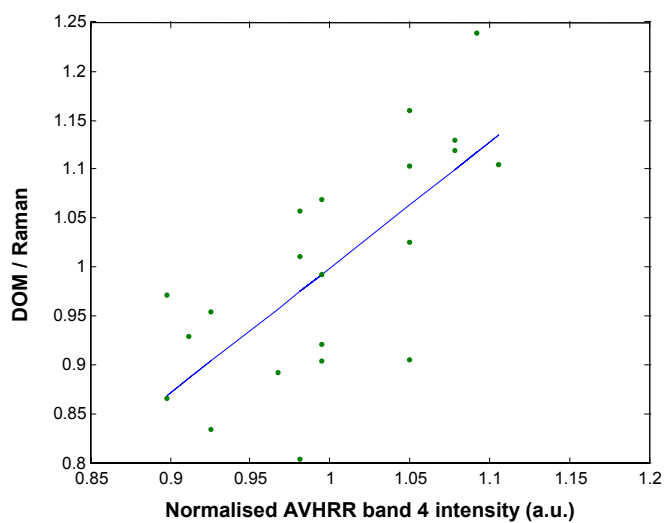


Fig. 13. Regression line for NOAA AVHRR band 4 intensities relative to August 13, 2000 along a shifted route (dotted line in map (b) of Fig. 8) versus DOM-to-Raman ratios. Data were normalised to the average.

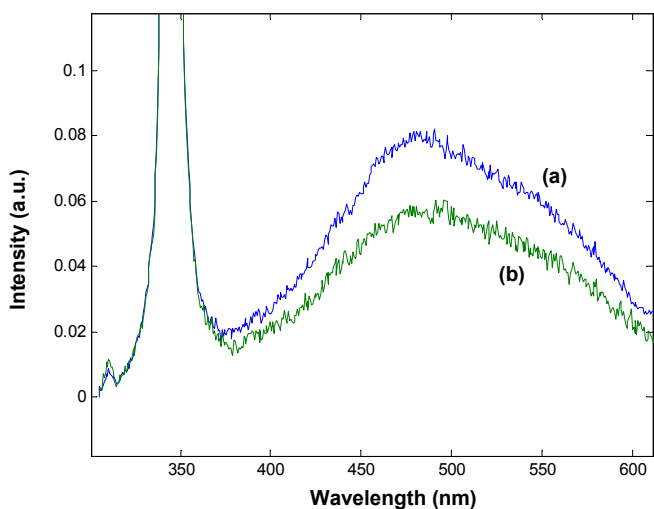


Fig. 14. Laser Induced Fluorescence spectra of DOM as measured for 308-nm excitation. a) DOM spectrum taken east of Sardinia, and b) DOM spectrum taken in the warmer area in the Central-Southern Tyrrhenian Sea. Spectra were normalised to the water Raman signal intensity.

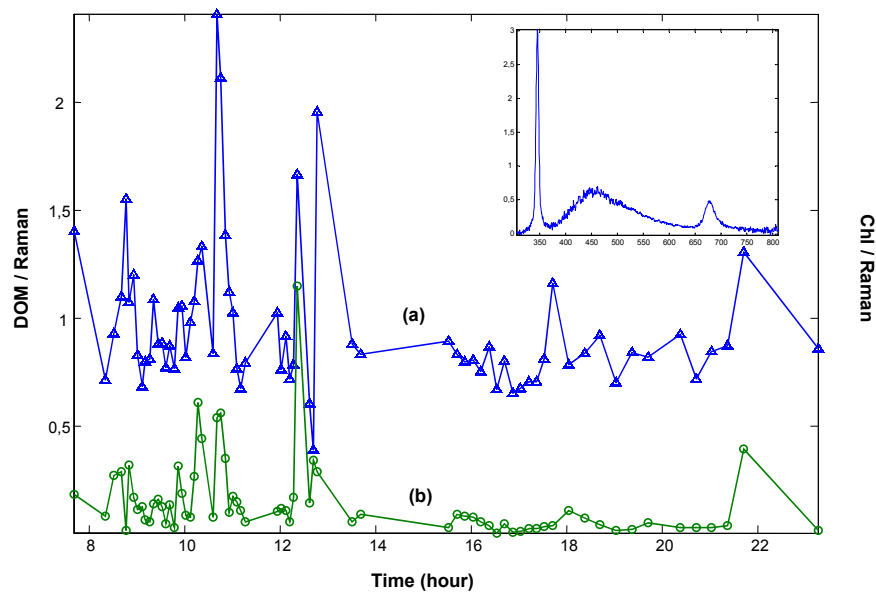


Fig. 15. Along track normalised data for DOM and Chlorophyll obtained with the 308-nm lidar system in the waters outside Catania. As an insert an individual spectrum is shown.'

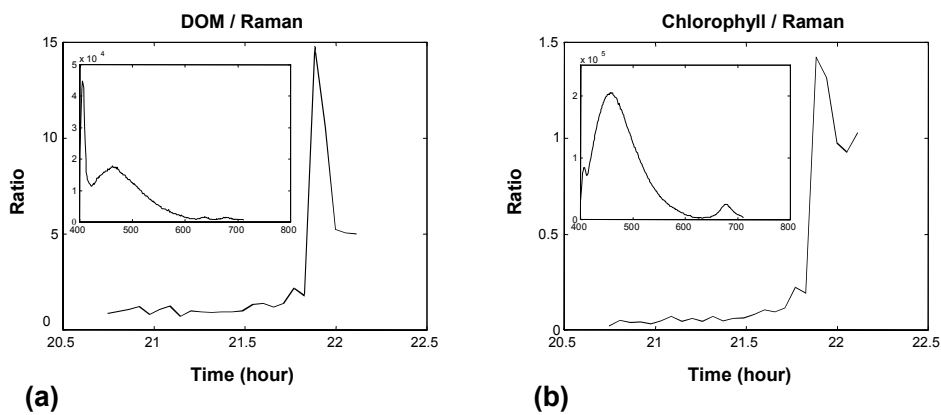


Fig. 16. Along track Raman normalised data for: (a) DOM and (b) Chlorophyll obtained with the LTH 355-nm fluorescence lidar as the ship is approaching the port of Civitavecchia. Data pertain to the dominating signal from the superficial water and are based on individual spectra as shown in the inserts.

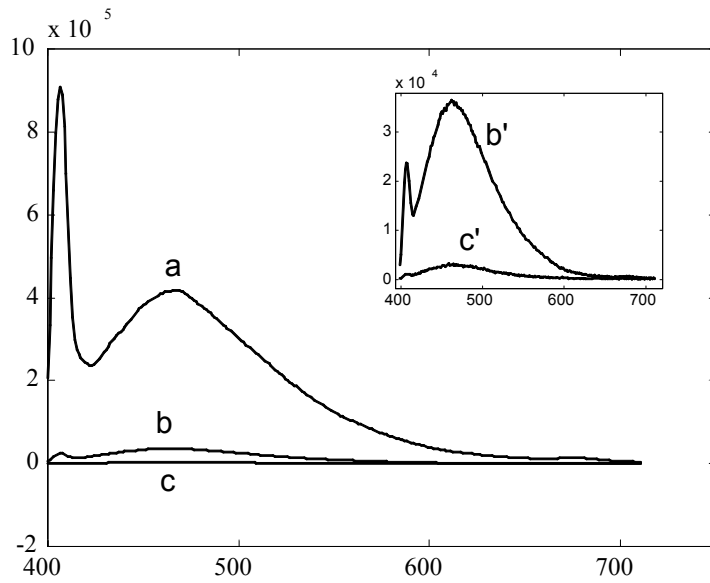


Fig. 17. Examples of depth-resolved water fluorescence signals recorded in waters around Favignana for: (a) 0-4 m, (b) 4-8 m, and (c) 8-12 m. Curves (b) and (c) are also shown magnified.

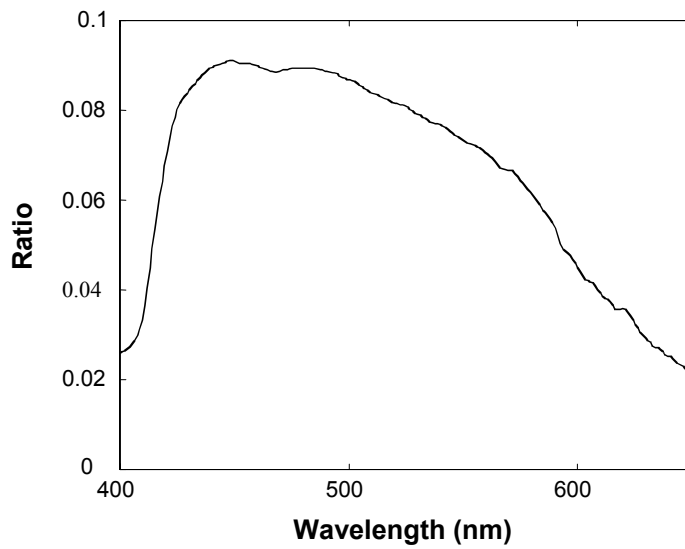


Fig. 18. Influence of the absorption of sea water as evidenced in a ratio curve of the fluorescence distribution at 4-8 m divided by the corresponding signal for 0-4 m.

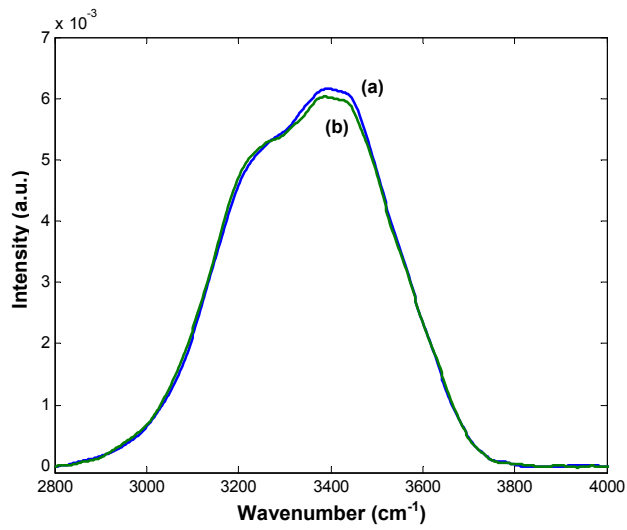


Fig. 19. Two high spectral resolution water Raman spectra obtained with the CNR-IFAc 308-nm system: (a) Raman spectrum taken near Ustica Island (water column temperature: 28.2°C), and (b) Raman spectrum taken on the open sea in front of Catania (water column temperature: 26.9°C). The water column temperature values refer to the average water temperature as measured with the ship temperature probe along a 7-m deep column.

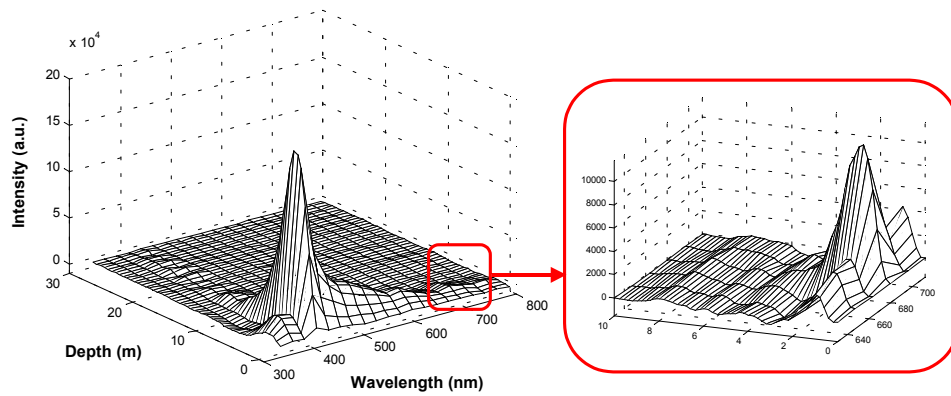


Fig. 20. Example of a single data set as acquired with the 355-nm range-resolving CNR-IFAc fluorosensor, the FLIDAR-N. As an insert a zoom with the chlorophyll fluorescence distribution along the water column is shown. Spectra are not corrected for water transmission.

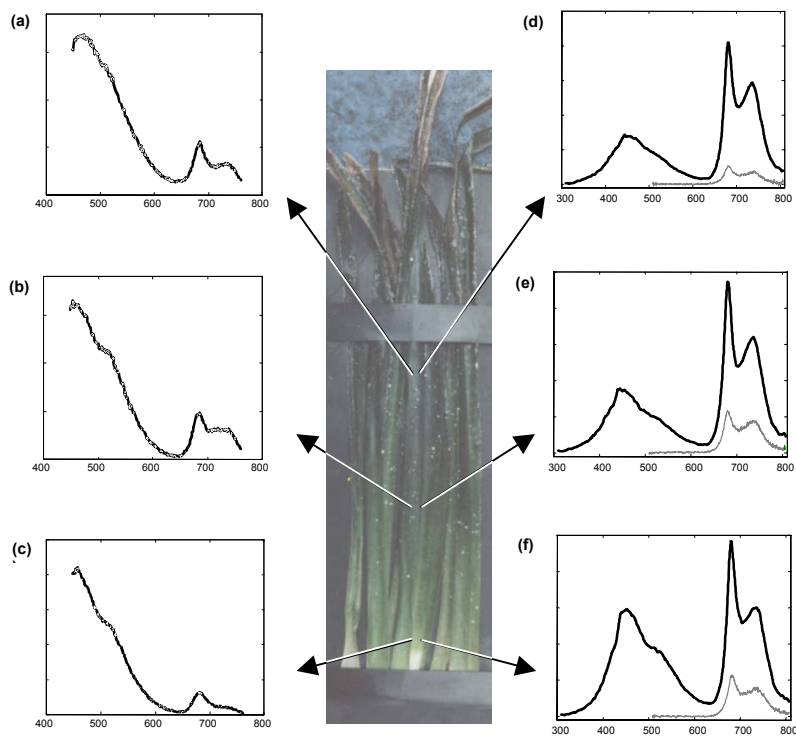


Fig. 21. Examples of Posidonia fluorescence spectra: (a), (b) and (c) were recorded with 355 nm excitation; (d), (e) and (f) were recorded with 308 nm and 480 nm excitations. Spectra from the lower, middle and top parts of the leaves are shown for each case.

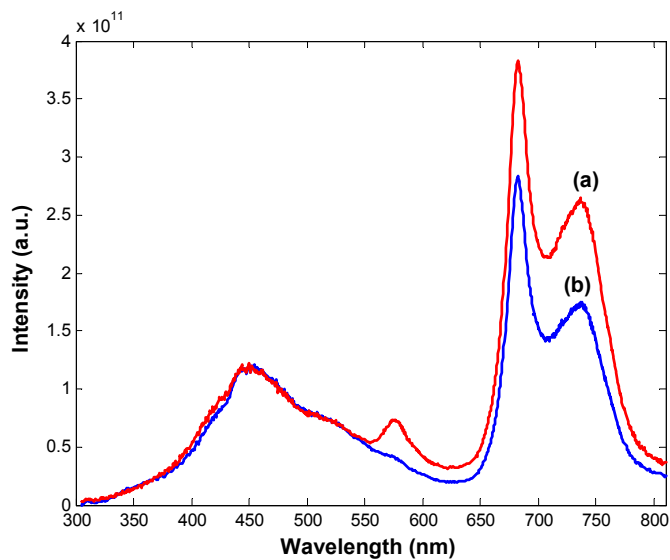


Fig. 22. Examples of Posidonia fluorescence spectra recorded for 308 nm excitation: (a) spectra obtained on samples collected at 15-m depth, and (b) spectra obtained on samples collected at 4-m depth.

Fluorescence lidar imaging of historical monuments

Petter Weibring, Thomas Johansson, Hans Edner, Sune Svanberg, Barbro Sundnér, Valentina Raimondi, Giovanna Cecchi, and Luca Pantani

What is believed to be the first fluorescence imaging of the facades of a historical building, which was accomplished with a scanning fluorescence lidar system, is reported. The mobile system was placed at a distance of ~60 m from the medieval Lund Cathedral (Sweden), and a 355-nm pulsed laser beam was swept over the stone facades row by row while spectrally resolved fluorescence signals of each measurement point were recorded. By multispectral image processing, either by formation of simple spectral-band ratios or by use of multivariate techniques, areas with different spectral signatures were classified. In particular, biological growth was observed and different stone types were distinguished. The technique can yield data for use in facade status assessment and restoration planning. © 2001 Optical Society of America

OCIS codes: 100.2960, 120.0280, 260.2510, 280.3640, 300.2530.

1. Introduction

Historical buildings constitute an important component of our cultural heritage. However, extensive control of their status and their conservation can often be troublesome and time-consuming tasks. From this point of view, the use of remote-sensing techniques may be an attractive method for quick and truly nondestructive monitoring of building surfaces. Color photography is one obvious approach; however, fluorescence techniques are known to be capable of revealing aspects that are not evident to the naked eye or to photography. The use of fluorescence in forensic science,¹ art inspection,² and tissue diagnostics³ is well known. All these applications are carried out in indoor, controlled environments, although sometimes competing background light, e.g., surgical lamps, make pulsed excitation and time-gated detection necessary.⁴

Fluorescence lidar techniques⁵ make it possible to

extend the application of fluorescence spectroscopy to the outdoor environment (remote sensing), where large distances and uncontrollable background light have to be dealt with. Point-monitoring fluorescence lidars have been used extensively for aquatic monitoring^{5–8} and for studies of terrestrial vegetation.^{9,10} More recently, the same techniques were used for point monitoring of stone facades of historical monuments.¹¹

The possibility of remote fluorescence imaging was demonstrated on plants and on parts of trees, the laser-illuminated scene was captured simultaneously in four spectral bands.^{12,13} This technique cannot be extended to large targets, at least not for a reasonable laser power, because of the competition between background daylight and the energy density of fluorescence light from the target. A push-broom type of lidar, in which the available excitation radiation is spread out as a horizontal streak, was also successfully developed. Fluorescence imaging at a distance of 50 m was demonstrated by scanning of a tree from its roots to the canopy.¹⁴

When even larger objects, such as buildings, are to be imaged in fluorescence, even the push-broom technique is not adequate, because spreading the laser light over too large a line produces unfavorable signal-to-background ratio conditions. In this case, a scanning technique seems to be the most suitable one. The laser beam is concentrated in a high-intensity spot on the target, which can be placed at a considerable distance from it and is observed by the receiving system with a narrow field of view. The received light can then be dispersed by a spectrome-

P. Weibring, Th. Johansson, H. Edner, and S. Svanberg (e-mail: sune.svanberg@fysik.lth.se) are with the Department of Physics, Lund Institute of Technology, P.O. Box 118, S-221 00 Lund, Sweden. B. Sundnér is with the Central Board for National Antiquities, S-114 84 Stockholm, Sweden. When this research was performed, V. Raimondi, G. Cecchi, and L. Pantani were with the Istituto di Ricerca sulle Onde Elettromagnetiche "Nello Carrara," Consiglio Nazionale delle Ricerche, Via Panciatichi 64, I-50127 Florence, Italy.

Received 7 March 2001; revised manuscript received 23 July 2001.

0003-6935/01/336111-10\$15.00/0

© 2001 Optical Society of America

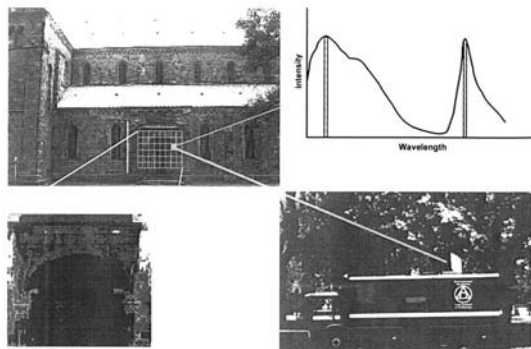


Fig. 1. Fluorescence lidar multispectral imaging at a historical building. Top left, photograph of the northern facade of the Lund Cathedral, with the portal area studied in the present research indicated. A specially selected vertical scan line is also indicated. Bottom right, photograph of the Swedish mobile lidar system during the fluorescence imaging measurements. Top right, single-point remote fluorescence spectrum for the facade. Filter bands are shown by hatched regions. Bottom left, fluorescence image of the $8\text{ m} \times 8\text{ m}$ marked area covering the northern portal. The image was recorded at 682 nm and displays biodeteriogen colonization.

ter and detected by a normal gated and intensified optical multichannel analyzer. With this procedure, a high signal-to-noise ratio can be obtained. If high spatial resolution is required, the scanning technique with a small laser spot on target requires quite a long recording time. This restriction poses no fundamental problems in building analysis because the targets are fixed ones.

A preliminary experiment was performed on a $1\text{ m} \times 1\text{ m}$ arrangement of stones of different origins that employs two fluorescence bands selected with interference filters and by photomultiplier detection.¹⁵ In the present paper, we report a fluorescence remote-sensing study of a large building, the medieval Lund Cathedral, by multispectral fluorescence techniques. It is believed that this is the first fluorescence multispectral imaging of a historic monument. The measurement method, including photographs of the northern facade of the cathedral and a fluorescence lidar system in measuring position, is shown in Fig. 1.

2. Experimental Techniques

A mobile lidar laboratory,^{16,17} which is adapted primarily for atmospheric monitoring by the differential absorption technique, was employed for the experiments. However, the system has a flexible design and previously was used in monitoring remote fluorescence.^{8,9,12-15,18} The optical and electronic configurations employed in the present experiments are shown in Fig. 2.

The fluorescence lidar transmitter was a frequency-tripled Nd:YAG laser generating radiation at 355 nm in 8-ns-long pulses at a repetition rate of 20 Hz. Typically the transmitted pulse energy was limited to 30 mJ in these experiments.

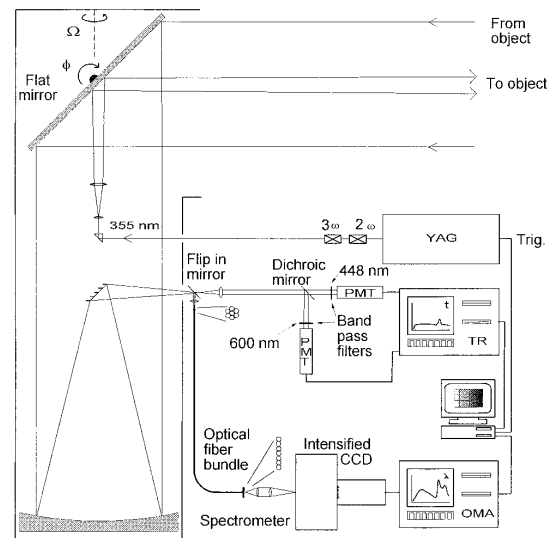


Fig. 2. Optical and electronic arrangement of the lidar system employed in measurements of the historic building. PMTs, photomultiplier tubes; OMA, optical multichannel analyzer; TR, transient digitizer.

The laser beam expander, which was coaxial with the receiving telescope, was normally adjusted to give an 8-cm-diameter laser spot on the target. For a typical distance of 60 m between the lidar and the target, the diameter of the image spot in the telescope focal plane was $\sim 1.3\text{ mm}$. A special fiber bundle, which contained seven individual fibers densely packed in a circle, captured the focal image spot. The bundle output was rearranged into a linear shape that matched the input slit of the spectrometer.

With the computer-controlled folding mirror the lidar was pointed at selected points for spectral data

collection or scanned row by row the facades for image generation. A signal integration of eight laser shots was normally used. Data storage and mirror advancement to the next measurement point took less than 1 s. Daytime measurements with high spectral resolution were possible through the detector time-gating technique with a 100-ns-wide gate set to open in coincidence with the arrival time of the fluorescence pulse.

Spectral calibration of the wavelength-resolved system was not performed. However, as we are interested mostly in differences in spectral signatures among different areas rather than in absolute shapes, and because some noise is introduced in the process, spectral correction was not implemented for the data presented in this paper.

3. Field Experiment

The Lund Cathedral, the largest Romanesque building in northern Europe, was constructed mostly in the early 12th century. However, it has been rebuilt several times. More recently, during the period 1833–1880 the cathedral was partly rebuilt and restored. The old western towers were replaced by the existing ones in the 1880s.

The main stone masonry consists of ashlar made from a dense quartzitic sandstone, quarried in the Höör area northeast of Lund. This sandstone is generally highly resistant to weathering. However, it undergoes a color change when it is exposed to the atmosphere, resulting in a thin black staining. The same sandstone was used as a building material in both in the 12th and the 19th centuries. There is, however, a difference: In the 19th century a harder and denser type was used. Certain areas of the exposed facade are made from sandstone quarried in the 12th century, whereas others are constructed with sandstone from the 19th century. In the renovations and reconstruction, older and newer stones have sometimes been mixed. The fundament was partly reconstructed with granite in the 19th century.

In connection with investigations of the building materials, damage to the stone material has also been examined. On the exterior walls of the cathedral, black staining, salt efflorescence, exfoliation, and biodeteriogen colonization (algae, lichens) have been investigated.^{19–21} This situation provides a challenge for testing fluorescence techniques for the determination of various biodeteriogens and stone types and their extension.

The one-week measurement campaign was held in late October 1997. The weather was unsettled, with occasional snowfall and temperatures a few degrees above freezing. Inasmuch as the laser-beam scans frequently started at ground level, the measurement area was blocked off. It should be noted that with an 8-cm laser spot size on target the 355-nm beam is eye safe according to current regulations.

Most measurements were concentrated on the northern portal, but also other parts of the building, such as the upper walls and the towers, were studied. The area close to the northern portal is shown in Fig.

1, together with a point fluorescence spectrum and a fluorescence image of the portal area (marked in the photo) recorded through a 682-nm filter. The positioning of the lidar at a minimum distance of 60 m from the northern facade gave the laser beam access to all the areas under investigation without serious geometrical distortion of the detected images.

4. Measurements and Analysis

Spectra of laser-induced fluorescence pertaining to stone and mineral samples were discussed previously.^{11,15,22–24} In this experiment three measurement modes were employed. First, single-point spectra were detected on different stone types and different biodeteriogens, in parallel with visual identification. A spectral library was built with these spectra and used for identification purposes in later measurements. In the second mode, vertical and horizontal scans, recording high-resolution spectra, were performed on the upper and side parts of the northern portal and on other parts of the facades.

In the last mode, fluorescence images were acquired by use of either the band filters or the spectrometer system. At the northern portal of the cathedral, an area of 8 m × 8 m was investigated in detail. Both a two-wavelength image and a high-spectral-resolution image, each one containing 6400 pixels, were acquired during 2-h-long runs. The images show different stone types and occasional biodeteriogen colonization. Unfortunately, exact records of the positions of the biological samples collected for analysis were not noted, and this complicates unambiguous biological identification of the recorded fluorescence images.

A. Point Monitoring

Point monitoring was performed at the northern portal, at some of the northern facade pilasters, and at other individual points. An observer, close to the facade, selected the measurement points and by radio communication directed the lidar operator, who activated the stepping motors of the steering mirror to bring the laser beam into position. Each motor step resulted in a position shift on the target of ~0.4 cm horizontally and ~1.1 cm vertically.

The northern portal is shown enlarged in Fig. 3, with some examples of fluorescence spectra at selected positions. Spectral signatures of different types of surface can be identified. The three spectra at the left belong to sandstones. The lowest of these spectra corresponds to a comparatively clean 19th-century stone; the middle one originates from a stone with a thin layer of biodeteriogens not distinguishable by visual inspection. This spectrum is clearly distinguished from that of the clean stone by the chlorophyll fluorescence in the red. The top left spectrum corresponds to sandstone covered by a dark crust. The spectrum at the center right of the picture shows the spectral signature from a stone with a stronger red signal. At this location it was also possible to identify biodeteriogen colonization with the naked eye. This comparison already confirms²⁵ the

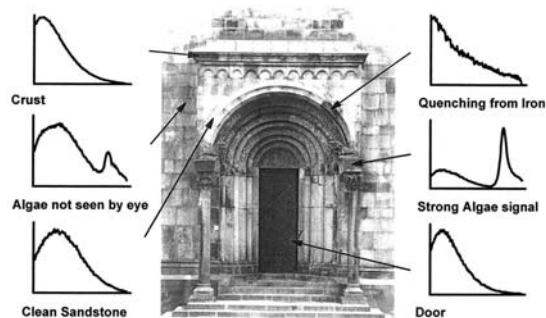


Fig. 3. Photograph of the northern portal and representative remotely recorded point-monitoring fluorescence spectra. The spectra are normalized in intensity and are shown for wavelengths from 440 to 740 nm.

capabilities of the fluorescence technique for the early identification, mapping, and control of biodeteriogen colonization. At the upper right of Fig. 3 the spectral signature of sandstone with rust on its surface is shown. The rust is due to a protruding iron bar, positioned for wall reinforcement. The fluorescence from the sandstone is quenched here by the iron

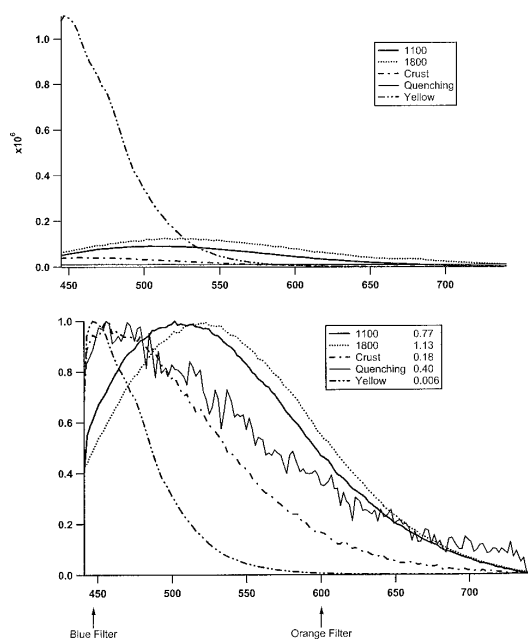


Fig. 4. Point-monitoring spectra of different types of stone in the cathedral facade. The spectra were recorded by accumulation of 20 shots at 60-m distance. Spectra are given with the detected intensities (top) and normalized to their maximum value (bottom). The generic spectral shapes of 12th- and 19th-century sandstone, stones with a crust, stones affected by quenching rust (iron ions), and a rarely occurring yellowish facade stone are given. In the normalized spectra, the intensity ratios for the signal levels at the orange (600-nm) and the blue (448-nm) filters used are also given.

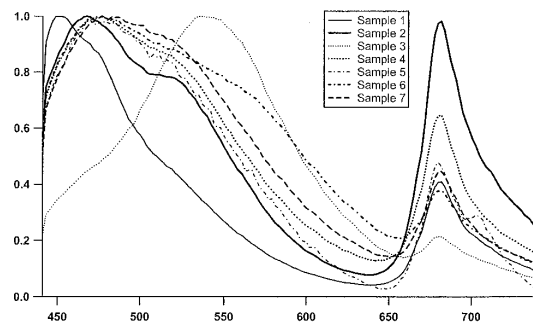


Fig. 5. Point monitoring spectra of different types of biodeteriogen colonization on the cathedral facade. The spectra were recorded by accumulation of 20 laser shots at 60-m distance and are intensity normalized.

ions,²⁶ giving a clear fingerprint of the facade areas influenced by the presence of iron. Figure 3 also includes the signature of the black-painted wooden door at the lower right.

A more systematic study of the different types of stone and biodeteriogen spectra is presented in Figs. 4 and 5. Figure 4 displays laser-induced fluorescence spectra of two different types of reasonably clean sandstone, of sandstone with a dark crust, of iron-quenched sandstone fluorescence, and finally, of a yellowish type of stone that is sparsely used in the facade. Spectra are shown both with the recorded intensity obtained for a fixed excitation pulse energy (top) and with intensity normalization (bottom), thus permitting better comparisons of the spectral shapes. None of the stones studied exhibited the typical chlorophyll fluorescence spectral signature; however, those stones are not clean stones but rather stones with natural surface aging, salt crust formation, and pollution deposition. The center positions of the transmission bands of the two filters, at 600 and 448 nm, employed in the lidar detection system for some

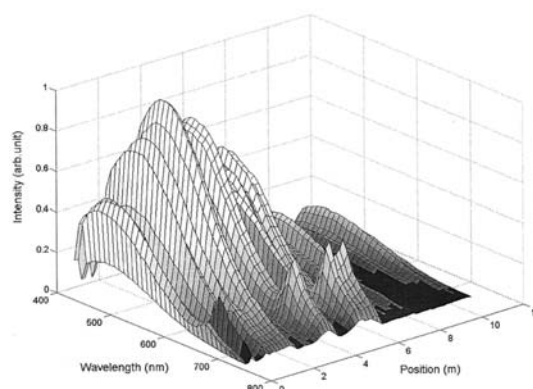


Fig. 6. Fluorescence spectra for an 11-m vertical line scan on the left side of the northern portal as indicated in Fig. 1. Spectra are shown in a three-dimensional surface plot.

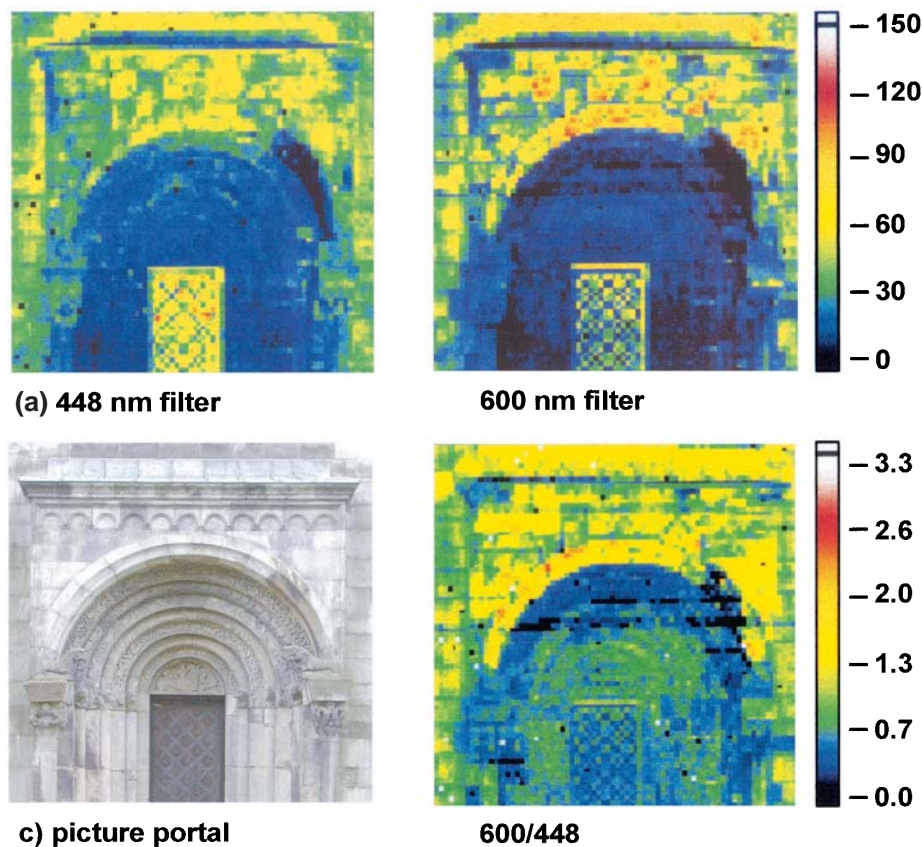


Fig. 7. Simultaneous recording of fluorescence images taken through (a) 448- and (b) 600-nm filters (two-channel method). The image of the ratio $I(600 \text{ nm})/I(448 \text{ nm})$ is shown in (d). Red corresponds to the highest intensity; yellow and green, to successively lower intensities; and blue and black indicate the lowest values, as indicated in the color bars.

measurements are indicated, and the ratio $I(600 \text{ nm})/I(448 \text{ nm})$ values between the fluorescence intensities at these wavelengths are shown. Such a ratio, which can vary widely as shown in Fig. 4, yields a first, rough, indication of the spectral shape. This procedure loses the intensity information but has some advantages, which we discuss below.

Spectral signatures from seven different samples of biodeteriogens are shown on a normalized scale in Fig. 5 as recorded remotely by the fluorescence lidar system. Species growing on the facades include green algae from the *Chaetophorales* taxa and the lichens *Scotiosporum umbrinum*, *Lepraria lobificans*, and *Lecanora dispersa* sp. lat. Facade areas with a reasonably dense colonization of particular species were selected to reduce the background fluorescence that was due to the stone. All spectra show the characteristic peak of chlorophyll *a* at $\sim 680 \text{ nm}$. The intensity falloff toward longer wavelengths differs among species; some species even exhibit a second peak, at $\sim 705 \text{ nm}$. There are also spectral differences throughout the visible region from violet

to red, which correspond to different accessory pigments. The shape differences exhibited in the spectra of Figs. 4 and 5 suggest that it should be possible to classify different areas of a facade on the basis of their fluorescence spectral signatures.

B. Line Scans

As a preparation for two-dimensional imaging, line scans were performed, particularly for investigation of spectral information dynamics. Each spectrum was integrated over 20 laser shots. Figure 6 shows a vertical scan taken on the left side of the northern portal, as indicated in Fig. 1. The intensity of the sandstone fluorescence varies quite strongly along the line. Unambiguous chlorophyll fluorescence signals are manifest in the middle of this vertical scan.

C. Filter Imaging

As a first step in fluorescence imaging, the fluorescence intensity through the 682-nm filter was recorded, as shown at the bottom left of Fig. 1. Because the filter matches the chlorophyll fluores-

cence spectral band, the areas affected by biodeteriogens appear bright. As the laser was quite stable in its output pulse energy and the biodeteriogen signatures are strong, the main features of the image can readily be interpreted, even if there is no compensation for geometrical effects, etc., which are discussed below.

Figures 7(a) and 7(b) show two images of the portal area [Fig. 7(c)] obtained simultaneously with two-channel detection at 448 and 600 nm, respectively. In the same way as it was possible to identify chlorophyll by its strong red intensity increase in single-wavelength imaging (Fig. 1), it is possible to identify the area of stone iron-ion-fluorescence quenching in each monochrome image, because of strong intensity reductions. In some cases the individual stones are discernible because of the mortar, which has strongly different fluorescence characteristics that compensate for the lacking geometrical resolution.

By forming the ratio $I(600\text{ nm})/I(448\text{ nm})$ between the signals of the two channels, one obtains a dimensionless quantity. Such a quantity is independent of the changes in distance and incidence angle, of the fluctuations of the laser pulse energy, and of (wavelength-independent) changes in the detection system's efficiency.

The ratio image [Fig. 7(d)] is therefore sensitive only to the physical and chemical characteristics of the surface and not to its geometry. The suppression of geometrical effects is particularly evident about the door. The intensity ratio changes by a factor of 2 from the flat surface of the portal (mostly 19th-century stone) and the area of ornamented 12th-century stone between the arch and the top of the door. Because only two wavelengths are used, the interpretation can be ambiguous. For instance, if a red filter image (as in Fig. 1) and a blue filter image are recorded for subsequent formation of a ratio image, clean stones, whose fluorescence falls off more slowly toward the red than is normally the case, could be interpreted as areas with small quantities of chlorophyll. It can also be noted that the door appears similar to stone in Fig. 7(d). As a conclusion, the limitations of the two-wavelength method suggest the use of multispectral imaging and advanced statistical information retrieval methods, such as principal-component analysis (PCA).

D. Multispectral Imaging

In PCA analysis^{27,28} the total spectral information contained in the image is projected onto an orthogonal set of spectral eigenvectors, which are chosen in such a way that the first eigenvector describes as much as possible of the covariance among the samples. The second eigenvector describes as much as possible of the residual covariance, and so on until all samples are included in the set of orthogonal eigenvectors. If a sufficient number of eigenvectors are used, each individual sample, here each spectrum in the scene recorded, can be reconstructed by a linear combination of the eigenvectors. The eigenvectors

are called principal components (PCs); and the expansion coefficients, the scores.

A fluorescence spectrum was detected in each of the 6400 points of the cathedral portal image. The data were then analyzed with a commercial program package for multivariate statistical analysis (The Unscrambler, CAMO ASA, Norway).²⁸ The multivariate analysis was restricted to the PCA outlined above.

Because the chlorophyll signature is quite different from the other spectral features and in this case is connected to biodeteriogens rather to the building material, it is useful to perform the spectral analysis in three steps, as follows.

In the first step, all the pixels that showed the chlorophyll fluorescence signature were isolated. The criterion used was that the integrated area of the chlorophyll signal should be more than 0.3% of the integrated fluorescence signal (the area under the full fluorescence curve). A polynomial fit to the sloping stone fluorescence background was used to separate the chlorophyll signal. Approximately 25% of the pixels fulfilled this criterion. The criterion was found to be sufficiently robust to pixel noise.

In a second step a PCA analysis was performed on the pixels selected in the first step and including only wavelengths longer than 650 nm. Before this analysis was made, the selected biodeteriogen spectra were corrected for the sloping stone fluorescence background with the fit procedure just described. In this way a full orthogonalization between biodeteriogens and other materials was achieved. The result of this analysis is shown in Fig. 8. In the upper left-hand quadrant the chlorophyll integral value is shown in a gray-scale image. The upper right-hand quadrant shows the shapes of the first two principal components (PC1 and PC2) as determined from the data. As expected, PC1 exhibits a strong peak at 680 nm, the main chlorophyll fluorescence signal. Some addition of the PC2 shape is needed to describe chlorophyll signals with a slow long-wavelength falloff (a positive addition of PC2 lowers the short-wavelength signal and increases the long-wavelength signal). If a sufficient amount of PC2 is added to PC1, a free-standing second peak emerges, as shown in one of the two experimental spectra included in Fig. 8 (corrected for the sloping stone fluorescence background; see also Fig. 5, sample 5). The spatial distribution of the expansion coefficients (scores) is shown as two gray-scale images of the portal (PC1 in the lower-left-hand quadrant; PC2 in the final quadrant).

Biodeteriogen colonization has occurred mostly on the cathedral wall behind the portal addition, related to the more-protected and moister environments found there compared with the exposed portal facade. Small scattered islands of growth were also found on other locations. The PC1 component is the more prominent in all the biodeteriogen pixels, but we also note that most pixel spectra need a PC2 contribution, corresponding to biodeteriogen spectral signatures with a slower slope toward the infrared. Exceptions are found on the two pillar capital fronts, which are dominated by species with strong PC1 signatures.

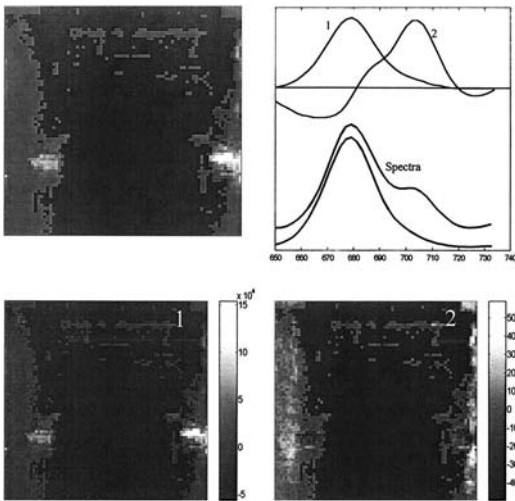


Fig. 8. Demonstration of chlorophyll imaging. All pixels that contain even a minimal chlorophyll signal have been selected and are indicated in gray shades (top left). A PCA is performed in the spectral region 650–740 nm for the chlorophyll signal feature, separated from the sloping stone fluorescence background. The two first PC vectors (PC1 and PC2) for the spectral material are shown at the top right, together with two examples of detected spectra. Finally, images of the scores of the two principal components are shown in gray scale: PC1 (bottom left) and PC2 (bottom right). Here higher intensity is indicated by a lighter color.

Thus the PC2 score image features an intensity reduction in those areas.

Excluding the biodeteriogen pixels from the analysis of the remaining areas reduces the risk of confusing stone fluorescence signatures with the blue–green fluorescence from biodeteriogen accessory pigments.

In the third step, a PC analysis was performed on the nonbiodeteriogen spectra/pixels. Figure 9 shows the first three principal components found and the score plots for PC2 versus PC1 and PC3 versus PC1.

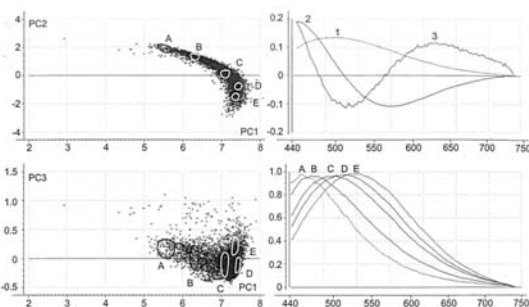


Fig. 9. The three first principal components (PC1–PC3) and their normalized score plots for all nonchlorophyll pixels. The individual spectra can be expressed as a weighted sum of principal components. The averaged spectral shapes from five characteristic locations along the PC2–PC1 and PC3–PC1 score plots are shown (A–E).

Five spectral shapes, averaged for the pixels that belong to the areas marked A–E in the PC2–PC1 and PC3–PC1 plots, are included in the figure. We recognize the shape of the pure PC1 eigenvector in the C area spectrum, whereas the other spectra have positive and negative contributions of PC2, shifting the intensity maximum toward blue and red, respectively.

The data in Fig. 9 correspond to normalized spectra. By using normalized data we secured the analysis from artifacts, as only spectral shape matters. In Fig. 10 a corresponding fully processed false color image of the whole scene is shown. We have merged the biodeteriogen data, whose interpretation is particularly straightforward and which have already been commented on, in their normalized version into Fig. 10, using three shades of red. Pixels with a high biodeteriogen PC1 score (sharp peak at 680 nm) are shown in light red, those with a high biodeteriogen PC2 score in darker red, and those with low values of both PC1 and PC2 scores (indicating little biodeteriogen colonization) with a very dark red color. It is easy to identify the violet area that indicates iron-ion fluorescence quenching because of the sharply falling-off intensity toward the red. It should be noted, though, that this area is even easier to recognize in nonnormalized data because of the very low signal intensity (see Fig. 4, top, and Fig. 7).

The ornamented 12th-century arched stone can be partly discriminated from the 19th-century portal facade stone. Areas related to the particular spectral signatures are shown in blue–indigo and green, respectively.

Multispectral imaging with a PCA interpretation does not require great knowledge of the target spectral features before one starts a measurement. By contrast, when one is using a limited number of receiving filter channels this knowledge is necessary to enable the channels' optimal spectral position to be chosen. The PCA analysis of the spectral signatures can also reveal information that is hidden from the eye. The ability to identify and distinguish different objects can be reduced because of the high signal levels of some objects in the target. Therefore, data are frequently normalized, as demonstrated in connection with Fig. 10.

5. Conclusions

Although further investigations are necessary, the experimental results have clearly demonstrated the feasibility of full-daylight, remote fluorescence imaging of architectural monuments, which could provide assessment of surface damage and help in restoration planning. Two imaging techniques were tested, both successfully. The usefulness and general applicability of principal-component analysis in improving image processing has been demonstrated. The results have also confirmed the possibility of achieving, in practical field work,

- Early detection of biodeteriogens before their presence can be observed with other techniques. It



Fig. 10. False-colored image with pixels superimposed upon a photograph of the northern portal. Areas with different characteristics can be identified. Thus, pixels with 12th-century stone characteristics are shown in blue-indigo, and those with 19th-century characteristics are shown in green. The violet pixels correspond to areas that exhibit iron-ion quenching. The normalized chlorophyll pixels from Fig. 8 have been merged in red color tones: Pixels with a large amount of biodeteriogen PC1 are light red; those with a high PC2 score, darker red; and those with both PC1 and PC2 low are shown in a very dark red color.

is important to note that, whereas biodeteriogen colonization on certain areas, such as the sculptures, was visually observable, such was not

the case for other areas for which extensive colonizations were clearly detected by both methods.

- Identification of the different stone types, which also opens interesting perspectives for reconstruction of the building's history.

The experiment was carried out without problems, in spite of unfavorable weather conditions. The images of the portal were taken at a distance of ~60 m, but the signal-to-noise ratio obtained during the experiment suggests that detection in full sunlight should still be feasible for at least at a distance of 100 m. Clearly, the capabilities of fluorescence techniques are further enhanced at the low ambient-light levels at night, and useful ranges up to 200 m can be expected.

The results of this research show that remote fluorescence imaging with this new lidar technology is technically practicable. However, additional research is still needed to refine the methodology and to define the data-assessment problems. Progress in solving these problems will require a close interaction between physicists in the remote-sensing field and scientists in the cultural heritage field. In particular, the identification and mapping of facade stone treatment and conservation is a field that shows great promise.²⁹ Early laboratory work and field monitoring indicate that a considerable potential exists. The study presented here establishes a useful proof of concept from which the newly emerging technology can develop.

This research was supported by the European Community under Access to Large-Scale Facility contract ERB FMGE CT950020 (DG12), by the Swedish National Space Board, the Knut and Alice Wallenberg Foundation, and the Consiglio Nazionale delle Ricerche (Italy) Special Project on Science and Technology for Cultural Heritage. The authors are grateful to L. Fröberg for making biological identifications. The kind assistance of and collaboration by E. Cinthio and the personnel of the Lund Cathedral are also gratefully acknowledged.

References

1. E. R. Menzel, *Laser Detection of Fingerprints*, 2nd ed. (Marcel Dekker, New York, 1999).
2. V. Zafropoulos and C. Fotakis, "Lasers in the conservation of painted artwork," in *Laser Cleaning in Conservation: an Introduction*, M. Cooper, ed. (Butterworth Heinemann, Oxford, 1998), Chap. 6.
3. S. Andersson-Engels, C. af Klinteberg, K. Svanberg, and S. Svanberg, "In vivo fluorescence imaging for tissue diagnosis," *Phys. Med. Biol.* **42**, 815–824 (1997).
4. K. Svanberg, I. Wang, S. Colleen, I. Idvall, C. Ingvar, R. Rydell, D. Jocham, H. Diddens, S. Bown, G. Gregory, S. Montán, S. Andersson-Engels, and S. Svanberg, "Clinical multi-colour fluorescence imaging of malignant tumours—initial experience," *Acta Radiol.* **38**, 2–9 (1998).
5. R. M. Measures, *Laser Remote Sensing: Fundamentals and Applications* (Wiley, New York, 1984).
6. R. A. O'Neill, L. Buja-Bijunas, and D. M. Rayner, "Field performance of a laser fluorosensor for the detection of oil spills," *Appl. Opt.* **19**, 863–870 (1980).
7. M. Bazzani, B. Breschi, G. Cecchi, L. Pantani, D. Tirelli, G. Valmori, P. Carozzi, E. Pelosi, and G. Torzillo, "Phytoplankton monitoring by laser induced fluorescence," *EARSeL Adv. Remote Sens.* **1**, 106–110 (1992).
8. L. Alberotanza, P. L. Cova, C. Ramasco, S. Vianello, M. Bazzani, G. Cecchi, L. Pantani, V. Raimondi, P. Ragnarson, S. Svanberg, and E. Wallinder, "Yellow substance and chlorophyll monitoring in the Venice Lagoon using laser-induced fluorescence," *EARSeL Adv. Remote Sens.* **3**, 102–110 (1995).
9. H. Edner, J. Johansson, S. Svanberg, E. Wallinder, M. Bazzani, B. Breschi, G. Cecchi, L. Pantani, B. Radicati, V. Raimondi, D. Tirelli, G. Valmori, and P. Mazzinghi, "Laser-induced fluorescence monitoring of vegetation in Tuscany," *EARSeL Adv. Remote Sens.* **1**, 119–130 (1992).
10. A. Rosema, G. Cecchi, L. Pantani, B. Radicati, M. Romoli, P. Mazzinghi, O. Van Kooten, and C. Kliffen, "Monitoring photosynthetic activity and ozone stress by laser induced fluorescence in trees," *Int. J. Remote Sens.* **13**, 737–751 (1992).
11. V. Raimondi, G. Cecchi, L. Pantani, and R. Chiari, "Fluorescence lidar monitoring of historical buildings," *Appl. Opt.* **37**, 1089–1098 (1998).
12. H. Edner, J. Johansson, S. Svanberg, and E. Wallinder, "Fluorescence lidar multicolor imaging of vegetation," *Appl. Opt.* **33**, 2471–2479 (1994).
13. H. Edner, J. Johansson, P. Ragnarson, S. Svanberg, and E. Wallinder, "Remote monitoring of vegetation using a fluorescence lidar system in spectrally resolving and multi-spectral imaging modes," *EARSeL Adv. Remote Sens.* **3**, 193–206 (1995).
14. J. Johansson, M. Andersson, H. Edner, J. Mattsson, and S. Svanberg, "Remote fluorescence measurements of vegetation spectrally resolved and by multi-colour fluorescence imaging," *J. Plant Physiol.* **148**, 632–637 (1996).
15. V. Raimondi, P. Weibring, G. Cecchi, H. Edner, T. Johansson, L. Pantani, B. Sundner, and S. Svanberg, "Fluorescence imaging of historical buildings by lidar remote sensing," in *Earth Surface Remote Sensing II*, G. Cecchi and E. Zilioli, eds., *Proc. SPIE* **3496**, 15–20 (1998).
16. H. Edner, K. Fredriksson, A. Sunesson, S. Svanberg, L. Unéus, and W. Wendt, "Mobile remote sensing system for atmospheric monitoring," *Appl. Opt.* **26**, 4330–4338 (1987).
17. P. Weibring, M. Andersson, H. Edner, and S. Svanberg, "Remote monitoring of industrial emissions by combination of Lidar and plume velocity measurements," *Appl. Phys. B* **66**, 383–388 (1998).
18. S. Svanberg, "Fluorescence lidar monitoring of vegetation status," *Phys. Scr.* **T58**, 79–85 (1995).
19. R. Löfvendahl, B. Sundner, *The Lund Cathedral. Stony Material and Damage Assessment* (Central Board for National Antiquities, Stockholm, Sweden, 1997; in Swedish).
20. P. Johansson, *The Lichen Flora on the Lund Cathedral* (Central Board for National Antiquities, Stockholm, Sweden, 1992; in Swedish).
21. P. Johansson, "The lichen flora on the Lund Cathedral," *Sven. Botan. Tidskr.* **87**, 25–30 (1993).
22. L. Celander, K. Fredriksson, B. Galle, and S. Svanberg, "Investigation of laser-induced fluorescence with applications to remote sensing of environmental parameters," Göteborg Institute of Physics Rep. GIPR-149 (Chalmers University of Technology, Göteborg, Sweden, 1978).
23. S. Svanberg, "Laser fluorescence spectroscopy in environmental monitoring," in *Optoelectronic for Environmental Science*, S. Martellucci and A. N. Chester, eds. (Plenum, New York, 1990), pp. 15–27.
24. G. Cecchi, L. Pantani, V. Raimondi, D. Tirelli, and R. Chiari, "The fluorescence lidar technique for the remote sensing of stony materials in ancient buildings," in *Remote Sensing for*

- Geography, Geology, Land Planning, and Cultural Heritage*, D. Arroyo-Bishop, R. Carla, J. B. Lurie, C. M. Marino, A. Panunzi, J. J. Pearson, and E. Zioli, eds., Proc. SPIE **2960**, 163–172 (1996).
25. G. Cecchi, L. Pantani, V. Raimondi, D. Tirelli, R. Chiari, L. Tomaselli, G. Lamenti, M. Bosco, and P. Tiano, "Fluorescence lidar technique for the monitoring of biodeteriogens on the cultural heritage," in *Remote Sensing for Geography, Geology, Land Planning, and Cultural Heritage*, D. Arroyo-Bishop, R. Carla, J. B. Lurie, C. M. Marino, A. Panunzi, J. J. Pearson, and E. Zioli, eds., Proc. SPIE **2960**, 137–146 (1996).
26. A. S. Marfunin, *Spectroscopy, Luminescence, and Radiation Centers in Minerals* (Springer-Verlag, Berlin, 1979).
27. K. R. Beebe and B. Kowalski, "An introduction to multivariate calibration and analysis," Anal. Chem. **59**, 1607A (1987).
28. K. Esbensen, T. Midtgaard, S. Schonkopf, and D. Guyoyf, *Multivariate Analysis—A Training Package* (CAMO ASA, Oslo, Norway, 1994).
29. G. Ballerini, S. Bracci, L. Pantani, and P. Tiano, "Lidar remote sensing of stone cultural heritage: detection of protective treatments," Opt. Eng. **40**, 1579–1583.

Fluorescence Lidar Imaging of the Parma Cathedral and Baptistery

D. Lognoli¹, G. Cecchi¹, I. Mochi¹, L. Pantani¹, V. Raimondi¹, R. Chiari²,
Th. Johansson³, P. Weibring³, H. Edner³, and S. Svanberg³

¹ CNR-Institute of Applied Physics "Nello Carrara", Via Panciatichi 64, I-50127 Firenze, Italy

E-mail: g.cecchi@ifac.cnr.it; phone: +39-055-4235263; fax: +39-055-410893.

² Institute of Petrography, Department of Earth Sciences, University of Parma, Viale delle Scienze 78, I-43100 Parma, Italy

E-mail: chiari@ipruniv.cce.unipr.it; phone: +39-0521-905345; fax: +39-0521-905305.

³ Department of Physics, Lund Institute of Technology, P.O. Box 118, S-221 00 Lund, Sweden

E-mail: Sune.Svanberg@fysik.lth.se; phone: +46-46-2227650; fax: +46-46--2224250.

Abstract

Extensive fluorescence multispectral imaging on the Cathedral and the Baptistery of Parma, Italy, is reported and discussed. Fluorescence spectra were recorded with a mobile lidar system scanning the monument surfaces with a frequency tripled Nd:YAG laser beam from a distance of about 80 m. For each pixel of the investigated area a high spectral resolution spectrum in the full visible range was acquired. The Principal Component Analysis technique was used to obtain thematic maps that outlined the areas subject to protective treatment, biological growth and other features, such as different types of stones and decoration pigments.

PACS: 42.62.Fi; 42.79.Qx.

1. Introduction

Cultural heritage conservation is an important issue that has a great impact on several aspects of our life, from cultural to economical ones. Historical buildings are a considerable part of our cultural heritage. However, the damage assessment and, in general, the control of the conservation status of a monument is a complex issue that involves the investigation and measurement of many parameters. In many cases these tasks also require the acquisition of samples and the subsequent analysis in the laboratory. Hence an extensive control of the historical building heritage can require considerable resources in terms of time, money and specialised personnel. Moreover, the acquisition of samples implies a violation of the integrity of the monument and a manipulation of the original material. In some cases this may lead to artefacts in the results, e.g. stone samples with spores or quiescent forms that become active only once isolated and cultivated in the laboratory. Hence the increasing importance given to the

development of *in situ* and non-destructive techniques for the monitoring of the cultural heritage.

The Laser Induced Fluorescence (LIF) technique is widely applied in many fields of scientific investigation and even of every-day life since it can allow for the detection of features that are not visible with the naked eye or for the characterisation of different substances by means of their fluorescence spectral signatures [1], [2]. It is also used in the field of cultural heritage, especially for painting inspection [3] and fluorescence microscopy [4]. Fluorescence lidar remote sensing [5] allows to apply the LIF technique in the outdoor environment. With respect to the traditional *in situ* techniques it offers the further advantage of operating from a remote location, thus allowing the control of areas that are difficult to reach without scaffolding.

Fluorescence lidar remote sensing has recently been demonstrated as a helpful tool for a quick measurement of several indicators that can be used to assess the conservation status of a historical building [6],[7],[8]. First field experiments were conducted on the Parma Baptistery in 1994 where a fluorescence lidar system was used for point monitoring of different lithotypes on the facade [9]. In the following years further experiments have investigated the fluorescence lidar remote sensing potentials for the characterisation of biodeteriogens on stone materials [7], [10], the investigation of protective treatments [11] and the effects of biocide treatments [12]. It is not until 1997, however, that the first experiment of lidar multispectral imaging was performed [13]. The case study concerned the Lund Cathedral, Sweden, on which a single area (8 m x 8 m) of the northern facade of the Cathedral was investigated by using the lidar multispectral imaging technique. The results showed good potential for achieving thematic maps aimed at the characterisation of the lithotypes and the detection and characterisation of biodeteriogens.

Fluorescence thematic maps are particularly attractive for the control of monuments, firstly because they furnish a piece of information that has a comprehensive relevance on the status of the whole monument, and a spatial definition that cannot be obtained by means of mere sampling. Moreover, the opportunity of recording time-dependent, repetitive fluorescence images opens new prospects for reliable control of the status changes of the monument. Another important aspect of thematic maps is that they make it easier to transfer the knowledge gained with a sophisticated analysis of the fluorescence data, which necessarily requires a specific scientific background, to the conservation specialist and/or to the decision-maker.

The present work aims to extend the results obtained in the previous projects with the following specific goals:

- a) exploit the potential of the lidar multispectral imaging technique for an extensive monitoring of historical buildings;
- b) investigate the practicability of the detection of protective treatments in the field;
- c) demonstrate the usefulness of fluorescence thematic maps obtained using multivariate techniques.

2. Experimental

The experiment was performed in Parma in September 2000. The Cathedral and the Baptistery of Parma are two of the most interesting medieval buildings in northern Italy.

The Cathedral (Fig. 1a) is a composite building in the Romanesque style. It was built before 1046 A.D. and, after the earthquake of 1117 A.D., was partially rebuilt. The reconstruction ended around 1294 A.D. with the erection of the bell tower. The facade is made of ashlar of different whitish and yellowish stones, mainly different types of sandstones (e.g. *Ostia*, *Sporno*, *Pietraforte*) and marbles (e.g. *Rosso Veronese*, *Bardiglio*, *Rosa Corallo*). The facade lower part shows three doorways. The central doorway is surmounted by a marble porch (*Protiro*) decorated with carved figures. The upper part of the facade is decorated with three orders of small arches. Some parts of the facade, particularly on the right side, are colonised by biodeteriogens or show black crusts. The marble porch was treated with a protective treatment in the 1990's.

The Baptistery (Fig. 1b) is considered to be one of the most beautiful buildings of the transition period between Romanesque and Gothic style. Its construction started in 1196 A.D. and ended in 1259 A.D.. Archive data regarding the building of the Baptistery tell of a break in the construction work of approximately 20 years, and completion of the building, particularly with regards to its embellishment with coating slabs, pillars, and bas-reliefs, around 1259 A.D.. The decoration of the upper part was completed in 1307. It has an octagonal structure with four orders of open arches and a fifth order of blind arches. It is completely covered with slabs of *Rosso Veronese*, a calcareous stone widely employed as decorative material due to its colour and typical texture. The lower part of the building has three carved doorways. The Baptistery underwent a recent restoration intervention including stone cleaning and protective treatment (*Paraloid*) different from that used for the *Protiro*.

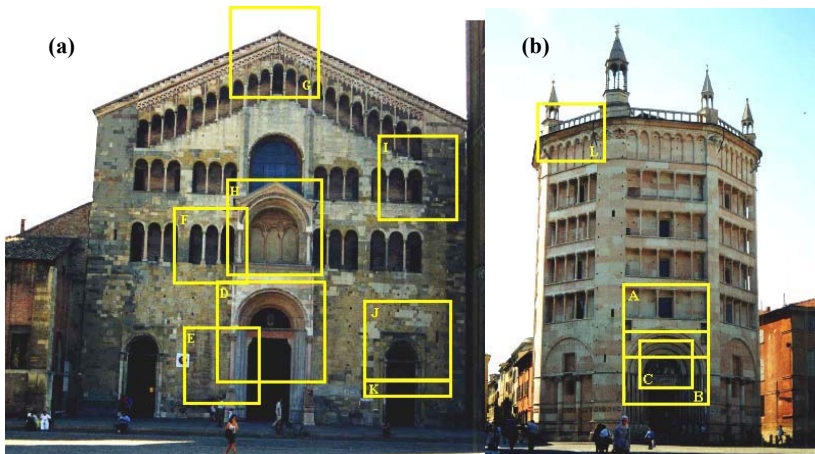


Fig. 1. Scenario for the fluorescence lidar multispectral imaging experiment in Parma: (a) the Cathedral, and (b) the Baptistery. The squares indicate the investigated areas that are labelled A, B, C, etc.

Both these monuments were chosen as targets for the first lidar experiment held in 1994 [9]. Even if the earlier measurements were restricted to a limited set of point measurements, the choice of these two monuments for this recent experiment offers also the opportunity to make a comparison between the old measurements and the new ones.

The measurements were performed using the Lund Laser Centre mobile lidar system. The lidar system, which is adapted primarily for atmospheric monitoring [14], has recently undergone a substantial upgrading [15]. The measurement routines were similar to those described in a previous paper [13]. The general optical and electronic lay-out of the system is shown in Fig. 2. Frequency tripled Nd:YAG laser pulses at 355 nm were transmitted at 20 Hz and a typical pulse energy of 30 mJ towards the monuments via a scanning roof-top mirror. Fluorescence light was collected with a 40-cm diameter 1-m focal length Newtonian telescope and focused into an optical fibre bundle, conveying the light with circular to linear geometrical transformation to the entrance slit of a spectrometer equipped with a gated and intensified CCD detector. The recorded spectrum was stored for each illuminated target spot for subsequent analysis.

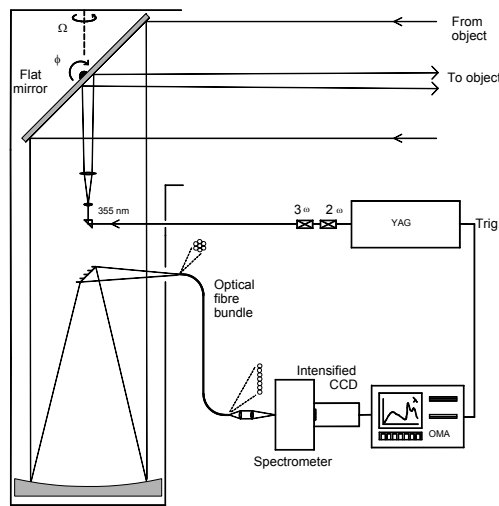


Fig. 2. Optical and electronic arrangement of the mobile lidar system employed for the fluorescence multispectral imaging measurements; OMA, Optical Multichannel Analyser.

During the experiment 12 areas of the two monuments were monitored: 8 areas on the Cathedral and 4 areas on the Baptistery. The locations of the monitored areas are shown in Fig. 1a and Fig. 1b. The concept of the multispectral imaging measurement is shown in Fig. 3: each area was scanned with the lidar system in order to obtain a matrix constituted of $m \times n$ pixels, each pixel being constituted by a high-resolution fluorescence spectrum ranging from 395 to 715 nm with a spectral resolution of ~ 10 nm. The lidar system is equipped with stepper motors driving the mirror scanning the target. The number of horizontal and the vertical steps of the motors were chosen so that the spatial resolution on the target areas A through L were as specified in Table 1. In the following

'X-m.n' indicates the fluorescence spectrum corresponding to the m:th raw and n:th column of the Area X.

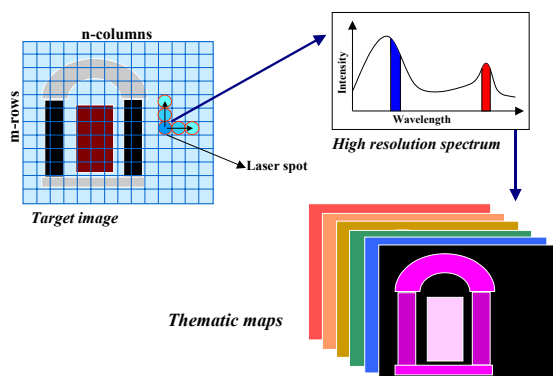


Fig. 3. Basic principles of lidar multispectral imaging on monuments: the investigated area on the surface of the monument can be ideally divided into $m \times n$ 'squares' and then scanned with the lidar system to obtain an image of the target; for each 'square' of the target image a full high resolution fluorescence spectrum is acquired. The laser beam expander can be adjusted so as to cover the whole 'square' or just a part of it to obtain a higher signal-to-noise ratio. The $m \times n$ set of fluorescence spectra is finally analysed to obtain thematic maps that outline specific fluorescence features of the target.

Each spectrum was acquired after accumulating fluorescence data over 3-12 laser shots. The ambient background was acquired at the beginning of each set of measurements and then subtracted. The lidar system was placed at about 80 m from the two targets. Such a distance ensures a small scanning angle on the target so that the differences in the size of the laser footprint are negligible.

Table 1 – Dimensions of the monitored areas and other related scanning data

BAPTISTERY							
Area Label	Number of pixels			Laser Spot Diameter	Pixel Step		Total surface area
	horizontal	vertical	Total		horizontal	vertical	
Area A	67	72	4824	6 cm	12 cm	12 cm	69.5 m ²
Area B	60	60	3600	6 cm	12 cm	12 cm	51.8 m ²
Area C	75	75	5625	6 cm	6 cm	6 cm	20.2 m ²
Area L	50	71	3550	6 cm	12 cm	12 cm	51.1 m ²
CATHEDRAL							
Area Label	Number of pixels			Laser Spot Diameter	Pixel Step		Total surface area
	horizontal	vertical	Total		horizontal	vertical	
Area D	75	74	5550	6 cm	12 cm	12 cm	79.9 m ²
Area E	68	68	4624	6 cm	12 cm	12 cm	66.6 m ²
Area F	70	70	4900	6 cm	12 cm	12 cm	70.6 m ²
Area G	70	70	4900	6 cm	9 cm	9 cm	39.7 m ²
Area H	70	70	4900	6 cm	12 cm	12 cm	70.6 m ²
Area I	60	60	3600	6 cm	12 cm	12 cm	51.8 m ²
Area J	70	70	4900	6 cm	12 cm	12 cm	70.6 m ²
Area K	70	10	700	6 cm	12 cm	12 cm	10.1 m ²

3. Multispectral imaging measurements

Figure 4 presents five fluorescence spectra showing some typical features found in the multispectral measurements. The spectra were collected in different areas of the Baptistery and of the Cathedral. The spectra were normalised at their corresponding maximum in the range from 395 to 650 nm to outline the different spectral shapes.

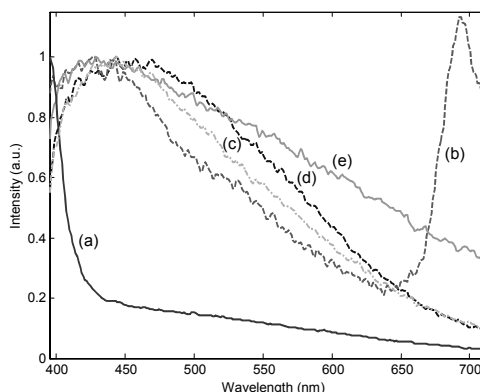


Fig. 4. Five typical fluorescence spectra collected in different points on the two monuments: (a) *Bardiglio* marble subject to protective treatment (pixel D-74.3); (b) *Rosso Veronese* limestone with biodeteriogens (pixel L-20.5); (c) *Rosso Veronese* limestone (pixel B-16.12); (d) *Rosso Veronese* limestone (pixel B-32.2); and (e) *Bardiglio* marble (pixel D-54.61).

The curve (a) presents the spectrum collected in pixel D-74.3 and shows very strong fluorescence in the lower wavelength region of the spectrum. This spectral feature is due to the presence of the protective treatment on the stone that in this case is a marble (*Bardiglio*).

The curve (b) refers to the spectrum of the pixel L-20.5: in the red region the spectrum shows the typical fluorescence peak of the chlorophyll at 680 nm, thus indicating a strong presence of biodeteriogens. The stone substrate is a calcareous stone, *Rosso Veronese*.

The curve (c) presents the spectrum of the pixel B-16.12. The stone is a whitish slab of *Rosso Veronese*. These spectral features are very similar to those detected during the previous experiment carried out in 1994 [9].

The curve (d) presents the spectrum relative to the pixel B-32.2. This spectrum refers to a reddish slab of *Rosso Veronese* and shows the typical fluorescence features of this stone, as specified above. In this case the relative increase of the fluorescence in the 500-600-nm region with respect to that in the blue one is typical of reddish slabs of *Rosso Veronese*.

The curve (e) presents the spectrum of the pixel D-54.61. This refers to a marble (*Bardiglio*) and shows a maximum at shorter wavelengths (approximately 420 nm) with respect to the other types of stones and still strong fluorescence contributions in the red region.

4. Data analysis and discussion of the results

The high resolution fluorescence spectra collected for each pixel of the scanned areas listed in Table 1 can be used to obtain thematic maps pointing out the main characteristics shown in the spectrum.

4.1 Method description

A rather straightforward method to produce a thematic map from a set of spectra is the so-called ratio imaging. The value of the ratio between the intensities of specific fluorescence bands is associated to each point of the image. The bands are chosen in order to obtain information on a certain characteristics of the target. This method is very simple and quick; besides it provides a way to get rid of many problems related to the observation geometry. The main disadvantage of this technique is the difficulty of approaching the analysis of spectra with unknown characteristics, that is the technique requires basic knowledge of the spectral features of the investigated parameters to choose the bands correctly and/or to separate different fluorescence contributions in the same spectral region.

A different approach for information retrieval from the fluorescence spectra is to use the PCA analysis [16], [17]. A PCA analysis is a projection of the spectral information onto a lower dimensional subspace. This subspace is built up by a set of orthogonal Principal Components (PCs), where the PCs are chosen in such way that the first PC describes as much as possible of the covariance among the samples, the second PC as much of the residual covariance and so on. New PCs are added until the residual is considered as just noise. Each PC is built up by one loading vector and one score vector. The loading vector is a projection vector, or the link between the original variables and the PC and the score vector is the samples coordinates in the PC, or new dimension.

The thematic map related to a specific parameter can be obtained by converting the scores of the relevant PC in a grey scale or in a false colour set.

4.2 Thematic maps

Fig. 5 shows a picture of the area H on the Cathedral (Fig. 5a) and three thematic maps (Fig. 5b, 5c and 5d). The first thematic map (Fig. 5b) is obtained by calculating the ratio between the integrated area in the range from 396 to 409 nm and that in the range from 410 to 448 nm. In this way the map points out in yellow/red colours the areas where there is still some protective treatment. The fluorescence spectrum of these pixels is very similar to the spectrum of the pixel D-74.3 shown in Fig. 4 (curve (a)). Fig. 5c and 5d are thematic maps obtained with the PCA method. Fig. 5e shows the shapes of the PC1, PC2 and PC3. The PCA analysis was applied in the range between 412 nm and 708 nm. This range was selected so as to exclude the spectral region where the fluorescence of the treatment was strongly dominant over typical stone signal. The PC1, PC2 and PC3 explain the 94.4%, 4.5% and 0.9% of the total variance, respectively. Two of the first three PCs, however, are dominated by the fluorescence of the treatment that generated most part of the total variance. PC1 is affected by the fluorescence of the treatment in the first part of the shape and by the fluorescence of the stones at longer wavelengths. PC2 can be easily associated to the treatment, but has still a small contribution from the stones. PC3 is not affected by the treatment and can be used to describe properties of the stones. Fig. 5c shows the scores associated to the PC3. Fig. 5d shows the scores

associated to the PC2 and then puts in evidence the areas where there are traces of protective treatment. This can be compared with the map in Fig. 5b. The map of Fig. 5d shows the limitation of the representation obtained with the PCA method: the PC2, and consequently the relative map, contains residual information on stones. The reason is that the set of PCs does not have a correspondence with the physical properties of the targets.

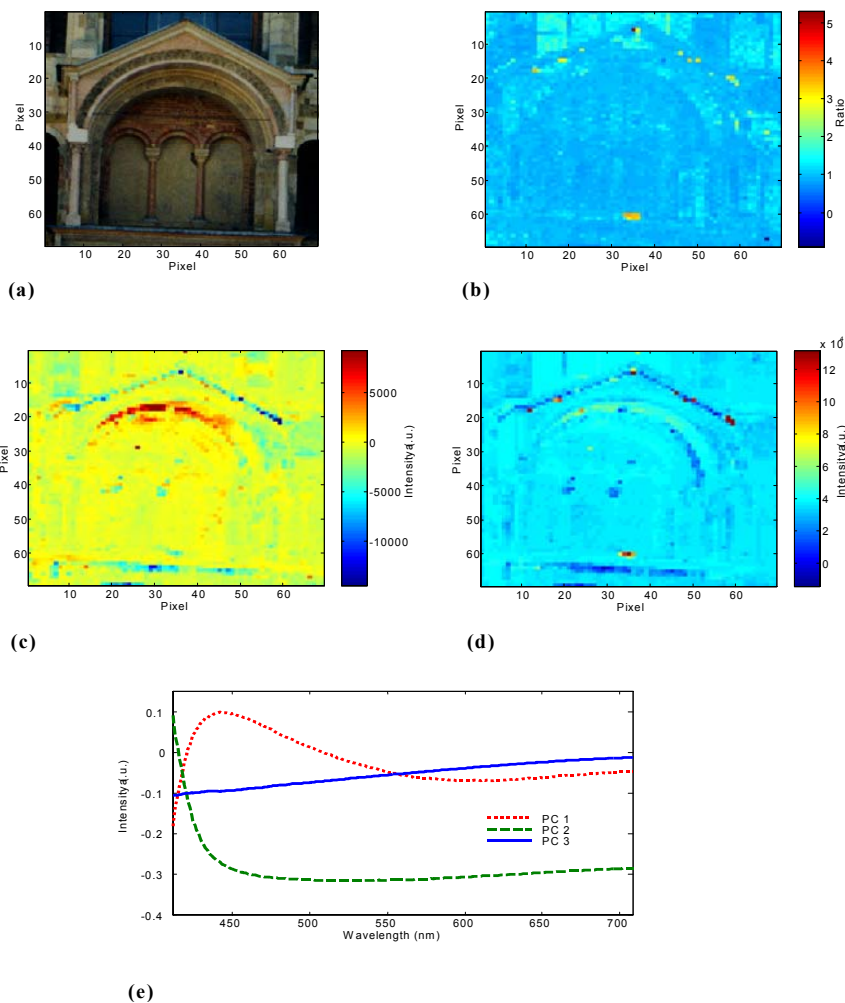


Fig. 5. Area H of the Cathedral: fluorescence data was analysed both by performing a ratio between integrated areas of the spectrum, and by the PCA method, to put in evidence the areas subject to protective treatment; (a) picture of the investigated area; (b) thematic map obtained by the ratio between the integrated area in the range from 396 to 409 nm and the integrated are in the range from 410 to 448 nm; (c) thematic map obtained with the scores associated to the PC3; (d) thematic map obtained with the scores associated to the PC2; (e) shapes of the PC1, PC2 and PC3.

Figures 6a and 6b show, respectively, a picture of the *Protiro* of the Cathedral (area D in Fig. 1a and Table 1) and a thematic map built so as to put in evidence the protective treatment. This map is obtained by calculating the ratio between the integrated area in the range from 396 to 408 nm and that in the range from 409 to 450 nm. The blue pixels refer to areas free from treatment, while the yellow-red ones refer to areas still covered with treatment.

Figure 7a presents a picture of the right portal of the Cathedral (area J in Fig. 1a and Table 1). This area of the facade features several different lithotypes, such as *Ostia* sandstone, *Bardiglio* marble, *Sporno* sandstone, *Pietraforte* sandstone, etc.. Figure 7b shows the relative thematic map for biodeteriogens colonisation. The blue areas indicate the presence of the biodeteriogens. The map was obtained with PCA in the spectral range from 650 to 710 nm. This range was chosen to select the chlorophyll fluorescence band.

A picture of the balustrade (area L in Fig. 1b and Table 1) on the roof of the Baptistery is shown in Fig. 8a. Fig. 8b shows the map of the ratio between the PC2 and PC1 scores: yellow-red areas indicate stones colonised by biodeteriogens. The shape of PC2, actually, is associated to the chlorophyll fluorescence spectral shape while the shape of PC1 is clearly related to the fluorescence of the substrate. In this image the laser beam is not normal to the scanned surface due to the large pointing angle. To avoid the influence of these geometrical effects, the PC1 scores were normalised.

Figure 9a shows a picture of the lunette (area C in Fig. 1b and Table 1) of the main portal of the Baptistery. The lunette hosts several sacred figures with blue decorations: one type of blue decoration is made of azurite; other blue decorations are made of lapis lazuli. Lapis lazuli is more precious than azurite and was used by the artist for decorating only the most important figure, the *Madonna*. The thematic map obtained with the PCA technique (Fig. 9b) points out some homogeneous blue areas very around the *Madonna* figure that can be due to the presence of lapis lazuli. The thematic map was obtained as a ratio between the PC4 and the PC1 scores. The PCs (Fig. 9c) were calculated in the range from 400 to 700 nm.

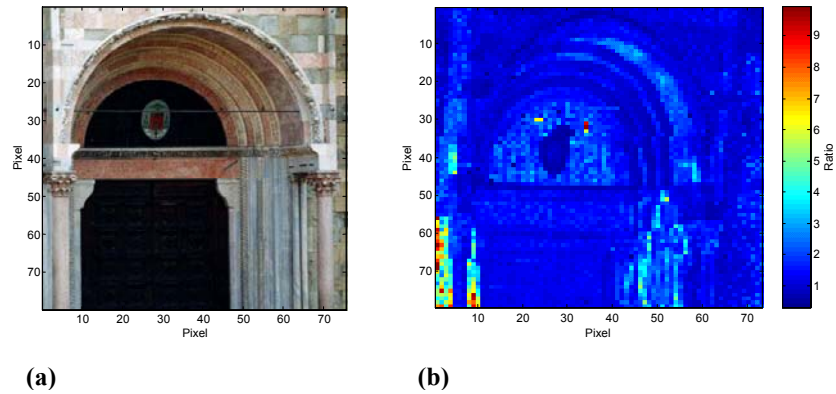


Fig. 6. Area D of the Cathedral: (a) picture of the investigated area; (b) thematic map obtained by the ratio between the integrated area in the range from 396 to 408 nm and the integrated area in the range from 409 to 450 nm; the yellow-red areas in the image indicate areas subject to protective treatment.

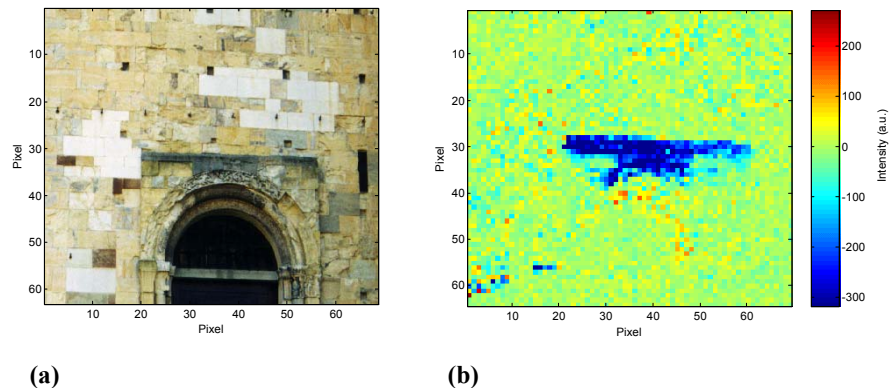


Fig. 7. Area J of the Cathedral: (a) picture of the investigated area; (b) thematic map obtained with PCA in the range from 650 to 710 nm; blue areas indicate stones affected by the colonisation of biodeteriogens.

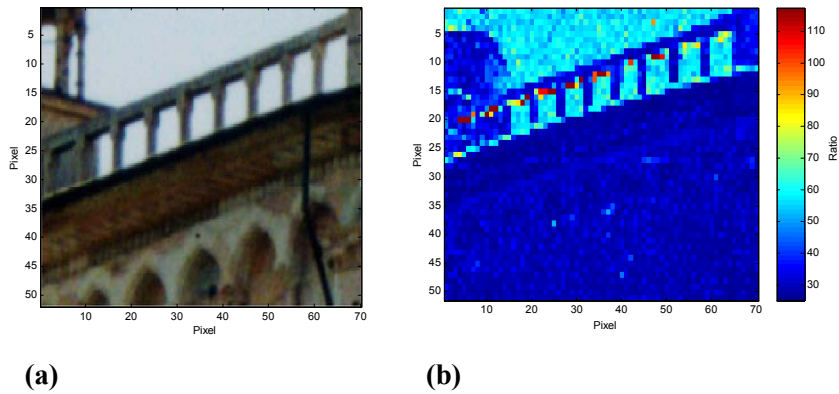


Fig. 8. Area L of the Baptistery (balustrade): (a) picture of the investigated area; (b) thematic map obtained by calculating the ratio between the PC2 and PC1 scores; the PCA was performed in the region from 400 to 700 nm; yellow-red areas in the image indicate stones colonised by biodeteriogens.

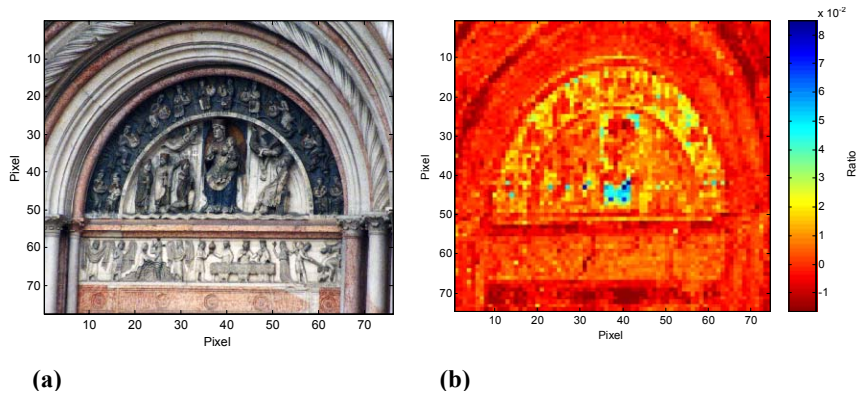


Fig. 9. Area C of the Baptistery: (a) picture of the investigated area; (b) thematic map obtained by calculating the ratio between the PC4 and PC1 scores; (c) shapes of the PC1, PC2, PC3 and PC4; the PCs were calculated in the range from 400 to 700 nm.

5. Conclusions

Multispectral fluorescence imaging data were obtained on several areas of the Cathedral and the Baptistery of Parma, Italy, with a mobile lidar system. The experiment has demonstrated the practicability of extensive monitoring of historical buildings with thematic maps. In particular, the thematic maps obtained from the Cathedral and the Baptistery outlined the presence of the areas subject to protective treatment and to biological growth.

Future work will address geometric rectification of the data as in satellite imaging and investigation of the proper pixel size on the target with respect to the scenario, as in the case of small areas with high resolution, that may be better recorded with non-scanning imaging [18].

Acknowledgements

This project was supported by the EU-IHP Access to Large Scale Infrastructure Programme (contract HPRI-CT-1999-00041), the Knut and Alice Wallenberg Foundation and the CNR *Special Project Safeguard of Cultural Heritage* programme. The authors thank the *Fabbricaria del Duomo di Parma* for the authorisation to carry out the lidar measurements and for the logistic support supplied in the field.

References

1. S. Svanberg, "Laser fluorescence spectroscopy in environmental monitoring", In *Optoelectronic for Environmental Science*, S. Martellucci and A.N. Chester, eds. (Plenum Press, New York 1990), p. 15-27.
2. A.S. Marfunin, *Spectroscopy, Luminescence, and Radiation Centers in Minerals*, Springer Verlag, Berlin (1979).
3. V. Zafiropulus and C. Fotakis, "Lasers in the conservation of painted artwork," in *Laser Cleaning in Conservation: an Introduction*, M. Cooper, ed. (Butterworth Heinemann, Oxford, 1998, Chap.6.
4. Fliermans, C. B., and E. L. Schmidt: "Lumino-fluorescence for autoecological study of a unicellular blue-green algae," *Journal of Phycology* **13**, 364-68 (1977).
5. R.M. Measures, *Laser Remote Sensing: Fundamentals and Applications* (Wiley, New York 1984).
6. G. Cecchi, L. Pantani, V. Raimondi, D. Tirelli, and R. Chiari, "The fluorescence lidar technique for the remote sensing of stony materials in ancient buildings", in *Remote Sensing for Geography, Geology, Land Planning, and Cultural Heritage* (D. Arroyo-Bishop et al., eds.), SPIE **2960**, 163-172 (1996).
7. G. Cecchi, L. Pantani, V. Raimondi, D. Tirelli, R. Chiari, L. Tomaselli, G. Lamenti, M. Bosco, and P. Tiano, "Fluorescence lidar technique for the monitoring of

- biodeteriogens on the cultural heritage,” in *Remote Sensing for Geography, Geology, Land Planning, and Cultural Heritage* (D. Arroyo-Bishop et al., eds.), SPIE **2960**, 137-146 (1996).
8. L. Pantani, G. Ballerini, G. Cecchi, H. Edner, D. Lognoli, T. Johansson, V. Raimondi, S. Svanberg, P. Weibring, " Experiments on stony monument monitoring by laser-induced fluorescence," *Journal of Cultural Heritage* **1**, S345-S348 (2000).
9. V. Raimondi, G. Cecchi, L. Pantani, and R. Chiari, "Fluorescence lidar monitoring of historical buildings", *Appl. Opt.* **37**, 1089-1098 (1998).
10. D. Lognoli, G. Lamenti, L. Pantani, D. Tirelli and L. Tomaselli, "Lidar remote sensing of stone cultural heritage: detection and characterization of biodeteriogens," in *Earth Surface Remote Sensing*, G. Cecchi, T. Engman, E. Zilioli Eds., SPIE **3868**, 339-346 (1999).
11. G. Ballerini, S. Bracci, L. Pantani and P. Tiano, "Lidar remote sensing of stone cultural heritage: Detection of protective treatments", *Opt. Eng.* **40**, 1579-1583 (2001).
12. D. Lognoli, G. Lamenti, L. Pantani, D. Tirelli, P. Tiano and L. Tomaselli., "Detection and characterisation of biodeteriogens on stone cultural heritage by fluorescence lidar", *Appl. Opt.-LP* **41**, 1780-1787 (2002).
13. P. Weibring, T. Johansson, H. Edner, S. Svanberg, B. Sundnér, V. Raimondi, G. Cecchi and L. Pantani, "Fluorescence lidar imaging of historical monuments," *Appl. Opt.-LP* **40**, 6111-6120 (2001).
14. H. Edner, K. Fredriksson, A. Sunesson, S. Svanberg, L. Unéus, and W. Wendt, "Mobile remote sensing system for atmospheric monitoring", *Appl. Opt.* **26**, 4330-4338 (1987).
15. P. Weibring, H. Edner and S. Svanberg, "Versatile mobile lidar system for environmental monitoring", to appear.
16. K.R. Beebe and B. Kowalski, "An introduction to multivariate calibration and analysis", *Anal. Chem.* **59**, 1607A (1987).
17. K. V. Mardia and J. T. Kent, "*Multivariate Analysis*" (Accademic Press, London, 1979).
18. H. Edner, J. Johansson, S. Svanberg and E. Wallinder, "Fluorescence lidar multicolor imaging of vegetation," *Appl. Opt.* **33**, 2471-2479 (1994).

Spectroscopic characterisation of non-melanoma skin tumours using multi-colour and lifetime fluorescence imaging

Thomas Johansson,^{1,2} Gianluca Valentini, PhD,³ Stefan Andersson-Engels, PhD,^{1,2} Gianfranco Canti, MD,⁴ Antonio Pifferi, PhD,³ Paola Taroni, PhD,³ Rinaldo Cubeddu, PhD,³ Katarina Svanberg, PhD, MD,^{1,5} Sune Svanberg, PhD, MDhc,^{1,2}

¹Lund University Medical Laser Centre, P.O. Box 118, SE-221 00 Lund Sweden

²Department of Physics, Lund Institute of Technology, P.O. Box 118, SE-22 100 Lund, Sweden

³Department of Physics and CEQSE-CNR, Politecnico di Milano, I-20133 Milano, Italy

⁴Department of Pharmacology, University of Milano, I-20129 Milano, Italy

⁵Department of Oncology, Lund University Hospital, SE-221 85 Lund, Sweden

Abstract

Two medical fluorescence imaging systems have been intercompared in a study of 13 non-melanoma skin tumours in 8 patients. The systems operate on two different principles; one images the time-integrated laser-induced fluorescence simultaneously in three different spectral bands, and a new composite image, processed using a contrast function displays the areas with the spectral signature characteristic of malignant disease. The other system is capable in capturing images with a high temporal resolution making it possible to use the fluorescence decay characteristics, which differ for normal and malignant tissue. Fluorescence techniques employed for tumour demarcation can operate either on endogenous or exogenous fluorophores. During recent years δ -aminolevulinic acid (ALA)-induced Protoporphyrin IX (PpIX) has been demonstrated to have substantial promise for both diagnosis and photodynamic therapy of tumours. In the present study of skin lesions, ALA was applied topically as a component of a cream, on the areas to be studied and imaging with both systems was performed after 1.5 and 6 hours, when PpIX had been produced with tumour selectivity. The investigation was also supported with spectral recordings in individual points using a fibre-based laser fluorosensor. Both fluorescence imaging system produced processed images, showing a clear demarcation of skin malignancies. Interesting differences in the imaging modalities were noted as a consequence of the different operating principles. It was concluded from this pilot study that both imaging techniques have a great potential as diagnostics tools. Thus, the projection for their utilization in further clinical specialities, where tumour demarcation is a real challenge, is promising.

Introduction

While a large variety of powerful diagnostic tools, in particular imaging systems, are available in the management of malignant disease, there are still areas where complementary techniques are desirable, because of diagnostic short-comings or simply for cost considerations. Fluorescence imaging techniques are strongly developing in many areas, and have during recent years proved to have considerable potential for the detection and demarcation of tumours. Natural chromophores in tissue fluoresce, and can provide information due to variations in concentration or chemical state. More spectacularly, exogenous fluorophores, which exhibit tumour selectivity, can be utilized for

tumour demarcation. Fluorescence diagnostics can either focus on the spectral distribution of the emitted radiation or on the decay characteristics of the fluorescence, which is connected to the different excited-state lifetimes of various chromophores. Both approaches have been shown to be useful for demarcating certain tissue types in medical diagnostics. Systems using the temporal aspects of the fluorescence decay frequently utilize the fact, that certain exogenous substances, in particular porphyrins, exhibit a longer lifetime than is typical for the natural fluorescence, the *autofluorescence*, of commonly occurring chromophores¹⁻³. Work in the time domain requires a short-pulse excitation on the few-ns scale, and the detection system must be able to provide a high temporal resolution to fully utilized differences in excited state lifetimes⁴⁻⁶. The time-integrated spectral shapes of the emission can show differences between normal and diseased tissue when relying only on endogenous chromophores, but are particularly different if tumour-seeking agents have been administered (See, e.g. Refs 7,8). In the present work we have utilized both temporal and spectral demarcation aspects and employed two different imaging systems in the study of the same skin malignancies in a number of patients. In this way valuable experience regarding the potential of the techniques could be gained.

Among the various exogenous agents that have been extensively studied for demarcating malignant lesions, and frequently also for use in photodynamic therapy (PDT), protoporphyrin IX is of particular interest. δ -aminolevulinic acid (ALA), utilized in the body as a precursor in the process of haem generation, can be administered in excess and will result in PpIX prior to the process of iron incorporation to form haem. Due to differences in enzymatic concentrations between normal and diseased tissue, PpIX which is strongly fluorescent and also photodynamically active, will be produced in higher concentrations in tumours. Early clinical work using ALA-PDT is reported in Ref. 9, and extensive continuing work, particularly regarding skin lesions has followed¹⁰⁻¹⁶. A particularly attractive aspect of ALA is the possibility to apply it topically as a component of a cream that is distributed over the skin tumour surface. The PpIX production with preference to tumour cells will then occur during the following hours, and typically diagnostics or treatment is performed 2-6 hours after administration. ALA solution can also be instilled in the bladder for diagnostics or treatment^{17,18}, and an ALA spray can be inhaled for bronchial applications¹⁹. The possibility to in these ways avoid intravenous injection, common for other fluorescent and photodynamically active substances, is of great clinical value. Related to this, the avoidance of a general skin sensitization typical for many common agents and calling for prolonged stays in reduced ambient illumination, is a great advantage.

Topical ALA sensitisation of 13 non-melanoma skin lesions in patients was performed in the present study, where we have utilized the two imaging modalities available to us in a comparative study. The main aim of the study was to assess the efficacies and relative merits of the methods in delineating tumours.

Study arrangements

Patients

Eight patients with in total 13 non-melanoma skin lesions were included in this study at the Lund University Hospital, with approval from its local ethics committee. The patients were referred to the Departments of Dermatology or Oncology at this hospital, for photodynamic treatment, and the diagnostic work was performed in connection with the therapy. Six of the patients were male, while two were females. Their mean age was 73 years, ranging from 58 to 84. Seven of the lesions were basal cell carcinomas (BCC), three were squamous cell carcinomas *in situ* (SCCIS), one was a

squamous cell carcinoma (SCC), and two were determined to be actinic keratosis (AK). Six of the lesions were located on the head, five on the extremities and two on the trunk. Detailed information regarding lesions and diagnostic recordings are given in Table 1.

Investigational procedure

The ALA cream was prepared by mixing 20% ALA powder (Porphyrin Products, Utah) with an oil-in-water emulsion (Essex cream). The cream was applied on the lesions including a surrounding skin zone approximately 1 cm wide. An occlusive bandage was applied to prevent the cream from removal or drying. An attempt was made to examine all the lesions under the same conditions. The timing could, however, not be kept precisely the same for all patients, due to patients concern and practicalities in the complex procedures with many instruments in a tight schedule. Approximately one and a half hour after the application (see exact time in Table 1), the ALA cream was carefully removed and fluorescence measurements with the two different imaging systems, and an additional point-measuring fluorosensor were carried out. The cream and the bandage were then reapplied and the fluorescence measurements were repeated just before and immediately after the photodynamic treatment, in most cases about 6 hours later, but for 2 patient (2 BCC lesions) the day after.

Before acquiring the images, fluorescence spectra were recorded inside and outside the lesion area, using the point-monitoring fluorosensor. Thereafter, normal photographs, multi-colour, and lifetime images of each lesion were recorded in sequence.

Fluorescence spectroscopy

In support of the imaging studies laser-induced fluorescence spectra were recorded using a fibre-optic point-monitoring fluorosensor, which was described in detail elsewhere²⁰. The basic construction of the system is shown in Fig. 1. A nitrogen laser-pumped dye laser operating at 405 nm to match the main porphyrin absorption peak was employed for excitation. A 600 µm core diameter quartz fibre was used to guide the excitation light to the measurement point on the examined tissue, where the distal end of the fibre was held in gentle contact. Tissue fluorescence was induced by the violet light. Part of this fluorescence entered the same fibre and was guided back to the analyzing spectrometer. First the fluorescence was reflected by 90 degrees in a 50% broad-band beam-splitter, which separated the detection and excitation beams, and was then focussed onto the slit of a spectrometer. The spectral interval 450-730 nm was simultaneously detected with a gateable image-intensified CCD array. By using a gate width of 100 ns, any spurious background light could be suppressed while capturing the desired signal. Point spectra were recorded from outside the lesion, at the border of the lesion and in its centre. Spectra were corrected for the non-even response of the recording system, by also recording a spectrum from a calibrated blackbody radiator. Wavelength calibration was performed by recording the spectrum from low-pressure arc lamps. A daily check of this calibration was performed, using the Hg emission lines in the fluorescence tubes in the ceiling.

Multi-colour imaging

Multi-colour imaging was carried out by simultaneously recording three spatially identical, but spectrally different images with the same intensified CCD video camera, using a system developed for endoscopic applications^{21,22,1,8}. The system, schematically illustrated in Fig. 2, was slightly modified from the previous studies. Three images were now produced, spectrally separated in three

wavelength bands by means of stacked, individually adjustable dichroic mirrors. One (named *A*) reflected light in the red region (580-750 nm), one (*B*) in the blue region (420-480 nm), and one (*D*) in the green-yellow region (480-580 nm). The profiles of the filtered bands are illustrated in Fig. 3. The tissue fluorescence was induced using a pulsed frequency-doubled Alexandrite laser emitting ultraviolet light at 390 nm. An optical fibre delivered the excitation light to the tissue. The fibre end was held at a distance of approximately 15 cm from the examined tissue to allow a spherical area of 5 cm in diameter to be illuminated. The fluorescence light was collected by an $f = 50$ mm camera objective lens. Approximately the same distance between the imaging system and the examined lesion was used for all recordings, ensuring the same magnification of all lesions. The gated image intensifier was synchronised with the laser. A gate width of 500 ns was used to efficiently suppress the ambient room light. Thereby, a normal reflected light image could be recorded simultaneously using a colour CCD video camera. Recorded fluorescence images were digitised in a frame grabber and stored in a computer.

Time-gated and lifetime imaging

The basic elements of the lifetime imaging system, described in detail in Refs 1 and 6, and outline in Fig. 4, were a nitrogen laser-pumped dye laser, emitting 1 ns-pulses at 405 nm at a repetition rate of 20 Hz, and an intensified CCD video camera. The image intensifier was gateable with a rise-time of 2 ns and had a gate width of 100 ns, which is much longer than any fluorescence lifetime studied in this investigation. Four gated images were recorded from each lesion using increasing delays of 0, 5, 10, and 20 ns, with respect to the arrival of the excitation pulses. This means that the first image contained the entire fluorescence, the second one included fluorescence emitted later than 5 ns following the excitation pulse, etc. Each recorded image was constructed as an accumulation of signals from 10 sequential laser pulses. The four images were recorded in a direct sequence, with a computer controlled delay generator to minimise the total recording time, being less than 3 seconds per lesion. An orange cut-off filter (Kodak Wratten #22) was used to block elastically scattered laser light and to remove the autofluorescence background below 600 nm. The entire optical arrangement was mounted on a tripod to minimise movement artefacts in the image acquisition. The images were captured and processed by high performance image boards installed in a PC computer

Evaluation of multi-colour images

As seen in Fig. 3, there is a slight leakage of red light in the blue detection band B. This means a cross-talk between the A and B bands. For this reason the B band was omitted from the analysis in the present study. The information in the A band corresponds mainly to protoporphyrin fluorescence, but to some degree also from weak tissue autofluorescence in this spectral region. The information in the D band originates from tissue autofluorescence only. The detection algorithm used is based on that healthy skin is characterised by a high tissue autofluorescence and a low porphyrin signal, while a premalignant or malignant tumour yields a low autofluorescence and a high porphyrin signal. Since the B-band signal, which is frequently used for normalisation (especially if a shorter excitation wavelength is used), can be expected to be almost proportional to the D-band signal, the use of the latter turned out to be adequate. The A- and D-band images are thus combined in a contrast enhanced image using the function:

$$F_c = (A - k_1 D) / (D + k_2) \quad (1)$$

with A and D defined above, and k_1 being a constant with different values for different tissues. Here, k_1 was defined for each lesion by adjusting the numerator to zero for an area in each image clearly being normal. The nominator will thus not necessarily represent a true porphyrin signal, but k_1 is rather defined to obtain as good a contrast as possible between tumour and normal tissue. A “small” constant k_2 was added to the denominator to prevent it from accidentally becoming zero or very small. By forming the ratio, not only a good contrast is obtained; the result is also independent on the exact measurement geometry and the illumination, which might be very non-uniform. The computer calculated the F_c value pixel by pixel and fed the result, via an output frame grabber, to a video mixer, where the fluorescence image could be mixed in as an overlay on the normal white-light image from the colour CCD camera.

In the evaluation, the standard deviation of the signal in a region identified as clearly normal was measured, indicating typical variations in the normal tissue fluorescence. As described above, the constant k_1 was defined so that the average function value F_c became zero in this region. A value, 13 times higher than this standard deviation, was used as a threshold for system classification of lesions. This number was obtained by fitting the outlines of the F_c function with the borders of the lesion as evaluated clinically.

Evaluation of time-gated and lifetime images

The time-gated images were evaluated in two ways, both by directly comparing the image contents in the different time gates, and also by processing the information in two or more of the time gates as an effective fluorescence lifetime. Based on a simplified model, the fluorescence decay versus time following prompt excitation can be modelled to be mono-exponential. We call this the effective fluorescence lifetime. For each pixel (i,j) in an image, four values were measured for different time delays t_k from the excitation pulse ($t = 0$). The fluorescence intensity can thus be written as:

$$F_{ij}(d_k) = C_{ij} \int_{t_k}^{\infty} I_{ij}(t) dt = C_{ij} \tau_{ij} I_{ij}(0) \exp(-t_k / \tau_{ij}), \quad (k = 1,..4) \quad (2)$$

where τ is the fluorescence decay time, and C is a constant depending on the system set-up. With simple algebra, the decay time τ can be obtained for each pixel location from a linear regression involving up to four of the delayed images. Both the fluorescence lifetime and amplitude matrixes can be calculated and plotted as grey-scale- or pseudo-colour images.

Results

An example of fluorescence results from the examined mixed basalioma lesion on the neck of Patient 7 (Table 1) is illustrated in Fig. 5. The recordings are made 6 hours and 15 minutes after the application of the ALA cream and just before PDT treatment. In the top row of the figure, a white light photo is presented together with a schematic map of the clinical judgement of the lesion. Both nodular and superficial compartments were identified. In the middle row, fluorescence emission spectra recorded by the point-monitoring fluorosensor are given for the positions indicated. The spectral bands of the dichroic mirrors used in the multi-colour imaging system are also indicated. To

the right, a false-colour coded image processed according to Eq. (1) is presented. A vertical intensity cross section across the processed image at the position indicated by the line is also given. At the bottom, images showing the computer line-out of tissue types are presented: to the right the region identified as tumour tissue (also repeated in a magnified version in the top row), and to the left the rest of the tissue (not indicated to be pre-malignant or malignant).

The results from the multi-colour imaging system for all lesions are presented in Fig. 6. As can be seen, the system indicates a lesion also after PDT, when most of the photosensitiser has been bleached away during the treatment process.

Typical results from the time-resolved fluorescence imaging system are shown in Fig. 7. Both the time-delayed and the lifetime images indicate the lesion in recordings before ALA treatment (Fig. 7a, top). In the lifetime image constructed from the longer time gates, the entire region where the ALA cream was applied is visible, with only a weak indication where the lesion is located, while the lifetime image using the short gates only, clearly indicates the extent of the lesion.

Very different results are obtained after the treatment (Fig. 7b, bottom). Now the time-delayed (or “after-glow”) image yields a lower intensity in the immediate surrounding of the lesion, while the lesion itself and the surrounding further away provide similar, slightly higher, intensities. In the short lifetime image one can almost delineate the lesion, while the lifetime image constructed from the longer time-gates is very even, without any indication of the lesion. The results from all lesions using the time-resolved system are presented in Table 2.

Discussion

This study, where the same malignant tumours were investigated with three instruments operating with laser-induced fluorescence, has yielded valuable information and provided insight in different tumour discrimination properties. A statistical evaluation of the point-monitoring spectra has not been performed, but the results are very similar to data from other studies already published elsewhere^{23,24}. A strong protoporphyrin signal and a relatively low autofluorescence signal could thus be seen inside the lesions, while the surrounding normal skin yielded lower protoporphyrin signal and a brighter autofluorescence. Following the laser treatment, the protoporphyrin was almost fully bleached away in the irradiated area.

It is interesting to follow the behaviour of the multi-colour imaging system data for the different examination times. Already 1.5 hours after the ALA application, the system can clearly distinguish the lesion from the normal surrounding skin. Just before PDT the diagnostic potential has improved only slightly. Also after the treatment the system could identify the lesion. This is probably mostly due to the fact, that the autofluorescence is lower in the lesion as compared to the healthy surrounding skin, and that some PpIX-related signal still remains. The fact that the blue channel (signal B) could not be utilised in the present analysis was of minor importance, since most of the autofluorescence for an excitation wavelength of 390 nm anyway falls in the D-band.

For the time-resolved data it is interesting to notice that the lifetime images gave better results after a short than after a longer application time. This is interpreted as follows: At short application times, the porphyrin signal is not completely dominating the red light detected through the detection filter. The effective lifetime was thus shorter in the surrounding tissue, where short-lived endogenous fluorophores contributed more to the effective lifetime. When the protoporphyrin signal was too dominating, the fluorescence lifetime approached the long protoporphyrin lifetime also in the surrounding tissue, which also carries a PpIX signal, although lower than in the tumour. It is in this

case interesting to note the difference, if only the short delay times were used to calculate the fluorescence lifetime. Then more of the short-lived tissue autofluorescence contributed to the effective lifetime, yielding better demarcation of the tumour as compared to the case when only long delays were used. Lifetime images based on short lifetimes yield similar results as the multi-colour system utilising the chosen algorithm for analysis of the data.

The long delay time image (“after-glow image”) provided mostly good or excellent tumour demarcation after both long and short ALA application times. However, this signal is not dimensionless and thus depends on the geometry and illumination. For a well-defined recording geometry as the one used in the present case this is not a major limitation.

Acknowledgements

The present work was supported by the European Community Access to Large Scale Facilities Programme (Contract ERBFMGECT950020).

References

1. S. Andersson-Engels, G. Canti, R. Cubeddu, C. Eker, C. af Klinteberg, A. Pifferi, K. Svanberg, S. Svanberg, P. Taroni, G. Valentini and I. Wang, Preliminary evaluation of two fluorescence imaging methods for detection of basal cell carcinomas of the skin, *Lasers Surg. Med.* **26**, 76-82 (2000).
2. R. Jones, K. Dowling, M.J. Cole, D. Parsons-Karavassilis, M.J. Lever, P.M.W. French, J.D. Hares and A.K.L. Dymoke-Bradshaw, Fluorescence lifetime imaging using a diode-pumped all-solid-state laser system, *Elec. Lett.* **35**, 256-258 (1999).
3. R. Cubeddu, P. Taroni and G. Valentini, Time-gated imaging system for tumor diagnosis, *Opt. Eng.* **32**, 320-325 (1993)
4. S. Andersson-Engels, J. Johansson and S. Svanberg, The use of time-resolved fluorescence for diagnosis of atherosclerotic plaque and malignant tumours, *Spectrochim. Acta* **46A**, 1203-1210 (1990).
5. R. Cubeddu, G. Canti, P. Taroni and G. Valentini, Time-gated fluorescence imaging for the diagnosis of tumors in a murine model, *Photochem. Photobiol.* **57**, 480-485 (1993).
6. R. Cubeddu, A. Pifferi, P. Taroni, G. Valentini and G. Canti, Tumor detection in mice by measurement of fluorescence decay time matrices, *Opt. Lett.* **20**, 2553-2555 (1995).
7. S. Andersson-Engels, C. af Klinteberg, K. Svanberg and S. Svanberg, In vivo fluorescence imaging for tissue diagnostics, *Phys. Med. Biol.* **42**, 815-824 (1997).
8. K. Svanberg, I. Wang, S. Colleen, I. Idvall, C. Ingvar, R. Rydell, D. Jocham, H. Diddens, S. Bown, G. Gregory, S. Montán, S. Andersson-Engels and S. Svanberg, Clinical multi-colour fluorescence imaging of malignant tumours - initial experience, *Acta Radiol.* **39**, 2-9 (1998).
9. J.C. Kennedy, R.H. Pottier and D.C. Pross, Photodynamic therapy with endogenous protoporphyrin IX: Basic principles and present clinical experience, *J. Photochem. Photobiol. B* **6**, 143-148 (1990).
10. K. Svanberg, T. Andersson, D. Killander, S. Andersson-Engels, R. Berg, J. Johansson, S. Svanberg and Y.L. Yang, Photodynamic therapy of human skin malignancies and laser-induced fluorescence diagnostics utilizing Photofrin and δ -amino levulinic acid, in *Photodynamic Therapy and Biomedical Lasers*, eds. P. Spinelli, M. Dal Fante and R. Marchesini, pp. 436-440 (Elsevier Science Publishers B.V., Amsterdam, the Netherlands, 1992).
11. K. Svanberg, T. Andersson, D. Killander, I. Wang, U. Stenram, S. Andersson-Engels, R. Berg, J. Johansson and S. Svanberg, Photodynamic therapy of non-melanoma malignant tumours of the skin utilizing topical δ -Amino levulinic acid sensitization and laser irradiation, *British J. of Dermatology* **130**, 743 (1994)
12. A.M. Wennberg, L.E. Lindholm, M. Ipsten and O. Larkö, Treatment of superficial basal cell

- carcinomas using topically applied delta-aminolaevulinic acid and a filtered xenon lamp, *Arch. Dermatol. Res.* **288**, 561-564 (1996).
13. T.J. Dougherty, C.J. Gomer, B.W. Henderson, G. Jori, D. Kessel, M. Korbelik, J. Moan and Q. Peng, Photodynamic therapy, *J. Natl. Cancer Inst.* **90**, 889-905 (1998).
 14. C. Fritsch, G. Goerz and T. Ruzicka, Photodynamic therapy in dermatology, *Arch. Dermatol.* **134**, 207-214 (1998).
 15. I. Wang, B. Bauer, S. Andersson-Engels, S. Svanberg and K. Svanberg, Photodynamic therapy utilizing topical δ -aminolevulinic acid in non-melanoma skin malignancies of the eyelid and the periocular skin, *Acta Ophthal. Scand.* **77**, 182 (1999).
 16. I. Wang, N. Bendsoe, C. af Klinteberg, A.M.K. Enejder, S. Andersson-Engels, S. Svanberg and K. Svanberg, Photodynamic therapy versus cryosurgery of basal cell carcinomas; results of a phase III randomized clinical trial, *Br. J. Dermatol.* **144**, 832-840 (2001).
 17. R. Waidelich, H. Stepp, R. Baumgartner, E. Weninger, A. Hofstetter and M. Kriegmair, Clinical experience with 5-aminolevulinic acid and photodynamic therapy for refractory superficial bladder cancer, *J. Urol. JID. - 0376374* **165**, 1904-1907 (2001).
 18. M. Kriegmair, D. Zaak, R. Knuechel, R. Baumgartner and A. Hofstetter, Photodynamic cystoscopy for detection of bladder tumors, *Semin. Laparosc. Surg. JID. - 9432584* **6**, 100-103 (1999).
 19. R. Baumgartner, R.M. Huber, H. Schulz, H. Stepp, K. Rick, F. Gamarra, A. Leberig and C. Roth, Inhalation of 5-aminolevulinic acid: a new technique for fluorescence detection of early stage lung cancer, *J. Photochem. Photobiol. B* **36**, 169-174 (1996).
 20. C. af Klinteberg, M. Andreasson, O. Sandström, S. Andersson-Engels and S. Svanberg, Compact medical fluorosensor for minimally invasive tissue characterisation, Submitted to *Rev. Sci. Instrum.* (2002).
 21. S. Andersson-Engels, J. Johansson and S. Svanberg, Medical diagnostic system based on simultaneous multispectral fluorescence imaging, *Appl. Opt.* **33**, 8022-8029 (1994).
 22. S. Andersson-Engels, R. Berg, K. Svanberg and S. Svanberg, Multi-colour fluorescence imaging in combination with photodynamic therapy of δ -amino levulinic acid (ALA) sensitised skin malignancies, *Bioimaging* **3**, 134-143 (1995).
 23. C. af Klinteberg, A.M.K. Enejder, I. Wang, S. Andersson-Engels, S. Svanberg and K. Svanberg, Kinetic fluorescence studies of 5-aminolaevulinic acid-induced protoporphyrin IX accumulation in basal cell carcinomas, *J. Photochem. Photobiol. B* **49**, 120-128 (1999).
 24. M. Soto Thompson, L. Gustafsson, S. Pålsson, N. Bendsoe, M. Stenberg, C. af Klinteberg, S. Andersson-Engels and K. Svanberg, Photodynamic therapy and diagnostic measurements of basal cell carcinomas using esterified and non-esterified 5-aminolevulinic acid, *J. Porphyrins Phthalocyanines* **5**, 147-153 (2001).

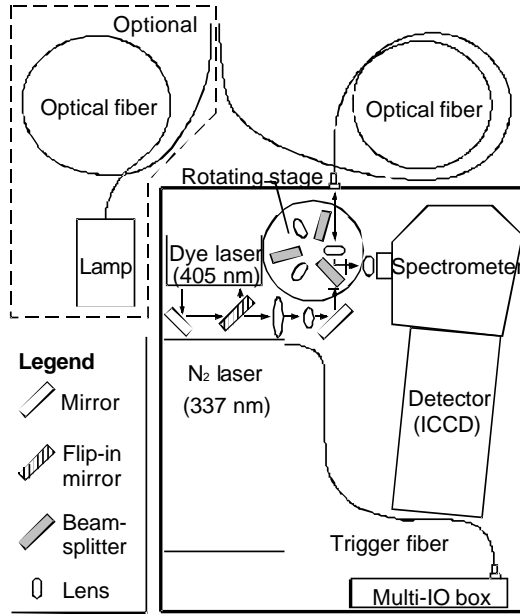


Fig. 1. Schematic illustration of the point monitoring fluorescence spectroscopy system (from Ref. 20).

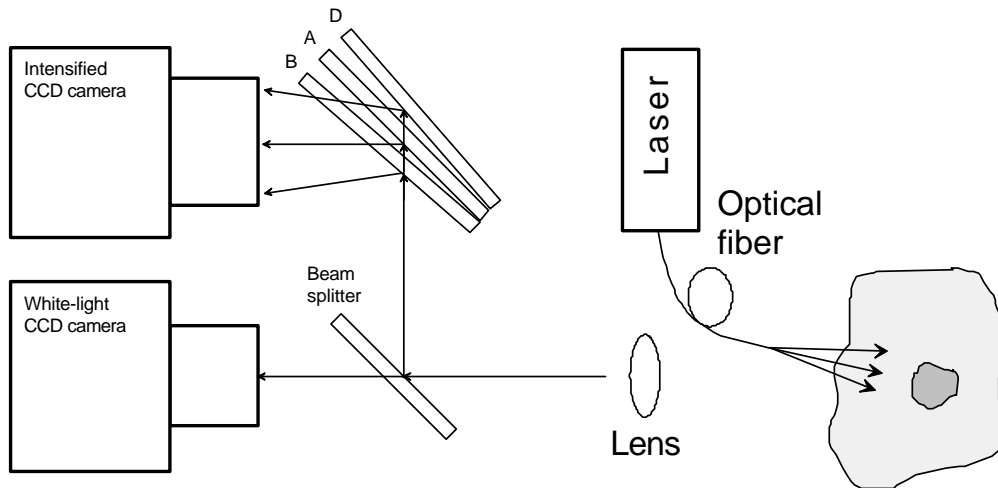
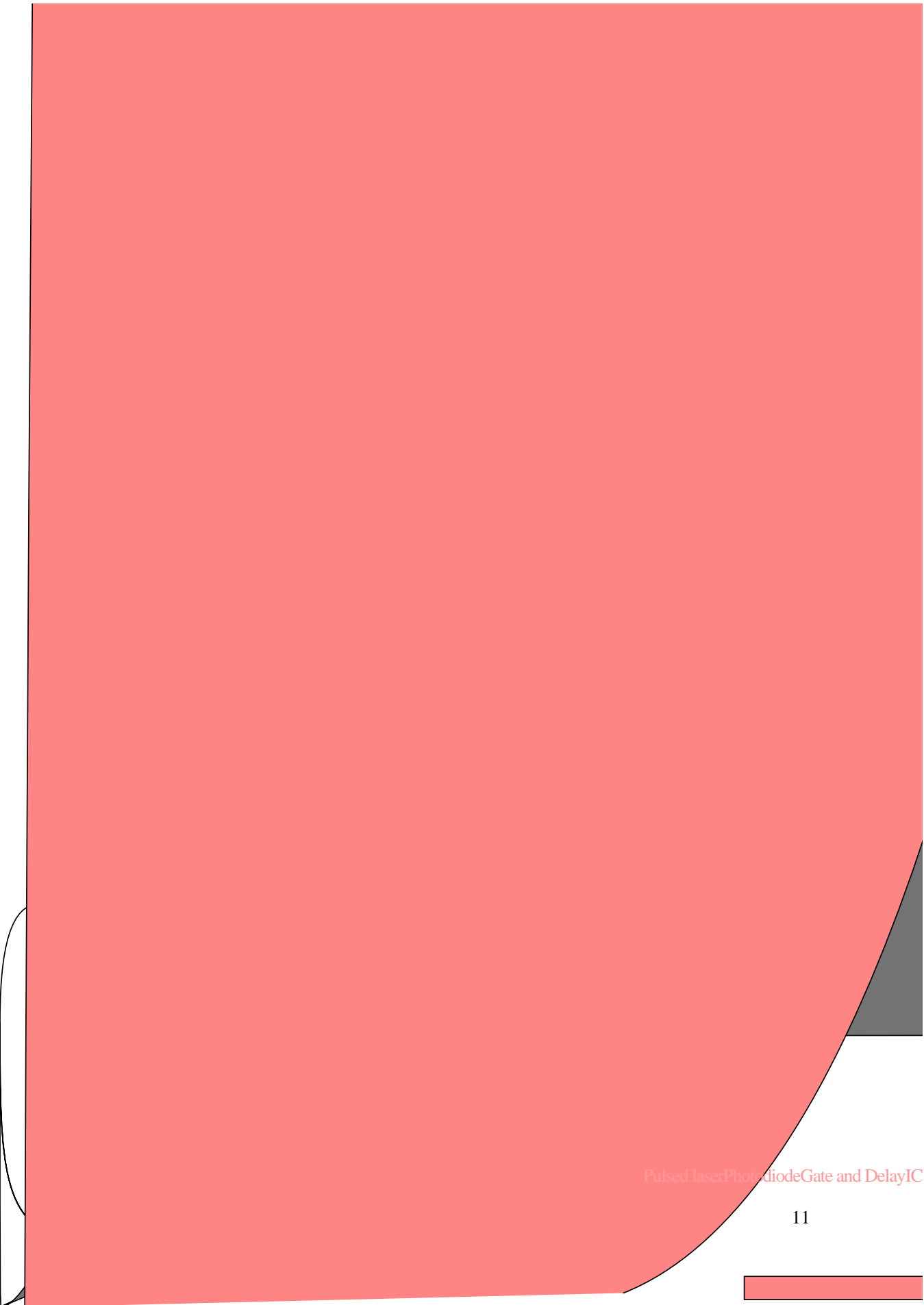


Fig. 2. The schematic arrangement of the multi-colour fluorescence imaging system using dichroic mirrors to separate the different wavelength bands.



Pulsed laser Photodiode Gate and Delay IC



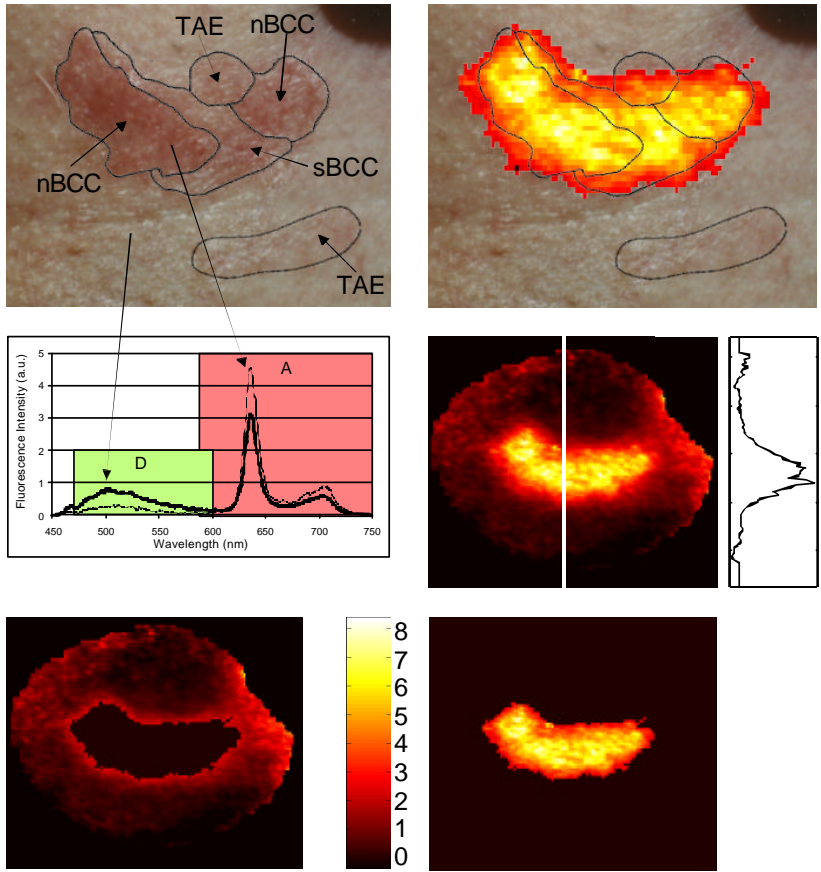
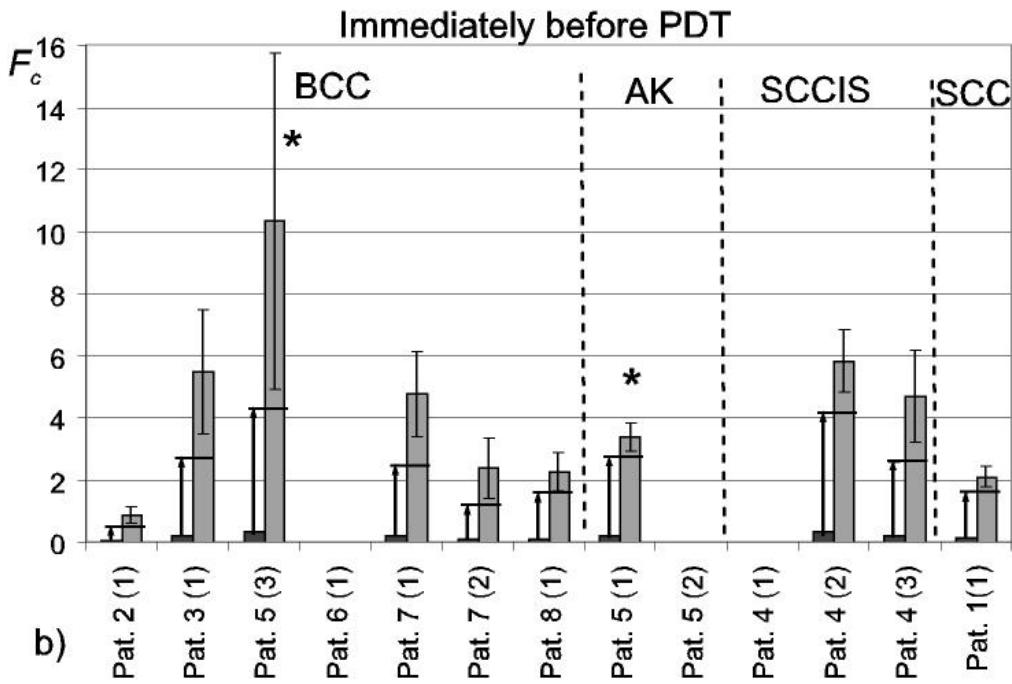
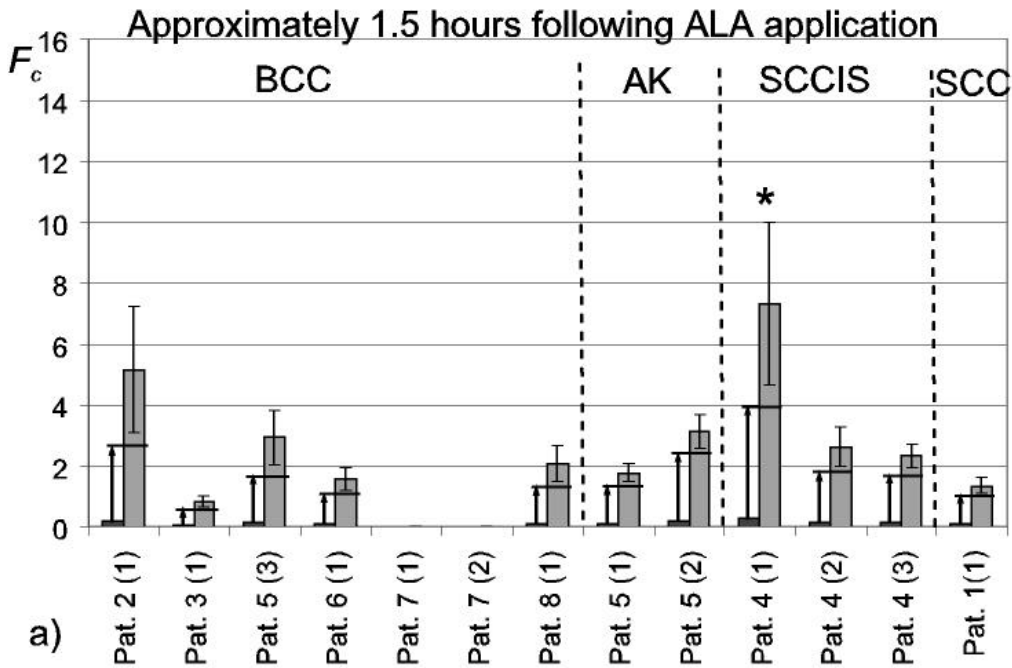


Fig. 5. Typical data from the multi-colour fluorescence imaging system are illustrated. The lesion examined is a mixed superficial and nodular BCC just below the left ear of patient number seven. The data are collected just before PDT, six hours and 15 minutes after ALA application. The images on top are white light photos of the lesion. To the left areas clinically judged as superficial (sBCC) and nodular BCC (nBCC), as well as regions of telangiectasia (TAE) are indicated. The unmarked areas are judged as normal skin. The same areas are indicated in the image to the right. In this image the fluorescence information for the area judged by the system to be suspicious is also shown as an overlay. In the middle row fluorescence emission spectra recorded from two positions are shown to the left. The wavelength bands A and D used in the image analysis are also indicated in the graph. To the right the same false colour coded representation of the processed multi-colour fluorescence image as given above is shown, but now for the entire area examined. A vertical scan across the centre of the image is also displayed in the evaluated F_c function value. In the bottom row, the same processed image is shown, to the right including only pixels above the threshold set for the system to judge the tissue to be a lesion, and to the left with pixels below this threshold only.



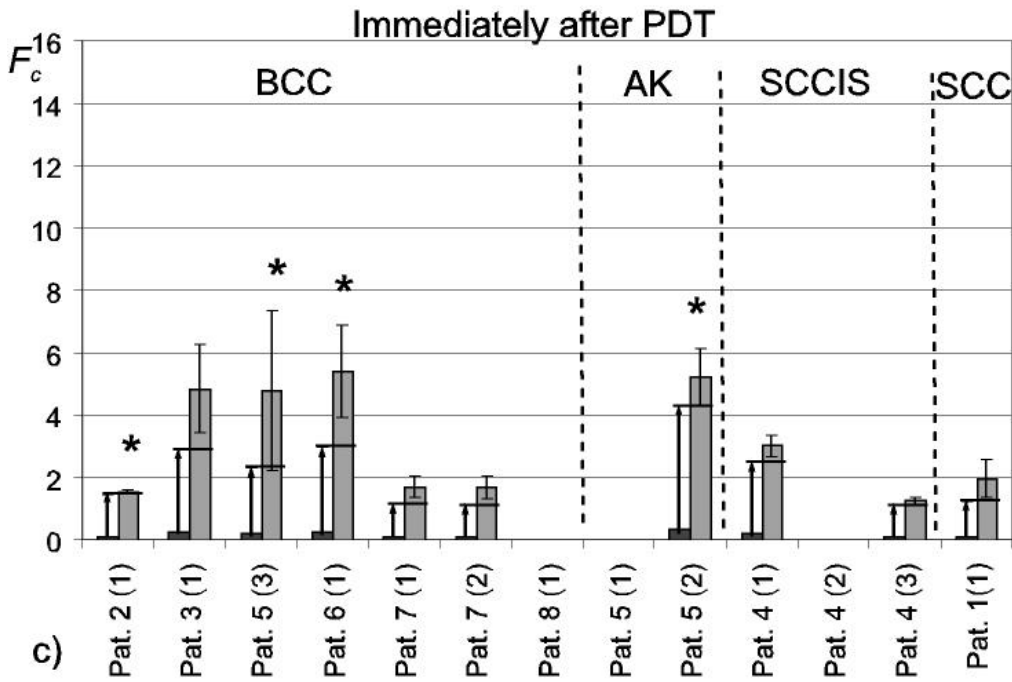


Fig. 6 The bar charts presents the evaluation results for the multi-colour fluorescence imaging system for each lesion. The left bar indicates the standard deviation of the F_c function in the normal area chosen. The average value of F_c in this region is set to zero by adjusting the constant k_1 in the analysis. Also the threshold value, defined as 13 times the standard deviation in the normal tissue, which the system uses to signal the lesion, is marked with an arrow and a vertical line. The right bar indicates the average function value F_c as well as its standard deviation for the area marked as suspicious by the system. Stars (*) indicate that the evaluated signals had a poor signal-to-noise ratio, and that the values may be less accurate. a) Results approximately 1.5 hours following ALA application, b) Results immediately before photodynamic treatment, and c) Results immediately after treatment.

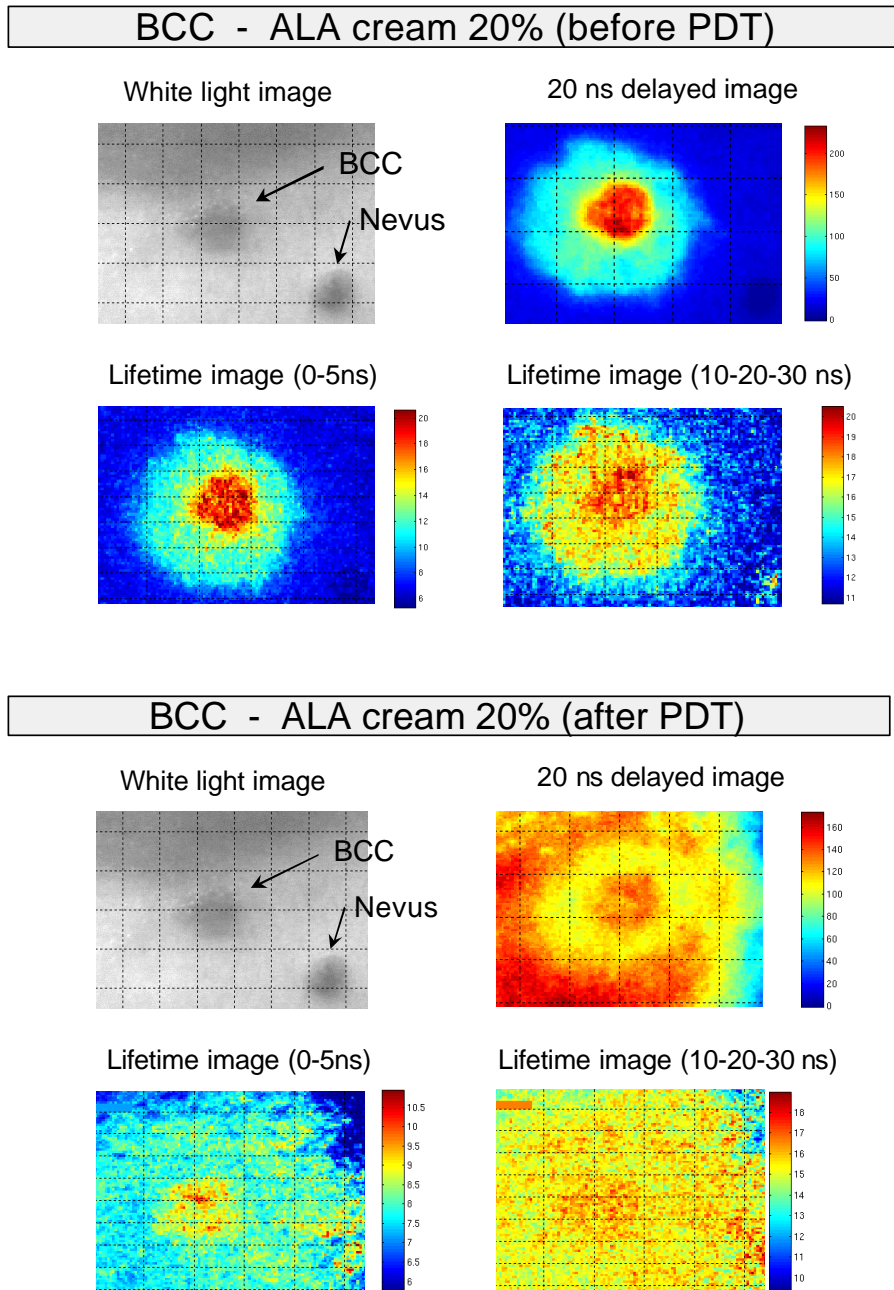


Fig. 7. Typical fluorescence lifetime images before (a) and after (b) PDT of a typical BCC lesion. In the upper left corner, a white light image of the lesion and the surrounding skin is shown. As can be seen there is a naevus close to the lesion. In the upper right corner a fluorescence image with a 20 ns delay is displayed. The two lower images represent effective lifetime images using two early gates (left) and three longer gates (right).

Patient	Lesion	Diagnosis	Location	Measurements	Prior treatment
1	1	SCC	Finger	1 h 30 min 3 h 20 min 5 h post PDT	Cryosurgery
2	1	BCC	Neck	1 h 30 min 4 h 50 min post PDT	2 × PDT
3	1	BCC	Lower leg	1 h 40 min 17 h 30 min post PDT	Cryosurgery
4	1	SCCIS	Belly	1 h 4 h 45 min post PDT	Cytostatic cream
	2	SCCIS	Shoulder	1 h 4 h 45 min post PDT	Cytostatic cream
	3	SCCIS	Lower arm	1 h 4 h 45 min post PDT	Cytostatic cream
5	1	AK	Chin	1 h 50 min 6 h 15 min post PDT	—
	2	AK	Chin	1 h 50 min 6 h 15 min post PDT	—
	3	BCC	Forehead	1 h 50 min 6 h 15 min post PDT	Surgical excision
6	1	BCC, nodular	Lower leg	1 h 30 min 24 h Post PDT	—
7	1	BCC, mixed superficial and nodular	Neck	6 h 15 min Post PDT	—
	2	BCC, superficial	Upper arm	6 h 15 min Post PDT	—
8	1	BCC, nodular and cystic	Nose	1 h 40 min 3 h 40 min	Surgical excision

Table 1. Data for the patients and lesions examined, including times when the lesions were examined by the three fluorescence instruments. SCC - squamous cell carcinoma, SCCIS – squamous cell carcinoma in situ, BCC - basal cell carcinoma, AK - actinic keratosis

a)

Patient	Lifetime	Intensity
2(1)	+/-	+
3(1)	++	++
5(3)	-	++
6(1)	++	++
7(1)	++	++
7(2)	+/-	+/-
5(1)	-	++
5(2)	-	++
4(1)	+	+/-
4(2)	++	++
4(3)	++	++
1(1)	++	++

b)

Patient	Lifetime	Intensity
2(1)	-	+/-
5(3)	-	??
6(1)	-	+
7(1)	-	+
5(1)	-	+
5(2)	-	+
4(1)	-	-
4(2)	-	+/-
4(3)	-	++
1(1)	-	++

Table 2. Results of the evaluation of the fluorescence lifetime imaging system data. The data were evaluated from the images as very strongly correlated with the area of the lesion (++), strongly correlated with the lesion (+), no contrast or badly correlated with the lesion (-), and undefined (??). a) Data obtained at the first measurement approximately 1.5 hours after application of ALA. b) Data obtained immediately before PDT.

Interstitial photodynamic therapy – diagnostic measurements and treatment in rat malignant experimental tumours

Maria Stenberg^{*a,b}, Marcelo Soto Thompson^{a,b}, Thomas Johansson^{a,b},
Sara Pålsson^{a,b}, Claes af Klinteberg^{a,b}, Stefan Andersson-Engels^{a,b},
Unne Stenram^{a,c}, Sune Svanberg^{a,b} and Katarina Svanberg^{a,d}

^aLund University Medical Laser Centre, Lund University, Sweden

^bDepartment of Physics, Lund Institute of Technology, Lund, Sweden

^cDepartment of Pathology, Lund University Hospital, Lund, Sweden

^dDepartment of Oncology, Lund University Hospital, Lund, Sweden

ABSTRACT

A recently developed multiple fibre system for treating malignant tumours with interstitial photodynamic therapy was used in studies on rats with colon adenocarcinoma inoculated into the muscles of the hind legs. The animals were intraperitoneally administrated δ -aminolevulinic acid (ALA), which is metabolised to protoporphyrin IX (PpIX) in the tissue. The treatment system consists of a laser light source, a beam-splitting system dividing the light into three or six output fibres and a dosimetry programme calculating the optimal fibre position within the tumour as well as the treatment time needed to obtain a given threshold value of the light dose. One aim of the study was to compare the treatment outcome with the modelled dosimetry predictions. Tumour reduction was examined three days *post* treatment. A volume decrease was found in 85% of the treated tumours. The mean volume reduction was 44%, with one tumour completely disappearing. Histopathological examination three days *post* treatment showed substantial necrotic parts which, however, to a smaller extent were present also for non-treated tumours. These results indicated that the tumours have been under treated and the light dose has to be increased. Measurements of the build-up and photo-induced bleaching of PpIX using laser-induced fluorescence were also performed during the experiments.

Keywords: interstitial photodynamic therapy; laser-induced fluorescence; ALA; PpIX

1. INTRODUCTION

Cancer is today a fairly common disease. Recent reports show that the cases of malignant tumours are increasing. In the search for new treatment modalities, photodynamic therapy (PDT) seems to be a conceivable alternative.^{1,2} A photosensitising drug is administrated intravenously, orally or topically and is accumulated in the tumour to a higher degree than the surrounding normal tissue. When the tissue is irradiated with light, a photochemical reaction, which involves the excitation of triplet oxygen to its singlet state, is induced. Singlet oxygen is very toxic and will thus induce tumour cell death. The method has several advantages. It offers a safe and efficient treatment with a short healing period and no or minor cosmetic damages in the treatment of e.g. skin malignancies.^{3,4} The treatment can be performed with minimal side effects and it can easily be performed on an outpatient basis. PDT has so far mainly been used for superficial lesions. This is due to poor light penetration through the tissue. To enhance the method new photosensitizers are under development and evaluation. A new report where esterified δ -aminolevulinic acid (ALA-me) was used shows promising results.⁵ Another alternative would be to use sensitizers with a high absorption in the near IR-wavelength range since the penetration of light in tissue is better for this wavelength region.⁶ Still the treatment depth will not be more than 3-7 mm. To be able to treat thicker and/or deeper lying tumours interstitial PDT can be used.^{7,8} This is performed by guiding the light into the tumour mass via a number of optical fibres inserted in the tumour. This gives a selective local treatment, which minimizes the effect on the surrounding healthy tissue.

* Correspondence: Department of Physics, Lund Institute of Technology, PO Box 118, SE-221 00 Lund, Sweden; E-mail: Maria.Stenberg@fysik.lth.se; WWW: <http://www-atom.fysik.lth.se>; Telephone: +46-46-222 31 19; Fax: +46-46-222 42 50

In this study a system for treating malignant tumours interstitially was used to treat colon adenocarcinoma inoculated into the muscle of the hind leg of Wistar/Furth rats. One aim of the present experimental study was to compare the treatment outcome with predicted dosimetry parameters given by the dosimetry programme.

2. MATERIALS AND METHODS

Briefly, the system consists of a diode laser light source, a beam-splitting unit dividing the light into three or six pathways and focusing the light down to optical fibres that are inserted into the tumour. Further, a software unit automatically controls the beam-splitting unit, and a dosimetry programme calculates the optimal fibre positions and optimal treatment time given a threshold light dose. As a photosensitizer δ -aminolevulinic acid (ALA), which is converted to protoporphyrin IX (PpIX) in the cells via the heme cycle, was used. During the treatment the build-up and photo-induced bleaching of PpIX were measured using laser-induced fluorescence (LIF). Volume reduction was examined three days *post* the interstitial PDT treatment. Histopathological changes were then also examined.

2.1. Animals and drug

In total 13 Wistar/Furth rats, each weighting approximately 250 g were treated (three more rats were included but treatment could not be successfully completed for these). The original cell line of the adenocarcinoma was induced in each of the hind legs of the rats by injection of cell suspension. After seven to eight days, the rats had developed a tumour with a volume of $19.1 \pm 5.9 \text{ cm}^3$ on each hind leg. One of the tumours was treated while the other served as a control tumour for the histopathological and statistical tumour examination. The rats were intraperitoneally administered with δ -aminolevulinic acid (Porphyrin Products, Logan UT, USA; Lot no.101598) at a dose of 100 mg/kg body weight 60 minutes before treatment. All animals were under general anaesthesia during the procedure. They were put asleep using chloral hydrate at a dose of 5 ml/kg body weight. A dose of 0.1-0.2 ml Temgesic was used for pain relieving.

2.2. Interstitial photodynamic system

Interstitial PDT treatment was performed using a multiple-fibre system recently developed at the Department of Physics, Lund Institute of Technology.⁹ The system consists of a light source, which is a CW InGaAsP diode laser designed for medical use (CeramOptec Ceralas PDT 635). The laser emits light at a wavelength of 635 nm and has a variable output power in the range of 0-2 W. The light is guided into an optical fibre with a core diameter of 600 μm (KP-600L, ANDA, Latvia) leading to the beam-splitting system, which divides and focuses the light into three or six individual output fibres. It also enables measurements of the light fluence rate within the tumours via the same fibres using six separate photo diodes mounted on flip-in stages at the optical fibre connectors. When the detector is flipped in the laser light into the fibre is blocked. The photo diodes are connected to a computer board with a multiplexed 10 bit ADC. These signals thus enable feedback light dosimetry and treatment control. A computer with a dosimetry software is used to control and automatically operate the beam-splitting unit. The programme also performs necessary dosimetry calculations. It calculates the optimal fibre positions and minimum treatment time using given tissue optical parameters such as the absorption coefficient, scattering coefficient and anisotropy factor of the tumour and surrounding tissue, as well as the tumour size, shape, light dose for successful treatment and output powers from the fibres.

2.3. Interstitial photodynamic therapy procedure

After 60 minutes of build-up time of PpIX following intraperitoneally injection of ALA the animals were treated with interstitial PDT. The time interval was based on kinetic studies.^{10,11} The skin covering the tumours was shaved to avoid hair in the operating field. The tumours were then exposed by removing the skin. The treatment fibres were carefully placed in the calculated positions as accurately as possible. Also a fibre for fluorescence measurements was inserted in a position in the tumour far from the source fibres. The fibres had a core diameter of 600 μm (KP-600L, ANDA, Latvia). Figure 1 shows a situation where a tumour is treated with three fibres inserted in the tumour mass. The fibres delivered an output power in the range of 50-160 mW each. The treatment time was 5 to 40 minutes depending on the given light threshold dose, size and shape of the tumours and the output from the fibres. The treatment was interrupted in time intervals of 60 seconds to measure the light fluence rate and the photo bleaching of PpIX within the tumour. The animals were sacrificed three days *post* treatment and both control and treated tumour were removed for histopathological examination. The animals were divided into three groups with different treatment parameters; see Table 1.

Table 1 The different groups of the animals.

Group number	Number of rats	Number of fibres	Total estimated absorbed light dose in the tumour region farthest from the light source (J/cm^3)
1	3	6	15
2	4	3	7.5
3	6	6	15

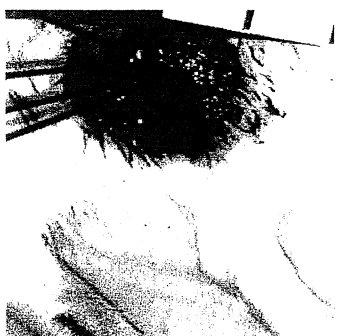


Figure 1 A treatment situation where a tumour is treated with three optical fibres inserted in the tumour mass. The fourth fibre is the one measuring fluorescence.

2.4. Laser-induced fluorescence (LIF)

The PpIX build-up and the PDT-induced bleaching of the photosensitizer during treatment were measured with an optical fibre-based fluorescence system described in detail by af Klinteberg *et al.*¹² The excitation source was a nitrogen-laser pumped dye laser with an excitation wavelength of 405 nm (Laser Science Inc, Cambridge, MA, model VSL-337 and DML-110, respectively) and a pulse repetition rate of about 15 Hz. The excitation light was focused into a fused silica optical fibre with a core diameter of 600 μm (Fiberguide Ind., Stirling, NJ, model SFS600N). The distal end of this fibre was positioned in the tumour as described above. The fluorescence light from the tissue was guided back to the instrument through the same fibre and focused on the entrance slit of a spectrometer (Oriel Corp., Stratford, CT, model MS125). An image-intensified diode array detector (Andor Technology, Belfast, Northern Ireland model DH501-25U-01) was used to record the fluorescence spectrum ranging from 400 to 800 nm. The fluorescence from twenty laser pulses was integrated to obtain spectra with high signal-to-noise ratios. The recorded spectra were displayed on a screen and stored in a computer for later evaluation. Fluorescence spectra were measured just before and during the treatment. A cuvette with Rhodamine 6G was used as an intensity standard and was measured before and after each treatment of the animals.

2.5. Volume reduction

The size of the tumours was measured with sliding callipers just before the treatment and at the time when the animals were sacrificed and the tumours were removed. The tumour volumes were calculated with the formula $(a \times b^2) \times \pi \times 4/3$, where a is the maximum diameter and b is the minimum diameter of the tumour. The growth rate of the individual tumours was calculated by forming the ratio between tumour volume *post* treatment divided by the tumour volume three days *pre* treatment. This value was used as an estimation, together with the histopathological examination, of the therapeutic efficiency.

2.6. Histopathological examination

Both treated and control tumours were histopathologically examined. The tumours were fixed in 4 % formaldehyde immediately following removal and embedded in paraffin. Heamatoxylin-eosin was used to stain sections, which were then examined under a microscope by a pathologist. The pathologist used lattice ocular to obtain the fraction of necrosis in the tumours.

3. RESULTS

3.1. Dosimetry predictions

To test the stability of the dosimetry programme some data simulations were made. The programme was used to calculate the treatment time for a homogenous tumour with a shape of a sphere. Six fibres with an output power of 100 mW each were used. The fibres were placed in the following position (x, y, z); fibre 1 ($r/\sqrt{2}, 0, 0$), fibre 2 ($0, r/\sqrt{2}, 0$), fibre 3 ($-r/\sqrt{2}, 0, 0$), fibre 4 ($0, 0, r$), fibre 5 ($0, 0, -r$), fibre 6 ($r/\sqrt{2}, r/\sqrt{2}, 0$).

0), fibre 4 (0, $-r/\sqrt{2}$, 0), fibre 5 (0, 0, $r/\sqrt{2}$) and fibre 6 (0, 0, $-r/\sqrt{2}$), where r is the tumour radius. This was assumed to be close to the optimal fibre positions for this geometry. The tissue optical parameters used were; $\mu_s=15.00 \text{ mm}^{-1}$, $\mu_a=0.07 \text{ mm}^{-1}$ and $g=0.9$ for the tumour and $\mu_s=15.00 \text{ mm}^{-1}$, $\mu_a=0.05 \text{ mm}^{-1}$ and $g=0.9$ for the surrounding tissue, where μ_s is the scattering coefficient, μ_a the absorption coefficient and g is the anisotropy factor. The treatment time was calculated for different tumour radius for an absorbed threshold light dose of 15 J/cm^3 . The results obtained from the dosimetry programme were compared with theoretical calculations of the treatment time obtained from the fluence rate, $\phi(r)$, using the analytical solution to diffusion theory in an infinite medium with the same optical properties as the tumour. Figure 2 shows the treatment time as a function of the tumour radius calculated with the dosimetry programme and the results using diffusion theory. This shows a good agreement and thus a good stability of the programme.

As an example of the dosimetry calculation obtained from the dosimetry programme, the fibre positions in one treated tumour are shown in Figure 3. The tumour had a shape of an ellipse with the size $19 \times 15.5 \text{ mm}$, maximum and minimum diameter, respectively. The calculated fibre positions (x, y, z) were; fibre 1 (-0.7, 6.0, 0.7), fibre 2 (4.5, -2.2, 0.0), fibre 3 (-3.0, -4.5, 0.7), fibre 4 (6.0, 2.2, -0.7), fibre 5 (-6.0, 0.7, -0.7) and fibre 6 (-0.7, -1.5, 0.0). The values are given in mm and are calculated from the centre of the tumour. The last co-ordinate indicates the depth in the tumour. Output powers from each fibre were 130, 120, 160, 110, 130 and 140 mW, respectively. The threshold light dose was set to 15 J/cm^3 , which gave a resulting treatment time of 15 minutes. Figure 4 shows the evolution of delivered light dose, which can be followed during the treatment.

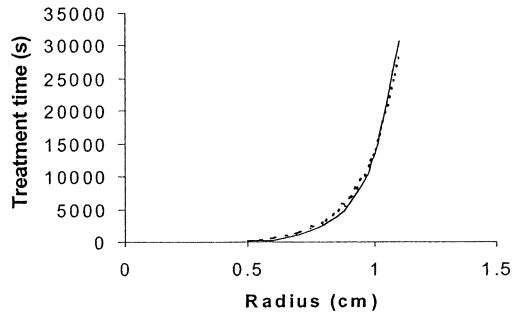


Figure 2 The treatment time as a function of tumour radius calculated using the dosimetry programme (solid line) and theoretic calculations using diffusion theory (dotted line).

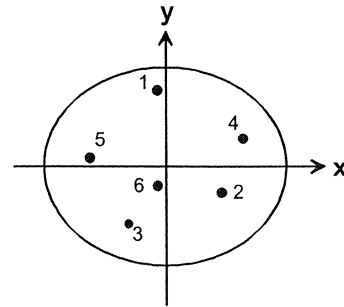


Figure 3 The optimal fibre positions given by the dosimetry programme.

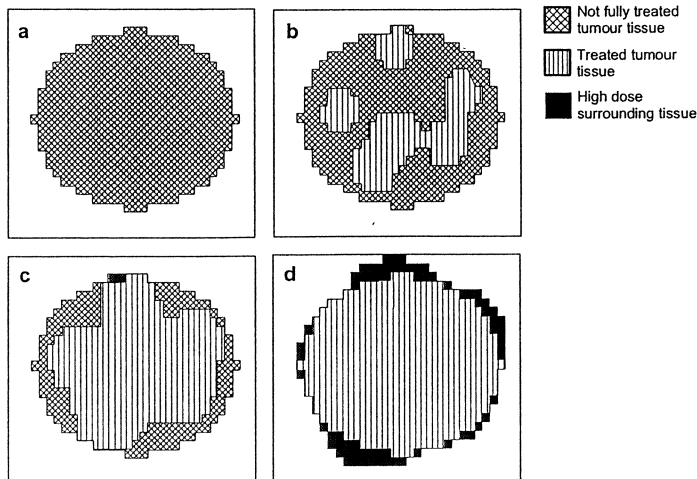


Figure 4 The evolution (a-d) of delivered light dose.

3.2. Photodynamic effects

The histopathological result showed that on an average 70% of the treated tumour mass was necrotic. As a reaction to the treatment a large amount of polymorphonuclear leucocytes were found in the necrotic area. The examination also showed that the area around the tumours was well supported with blood vessels, supplying the tumour with oxygen. Possible channels produced by inserting the optical fibres in connection with the treatment from the fibres were found in some samples. As an example a histopathological section of one treated tumour is shown in Figure 5. Necrotic parts were also present to a smaller extent (on an average 38% of the tumour mass) in the control tumours (spontaneously).

The evaluated relative tumour volumes three days *post* treatment are given in Figure 6. The results from 13 rats are shown. Among the treated tumours 85% decreased in volume, with one tumour completely disappearing. The mean volume reduction of all treated tumours was 44%. Two tumours increased their volume. Volumes of the control tumours were on an average unchanged.

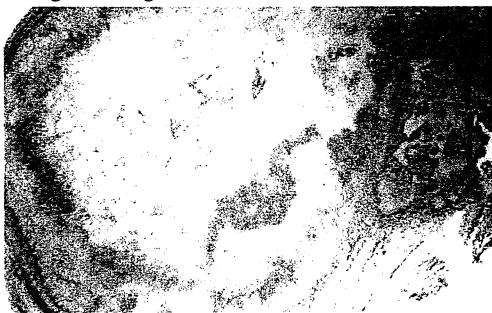


Figure 5 The treated tumour showing approximately 90% necrosis (light grey region in the centre of the picture) and bands of polymorphonuclear leucocytes. The right top of the picture shows vital tumour.

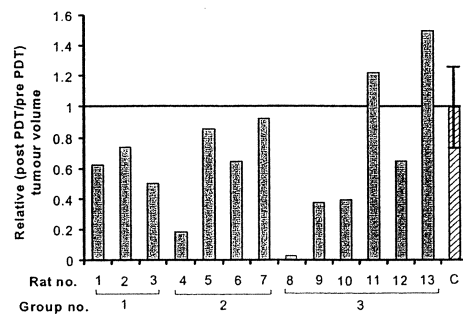


Figure 6 The relative tumour volume. 85% of the tumours decreased their volume. The over-all tumour reduction was on an average 44%. C indicates the average of the control tumours \pm standard deviation.

3.3. Photo bleaching

Measurements with laser-induced fluorescence of photo bleaching of PpIX indicated that the sensitizer was in all cases completely bleached away as a result of the PDT treatment. Figure 7 shows the photo bleaching of the 635 nm peak of PpIX and in Figure 8 the whole spectra are shown.

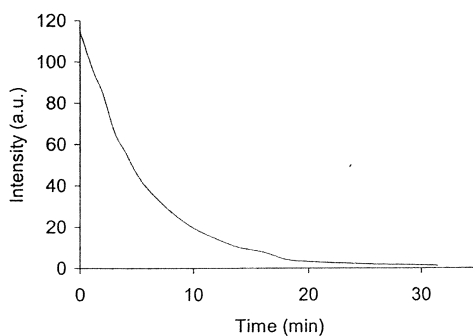


Figure 7 Photo bleaching of the PpIX peak at 635 nm measured with LIF during the interstitial PDT treatment.

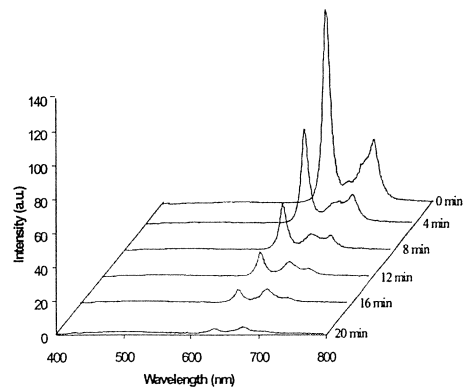


Figure 8 LIF spectra for PpIX bleaching measured during treatment.

4. DISCUSSION

Interstitial photodynamic therapy is a fairly new method of treating large tumours with very good treatment efficiency. The method has the potential of providing good selectivity with large damage to the target tissue while the effects on the surrounding tissue are minimized. The method offers a possibility to treat tumours that are large and difficult to reach with superficial illumination. Several reports in the literature, including this one, show that interstitial PDT is a promising method.^{8,13}

The system used in these experiments has several unique features. It calculates the optimal positions of the fibres to obtain an effective treatment. These calculations are based on the size and shape of the tumour and the output effect from each fibre. The dosimetry programme also calculates the treatment time for a given threshold light dose. The treatment time is sufficiently long to obtain tumour necrosis but short enough so that the effect on the surrounding tissue is minimized.

The light dose delivered to the tissue is graphically illustrated on the computer screen and can be followed during the treatment. When a high dose is reached in one part of the tissue the light delivered in this part can be switched off by closing the output gate for the corresponding optical fibre. Measuring the fluence rate inside the tumour as well as the photo bleaching offers a feedback into the dosimetry and a better treatment control. When the fluorescence from the photosensitizer is too low it is no longer useful to continue and the treatment can therefore be interrupted.

An aim of this study was to compare the predicted light dose with the treatment outcome. The results from the histopathological examination showed that in average 70 % of the treated tumour mass was necrotic. This indicates that the threshold light dose has to be increased to make the treatment more efficient. Necrotic areas were also found in the control tumours. This is probably due to the fact, that tumours had grown too large, which for this tumour model induces necrosis. To be able to better correlate the necrotic tumour volumes with the treatment parameters, a better tumour model would be desirable. Another possible improvement would be to increase the accuracy with which the optical fibres were positioned. For this purpose an ultra-sound imaging system can be used, which will also give better measurements of the size and shape of the tumour.

Further improvements of the system are planned. Optical fibres with a smaller core diameter are preferable, causing less mechanical damage on the tissue. Then an improved light source with ability to effectively couple the light into smaller optical fibres is also needed. Sensitizers absorbing light in the near IR wavelength range will allow an increase in the penetration depth of the light and larger tumours could thus be treated. New experiments along these lines are planned for the future.

ACKNOWLEDGEMENTS

The skilful handling of tumour induction by Monica Radnell is greatly appreciated as well as the help with the animals during treatment by Niels Bendsoe and Charlotta Gustavsson. This work was funded by the Swedish Strategic Research Foundation (SSF).

REFERENCES

1. F. Stewart, P. Baas, and W. Star, "What does photodynamic therapy have to offer radiation oncologists (or their cancer patients)?", *Radiother. Oncol.* 48, pp. 233-248, 1998.
2. C. Fritsch, G. Goerz, and T. Ruzicka, "Photodynamic therapy in dermatology", *Arch. Dermatol.* 134, pp. 207-214, 1998.
3. K. Svanberg, T. Andersson, D. Killander, I. Wang, U. Stenram, S. Andersson-Engels, R. Berg, J. Johansson and S. Svanberg, "Photodynamic therapy of non-melanoma malignant tumours of the skin using topical δ -amino levulinic acid sensitization and laser irradiation", *Br. J. Dermatol.* 130, pp. 743-751, 1994.
4. I. Wang, N. Bendsoe, C. af Klinteberg, A.M.K. Enejder, S. Andersson-Engels, S. Svanberg, and K. Svanberg, "Photodynamic therapy versus cryosurgery of basal cell carcinomas; results of a phase III randomized clinical trial", to appear.
5. M. Soto Thompson, L. Gustafsson, S. Pålsson, N. Bendsoe, M. Stenberg, C. af Klinteberg, S. Andersson-Engels, and K. Svanberg, "Photodynamic therapy and diagnostic measurements of basal cell carcinomas using esterified and non-esterified 5-aminolevulinic acid", to appear.

6. G. Jori, "Tumour photosensitizers: approach to enhance the selectivity and efficiency of photodynamic therapy", *J. Photochem. Photobiol. B* 36, pp. 87-93, 1996.
7. T.J. Dougherty, R.E. Thoma, D.G. Boyle, and K.R. Weishaupt, "Interstitial photoradiation therapy for primary solid tumors in pet cats and dogs", *Cancer Res.* 41, pp. 401-404, 1981.
8. J.P.A. Marijnissen, J.A.C. Versteeg, W.M. Star, and W.L.J. van Putten, "Tumor and normal response to interstitial photodynamic therapy of the rat R-1 rhabdomyosarcoma", *Int. J. Radiat. Oncol. Biol. Phys.* 22, pp. 963-972, 1992.
9. T. Johansson, M. Soto Thompson, M. Stenberg, C. af Klinteberg, S. Andersson-Engels, S. Svanberg, and K. Svanberg, "Fibre-optic system for interstitial photodynamic therapy of massive tumours employing optical feed-back for light dosimetry", Manuscript in preparation.
10. J. Johansson, R. Berg, K. Svanberg, and S. Svanberg, "Laser-induced fluorescence studies of normal and malignant tumour tissue of rat following intravenous injection of δ -amino levulinic acid", *Lasers Surg. Med.* 20, pp. 272-279, 1997.
11. N. van der Veen, H.L.L.M. van Leengoed, and W.M. Star, "*In vivo* fluorescence kinetics and photodynamic therapy using 5-aminolaevulinic acid-induced porphyrin: increased damage after multiple irradiations", *Br. J. Cancer* 70, pp. 867-872, 1994.
12. C. af Klinteberg, M. Andreasson, O. Sandström, S. Andersson-Engels, and S. Svanberg, "Compact medical fluorosensor for minimally invasive tissue characterisation", Manuscript in preparation.
13. C.P. Lowdell, D.V. Ash, I. Driver, and S.B. Brown, "Interstitial photodynamic therapy. Clinical experience with diffusing fibres in the treatment of cutaneous and subcutaneous tumours", *Br. J. Cancer* 67, pp. 1398-1403, 1993.

Feasibility study of a system for combined light dosimetry and interstitial photodynamic treatment of massive tumors

Thomas Johansson, Marcelo Soto Thompson, Maria Stenberg, Claes af Klinteberg, Stefan Andersson-Engels, Sune Svanberg, and Katarina Svanberg

A system for the photodynamic laser treatment of massive tumors that employs multiple optical fibers to be inserted into the tumor mass is described. The light flux through the tumor can be assessed by use of the individual fibers both as transmitters and as receivers. With a computer model that describes the diffusive light propagation, optical dosimetry is under development. The system has been tested in an experimental animal tumor model in preparation for clinical work. Currently, delta-aminolevulinic acid is used as a sensitizer, activated by 635-nm radiation from a 2.0-W compact diode laser system. With the availability of future, highly selective drugs absorbing approximately 750 nm, larger tumor volumes should be treatable, and surrounding, sensitive normal tissue should be spared. © 2002 Optical Society of America

OCIS codes: 170.5180, 170.3660, 170.1610, 300.2530, 060.2310.

1. Introduction

Despite extensive research and developmental activities regarding techniques for the abatement of cancer, the disease continues to take high tolls in human suffering and lives. Among the many new treatment modalities emerging, photodynamic therapy (PDT) offers potentially unique advantages in terms of selectivity and efficacy.¹⁻³ PDT relies on a preferential tumor retention of an administered photosensitizing agent, which is followed by a laser-mediated release of singlet oxygen in tumor cells. With the introduction of delta-aminolevulinic acid (ALA), a sensitizer precursor that induces protoporphyrin IX (PpIX) as a sensitizing agent, the clinical applications of PDT increased a great deal, especially with respect to skin tumors prepared with topically applied ALA cream.⁴⁻⁹

It is important in the development of more efficient

PDT to have chemically well-defined sensitizers that exhibit a high contrast between tumor cells and normal tissue and that are nontoxic and swiftly cleared from the organism. Because light penetration of tissue under the influence of absorption and scattering increases toward the near infrared region, it is advantageous to have sensitizer absorption in that region rather than at 635 nm pertaining to PpIX. Further, the quantum yield in terms of singlet oxygen production should be as high as possible. Sensitizers such as mesotetra hydroxyphenylchlorine ($\lambda_{\text{abs}} = 652$ nm), lutetium texaphyrin ($\lambda_{\text{abs}} = 732$ nm), and bacteriochlorin ($\lambda_{\text{abs}} = 760$ nm) are interesting in this context. Still, the tumor-eradication depth achievable in surface irradiation will be limited to 3–7 mm because of tissue absorption. Although the penetration is sufficient for treatment of most skin malignancies and lesions in hollow organs treated endoscopically, solid tumors remain outside the region of treatment. An adjunct PDT treatment can still be performed after surgical debulking of the tumor.

The system described here is developed for PDT of massive and potentially inoperable tumors by use of interstitial optical fibers for illumination of the tumor mass. Interstitial PDT has certainly been applied before (see, e.g., Refs. 10–13). What is new in the research presented here is the integration of optical dosimetry and diagnostics to permit an optimized

T. Johansson, M. Soto Thompson, M. Stenberg, C. af Klinteberg, S. Andersson-Engels, and S. Svanberg (Sune.Svanberg@fysik.lth.se) are with the Department of Physics, Lund Institute of Technology, P.O. Box 118, S-221 00 Lund, Sweden. K. Svanberg is with the Department of Oncology, Lund University Hospital, S-221 85 Lund, Sweden.

Received 7 March 2001; revised manuscript received 20 August 2001.

0003-6935/02/071462-07\$15.00/0

© 2002 Optical Society of America

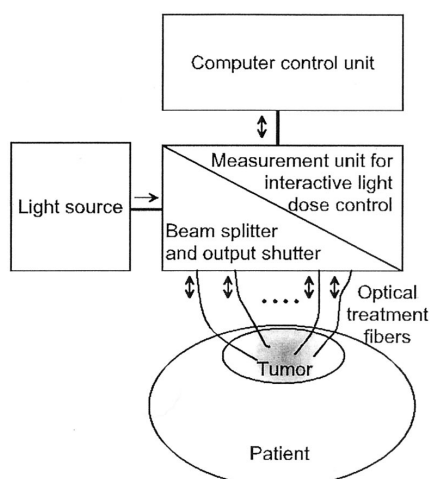


Fig. 1. Schematic view of a multifiber interstitial PDT system with optical feedback.

treatment. The working principles of the system are illustrated in Fig. 1.¹⁴ First, the optimal fiber positions, the fluence rate in the treated region, and the required treatment time are calculated. Continuous laser radiation of an appropriate wavelength is then divided into a number of individual optical fibers, which are inserted in the appropriate positions in the tumor mass while positioned in the lumen of syringe needles. Apart from being able to deliver light into the tumor, each fiber can also act as an antenna that receives light from the other fibers, thus allowing a measurement of the light flux. Each fiber can be quickly switched from a transmitter to a receiver mode of operation. The data from the measurements can be fed into the dosimetry model, which calculates the light distribution in the tumor to allow adjustments of the fiber-transmitted power to achieve an optimal treatment. During the treatment, the diagnostic light flux measurements are repeated a few times because it is known that tissue's optical properties are altered during the treatment.¹⁵ The purpose is to ensure that each tumor cell is placed in a sufficiently effective photon bath for eradication. In the continued development of the system, the same fibers will be used for a number of other optical measurement tasks, which are important for optimizing the process. Parameters to be determined are oxygen concentration through the tumor, concentration of the sensitizer, and temperature at each of the fiber tips.

2. Description of the System for Interstitial Photodynamic Therapy

A. Hardware Integration

The major parts of the optical layout of the interstitial treatment system are schematically shown in Fig. 2. The laser unit is a 2-W cw diode laser (Cer-

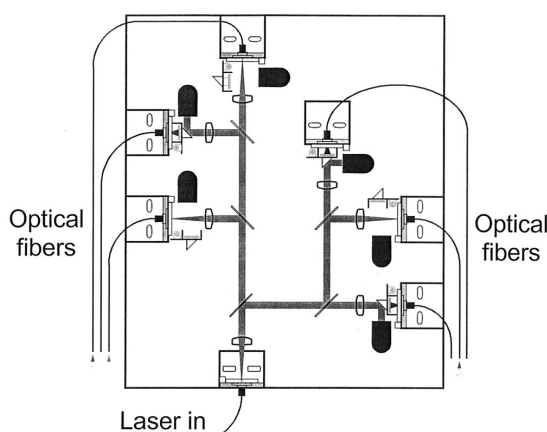


Fig. 2. Setup of the beam-splitting-light-flux-measuring unit.

alas PDT 635, CeramOptec, Bonn, Germany) operating at 635 nm. The laser light is coupled into an optical fiber with a core diameter of 400 μm (KP-400L, ANDA, Livani, Latvia). This fiber is connected to a beam-splitting unit in which the light is divided into six different pathways. These six light beams are individually focused into six 400- μm fibers.

Beam splitters and lenses are used to divide the light and focus it into the output fibers. The components are placed on an aluminum plate of dimensions 300 mm \times 250 mm \times 8 mm, and the optical axis is at a height of 50 mm. The fiber from the laser is connected to the beam-splitting unit with an SMA connector (VERTX, Sweden). This fiber output end is at the focus of an $f = 12\text{-mm}$ lens (Melles Griot 01 LAG001/067) used to collimate the light. A 50:50 beam splitter divides the light into two equal parts. The optical components are the same for both beams, but the geometrical paths are slightly different to minimize the size of the beam-splitting unit. The next component is a 33:67 beam splitter in which the 33% light is focused into one of the treatment fibers with a lens of the same type as employed in the collimator. These treatment fibers are also connected with SMA connectors. The other part from the 33:67 beam splitter is again divided into two equal parts with a 50:50 beam splitter and focused with identical lenses into their individual treatment fibers.

The beam-splitting unit thus divides the treatment light into six optical fibers. However, the unit has also been adapted to allow measurement of the light fluence rate at the individual fiber tip locations for dosimetry purposes. When measurements are made, at least one of the fibers has to transmit light, so that the other fibers can be used to measure the fluence rate of the light from that fiber at the positions of the other fiber tips. To do this, six independent photodiodes, each with a detector surface of 16 mm², can be rotated into the light path of the incom-



Fig. 3. Photograph of the system with six emitting fibers and a dosimetry chart displayed on the computer screen.

ing light from the treatment fibers; see Fig. 2. The signals measured by the diodes were calibrated by placement of the fibers into a large tank filled with an Intralipid (Fresenius, Kabi, Uppsala, Sweden)/ink mixture with optical properties determined by independent measurements by use of an integrating sphere setup. Direct current motors with appropriate gearboxes and friction clutches swing the gatelike mounts into position. Then the outgoing laser light is automatically blocked on the other side of the gate. The photodiodes are connected to a computer board with a multiplexed 10-bit analog-to-digital converter, measuring signals in the interval 0–5 V. A photograph of the system is shown in Fig. 3, with all six fibers transmitting light and a dosimetry chart displayed on the computer screen.

B. Software for System Steering

A custom-made computer program was written for the dosimetry calculations to control the beam-splitting unit and to measure the light flux.¹⁶ The development platforms used for this purpose were LabVIEW (National Instruments, Austin, Tex.) and C++ (Microsoft Corporation, Seattle, Washington). The program is divided into two parts. In the first part, the operator has to define absorption and scattering parameters for the tumor and the healthy surrounding tissue. The absorption coefficients used were 0.07 and 0.05 mm^{-1} for tumor and muscle tissue, respectively, while a value of 1.6 mm^{-1} was used for the reduced scattering coefficient for both types of tissue. Also, the shape and size of the tumor have to be defined. The operator can determine where to place the different fibers, or, alternatively, the computer can calculate the optimal positions. The criterion used is that the calculated light dose absorbed

by the photosensitizer should exceed a predefined limit in the entire tumor, while the volume outside the tumor, for which this limit is exceeded, is minimized. The threshold used in this study was 15 J/cm^3 . The system can now calculate the absorbed fluence rate in every part of the tissue because of the individual fibers. The calculations are performed by solution of the diffusion equation numerically by use of the finite element method.^{17–19} The numerical method was tested for simple geometries in which an analytical solution is available and a good agreement was found.

The second part of the program is used during the treatment. The program guides the operator through different steps such as loading the right setup file, assigning a name for the output file, putting the fibers into position, and turning the laser on. After this, the operator can press the start button, and the treatment is initiated. The map that is calculated in the first step is now used to display the calculated absorbed dose. This map is frequently updated throughout the entire treatment so that the operator has a feeling of what is happening during the treatment. At regular time steps, the computer interrupts the treatment and initiates a series of measurements of the light. The measurements are done in two ways. The first measurement method is the use of one fiber as the transmitter and the other ones as receivers. Each fiber is used as a transmitter in sequence. The second measurement method is to use five fibers as transmitters and the last one as a receiver. Each fiber is also used sequentially as a receiver. All these data are saved to a file for later evaluation. The system will stop the treatment when the calculated time for full treatment is reached. This means that the different fibers suc-

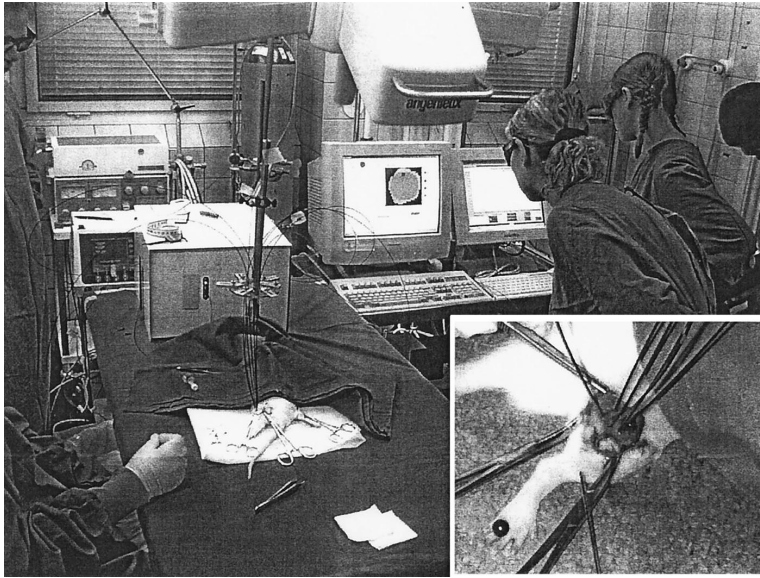


Fig. 4. Photograph of an animal treatment session.

cessively shut down their emission (when the motors swing in the detector that blocks the corresponding laser beam) when the individual tasks have been fulfilled.

3. Initial System Performance Studies

Interstitial photodynamic treatments of Wistar-Furth rats were performed in three campaigns, comprising three, four, and six animals, respectively. The rats, each weighing approximately 250 g, had been subcutaneously inoculated on both hind legs with cells from chemically induced adenocarcinoma.²⁰ Approximately one week after inoculation the tumors typically had diameters of 10–20 mm. Each rat was intraperitoneally injected with ALA at a dose of 100 mg/kg body weight. Treatments were performed 1–2 h after the injection. In total, 13 tumors were treated in anesthetized animals. For 11 of the animals, the skin over both tumors was cut open, and the tumors and muscle surfaces were exposed. Three or six fibers were inserted into one of the tumors at predetermined locations. The tumor on the other leg served as an untreated control in the last two campaigns. In eight of the animals, six channels into the control tumor mass were made with the syringe in the same way as for the treated tumor. For the two last animals, the fibers and syringe needles were inserted into the tumor masses (treated and control) through the skin instead of first exposing the free surface by surgery. This procedure was found to work technically well with the additional advantage of perturbing the tumor area less. Frequently, an extra, diagnostic fiber was inserted into a position between the treatment fibers for assessing the PpIX accumulation and PDT-induced bleach-

ing.²¹ A fluorosensor, which has been fully described in Ref. 22, was used for those measurements. Optical measurements for assessing the light fluence rate through the tumor were made, and PDT treatment as described above was iteratively performed. For treated and control tumors the skin was closed with stitches after the procedure, and the rats were left with food and water *ad libitum* for three days before sacrifice and tumor extraction and preparation for histopathology. A photograph of the treatment scene is shown in Fig. 4. A primary evaluation was made by measurement of the tumor volume before the treatment and three days after. Two orthogonal dimensions were measured, and the corresponding ellipsoid volume was calculated. After the measurements of the size, the tumors were placed in 20% formaldehyde for subsequent routine histopathology.

4. Results

The output power from each individual treatment fiber depends somewhat on the fiber used. The power could easily decrease 20% if the fiber not was properly polished. The total throughput of the beam-splitting unit was 45%, with the light power reasonably uniformly distributed between the individual fibers. Curves of the measured signals as a function of distance from the emitter in the homogeneous Intralipid/ink phantom used for calibration purposes are shown in Fig. 5. They gave a similar sensitivity for all diodes but one. The sensitivity was 0.055 W/(cm² V), yielding a measurement range of 0–275 mW/cm².

An illustration of how the treatment of a tumor utilizing six fibers progresses until the point at which the whole tumor has received the threshold light dose

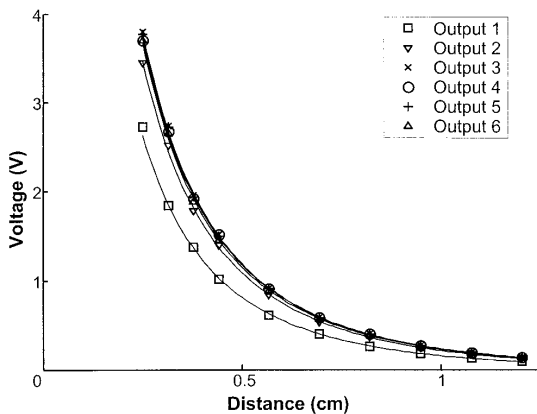


Fig. 5. Measured signals as a function of distance measured in an Intralipid/ink phantom. These curves were used to calibrate the detection sensitivity of the six fibers in the detection mode.

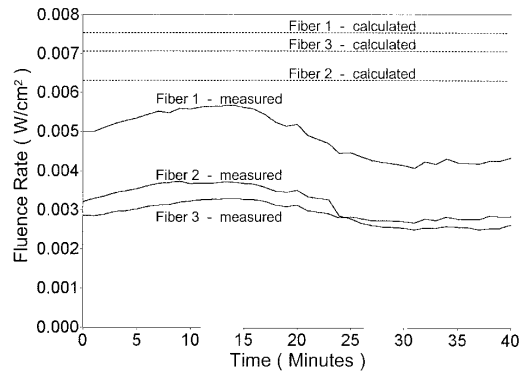


Fig. 7. An example of graphs of measured fluence rates during a treatment that used three treatment fibers. Each graph represents the measured fluence rate for that detection fiber when the other two fibers were transmitting treatment light. The predicted values calculated before the treatment started are also indicated.

is shown in Fig. 6. The figure illustrates the absorbed light dose in a plane through the tumor at four times during the treatment. An example of measured fluence rates during another treatment in which only three fibers were used is illustrated in Fig. 7.

The laser-induced tissue fluorescence level at a point 7 mm down from the surface of the tumor is shown in Fig. 8 before the start and during the course of the treatment. The bleaching of the PpIX can clearly be seen. The absorbed light dose can be as-

sessed from either the absolute value of the 635-nm peak, the intensity of which is inversely proportional to the absorbed light dose, or from the relative intensity at 650 and 635 nm, which monitors the successive build-up of photodegradation products.²³ Figure 8 shows the changes in fluorescence intensity at the 635-nm peak during the treatment.

The temporal development results are shown for 13 tumors in Fig. 9. It was found that 11 out of 13 tumors (85%) reduced their size over the short period of three days following PDT. The average reduction

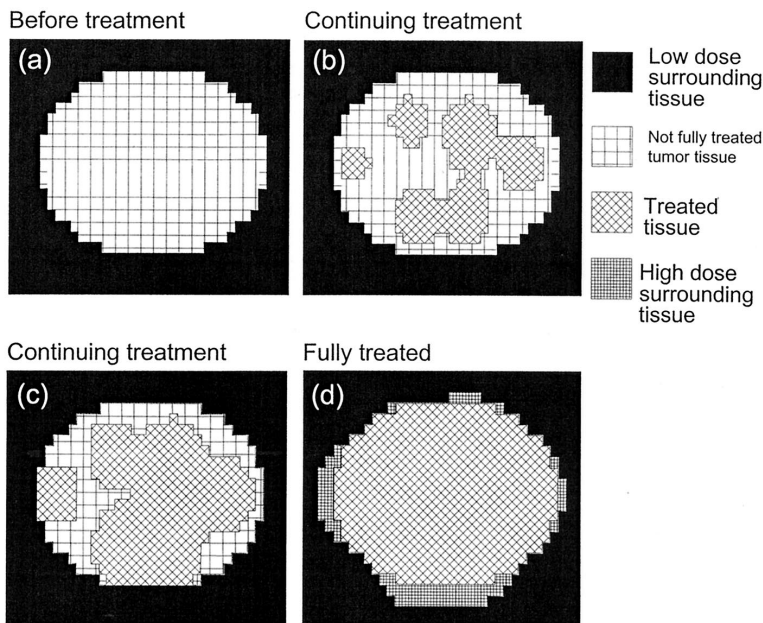


Fig. 6. Dosimetry modeling and temporal evolution of delivered light dose. The dose at distances very close to the source fibers, a region in which the diffusion approximation is not valid, was increased manually.

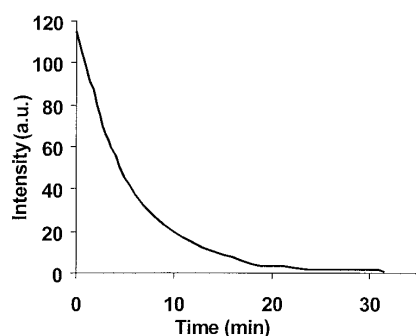


Fig. 8. Demonstration of bleaching of PpIX inside the tumor mass, owing to the flux of red photons through the tumor. The fluorescence intensity at 635 nm was recorded.

for the 13 tumors was 34%. For ten of the tumors, reference tumors of the other hind leg were prepared in a way similar to the treatment of the tumors, as discussed above. The results from the tumor inter-comparison (treated versus nontreated) are shown in Fig. 10. Here it can be seen that six out of ten tumors (60%) were reduced compared with the controls. The average reduction for the ten tumors (with respect to their respective reference tumor) was 28%.

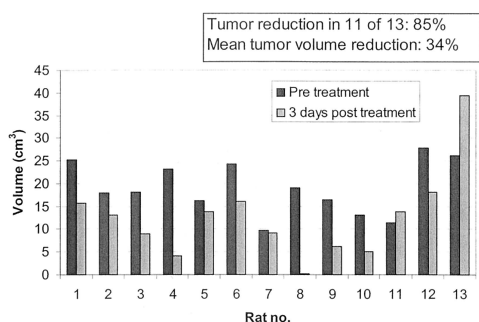


Fig. 9. Comparison of tumor volume before and three days after interstitial PDT in Wistar-Furth rats.

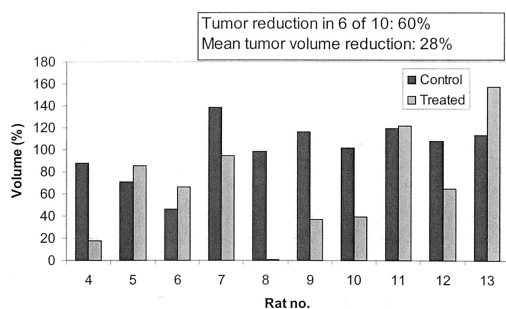


Fig. 10. Comparison of volume development for treated and control tumors during a three-day period starting just before the PDT and extending three days after.

It should be noted that the outcome is obscured by the fact that for two control tumors (in rats #5 and #6) a strong spontaneous reduction occurred.

The histopathological examinations visualized a large central necrosis in the treated tumors. Most treated tumors also had remaining vital regions with tumor cells close to the border to the muscle. Also, the control tumors showed regions of necrosis.

5. Discussion

A system for interstitial PDT of massive tumors, believed to be novel, has been developed and undergone an initial evaluation. It has proved to work reliably and to be useful for treating tumors that are not candidates for superficial illumination PDT owing to their size. The treatment outcome was, however, not fully satisfactory. Complete response was not obtained for most tumors, neither in the tumor-size measurements nor in the histopathological examination. Improvements are thus necessary. The threshold used for the absorbed light dose for killing the tumor cells may need to be increased. It would furthermore be of interest to know the oxygenation of the tissue, as it is important to have enough oxygen available for the PDT to be efficient. Also, three days is clearly an extremely short time for assessing the treatment outcome. Even though extensive parts of the tumors were killed, they did not reduce much in size after this short time. Still, using both size-evaluation methodologies presented in Figs. 9 and 10, we found that the interstitial treatment was effective in reducing the tumor mass. The evaluation time was chosen by taking practical considerations into account. The untreated tumors grew quickly, and a longer evaluation time would not have been good, as the general condition of the animals would have been much more affected. In addition, the spontaneous necrotic regions also developing in the control tumors made the evaluation uncertain. The model used for this initial evaluation was thus not ideal.

An extensive developmental plan for the system and treatment procedures now exists. We intend to use many of the procedures developed for other treatment modalities, for positioning the fibers. In most applications of brachytherapy, the radioactive-substance-loaded needles are positioned under visual inspection and palpation only. However, other applications may need more accurate positioning. The full clinical implementation of this system might thus require the integration of the new technology with stereotactic techniques, frequently used in the management of brain tumors. As a first step in future treatments, we plan to measure the tumor dimensions and guide the fiber positioning with ultrasound techniques.

The system will be improved in several ways. The data recorded on the flow of light through the tumor were so far not used as direct feedback for the ongoing treatment. The experience gained in animal and first clinical implementation will allow the setting of the parameters for an interactive feedback loop. We

also plan to integrate fluorescence measurements in each of the treatment-measurement fibers. This will allow an assessment of the distribution of the sensitizer concentration through the tumor mass. If the fiber tips are prepared with a suitably chosen rare-earth salt, melted into the quartz, it will be possible to measure sharp temperature-sensitive lines²⁴ superimposed on the broadband tissue fluorescence. This will allow determination of the temperature at the fiber locations. Possible synergism between photodynamic and thermal therapy might be exploited. It will be possible to see if coagulated blood makes the temperature rise at the fiber surface, blocking further light delivery. Because the availability of tissue oxygen is important for successful PDT, spectroscopic assessment of this parameter should be considered.

Clearly, the goal of the project is to progress to the state of clinical use as soon as possible. We are now convinced that the technique could be used to treat tumors not candidates for superficial PDT and that many clinical treatments would benefit from this modality. Those tumors are much better suited for this type of treatment than the ones treated in this initial study.

Important contributions to this project in its earlier stage were made by Roger Berg, Jonas Johansson, Nicklas Ohlsson, and Ola Rylow. We are also grateful to Lotta Gustafsson and Monica Radnell for help in the animal treatments and to Elisabeth Kjellén, Niels Bendsoe, and Unne Stenram for valuable discussions and assistance. This research was supported by the Swedish Board for Technical and Industrial Development and the Swedish Strategic Research Foundation.

References

1. S. L. Marcus, "Photodynamic therapy of human cancer: clinical status, potential and needs," in *Future Directions and Applications in Photodynamic Therapy*, C. J. Gomer, ed., Proc. SPIE **IS-6**, 5-56 (1990).
2. L. I. Grossweiner, *The Science of Phototherapy* (CRC Press, Boca Raton, Fla., 1994).
3. T. J. Dougherty, C. J. Gomer, B. W. Henderson, G. Jori, D. Kessel, M. Korbelik, J. Moan, and Q. Peng, "Photodynamic therapy," *J. Natl. Cancer Inst.* **90**, 889-905 (1998).
4. J. C. Kennedy, R. H. Pottier, and D. C. Pross, "Photodynamic therapy with endogenous protoporphyrin IX: basic principles and present clinical experience," *J. Photochem. Photobiol. B* **6**, 143-148 (1990).
5. J. C. Kennedy and R. H. Pottier, "Endogenous protoporphyrin IX, a clinically useful photosensitizer for photodynamic therapy," *J. Photochem. Photobiol. B* **14**, 275-292 (1992).
6. K. Svanberg, T. Andersson, D. Killander, I. Wang, U. Stenram, S. Andersson-Engels, R. Berg, J. Johansson, and S. Svanberg, "Photodynamic therapy of non-melanoma malignant tumours of the skin using topical δ -amino levulinic acid sensitization and laser irradiation," *Br. J. Dermatol.* **130**, 743-751 (1994).
7. Q. Peng, T. Warloe, K. Berg, J. Moan, M. Kongshaug, K.-E. Giercksky, and J. M. Nesland, "5-aminolevulinic acid-based photodynamic therapy: clinical research and future challenges," *Cancer* **79**, 2282-2308 (1997).
8. I. Wang, B. Bauer, S. Andersson-Engels, S. Svanberg, and K. Svanberg, "Photodynamic therapy utilising topical δ -aminolevulinic acid in non-melanoma skin malignancies of the eyelid and the periorcular skin," *Acta Ophthalmol. Scand.* **77**, 182-188 (1999).
9. I. Wang, N. Bendsoe, C. af Klinteberg, A. M. K. Enejder, S. Andersson-Engels, S. Svanberg, and K. Svanberg, "Photodynamic therapy versus cryosurgery of basal cell carcinomas: results of a phase III randomized clinical trial," *Br. J. Dermatol.* **144**, 832-840 (2000).
10. T. J. Dougherty, R. E. Thoma, D. G. Boyle, and K. R. Weishaupt, "Interstitial photoradiation therapy for primary solid tumors in pet cats and dogs," *Cancer Res.* **41**, 401-404 (1981).
11. J. P. A. Marijnissen, J. A. C. Versteeg, W. M. Star, and W. L. J. van Putten, "Tumor and normal response to interstitial photodynamic therapy of the rat R-1 rhabdomyosarcoma," *Int. J. Radiat. Oncol. Biol. Phys.* **22**, 963-972 (1992).
12. C. P. Lowdell, D. V. Ash, I. Driver, and S. B. Brown, "Interstitial photodynamic therapy. Clinical experience with diffusing fibres in the treatment of cutaneous and subcutaneous tumours," *Br. J. Cancer* **67**, 1398-1403 (1993).
13. S. F. Purkiss, R. Dean, J. T. Allardice, M. Grahn, and N. S. Williams, "An interstitial light delivery system for photodynamic therapy within the liver," *Lasers Med. Sci.* **8**, 253-257 (1993).
14. S. Svanberg, S. Andersson-Engels, R. Berg, J. Johansson, and K. Svanberg, "System for laser treatments of tumours," Swedish patent 503 408 (10 June 1996).
15. A. M. K. Nilsson, R. Berg, and S. Andersson-Engels, "Measurements of the optical properties of tissue in conjunction with photodynamic therapy," *Appl. Opt.* **34**, 4609-4619 (1995).
16. N. Ohlsson and O. Rylow, "Development of a multifibre system for interstitial photodynamic therapy of malignant tumours," MSc thesis (Lund Institute of Technology, Lund, Sweden, LRAP-240, 1998).
17. S. R. Arridge, M. Schweiger, M. Hiraoka, and D. T. Delpy, "A finite element approach for modeling photon transport in tissue," *Med. Phys.* **20**, 299-309 (1993).
18. N. S. Ottosen and H. Petersson, *Introduction to the Finite Element Method* (Prentice Hall International, London, 1992).
19. S. S. Rao, *The Finite Element Method in Engineering* (Pergamon, New York, 1989).
20. G. Hedlund and H. O. Sjögren, "Induction of transplantation immunity to rat colon carcinoma isografts by implantation of intact fetal colon tissue," *Int. J. Cancer* **26**, 71-73 (1980).
21. J. Johansson, R. Berg, K. Svanberg, and S. Svanberg, "Laser-induced fluorescence studies of normal and malignant tumour tissue of rat following intravenous injection of δ -amino levulinic acid," *Lasers Surg. Med.* **20**, 272-279 (1997).
22. C. af Klinteberg, M. Andreasson, O. Sandström, S. Andersson-Engels, and S. Svanberg are preparing a manuscript to be called "Compact medical fluorosensor for minimally invasive tissue characterization."
23. T. Andersson, R. Berg, J. Johansson, D. Killander, K. Svanberg, S. Svanberg, and Y. L. Yang, "Photodynamic therapy in interplay with fluorescence diagnostics in the treatment of human superficial malignancies," in *Optical Methods for Tumor Treatment and Detection: Mechanisms and Techniques in Photodynamic Therapy*, T. J. Dougherty, ed., Proc. SPIE **1645**, pp. 187-199 (1992).
24. K. T. V. Grattan and Z. Y. Zhang, *Fiber Optic Fluorescence Thermometry* (Chapman & Hall, London, 1995).

Photodynamic Therapy of Basal Cell Carcinoma with Multi-fibre Contact Light Delivery

M. Soto Thompson^{*,**}, T. Johansson^{*,**}, N. Bendsoe^{†,**}, A. Derjabo[§], J. Kāpostins[§], S. Pålsson^{*,**}, U. Stenram^{*,**}, S. Andersson-Engels^{*,**}, J. Spigulis⁰, S. Svanberg^{*,**} and K. Svanberg^{†,**}

*Department of Physics, Lund Institute of Technology, P.O. Box 118, S-221 00 Lund, Sweden

†Department of Dermatology, Lund University Hospital, S-221 85 Lund, Sweden

‡Department of Pathology, Lund University Hospital, S-221 85 Lund, Sweden

§Latvian Oncology Centre, Hipocrata 4, Riga, LV-1079, Latvia

⁰Department of Atomic Physics and Spectroscopy, University of Latvia, Skunu 4, Riga, LV-1586, Latvia

[†]Department of Oncology, Lund University Hospital, S-221 85 Lund, Sweden

^{**}Lund University Medical Laser Centre, P.O. Box 118, S-221 00 Lund, Sweden

Keywords: Basal Cell Carcinoma, Dosimetry, Interstitial, Photodynamic Therapy, Fluorescence

Abstract

Photodynamic therapy employing δ -amino levulinic acid (ALA) and 635 nm laser irradiation was performed on 29 nodular basal cell carcinoma in 20 Latvian patients, introducing this treatment modality in the Republic of Latvia. While conventional superficial light irradiation was performed for 17 of the tumours, a novel multi-fibre contact light delivery mode was used for 12 tumours. The latter treatment mimicks interstitial light delivery to a thick or deep-lying tumour. On a 7 month follow up, about 80% of the tumours in each treatment category showed a complete response, providing an encouraging prospect also for a true interstitial and interactive treatment modality now under development.

Background

Photodynamic therapy (PDT) utilising topical application of δ -aminolevulinic acid (ALA) has been evaluated in the treatment of various skin malignant and non-malignant lesions¹⁻³. A few randomised clinical trials have also been carried out in order to compare the topical PDT method with other conventional treatment modalities (See, e.g. Ref. 4). For thin lesions, such as superficial Basal Cell Carcinoma (sBCC) and precancerous conditions in the skin, such as actinic keratoses, the technique seems to gain general acceptance. Clearly, there are several treatment modalities in the treatment of BCC. However, within the group of sBCC, ALA-PDT can be considered as the first treatment of choice in particular cases, such as in larger tumours and also in recurrent lesions where other treatment modalities have been performed. As the cosmetic outcome with ALA-PDT generally is very good or excellent⁴, tumour growth in exposed areas, such as the face and upper thoracic wall, can be considered of particular interest.

In superficial tumour growth in the skin, one treatment session is usually sufficient for tumour eradication. For thicker tumours, such as nodular BCCs (nBCC) most often repeated treatment is needed. The situation is the same for PDT of other non-malignant lesions, such as the verrucae virogenes, in which several treatment sessions have to be performed⁵. This group of patients is increasing due to more frequently performed organ transplantation with immunosuppressive treatment. It is also a well known fact that there is a general increase in the incidence of skin malignancies, and ALA-PDT may play an increasing role since the topical treatment modality is comparatively easy to perform.

PDT is usually performed with light in the red part of the wavelength spectrum in order to avoid heavy influence of, e.g., blood absorption. In the case of ALA, one important absorption peak of the ALA-induced photoactive product Protoporphyrin IX (PpIX) is located at 635 nm. At this wavelength the light penetration in tissue is approximately a few millimetres^{6,7}. This depth is usually sufficient in the treatment of sBCC. In thicker tumours the treatment may result in a good healing of the surface tissue but residual tumour may reside underneath.

In order to evaluate the possibility to deliver light more efficiently under such circumstances interstitial PDT (IPDT) is of interest, in particular, if the treatment could be performed in only one or two sessions. As compared to several fractions of ionising radiation or extensive surgery with skin transplantation, this would be an attractive clinical option. In IPDT, light is transported through one or multiple optical fibres, which normally are inserted into the tumour mass. Clearly, there are many applications of IPDT for deep-lying lesions. A number of investigations have been performed employing interstitial light delivery to the tumour⁸⁻¹¹.

Our group is also investigating the potential of interstitial PDT combined with interactive diagnostics and dosimetry. An IPDT system was constructed for light delivery through a multiple fibre arrangement¹²⁻¹⁵. The fibres used for light delivery could also be utilised in other modes for measuring the delivered light dose, for monitoring the drug-related fluorescence, the oxygen content in the tissue and temperature changes during the

treatment. The monitoring of optical parameters relevant for light interaction with tissue is of great importance for developing adequate light dosimetry.

Objectives

The present paper describes PDT treatments of patients with BCCs using our IPDT system adapted with a powerful diode laser, operating at 635 nm^{12,16}. Topical application of ALA was used for inducing the preferential production of photosensitizing agent Protoporphyrin IX (PpIX) in the tumour. The treatment was performed as a feasibility study to evaluate the clinical use of the multiple fibre arrangements with the fibres mounted in close contact to the area under treatment while still not perforating the skin. This arrangement, mimicking the treatment of a tumour symmetrically extending above the (skin) surface, constitutes a valuable development step towards general purpose IPDT. The fibres were placed according to a custom-made computer programme for dosimetry calculations. A comparison with conventional PDT using superficial illumination through one fibre perpendicularly mounted at a distance from the area under treatment was performed. The two treatment modalities are schematically indicated in Figure 1. Even if the material is limited, the treatment results are encouraging. To our knowledge this is the first time this type of multi-fibre contact (MFC) PDT mode with *interactive online* dosimetry calculations has been clinically performed. The work reported in the present paper also constitutes the first PDT treatments performed in the Republic of Latvia.

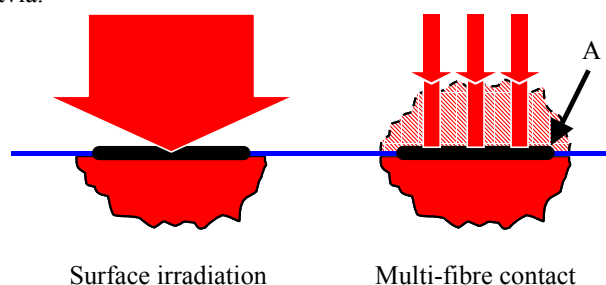


Figure 1 Conceptual difference between PDT with superficial illumination (left) and multi-fibre contact PDT (right). Multi-fibre contact PDT could serve as a model for interstitial PDT, where an upper part of the tumour is imaginary. The indicated point A represents a location to which the treatment light must arrive after extensive multiple scattering.

Patients and methods

Patient selection

The present study was performed in an interdisciplinary collaboration between groups in Riga and Lund, comprising oncologists, pathologists, as well as physicists. Patients were referred to the Department of Oncology at the Latvian Oncology Centre, Riga, from general practitioners distributed over Latvia. All lesions were classified before the treatment either by a punch biopsy procedure for histopathological examination, or by scalpel scrapings for cytological examination. All diagnostic material was sent for microscopic investigation centrally at the Department of Pathology, Riga. Patients with verified BCC were referred to the Oncology Centre for treatment. The patients were

presented with five different treatment modality options, out of which one was ALA-PDT. Approximately half the number of the referred patients chose ALA-PDT as their treatment modality. Approval from the local ethics committee at the Latvian Oncology Centre was obtained for the trial as a feasibility demonstration project.

In total twenty patients (8 male, 12 female; median age 70 years (29-86 years)) with 29 BCC lesions were included. More than half of the lesions (19/30) were located on the back of the patients. Seven lesions were located in the face, two on the thoracic wall and one on the upper arm. All BCC lesions except 2 exhibited a thickness of 2 millimetres or more, and all were classified as nodular BCC:s. A listing of the patients, their lesions, details about the treatments and the histological, clinical and cosmetic outcome is given in Table 1, and in Table 2 the treatment data for the MFC-PDT lesions are given.

Patient #	Age	Gender	Tumour data			PDT Mode		Follow-up – Treatment results						
			Lesion#	Location	Earlier treatment			PAD-microscopy		Histological Outcome	Visual evaluation			
						Cytol.	Microsc.	Clinical outcome			Cosmetic outcome			
			MFC	Sup.	1 month	7 months	1 month	7 months						
1	43	F	1	Back	Surg x 2	-	X	X	-	CR	CR	PR	Acceptable	Good
2	40	M	2	Back	None	-	X	X	-	CR	CR	CR	Excellent	Excellent
3	65	M	3	Back	None	-	X	X	-	PR*	CR	CR	Good	Good
4	69	F	4	Back	None	X	-	-	-	-	-	CR	-	Excellent
5	70	M	5	Back	None	-	X	X	-	CR	CR	-	Good	-
5	70	M	6	Back	None	X	-	-	X	CR	CR	-	Good	-
5	70	M	7	Back	None	-	X	X	-	CR	CR	-	Good	-
6	70	M	8	Back	None	X	-	-	X	CR	CR	CR	Good	Good
7	73	F	9	Back	None	-	X	X	-	CR	CR	CR	Acceptable	Excellent
7	73	F	10	Back	None	X	-	X	X	CR	CR	CR	Excellent	Excellent
8	75	M	11	Back	None	-	X	X	-	CR	CR	CR	Good	Excellent
9	59	F	12	Chin	None	-	X	X	-	CR	CR	CR	Acceptable	Acceptable
10	65	F	13	Thorax	None	X	-	X	X	CR	CR	CR	Good	Excellent
11	76	F	14	Back	Surg	-	X	X	-	CR	CR	-	Acceptable	-
11	76	F	15	Back	Surg	-	X	X	-	CR	CR	-	Acceptable	-
11	76	F	16	Back	Surg	-	X	X	-	CR	CR	-	Acceptable	-
12	29	F	17	Back	None	X	-	X	X	CR	CR	CR	Good	Excellent
13	48	F	18	Trunk	None	X	-	X	X	CR	CR	CR	Acceptable (Hyperpig.)	Acceptable (Hyperpig.)
14	73	F	19	Face	None	-	X	X	-	CR	CR	CR	Excellent	Excellent
15	73	F	20	Face	None	-	X	X	-	CR	CR	CR	Good	Excellent
15	73	F	21	Face	None	-	X	X	-	CR	CR	CR	Good	Excellent
15	73	F	22	Face	None	-	X	X	-	CR	CR	CR	Good	Excellent
16	86	F	23	Face	None	-	X	X	-	CR	CR	-	Excellent	-
17	82	M	24	Arm	None	-	X	X	-	CR	CR	-	Good	-
18	79	M	25	Back	None	X	-	-	-	-	-	-	-	-
19	79	F	26	Back	None	X	-	-	X	CR	CR	CR	Good	Excellent
20	77	M	27	Face	None	X	-	-	X	CR	CR	CR	Good (Hypopigm.)	Good (Hypopigm.)
20	77	M	28	Back	None	X	-	-	X	PR	PR	PR	Good	Good
20	77	M	29	Back	None	X	-	-	X	PR	PR	PR	Good	Good

*Retreatment 1 week post 1st treatment session

Table 1 Patient data and clinical evaluation

Tumour data			Treatment data				
Lesion #	Size (mm)	Thickness (mm)	Fibres used		Total output power (W)	Treatment time (s)	Total delivered energy (J)
			3	6			
4	7 x 8	2-3	X		0.511	729	372
6	12 x 16	2-3	X		0.510	1800	918
8	9 x 11	2-3	X		0.535	1740	931
10	15 x 15	2-3		X	0.635	390	248
13	20 x 25	2		X	0.645	1786	1152
17	12 x 12	2	X		0.545	1620	883
18	11 x 15	2		X	0.594	452	270
25	9 x 12	1		X	0.634	432	274
26	9 x 9	2-3	X		0.59	566	334
27	5 x 7	6-7	X		0.59	1160	684
28	6 x 6	3-4	X		0.59	151	71
29	5 x 5	4-5	X		0.59	488	288

Table 2 Tumour and treatment data for MFC-PDT lesions

Sensitising agent

As a tumour sensitizer δ -amino levulinic acid (Medac, Batch-No.: M01130 AA; 5-aminolevulinic acid) was used. The ALA powder was dissolved in a few drops of physiological saline solution (0.9 %) and mixed with an oil-in-water emulsion (Essex creme) to a concentration by weight of 20 % ALA. The preparation of the tumour area and adjacent surrounding skin was done by cleansing it with 70% ethanol. The treatment area, including a margin of approximately 10 millimetres outside the visible tumour borders, was topically applied with the ALA-containing creme. A plastic film (Tegaderm™) was applied to maintain the creme. As a light protecting shield a layer of a cotton-based medical coverage (Mefix®) was attached to the area.

Fluorescence measurements

The kinetics of the ALA-induced PpIX was monitored by using two different, clinically adapted, point monitoring fluorosensors (details of the systems are presented below). The measurement followed a scheme described in detail previously^{17,18}. These diagnostic measurements were performed at seven different times during the whole treatment procedure. First the autofluorescence from normal skin constituents was recorded serving as a reference for following measurements made at one, two, and four hours after the application of the ALA cream. Also measurements were performed in connection with the therapeutic treatment: before, directly after, and one hour after activation of the PpIX by the therapeutic light. With this scheme we were able to follow the build-up, the photodegradation after the therapeutic treatment as well as the regeneration of the PpIX during the whole treatment. Occasionally, due to practical reasons, some of the

measurements were not conducted on all patients; this applies especially for the measurement one hour after the treatment.

At each time the sites measured were located 10, 5, and 2 millimetres outside of the visible tumour border as well as at the tumour border and at the tumour centre. For lesions of a diameter larger than approximately 8-10 millimetres also a position two millimetres inside the tumour border was measured. Every location was measured three times at the same relative distance to the tumour while moving the fibre slightly between each measurement to avoid local bleaching of the PpIX and to reduce intra-patient variations. During every measurement the site was prepared by temporarily (approximately for three minutes) removing the dressing and excess ALA cream. To measure the spectral response of the systems and providing a spectral correction, a calibrated blackbody radiation source was used.

One of the fluorescence monitoring systems consists of a fibre-based optical multichannel analyser¹⁹. The excitation wavelength used is 405 nm with a pulse length of approximately 3 ns and with a pulse energy of approximately 10 μ J, achieved with a nitrogen laser-pumped dye laser system (Laser Science, Inc. Models VSL 337 and DLM 220, respectively). The excitation light is focused via a 50% beam-splitter onto the proximal tip of a 600 μ m core low-fluorescent quartz fibre. When measuring, the distal tip of the fibre is held in contact with the tissue and the induced fluorescence is guided back through the fibre, deflected by the beam-splitter and focused onto the entrance slit of a spectrometer (Oriel Corp. MS 125) The fluorescence spectrum (200-800 nm) was recorded on a thermoelectrically cooled, image-intensified and gated CCD detector (Andor Technology Instaspec V ICCD) having 1024 \times 128 pixels. In front of the entrance slit a cut-off filter (Schott GG420) was placed to prevent any elastically back-scattered light from reaching the detector.

To increase the signal-to-noise ratio the fluorescence from 20 pulses was added for each point measured. Every such measurement took approximately 2 seconds. For intensity reference, the peak maximum (at approximately 580 nm) of a fluorescence standard (10 mg Rhodamine 6G dissolved in 60 ml ethylene glycol) was recorded in connection with every measurement occasion.

A second fluorosensor system²⁰ was also used to monitor the PpIX fluorescence before, during and after the treatments. The excitation light at 396 nm comes from a continuous wave, violet blue diode laser (Nichia NLHV500). A narrow interference filter (CVI Inc. F25-400-4-0.5) is used to clean up unwanted emission at longer wavelengths. The light is reflected off a dichroic beamsplitter (CVI Inc. LWP-45-RS405-TP-700) and guided into a 600 μ m multimode fused silica fibre (Fiberguide Industries, Superguide) which was held against the tissue. The power at the fibre output was about 1 mW. The tissue fluorescence light is conducted back through the fibre and is transmitted through the beamsplitter and a cut-off filter (Schott GG420), which prevents back-scattered laser light from entering the spectrometer (Ocean Optics Inc. S2000). The light is detected on a 2048 element diode array with a spectral resolution of about 5 nm. The integration time was 250 milliseconds.

Treatment system and study design

A 2 W continuous wave diode laser (CeramOptec Ceralas™ PDT 635) operating at a wavelength of 635 nm was used to activate the PpIX built up in the tumour area. In seventeen lesions the treatment was performed with one fibre with a core diameter of 400 μm perpendicularly mounted at a distance from the area to be treated. A microlens at the end of the fibre provides a uniform top-hat distribution of light avoiding hot spots. The total output power from the laser was varied from 0.22 W to 1.8 W depending on the diameter of the treatment area. The fluence rate was kept in the range of 110-130 mW cm^{-2} or lower not to induce hyperthermal effects^{18,21-23}. The total absorbed dose delivered was 60 J cm^{-2} in all lesions. This resulted in treatment times of approximately 450-1000 seconds, with treatment areas varying between 3-18 cm^2 .

In twelve lesions a multi-fibre arrangement was utilised with either 3 or 6 fibres (8 and 4 lesions, respectively) to deliver the therapeutic light. The fibres were placed in gentle contact with the treatment area. This light delivering system¹² consists of the same laser described above and a beam-splitting unit, as shown in Figure 2. An optical fibre with a core diameter of 400 μm (Anda KP-400L) is used to couple the light from the laser into the beam splitting unit. Here, the light is divided into three or six different beams via a set-up of different lenses and beam-splitters. At the end of each pathway, the light is focused into a treatment fibre (Anda KP-400L). The total output through the treatment fibres is approximately 600 mW. An aluminum ring with holes in separately mounted holders was used to position the fibres as illustrated in Figure 3.

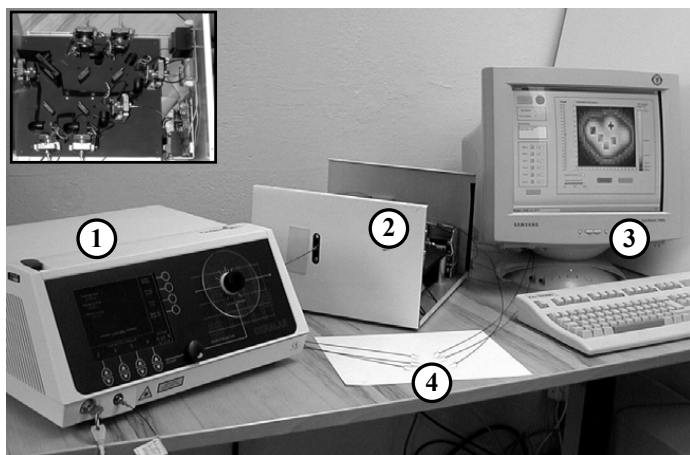


Figure 2 Overview of the therapeutic system; 1) input laser source; 2) beam-splitting unit with top cover removed; 3) controlling hard- and software; 4) output fibres. Top left: Top view of the beam-splitting unit.

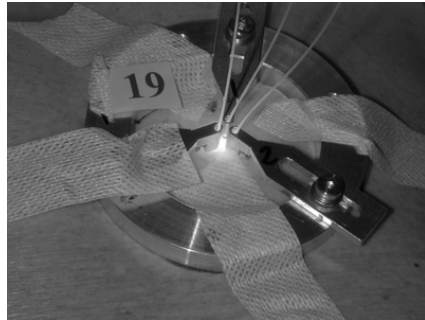


Figure 3 Fibre holder set-up during tumour treatment, with the aluminum ring attached to the patient using adhesive tape. A second fixation to the fibres placed at some distance from the tumour is also utilized (not shown).

The treatment fibres are used to transmit the laser light into the tumour, but can also act as receivers to measure the light fluence rate at the fibre tip. When measuring the fluence rate, a photo diode is switched into the pathway (at the point where the laser light is focused onto the fibre) preventing the laser light from that fibre to reach the tumour. This allows the photodiode to detect the light from the other fibres reaching that part of the tumour. These signals were separately calibrated to fluence rate by placing the fibres into a tank with an Intralipid®/ink mixture with known optical properties.

Specially developed software based on LabVIEW (National Instruments) and C++ (Microsoft Corporation) is used to control the light delivery system. In the first part of the program, the operator has to define the treatment set-up, i.e. the shape and size of the tumour, absorption coefficients and reduced scattering coefficients of the tumour and the healthy surrounding tissue. Then the fibre positions can be either manually selected or the computer can calculate the optimal position. After this, the system can calculate the absorbed fluence rate in the different parts of the tissue.

In the second part of the program, the operator is guided through a few steps such as to put the fibres in the right position, turn the laser on etc, after which the treatment can start. During the treatment, a frequently updated map shows how much light has been delivered to the different parts of the tumour. The map marks in false colours where the tumour threshold dose has been reached. This serves only as a guide because the false colour coding is based on theoretical calculations from the set-up of the treatment. With regular intervals e.g. 30 s, the treatment is interrupted and the fluence rate is measured at the fibre tips. These measurements show if the optical parameters have changed during the treatment. If so, the treatment time has to be altered to fulfil the criterions of treatment. The dose build up in a particular treatment case is illustrated in Figure 4.

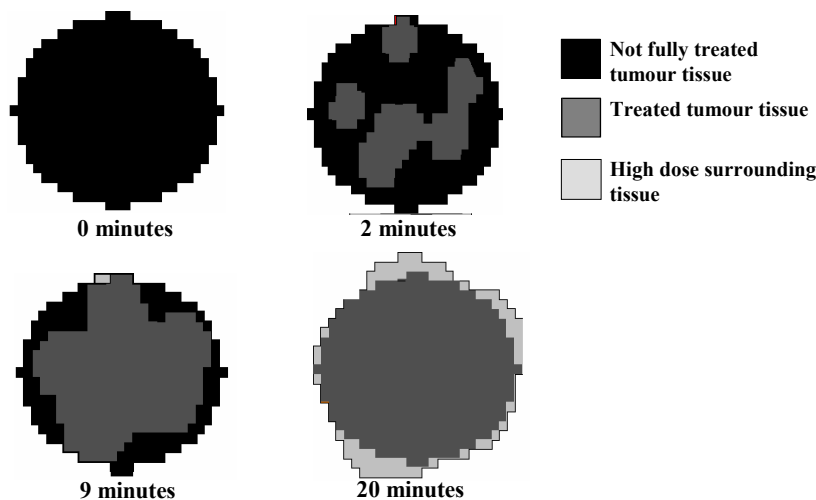


Figure 4. Illustration of the build up of dose in a particular treatment case. The absorption and scattering coefficients for tumour were set to 0.07 mm^{-1} and 1.6 mm^{-1} , respectively, while the corresponding values for normal tissue were 0.05 and 1.6 mm^{-1} . As a threshold dose for full treatment the value 30 J cm^{-3} was selected.

Tumour and treatment data for the 12 cases of MFC-PDT are given in Table 2. As can be seen, treatment times ranged up to 30 minutes and the Joule dose delivered was substantial. The reason for the large integrated dose delivered is the requirement, that the outermost parts of the tumour, say point A in the right part of Figure 1, must be reached by a sufficient number of photons delivered in multiple scattering through the neighbouring tissue from a fibre tip, that can be at a substantial distance away from these external tumour parts. That the light really reached these locations in a way, which is very indirect compared to the direct irradiation illustrated in the left part of Figure 1, is evidenced by the strong bleaching of the PpIX also in these external parts, as recorded by laser-induced fluorescence. Because of the efficient bleaching there is never a risk of overtreating an area although a large light dose is delivered – the treatment is effectively self-terminating. Instead, the selective uptake of the drug in the tumour becomes the factor of major importance.

The follow-up cytological examination on all the treated tumours was performed at the Latvian Oncology Centre. Tissue biopsies were collected for all the tumours treated with MFC-PDT and investigated at the Department of Pathology at the Lund University Hospital.

Results

Fluorescence diagnostic data

Before discussing the clinical outcome of the photodynamic treatments we will show some data from the fluorescence measurements on the tumours. Data from tumour

number 6 (Table 1) are displayed in Figure 5, as obtained with the fluorosensor based on a pulsed excitation source at 405 nm. Recordings at different locations with regard to the tumour extension as described above are shown. The expected observation of a blue fluorescence reduction in the tumour area is verified in the upper part of the figure, pertaining to the time before ALA application. Right before the PDT treatment (six hours after ALA application), the strong selective build-up of PpIX in the tumour area is illustrated in the middle part of the figure. Finally, heavy PpIX bleaching is evident all through the treated area. Bleaching is also evident at 10 mm outside the visible tumour border.

Figure 6 shows the bleaching of the PpIX during a tumour treatment employing the multi-fibre contact PDT mode. Data are from tumour number 6 (Table 1), and the individual curves are recorded at the same location just inside the tumour border and corresponding to a point like A in Fig. 1. This recording and the evaluated bleaching data – the intensity of the 635 nm fluorescence peak - shown in Figure 7, clearly illustrate how the required dose is successively delivered to the outer tumour parts in diffusive light scattering.

Clinical outcome

The results of the treatments are included for each treated tumour in Table 1. At 1 month after the treatment all but two patients returned for histological and visual assessment. It was found that 25 out of 27 inspected tumours (93 %) showed a complete response, while the remaining two had a partial response. In particular, 8 out of 10 inspected tumours (80%), treated by MFC-PDT showed a complete response, while the two remaining (which both were very thick) showed partial response.

Seven months after the treatment the patients (except for four individuals) again returned to the Oncology Centre for clinical assessment. 17 out of 20 inspected tumours (85%) showed a complete response, while the remaining three had a partial response. Out of these partial responding tumours one had resisted many earlier attempts for curing. Again, 8 out of 10 evaluated tumours (80%) treated by MFC-PDT showed a complete response, with the two remaining (the same thick ones as at the 1 month follow up) showed a partial response. All patients with only partial response were subsequently treated by other modalities at the Latvian Oncology Centre.

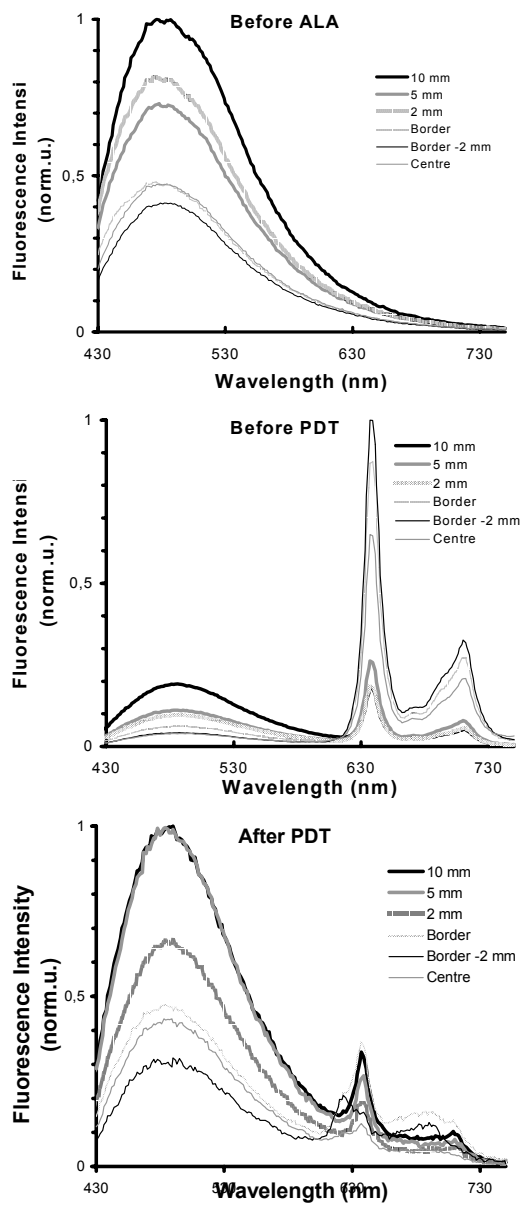


Figure 5 a,b,c. Case study of the temporal and geometrical variation of the fluorescence spectra of the skin a) before applying the ALA cream, b) before PDT; 6h after ALA cream application, c) after the therapeutic light delivery. In all of the figures above the measured sites were: 10, 5, and 2 mm outside the visible tumour border, at the tumour border, and 2 mm inside the tumour border, and at the tumour centre. Every spectrum is the mean value of three independent measurements at the same distance to the tumour border.

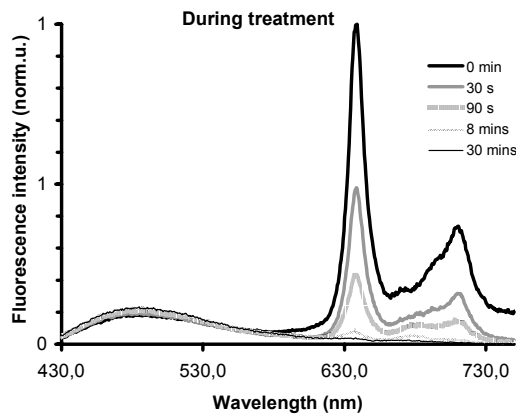


Figure 6 Temporal evolution of the skin fluorescence in one fixed point during multi-fibre contact PDT. At each measurement occasion the therapeutic light has been shut off. The different curves correspond to increasing irradiating times.

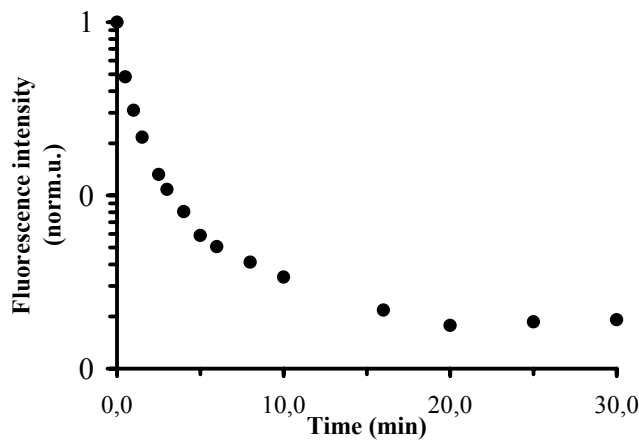


Figure 7 The fluorescence intensity at the 635 nm PpIX peak during the course of a PDT treatment.

The cosmetic outcome was also evaluated both at the 1- and the 7-month follow-up occasions. At the latter, more relevant evaluation, 12 out of 20 locations (60%) showed an excellent cosmetic outcome, while 6 had a good and 2 an acceptable outcome. In particular, 5 out of 10 MFC-PDT treated tumours showed an excellent cosmetic outcome. As an example of the extensive photographic documentation performed on the patients, a tumour, treated with MFC-PDT, is shown in Figure 8, before, 6 days after and 7 months after the PDT.



Figure 8 Photographs before, 6 days after and 7 month after MFC-PDT of tumour nr 4 (Table 1)

Conclusions

Photodynamic tumour therapy could successfully be introduced on the Latvian health-care scene in treatments of 29 nodular basal cell carcinomas in 20 patients. The efficacy as judged at a 7 month follow-up was 85 % complete response, and partial response in the remaining tumours. This is comparable with the outcome of a recent Swedish clinical trial⁴. Of particular interest was the use of a new treatment modality employing multi-fibre contact delivery of the therapeutic light. This is a developmental variety of interstitial and interactive PDT, which is now being developed for the eradication of thick and /or deep-lying tumours. Even if the number of treated tumours is limited, the contact delivery modality indicates the same efficacy as the conventional surface irradiation. The comparable and good cosmetic outcome indicates that the new modality, of great potential for future complex tumour treatment cases, is not accompanied with excess heat delivery to the tissue.

Acknowledgements

This work was supported by the European Commission under the EU-IHP Access to Research Infrastructures Programme (Contract HPRI-CT-1999-00041), the Swedish Strategic Research Foundation and the Swedish Institute (Visby Programme).

References

1. Kennedy JC, Pottier RH, Pross DC. Photodynamic therapy with endogenous protoporphyrin IX: Basic principles and present clinical experience. *J Photochem Photobiol B* 1990; **6**: 143-8.
2. Svanberg K, Andersson T, Killander D, *et al.* Photodynamic therapy of non-melanoma malignant tumours of the skin utilizing Topical δ -amino levulinic acid sensitization and laser irradiation, *British J of Dermatology* 1994; **130**: 743.
3. Peng Q, Warloe T, Berg K, *et al.* 5-aminolevulinic acid-based photodynamic therapy: Clinical research and future challenges. *Cancer* 1997; **79** : 2282-308.
4. Wang I, Bendsoe N, af Klinteberg C, *et al.* Photodynamic therapy versus cryosurgery of basal cell carcinomas; results of a phase III randomized clinical trial. *Br J Dermatol* 2001; **144**: 832-40.
5. Stender I-M, Na R, Fogh H, *et al.* Photodynamic therapy with 5- aminolevulinic acid or placebo for recalcitrant foot and hand warts: randomised double-blind trial. *The Lancet* 2000; **355**: 963-6.
6. Star WM. Light dosimetry *in vivo*. *Phys Med Biol* 1997; **42**: 763-87.
7. Svaasand LO, Wyss P, Wyss MT, *et al.* Dosimetry model for photodynamic therapy with topically administered photosensitizers. *Lasers Surg Med* 1996; **18**: 139-49.
8. Lowdell CP, Ash DV, Driver I, Brown SB. Interstitial photodynamic therapy. Clinical experience with diffusing fibres in the treatment of cutaneous and subcutaneous tumours. *Br J Cancer* 1993; **67**: 1398-403.
9. Dougherty TJ, Thoma RE, Boyle DG, Weishaupt KR. Interstitial photoradiation therapy for primary solid tumors in pet cats and dogs. *Cancer Res* 1981; **41**: 401-4.
10. Marijnissen JPA, Versteeg JAC, Star WM, van Putten WLJ. Tumor and normal response to interstitial photodynamic therapy of the rat R-1 rhabdomyosarcoma. *Int J Radiat Oncol Biol Phys* 1992; **22**: 963-72.
11. Purkiss SF, Dean R, Allardice JT, *et al.* An interstitial light delivery system for photodynamic therapy within the liver. *Lasers Med Sci* 1993; **8**: 253-7.
12. Johansson T, Soto Thompson M, Stenberg M, *et al.* Feasibility study of a novel system for combined light dosimetry and interstitial photodynamic treatment of massive tumors. *Appl Opt* 2002; **41**: 1462-8.
13. Stenberg M, Soto Thompson M, Johansson T, *et al.* Interstitial photodynamic therapy - diagnostic measurements and treatment in malignant experimental rat tumours. *Proc. SPIE*; **4161**: 151-7.
14. Soto Thompson M, Johansson T, Pålsson S, *et al.* Novel system for integrated interstitial photodynamic therapy, dosimetry measurements and prediction of treatment outcome. 2001; IPA World Congress of Photodynamic Medicine, Vancouver, BC, Canada.
15. Soto Thompson M, Stenberg M, Johansson T, *et al.* Novel system for integrated interstitial photodynamic therapy; dosimetry measurements and treatment outcome. 2001; IPA World Congress of Photodynamic Medicine, Vancouver, BC, Canada.

16. Svanberg S, Andersson-Engels S, Berg R, *et al.* System for laser treatments of tumours. Swedish Patent SE9501278, 1996.
17. af Klinteberg C, Enejder AMK, Wang I, *et al.* Kinetic fluorescence studies of 5-aminolaevulinic acid-induced protoporphyrin IX accumulation in basal cell carcinomas. *J Photochem Photobiol B* 1999; **49**: 120-8.
18. Soto Thompson M, Gustafsson L, Pålsson S, *et al.* Photodynamic therapy and diagnostic measurements of basal cell carcinomas using esterified and non-esterified 5-aminolevulinic acid. *J Porphyrins Phthalocyanines* 2001; **5**: 147-53.
19. af Klinteberg C, Andreasson M, Sandström O, *et al.* Compact medical fluorosensor for minimally invasive tissue characterisation, 2002; (to appear)
20. Gustafsson U, Pålsson S, Svanberg S. Compact fibre-optic fluorosensor using a continuous wave violet diode laser and an integrated spectrometer. *Rev Sci Instrum* 2000; **71**: 3004-6.
21. Svaasand LO. Photodynamic and photohyperthermic response of malignant tumors. *Med Phys* 1985; **12**: 455-61.
22. Warloe T, Peng Q, Moan J, *et al.* Photochemotherapy of multiple basal cell carcinoma with endogenous porphyrins induced by topical application of 5-aminolevulinic acid. In: *Photodynamic Therapy and Biomedical Lasers* (Spinelli P, Dal Fante M, Marchesini R, eds), Amsterdam: Elsevier Science Publishers B.V., 1992: 449-53.
22. Pålsson S, Gustafsson L, Soto Thompson M, *et al.* Kinetics of the superficial perfusion and temperature in connection with photodynamic therapy of basal cell carcinomas using esterified and non-esterified 5-aminolevulinic acid, 2001; (to appear)